Angular Structure of High Transverse Momentum Production in Semi-Inclusive Deep Inelastic Scattering at Next-to-Leading Order

Dissertation
der Mathematisch-Naturwissenschaftlichen Fakultät
der Eberhard Karls Universität Tübingen
zur Erlangung des Grades eines
Doktors der Naturwissenschaften
(Dr. rer. nat.)

vorgelegt von
Felix Kunzelmann
aus Stuttgart

Tübingen
2025

Gedruckt mit Genehmigung der Mathematisch-Naturwissenschaftlichen Fakultät der Eberhard Karls Universität Tübingen.

Tag der mündlichen Qualifikation:	19.01.2026
Dekan:	Prof. Dr. Thilo Stehle
1. Berichterstatter:	Prof. Dr. Werner Vogelsang
2. Berichterstatter:	apl. Prof. Dr. Marc Schlegel

Abstract

Nearly all visible matter in the universe is made of protons and neutrons, yet their internal structure is not fully understood. In particular, the dynamics of the quarks and gluons inside them remains an open question. To address this, the Electron-Ion Collider (EIC), currently under construction at Brookhaven National Laboratory, is designed to provide an unprecedented three-dimensional view of the internal structure of a proton, including the transverse momentum distribution of its constituents.

To match the experimental precision of the EIC, equally precise theoretical predictions are essential. One of the key processes that the EIC will study is semi-inclusive deep inelastic scattering (SIDIS), where the transverse momentum of the produced hadron offers crucial insights into the momentum distribution of the internal structure of the proton.

In general, the generation of transverse momentum in the final-state hadron can have two sources. On the one hand, from the internal structure of the proton, which provides the scattering parton with an initial transverse momentum, and on the other hand, from a recoil off an additionally radiated particle.

This thesis focuses on the second case: transverse momentum generated via perturbative Quantum Chromodynamics (QCD) effects. It presents the first fully differential next-to-leading order calculation of SIDIS at high transverse momentum, retaining the full angular structure of the cross section. This angular structure is vital for isolating transverse momentum dependent effects in experimental data and in extracting transverse momentum dependent parton distribution functions.

By providing all the required ingredients for the next-to-leading order calculation and laying out the technical and conceptual steps in detail, this thesis aims to offer a solid foundation for future numerical studies and extensions to lower transverse momenta. It aims to provide a solid basis for comparison with the low transverse momentum results and supports ongoing efforts to unravel the inner structure of the proton through high-precision QCD.

Kurzfassung

Nahezu die gesamte sichtbare Materie im Universum besteht aus Protonen und Neutronen, dennoch ist ihre innere Struktur noch nicht vollständig verstanden. Insbesondere die Bewegungsprozesse der Quarks und Gluonen in ihrem Inneren sind nach wie vor ungeklärt. Um diese Frage zu klären, wurde der gerade am Brookhaven National Laboratory im Bau befindliche Electron-Ion Collider (EIC) entworfen. Er soll einen nie dagewesenen Einblick in den dreidimensionalen inneren Aufbau der Protonen und insbesondere die transversale Impulsverteilung ihrer Bestandteile ermöglichen.

Um der experimentellen Präzision des EIC gerecht zu werden, sind genauso präzise theoretische Vorhersagen unerlässlich. Einer der zentralen Prozesse, die der EIC untersuchen wird, ist die semi-inklusive tief inelastische Streuung (SIDIS), bei der der transversale Impuls des erzeugten Hadrons wichtige Erkenntnisse über die Impulsverteilung der inneren Struktur des Protons liefert.

Im Allgemeinen kann die Erzeugung von transversalen Impulsen des Hadrons im Endzustand zwei Ursachen haben. Einerseits aus der inneren Struktur des Protons, die dem streuenden Parton einen anfänglichen Impuls verleiht, und andererseits aus dem Rückstoß eines zusätzlich abgestrahlten Teilchens.

Diese Arbeit konzentriert sich auf den zweiten Fall: transversaler Impuls, der durch perturbative Effekte der Quantenchromodynamik (QCD) erzeugt wird. Sie präsentiert die erste vollständige differentielle Berechnung von SIDIS in nächstführender Ordnung bei hohem transversalen Impuls unter Wahrung der vollständigen Winkelstruktur des Querschnitts. Die Winkelstruktur ist entscheidend für die Trennung transversalimpulsabhängiger Effekte in experimentellen Daten und für die Ableitung transversalimpulsabhängiger Partonverteilungsfunktionen.

Durch die Darlegung aller erforderlichen Komponenten für die Berechnung der nächstführenden Ordnung und die detaillierte Darstellung der technischen und konzeptionellen Schritte soll diese Arbeit eine robuste Grundlage für zukünftige numerische Studien und für Erweiterungen auf geringere transversale Impulse bieten. Sie soll eine solide Basis für den Vergleich mit den Ergebnissen bei niedrigem Transversalimpuls bieten und die laufenden Bemühungen zur Entschlüsselung der inneren Struktur des Protons durch hochpräzisions QCD unterstützen.

Contents

Chapter 1

Introduction

One of the oldest and most fundamental questions in human history is deceptively simple: *What is the world made of?* The idea that matter is composed of indivisible building blocks has appeared across many ancient civilizations [1]. Although these early theories lacked experimental evidence, they shared the notion that nature is ultimately constructed from elementary, indivisible components.

In ancient Greece, the philosopher Democritus and his teacher Leucippus coined the term "atom" - from the Greek word *atomos*, meaning "uncuttable" - for those elementary building blocks of nature [2]. They imagined atoms to be imperceivably small and differing in shape. Visible matter was supposed to be built from those atoms and get its characteristics from their mixing ratio. Although this theory was speculative, it captured the deep human desire to reduce the complexity of the natural world to its simplest constituents.

The search for the basic elementary components of nature in the modern scientific era began in the early 19th century, when John Dalton used the term "atom" to describe chemical elements, assuming that these atoms are the most basic components of nature [3]. He proposed that each element consists of identical atoms and that all substances are composed of a combination of elements. This provided the foundational structure of chemistry, where atoms can be combined into molecules according to fixed ratios. In his theory, he asserted that atoms could neither be created nor destroyed, only rearranged [4].

However, while studying atoms more closely, the apparent simplicity of Dalton's atomic theory had to give way to a deeper internal structure of the atom. In 1897, Joseph John Thomson discovered the electron, a negatively charged constituent of the atom, demonstrating that atoms are not indivisible [5]. A decade later, Ernest Rutherford identified the atomic nucleus as a small, dense region at the center of the atom [6]. He introduced the concept of the atomic number, corresponding to the positive charge carried by the nucleus, and postulated the existence of an additional electrically neutral particle to account for

the mass of the nucleon. This neutron was experimentally confirmed by James Chadwick in 1932 [7].
These discoveries led to a new understanding of matter: all known elements were found to be composed of just three particles: electrons, protons, and neutrons. For a time, it seemed that the quest to find the fundamental building blocks of nature, which started with the ancient Greeks, had come to an end.
However, this only marked the beginning of modern particle physics. In the 1950s and 1960s, the construction of high-energy particle accelerators opened a new frontier. It was now possible to probe matter at even smaller scales, and, most prominently, accelerator experiments revealed an enormous number of new short-lived, strongly interacting particles. The overwhelming number and apparent lack of structure among these new particles led to the term "particle zoo" and presented a new challenge: to uncover the underlying structure and organize these particles.
The breakthrough came with the realization - pioneered by Robert Hofstadter through deep inelastic scattering experiments [8] - that strongly interacting particles are not fundamental, but have an internal structure: they are bound states of quarks held together by massless force-carrying particles: the gluons. This insight led to the formulation of Quantum Chromodynamics (QCD), the theory covering the strong interactions and dynamics of quarks and gluons.
Since its formulation, QCD has been remarkably successful in explaining the structure of hadrons. It became the predominant theory for precision physics in high-energy collisions owing to an emergent property of QCD, where the coupling strength decreases at high energies: asymptotic freedom [9–11]. Despite enormous advances in QCD over the past half-century, the dynamics of quarks and gluons inside hadrons are not fully understood. The questions of how mass arises from the interactions of quarks and gluons inside the hadron, how spin emerges from the properties of the hadron's constituents, and how quarks and gluons are distributed inside the hadrons are still unanswered. All these questions are among the key science goals of the upcoming Electron-Ion Collider (EIC) [12–15]. In particular, the EIC is designed to study the three-dimensional structure of nucleons, with a central goal of mapping out the transverse momentum dependent distributions (TMDs) of quarks and gluons within the proton with unprecedented resolution.
Established TMD studies most notably include the HERMES experiment at the HERA particle accelerator at DESY [16] and the COMPASS experiment at the LHC at CERN [17], which pioneered TMD studies in the early 2000s. In recent years, efforts to extract TMDs through global fits to existing data have intensified [18–23]. These studies yield notable discrepancies in the extracted TMDs, despite being based on largely overlapping data sets. Such tensions are expected to diminish with the influx of new results from

existing experiments and, ultimately, with the more precise data that will be generated at the upcoming EIC. Nevertheless, it remains essential to complement experimental progress with more precise theoretical calculations, thereby providing a solid foundation for future global fits and ensuring a consistent interpretation of the data.

The EIC will utilize a process called electron-proton scattering extensively to study the proton's interior. This process provides a clean method to access the structure of the proton. Since the electron is point-like and lacks internal structure, any observed structure coming from the incident particles must therefore come from the initial proton. In particular, the EIC will use semi-inclusive deep inelastic scattering (SIDIS) processes to access the TMDs of quarks and gluons inside the proton; here, both the scattered electron and one produced hadron in the final state are observed. The measurement of the final-state hadron will contain the necessary information to recover the transverse momentum exchanged during scattering. In addition, it will be necessary to separate the results with respect to the angular distributions of the outgoing electron to extract the TMDs from the results.

SIDIS provides a unique window into transverse momentum dependent distributions, as the observed momentum of the final state hadron is directly linked to the internal structure of the incident proton. However, it is important to recognize that transverse momentum in the final state can also be generated perturbatively through the recoil of an additional radiated particle, possibly resulting in large transverse momenta. This mechanism does not reflect intrinsic structure of the proton, as the transverse momentum is solely generated by perturbative effects.

This results in two regimes. A low p_T regime, where the transverse momentum of the hadron is primarily generated by the intrinsic motion of the partons inside the proton and is described by TMD factorization. And a high p_T regime, where the resulting transverse momentum of the hadron is generated by perturbative effects and described by collinear factorization.

While each regime offers a clear picture for the respective transverse momentum scales, they overlap in a region of intermediate transverse momentum where both approaches should, in theory, be valid. In practice, however, a matching of the results from both regions reveals inconsistencies for some observables [24, 25]. This has motivated efforts to improve the understanding of both regimes and to explore alternative strategies for interpolating between them [26]. Moreover, even in the region of high transverse momentum - where perturbative QCD should provide reliable predictions - existing calculations do not fit the experimental data [27], demanding further investigations in that regime.

For the high p_T regime, the next-to-leading order corrections to SIDIS were first computed about two decades ago [28–30] and revisited in light of new data in 2019 [31], substantiating the tension mentioned in [27].

To deepen our understanding of this regime, it is natural to extend these calculations to retain the explicit angular structure, which is integrated over in the previously mentioned literature. By explicitly calculating the angular structure for the high transverse momentum regime, it is possible to extract the structure functions, and in turn it allows, in principle, the extraction of TMDs. The fully differential leading order calculation with explicit angular structure was performed in [32–34]. The present work extends this calculation to next-to-leading order accuracy, meeting the precision demand of the upcoming EIC and strengthens the theoretical foundation needed to deduce the three-dimensional structure of the proton from its high precision measurements.

This thesis continues in Chapter 2 by introducing basic concepts of QCD, with a focus on perturbative calculations. The QCD Lagrangian is introduced, emphasizing its gauge symmetries and non-abelian nature. From there, the discussion transitions to perturbative QCD by establishing the running of the QCD coupling and outlining how predictions involving strongly interacting particles can be made. Subsequently, the origin of potential divergences is discussed, and methods for regularizing and renormalizing them are provided. The chapter concludes by exploring the concept of factorization, focusing on the handling of collinear divergences.

Chapter 3 introduces the central process of this thesis: semi-inclusive deep inelastic scattering. The kinematics of the process are developed in all relevant reference frames, and the hadronic and leptonic tensors are introduced, which naturally separate the hadronic and leptonic interactions. Both tensors are then decomposed into components associated with distinct angular dependencies to facilitate the extraction of angular modulations in experimental observations. This chapter also applies the factorization formula to SIDIS and introduces useful variables for calculating SIDIS cross sections.

The following section, Chapter 4, is dedicated to the technical aspects of perturbative calculations, providing a comprehensive overview of all strategies and procedures used in the next-to-leading order calculation. It starts by explaining the computation of color factors and spinor sums and continues with the practical evaluation of loop integrals, which arise from virtual corrections at next-to-leading order. Next, a brief overview of calculations in d-dimensions is presented before diving into the computation of phase space factors and the associated phase space integration. Finally, the subtraction of collinear divergences using splitting functions is discussed in this chapter.

The leading-order cross section of SIDIS at high transverse momentum is calculated in Chapter 5. It presents the computation of the qq-channel in detail and provides results for the qg- and gq-channels, all while retaining linear terms in the dimensional regulator ϵ, which are required for the next-to-leading order calculation.

The heart of this thesis is contained in Chapter 6, which presents the full next-to-leading

order calculation of SIDIS at high transverse momentum. It begins with a discussion of the virtual corrections for all relevant channels and is laid out in great detail for the qq-channel. This is followed by an in-depth treatment of the real corrections. Going into detail for the calculation of the most complex qq-channel and focusing on the differences for the other channels. Lastly, the real and virtual corrections are combined, and collinear divergences are systematically subtracted to obtain the finite, fully differential hard partonic cross section at next-to-leading order accuracy.
Chapter 7 provides a brief summary of the thesis and outlines promising directions for future work.
Finally, the Appendix contains more detailed intermediary results, some explicit code, the collection of all used tools and the declaration of authorship.

Chapter 2

Theoretical Framework

This chapter establishes the theoretical foundation for the analysis presented in the subsequent sections. It provides an overview of the key principles of Quantum Chromodynamics, with an emphasis on aspects relevant to high-energy processes. While technical derivations are deferred to Chapters 3 and 4, this section aims to present a clear conceptual understanding of the fundamental structures underlying perturbative QCD.

The discussion begins with a concise review of Quantum Chromodynamics, highlighting the central role of gauge symmetry and the non-abelian gauge group SU(3), which governs the interactions of color-charged particles, such as quarks and gluons. This section also introduces several essential identities used later for the computation of color factors.

Next, the construction of the QCD Lagrangian is outlined, beginning with the free Lagrangian and proceeding with the introduction of local gauge invariance. The requirement of local gauge symmetry not only introduces interactions but also necessitates the inclusion of gluon fields as mediators of the strong force. Together with the gluons, the auxiliary ghost particles are introduced to complete the QCD Lagrangian.

Various approaches exist for computing physical observables from the QCD Lagrangian. However, the focus of this work is on the high-energy regime. In this context, the concept of asymptotic freedom plays a crucial role. The energy dependence of the strong coupling constant, governed by the renormalization group equation, provides the theoretical justification for applying perturbative methods at large momentum transfers. Section 2.2 derives the running of the QCD coupling and explains how it facilitates a perturbative expansion of the strong interaction.

The theory of perturbative QCD is then introduced in detail. Beginning with the definition of scattering cross sections, the formalism proceeds through the S-matrix, the construction of the scattering amplitudes, and the definition of the Feynman rules.

Beyond leading order, perturbative calculations inevitably contain divergences. These di-

vergences, arising from ultraviolet (UV), infrared (IR), and collinear regions of loop and phase space integrals, require sophisticated techniques for their proper treatment. Sections 2.5 and 2.5.1 introduce the origin of these divergences and outline how they can be systematically regularized, in particular, through dimensional regularization in Section 2.5.2.
Furthermore, renormalization is presented as a means to absorb UV divergences into redefined physical parameters in Section 2.5.3. The importance of renormalization schemes is discussed, with a focus on the $\overline{\text{MS}}$ scheme.
While the focus of this thesis remains on the perturbative regime, long-distance (non-perturbative) physics must still be accounted for. This is achieved through factorization, which separates perturbatively calculable short-distance hard scattering from non-perturbative quantities such as parton distribution functions (PDFs) and fragmentation functions (FFs). Additionally, the factorization theorem provides a mechanism for the systematic subtraction of collinear divergences, which are absorbed into the PDFs and FFs, ensuring the finiteness of perturbatively calculable observables. This is explained in Section 2.6.

2.1 Quantum Chromodynamics

The 1950s marked the advent of spark chambers and bubble chambers[1], revolutionary technologies that led to the discovery of a vast number of new, strongly interacting particles, collectively known as hadrons. The sheer abundance of these newly observed particles made it difficult to accept them all as fundamental particles. The situation was chaotic.
An initial attempt was made to classify these particles by their electric charge and isospin, a concept originally developed by Werner Heisenberg and Eugene Wigner to describe the binding of protons and neutrons in atomic nuclei [36, 37]. In the following years, Murray Gell-Mann and Kazuhiko Nishijima expanded this concept by introducing strangeness as a new quantum number [38–40]. This effort to organize the "particle zoo" culminated in the introduction of the eightfold way, a classification scheme proposed independently by Murray Gell-Mann and Yuval Ne'eman in 1961 [41, 42]. By 1964, Murray Gell-Mann and George Zweig further refined this idea with the quark model, which proposed that hadrons are not fundamental particles but rather bound states of fundamental point-like spin-1/2 particles known as quarks [43–45]. This model originally included three quark flavors: up, down, and strange. In this framework, hadrons are regarded as bound states of quarks and can be classified into two categories: baryons, composed of three quarks,

[1] David A. Glaser was awarded the 1960 Nobel Prize in Physics for the invention of the bubble chamber [35].

and mesons, composed of a quark-antiquark pair. The introduction of the three quark flavors provided an elegant explanation for the group structure of the eightfold way and even allowed for predictions of previously undiscovered particles. One such prediction was the Ω^- baryon, composed of three strange quarks, which was subsequently observed at Brookhaven National Laboratory in 1964 [46]. Despite its success, the quark model faced a fundamental problem: it seemingly violated the Pauli exclusion principle [47]. It did not seem possible to have three identical quarks in a bound state, but this was exactly what the theory predicted for the new Ω^- baryon and also for the already established Δ^{++} baryon[2], which, in the quark model, consists of three up quarks. This inconsistency was resolved by introducing color as a new quantum number for the quarks. Oscar W. Greenberg and Yoichiro Nambu independently proposed that quarks carry one of three color charges [50, 51], the cornerstone of Quantum Chromodynamics.

Despite the predictive power of the quark model, many physicists remained skeptical about quarks being real physical particles. All searches for free quarks have failed, leading some to believe that quarks are merely a mathematical construct to describe hadrons rather than actual fundamental particles. This perspective changed in 1969, when deep inelastic scattering experiments at the Stanford Linear Accelerator Center (SLAC) provided the first direct evidence that protons are composed of smaller, point-like constituents [52, 53]. Over the next decade, the quark model was further refined. In 1970 Sheldon Lee Glashow, John Iliopoulos and Luciano Maiani predicted the existence of a fourth quark flavor, charm [54]. In 1973, Makoto Kobayashi and Toshihide Maskawa predicted a third family of quarks with the bottom and top quarks [55], for which they were awarded half of the 2008 Nobel Prize in Physics. In the following year, experiments caught up, and the charm quark was discovered experimentally by two independent research teams. One at SLAC, led by Burton Richter [56] and one at the Brookhaven National Laboratory, led by Samuel C. C. Ting [57]. For their discovery, Samuel C. C. Ting and Burton Richter were awarded the 1976 Nobel Prize in Physics.

While the bottom quark was experimentally confirmed in 1977 at Fermilab [58], the discovery of the top quark proved more challenging because of its astonishingly large mass of 172 GeV, which is nearly as massive as a gold atom. It was not until 1995 that two research teams at Fermilab observed the top quark [59, 60].

The quark model was a huge success, but it has one major disadvantage. It does not describe the dynamics of quark interactions. To fully describe this interaction, theorists turned to gauge theories, which were already successful in describing electromagnetism. The key inspiration came from Chen Ning Yang and Robert Mills, who developed a frame-

[2]The Δ^{++} baryon had already been detected in 1952 at the University of Chicago cyclotron [48, 49].

work for gauge theories based on non-abelian Lie groups [61] in 1954. Building upon this, in 1973, Harald Fritzsch, Murray Gell-Mann, and Heinrich Leutwyler formulated a theory where the strong force arises from a local SU(3) gauge symmetry. This gauge symmetry gives quarks the color that was introduced by Greenberg in 1964 [50]. The theory born from this became known as Quantum Chromodynamics.
Readers interested in the formal construction of the QCD Lagrangian can refer to standard textbooks, such as [62–65]. Before diving into these aspects, however, it is useful to first recall some mathematical preliminaries about Lie groups, which form the backbone of gauge theories.

2.1.1 The Lie Group SU(3)

A fascinating insight from physics is that all fundamental forces can be described using the Lagrangian formalism. Moreover, three of the four fundamental forces - the electromagnetic, weak, and strong interactions - can be unified within a single framework: the Standard Model. Each of these theories are gauge theories. The concept of gauge theories is based on the idea of symmetry. These symmetries are captured by the gauge groups, which are the subject of this section.
The gauge group for Quantum Electrodynamics is the Lie group U(1). For the electroweak interaction, it is $\mathrm{SU}(2) \otimes \mathrm{U}(1)$. The gauge group for the interactions of interest here, the strong interactions, is SU(3). A key distinction between Quantum Electrodynamics and Quantum Chromodynamics lies in the nature of their respective gauge groups. The gauge group for QED, the group U(1), is abelian, while SU(3), the gauge group of QCD, is non-abelian meaning that its elements do not commute. This has far-reaching consequences, as can already be seen in the following sections.[3]
The most prominent examples of Lie groups in physics are the special linear group of degree N, $\mathrm{SL}(N)$, the orthogonal group of degree N, $\mathrm{O}(N)$, its special subgroup $\mathrm{SO}(N)$ and the unitary group of degree N, $\mathrm{U}(N)$, with its special subgroup $\mathrm{SU}(N)$. All these Lie groups are subgroups of the group of all invertible matrices $\mathrm{GL}(N)$, and for the purpose of this thesis, it is sufficient to view Lie groups as subgroups of the group of all invertible matrices. This is generally true for all compact Lie groups [71], and only compact Lie groups are considered here. This is by no means necessary, but it makes it easier to understand the definitions. By choosing matrices to describe a Lie group, the multiplication of two group elements is automatically defined as matrix multiplication. In fact, this description of Lie group elements as matrices is a representation, since it defines an action of a group

[3] Here the focus is on the relevant information for this thesis about Lie groups. For a more complete introduction to Lie Groups see [66–70].

element on a vector, again by multiplication. The smallest faithful[4] representation of a Lie group is called fundamental representation.[5] In the following, the fundamental representation is the default representation and is always assumed unless stated otherwise. The only other representation that will be encountered is the adjoint representation. If this representation is used, it is always clearly stated.

Lie Groups and corresponding Lie Algebras

Lie groups encode all the information required to describe the symmetries of field theories. However, their structure can often be analyzed more efficiently using an alternative approach. A key observation is that many fundamental properties of Lie groups are determined by their behavior at the identity. This insight leads to the introduction of Lie algebras, which provide a rigorous mathematical framework for studying these symmetries while having the simpler properties of a vector space. For matrix Lie groups, there is a simple way to compute the corresponding Lie algebra. This is done via the exponential function of a matrix $X \in \mathcal{M}_n(\mathbb{C})$ defined by the series expansion[6]:

$$\mathrm{e}^X := \sum_{k=0}^{\infty} \frac{X^k}{k!} \ . \tag{2.1}$$

With that the Lie algebra of a matrix Lie group G is the set

$$\mathfrak{g} := \left\{ X \in \mathcal{M}_n(\mathbb{C}) \middle| \ \mathrm{e}^{\mathrm{i}tX} \in G \ \ \forall\, t \in \mathbb{R} \right\} \ , \tag{2.2}$$

together with the Lie bracket given by

$$[X, Y] := XY - YX \ \ \forall\, X, Y \in \mathfrak{g} \ . \tag{2.3}$$

It is common to denote the Lie algebra in lower-case Fraktur of the corresponding Lie group symbol, here $\mathfrak{g}$. For a Lie algebra, the Lie bracket must satisfy the Jacobi identity:

$$[[X, Y], Z] + [[Z, X], Y] + [[Y, Z], X] = 0 \quad \forall X, Y, Z \in \mathfrak{g} \ . \tag{2.4}$$

For a matrix Lie group with a Lie bracket given by (2.3), this can be verified by an explicit calculation.

The basis elements of the Lie algebra are also called (infinitesimal) generators of the

[4] Faithful means that the representation is injective. So each group element is represented by a different matrix.

[5] In the mathematical literature this representation is often called the defining representation.

[6] For a proof of convergence see [67], Prop. 2.1.

corresponding Lie group. This is justified by the fact that all elements of the Lie group that are close to the identity can be expressed by the exponential of an element of the corresponding algebra. The Lie algebra of a matrix Lie group can be visualized as the tangent space at the identity of the Lie group.

The Case of SU(N)

Let us now focus on the most relevant Lie group in this work, the group SU(3) - or to be even more specific - the color gauge group SU(3). The Lie algebra of this group is given by the traceless Hermitian matrices:

$$\mathfrak{su}(N) = \left\{ X \in \mathcal{M}_N(\mathbb{C}) \middle| X^\dagger = X \ , \ \mathrm{Tr}(X) = 0 \right\} \ , \tag{2.5}$$

together with the commutator as the Lie bracket. The next step is to define the generators of SU(N). For the group SU(3), they are given by the Gell-Mann matrices [72]

$$\begin{aligned}
\lambda_1 &= \begin{pmatrix} 0 & 1 & 0 \\ 1 & 0 & 0 \\ 0 & 0 & 0 \end{pmatrix} \qquad \lambda_2 = \begin{pmatrix} 0 & -\mathrm{i} & 0 \\ \mathrm{i} & 0 & 0 \\ 0 & 0 & 0 \end{pmatrix} \qquad \lambda_3 = \begin{pmatrix} 1 & 0 & 0 \\ 0 & -1 & 0 \\ 0 & 0 & 0 \end{pmatrix} \\
\lambda_4 &= \begin{pmatrix} 0 & 0 & 1 \\ 0 & 0 & 0 \\ 1 & 0 & 0 \end{pmatrix} \qquad \lambda_5 = \begin{pmatrix} 0 & 0 & -\mathrm{i} \\ 0 & 0 & 0 \\ \mathrm{i} & 0 & 0 \end{pmatrix} \qquad \lambda_6 = \begin{pmatrix} 0 & 0 & 0 \\ 0 & 0 & 1 \\ 0 & 1 & 0 \end{pmatrix} \\
\lambda_7 &= \begin{pmatrix} 0 & 0 & 0 \\ 0 & 0 & -\mathrm{i} \\ 0 & \mathrm{i} & 0 \end{pmatrix} \quad \lambda_8 = \frac{1}{\sqrt{3}} \begin{pmatrix} 1 & 0 & 0 \\ 0 & 1 & 0 \\ 0 & 0 & -2 \end{pmatrix}
\end{aligned} \tag{2.6}$$

with a normalization factor of 1/2. So the generators of SU(3) are

$$T_a := \frac{1}{2} \lambda_a \ . \tag{2.7}$$

These matrices satisfy:

$$\mathrm{Tr}(T_a T_b) = \frac{1}{2} \delta_{ab} \ , \tag{2.8}$$

with the Kronecker delta δ_{ab}. Next, the structure constants f_{abc} are introduced. These constants are independent of the representation and can be defined via the Lie bracket as

$$[T_a, T_b] = \mathrm{i} f_{abc} T_c \ . \tag{2.9}$$

They are not independent under a rescaling of the generators. For the group SU(N), they are most often normalized to

$$f_{acd}f_{bcd} = N\delta_{ab} \ , \tag{2.10}$$

as is done here.[7] This fixes the normalization of the generators of the fundamental representation to be: $\mathrm{Tr}(T_aT_b) = \frac{1}{2}\delta_{ab}$. With these definitions, the structure constants can also be written as

$$f_{abc} = -2\mathrm{i}\mathrm{Tr}([T_a, T_b]T_c) \ , \tag{2.11}$$

which clearly shows the cyclic nature of the structure constants. Together with the anticommutativity of the commutator, the structure constants are shown to be completely antisymmetric. For an abelian Lie group, these structure constants would vanish. For SU(2) they are given by $f_{abc} = \epsilon_{abc}$, with the fully antisymmetric epsilon tensor and for SU(3) the non-zero structure constants are:

$$f_{123} = 1, \quad f_{147} = -f_{156} = f_{246} = f_{257} = f_{345} = -f_{367} = \frac{1}{2}, \quad f_{458} = f_{678} = \frac{\sqrt{3}}{2} \ .$$

From the Jacobi identity in Equation (2.4), which is also given in terms of Lie brackets, it follows that the structure constants satisfy

$$f_{abd}f_{dce} + f_{bcd}f_{dae} + f_{cad}f_{dbe} = 0 \ . \tag{2.12}$$

The other most important representation is the adjoint representation. It is defined by the adjoint action of the Lie group $\mathfrak{g}$. For every element $X \in \mathfrak{g}$ the adjoint action is the linear map:

$$\begin{aligned} \mathrm{ad}_X : \mathfrak{g} &\to \mathfrak{g} \\ Y &\mapsto \mathrm{ad}_X(Y) := [X, Y] \ . \end{aligned} \tag{2.13}$$

The linear map to the endomorphisms of $\mathfrak{g}$

$$\begin{aligned} \mathrm{ad} : \mathfrak{g} &\to \mathfrak{gl}(\mathfrak{g}) \\ X &\mapsto \mathrm{ad}_X \end{aligned} \tag{2.14}$$

is called the adjoint representation of $\mathfrak{g}$. The adjoint representation for matrix Lie algebras can be described by the structure constants. For a basis T_a of a Lie algebra, the matrix

[7] In the mathematical literature they are often normalized to $f_{acd}f_{bcd} = \delta_{ab}$.

elements of a basis of the adjoint representation are given by

$$(\mathrm{ad}_{T_a})_{bc} = -\mathrm{i} f_{abc} \ . \tag{2.15}$$

This can be demonstrated by the following calculation:

$$T_b(\mathrm{ad}_{T_a})_{bc} = \mathrm{ad}_{T_a}(T_c) = [T_a, T_c] = \mathrm{i} f_{acb} T_b = -\mathrm{i} f_{abc} T_b \ . \tag{2.16}$$

For SU(3) those are eight 8×8 matrices.
Another important quantity are the Casimir operators. They were introduced by Hendrik Casimir in 1931 [73] and play a central role in the explicit calculation of color factors in the theory of strong interactions. These calculations will be handled in more detail in Section 4.1. The Casimir operators, more specifically, the quadratic Casimir operators, are easily defined in matrix Lie groups because the multiplication of group elements is already defined. The Casimir operators depend on the chosen representation. Therefore, let T_a^R be the generators in a specific representation, then $\hat{C}_R := T_a^R \, T_a^R$ is the quadratic Casimir operator of the representation R, where the sum a over all generators is implicit. The Casimir operator does not depend on the choice of basis and commutes with all elements of the Lie algebra in this representation.[8] By Schur's lemma [74], it follows that the quadratic Casimir operator is proportional to the identity.[9] This identity is split off from the Casimir operator to obtain

$$C_R \mathbb{1}_R := T_a^R \, T_a^R \ . \tag{2.17}$$

A good starting point for the calculation of the Casimir operators for SU(N) is the inner product. The generators of SU(N) can always be chosen to be orthogonal in every representation, so the index T_R of a representation R can be defined as

$$T_R \delta_{ab} := \mathrm{Tr}\left(T_a^R \, T_b^R\right) \ . \tag{2.18}$$

For the fundamental representation, Equation (2.8) yields for the index

$$T_F = \frac{1}{2} \tag{2.19}$$

[8] This is true for all compact semisimple Lie algebras. In particular, for all Lie algebras in the Standard Model.
[9] For Schur's lemma, the representation must be irreducible. This is true for the fundamental and adjoint representations.

and equations (2.10) and (2.15) imply that the index of the adjoint representation is:

$$T_A = N \ . \tag{2.20}$$

To get to the Casimir Operator, the indices a and b in Equation (2.18) are set equal to get:

$$T_R \delta_{aa} = \mathrm{Tr}\left(T_a^R \, T_a^R\right) = C_R \mathrm{Tr}\left(\mathbb{1}_R\right) \ , \tag{2.21}$$

where Equation (2.17) is used in the second step. The function δ_{aa} gives the dimension of the group, i.e., the number of group generators. For SU(N) this is $\delta_{aa} = N^2 - 1$. The trace over the identity gives the dimension of the representation. For the fundamental representation of SU(N) this is $\mathrm{Tr}\left(\mathbb{1}_F\right) = N$. While the dimension of the adjoint representation is $\mathrm{Tr}\left(\mathbb{1}_A\right) = N^2 - 1$. This results in the Casimir operator for the fundamental representation of SU(N) of

$$C_F = \frac{N^2 - 1}{2N} \tag{2.22}$$

and for the adjoint representation of

$$C_A = N \ . \tag{2.23}$$

This provides sufficient knowledge of matrix Lie groups to deal with the necessary symmetries of the Lagrangian of QCD. A brief introduction on how this Lagrangian is built from these symmetries is provided in the next section.

2.1.2 The QCD Lagrangian

The Lagrangian is the most fundamental building block for the theory of strong interactions. It describes how the particles behave and how they interact. This section provides a brief introduction to the construction of the Lagrangian. The starting point of the summary[10] is the free Lagrangian for the quark fields

$$\mathcal{L}_{\text{free}} := \sum_{f=1}^{N_f} \overline{\Psi}_f (i\gamma_\mu \partial^\mu - m_f) \Psi_f \ , \tag{2.24}$$

[10] It is based on the introduction I gave in my master's thesis [75].

where N_f is the number of quark flavors and m_f are the masses of those quarks. The γ_μ are the Dirac matrices [76], where here and in the following a summation over repeated indices is implied. The free Lagrangian is a functional of the quark fields Ψ_f and their derivatives. It should be called Lagrangian density; however, when dealing with field theories, the Lagrangian only appears as a density. Therefore, the word "density" is omitted. Additionally, the slash notation will be used in the following:

$$\not{a} := \gamma_\mu a^\mu \ . \tag{2.25}$$

The quark fields Ψ_f are actually triplets of quark fields that are Dirac spinor valued, so:

$$\Psi_f = \begin{pmatrix} \Psi_f^1 \\ \Psi_f^2 \\ \Psi_f^3 \end{pmatrix} \ , \tag{2.26}$$

with Ψ_f^i being Dirac spinor valued quark fields for $i \in \{1, 2, 3\}$, corresponding to the three colors of quarks. The colors are commonly named red, green, and blue.[11] The SU(3) gauge transformation acts on these color triplets. The free Lagrangian $\mathcal{L}_{free}$ is already invariant under a global SU(3) gauge transformation, where the fields transform as

$$\Psi_i \to (\mathrm{e}^{\mathrm{i}\alpha^a T^a})_{ij} \Psi_j \ , \tag{2.27}$$

where T^a are the eight generators of SU(3) in the fundamental representation. A problem arises when going from this global transformation to a local transformation, where the coefficients α^a can now depend on the spacetime coordinate x_μ. Keeping the invariance of the free Lagrangian forces the introduction of a gauge field $\mathcal{A}$, a 1-form on spacetime with values in the Lie algebra $\mathfrak{su}(3)$. Using these, the ordinary derivative can be elevated to obtain the covariant derivative:

$$D_\mu := \partial_\mu - \mathrm{i} g_s \mathcal{A}_\mu \ , \tag{2.28}$$

where g_s defines the strength of the interaction and is called strong coupling constant. It is common to expand the gauge field $\mathcal{A}$ in terms of the generators of SU(3) in the fundamental representation T^a, as they form a basis of $\mathfrak{su}(3)$:

$$\mathcal{A}_\mu = A_\mu^a T^a \ . \tag{2.29}$$

[11] Of course this has nothing to do with actual colors, but is a handy representation of the threefoldness of the quarks.

The coefficients in this basis are the eight gluon fields A^a_μ. These gluon fields transform as follows:

$$A^a_\mu(x) \to A^a_\mu(x) + \frac{1}{g_s}\partial_\mu \alpha^a(x) - f_{abc}\alpha^b(x)A^c_\mu(x) \ , \tag{2.30}$$

where f_{abc} are the totally antisymmetric structure constants of SU(3). Replacing the standard derivative with the gauge-covariant derivative in the free Lagrangian results in

$$\begin{aligned} \mathcal{L}_{\text{free+int}} :&= \sum_{f=1}^{N_f} \overline{\Psi}_f(\mathrm{i}\gamma^\mu D_\mu - m_f)\Psi_f \\ &= \sum_{f=1}^{N_f} \overline{\Psi}_f(\mathrm{i}\gamma^\mu(\partial_\mu - \mathrm{i}g_s A^a_\mu T^a) - m_f)\Psi_f \end{aligned} \tag{2.31}$$

which is invariant under a local SU(3) gauge transformation.
To elevate the newly introduced field A to a physical field, the kinetic term for the gauge field must be added to the Lagrangian. It is given by:

$$\mathcal{L}_{\text{gluon}} := -\frac{1}{4}G^a_{\mu\nu}G_a^{\mu\nu} \ , \tag{2.32}$$

with a SU(3) valued 2-form, the field strength tensor G is given in its components by

$$G^a_{\mu\nu} = \partial_\mu A^a_\nu - \partial_\nu A^a_\mu + g_s f_{abc} A^b_\mu A^c_\nu \ . \tag{2.33}$$

Owing to the non-abelian nature of SU(3), the gluons can self-interact. This feature is captured by the last summand in the gluon field strength tensor. For an abelian group, all structure constants are zero, and the self-interaction of the fields is switched off.
The next step is the quantization of the theory. For this, the gauge is fixed by introducing a gauge-fixing term. For the manifest covariant Lorenz gauge, $\partial^\mu A^a_\mu = 0$, the gauge fixing term takes the form

$$\mathcal{L}_{\text{gauge}} := -\frac{\xi}{2}(\partial^\mu A^a_\mu)^2 \ , \tag{2.34}$$

with a gauge parameter ξ. In general, the gauge parameter can be retained and does not contribute to any physical observable. In the following, the Feynman gauge ($\xi = 1$) is chosen to simplify the calculations. The quantization in this gauge[12] forces the

[12] In the noncovariant axial gauge ($A^a_3 = 0$), the unphysical polarizations of the gluon would be excluded outright, so no ghost field is required. However, this gauge has its own complications. [77]

introduction of scalar anticommuting Faddeev-Popov ghost fields[13] [78] c^a:

$$\mathcal{L}_{\text{ghost}} := \partial_\mu \bar{c}_a \partial^\mu c^a + g_s f_{abc} (\partial^\mu \bar{c}^a) A^b_\mu c^c \ . \tag{2.35}$$

Finally, this procedure yields the Lagrangian of QCD as the sum of these contributions:

$$\mathcal{L}_{\text{QCD}} := \mathcal{L}_{\text{free+int}} + \mathcal{L}_{\text{gluon}} + \mathcal{L}_{\text{gauge}} + \mathcal{L}_{\text{ghost}} \ , \tag{2.36}$$

which is:

$$\begin{aligned} \mathcal{L}_{\text{QCD}} := & \sum_{f=1}^{N_f} \overline{\Psi}_f (\mathrm{i}\gamma^\mu (\partial_\mu - \mathrm{i} g_s A^a_\mu T^a) - m_f) \Psi_f - \frac{1}{4} G^a_{\mu\nu} G^{\mu\nu}_a \\ & - \frac{1}{2} (\partial^\mu A^a_\mu)^2 + \partial_\mu \bar{c}_a \partial^\mu c^a + g_s f_{abc} (\partial^\mu \bar{c}^a) A^b_\mu c^c) \ . \end{aligned} \tag{2.37}$$

It becomes evident that the Lagrangian for the fermions cannot exist in isolation. The requirement of local gauge invariance inherently necessitates interactions among these particles. These interactions are mediated by gluons. As physical particles, they require their own kinetic term in the Lagrangian. The final step in the construction of the Lagrangian of QCD is fixing the gauge. This was done using a manifestly Lorenz-invariant gauge fixing term. However, this term in turn forced the introduction of an additional term to eliminate the unphysical degree of freedom of the gluon fields. This was handled by the introduction of Faddeev-Popov ghosts.

There are multiple approaches to computing physical observables from the Lagrangian given above, depending on the energy regime. At low energies, techniques such as lattice QCD [79][14] or chiral perturbation theory [83][15] are commonly employed. At higher energies, perturbative techniques become applicable. This is possible because the strength of the strong coupling decreases at high energies. This energy dependence of the coupling strength is known as the running of the coupling constant. In fact, the variation of the coupling constants with energy is a general feature of the Standard Model of particle physics. The fact that the strong coupling decreases at larger momentum transfers was first discovered by Gross, Wilczek [9] and independently by Politzer [10, 11]. This property of QCD is known as asymptotic freedom, for which they were awarded the 2004 Nobel

[13] In an abelian gauge theory these ghost fields do not contribute, since they only interact with the gauge fields if $f^{abc} \neq 0$.

[14] For an overview see [80–82].

[15] For an overview see [84, 85].

Prize in Physics. The manner in which the coupling constants evolve is governed by the renormalization group, which is discussed in the following section.

2.2 Renormalization Group and the Running Coupling

The renormalization group is a striking example of how a new perspective on familiar concepts can lead to profound discoveries. While it is well known that perturbative higher-order calculations of physical observables in quantum field theory result in ultraviolet divergences arising from unconstrained loop momenta, the deeper implication is that they drive the running of the coupling.

To obtain meaningful predictions, these infinities must be handled using a process called renormalization, in which divergences are absorbed into counterterms introduced in the Lagrangian. The procedure of regularization, which governs how to control divergences in the first place, and renormalization, which subtracts them, are discussed in more detail in Sections 2.5.1 and 2.5.3, respectively. For now, the key point is that renormalization necessarily introduces a new, arbitrary mass scale, typically denoted by μ_R.

This scale enters the theory through the redefinition of parameters, and therefore the coupling constant becomes scale dependent. For QCD this is the strong coupling:

$$\alpha_s := \frac{g_s^2}{4\pi} \ . \tag{2.38}$$

The same holds true in QED, where the fine structure constant is given by

$$\alpha := \frac{e^2}{4\pi} \ . \tag{2.39}$$

Since μ_R is arbitrary and can be chosen freely, it is natural - and physically necessary - to require that observable quantities be independent of this scale. This constraint leads to the renormalization group equation, which governs how the coupling constant changes with the renormalization scale

$$\mu_R^2 \frac{\mathrm{d}\alpha_s(\mu_R^2)}{\mathrm{d}\mu_R^2} = \beta(\alpha_s) \ . \tag{2.40}$$

This equation is derived, for example, in Section 2 of [62]. The function $\beta(\alpha_s)$, known as the beta function, encodes the scale dependence of the coupling. In QCD, it can be

expanded perturbatively in powers of the strong coupling:

$$\beta(\alpha_s) = -\sum_{n=0}^{\infty} \beta_n \left(\frac{\alpha_s}{4\pi}\right)^{n+2} \ . \tag{2.41}$$

The coefficients β_n are calculable in perturbation theory. The efforts of calculating these coefficients go back to the early days of QCD, and by today $\beta(\alpha_s)$ is known up to five-loop accuracy, that is, up to β_4 [9, 10, 86–95]. The first two coefficients of the expansion are:

$$\beta_0 = \frac{11}{3} C_A - \frac{4}{3} T_F N_f \tag{2.42}$$

$$\beta_1 = \frac{34}{3} C_A^2 - \frac{20}{3} C_A T_F N_f - 4 C_F T_F N_f \ , \tag{2.43}$$

with the Casimir operators $C_A = 3$, $C_F = 4/3$, the index of the fundamental representation $T_F = 1/2$ and the number of active quark flavors N_f. The known coefficients become increasingly complicated, and all further coefficients $\beta_{n\geq 2}$ are also dependent on the renormalization scheme.

For comparison, the two-loop beta function of QED is given by [96]:

$$\beta(\alpha) = \frac{1}{3\pi}\alpha^2 + \frac{1}{4\pi^2}\alpha^3 + \mathcal{O}(\alpha^4) \ . \tag{2.44}$$

A fundamental difference between QED and QCD is immediately apparent: the QED beta function is positive, whereas the QCD beta function is negative (provided $N_f \leq 16$). The negativity of the QCD beta function is a consequence of the non-abelian structure of the theory, which allows self-interactions among gluons - a feature absent in abelian gauge theories like QED. This difference leads to drastically different behavior of the coupling constants.

At leading order, the renormalization group equation (2.40) can be solved analytically. For QED, the running of the fine structure constant is given by

$$\alpha(\mu_R^2) = \frac{\alpha(\mu_0^2)}{1 - \frac{\alpha(\mu_0^2)}{3\pi} \ln\left(\frac{\mu_R^2}{\mu_0^2}\right)} \ . \tag{2.45}$$

The minus sign in the denominator is a consequence of the positive sign of the beta function. This expression shows that the electromagnetic interaction grows stronger at higher energies. For example, at low energies ($\sim$ 1eV), the coupling is approximately $\alpha \approx 1/137$, whereas at the electroweak scale ($\sim$ 91GeV)[16], it increases to $\alpha \approx 1/129$ [97–

[16] The mass of the Z-Boson is 91 GeV.

99].

This increase can be attributed to vacuum polarization, where the physical charge is screened by virtual particle-antiparticle pairs at low energies. However, this behavior implies that the coupling diverges at extremely high energies. This energy, where the coupling diverges, is called the Landau pole [100].[17] However, one cannot expect to extract accurate results at high couplings from a perturbative beta function; therefore, the Landau pole might just be an artifact of the perturbative approximation breaking down, rather than a true physical singularity. The evolution of the QED coupling strength at one-loop approximation is shown in figure 2.1a.

In contrast, the QCD coupling behaves very differently. At leading order, its running is given by

$$\alpha_s(\mu_R^2) = \frac{\alpha_s(\mu_0^2)}{1 + \frac{11C_A - 2N_f}{12\pi}\alpha_s(\mu_0^2)\ln\left(\frac{\mu_R^2}{\mu_0^2}\right)} \,. \tag{2.46}$$

This expression is shown in Figure 2.1b. In QCD, the coupling decreases at high energies and increases at low energies. At very low energies, the coupling becomes large, and the perturbative expansion breaks down. This fact seems to lead to confinement, a phenomenon that ensures that at low energies, quarks and gluons are never observed as free particles, but only as bound color-neutral states: as hadrons. However, at these small energies, the coupling constant is sufficiently large that the perturbative expansion can no longer be trusted. To find more than just hints of confinement, a different approach, such as lattice QCD, must be used. Although this increase in coupling strength could suggest a Landau pole in the infrared, numerical studies indicate that the coupling saturates at values of approximately 1-3, rather than diverging [102].

At high energies, where the strong coupling becomes small, the way for perturbative calculations is cleared. This property is called asymptotic freedom and, as stated previously, David Gross, Frank Wilczek and David Politzer were awarded the 2004 Nobel Prize in Physics for this discovery. Asymptotic freedom allows quarks and gluons to behave as effectively free particles in high-energy processes, even though they cannot be directly observed at low energies. It also enables the use of perturbation theory at high energies to describe the dynamics of the fundamental particles of QCD. However, it is still complicated to extract meaning from the perturbative calculations, since they only consider quarks and gluons as initial and final particles, whereas in experiments, the incoming and

[17] The scale of the Landau pole in this simple picture is of the order of 10^{280}eV, but by considering the whole standard model or even supersymmetric extensions, the pole moves down to around 10^{26}eV. But even there, the pole poses no problem [101].

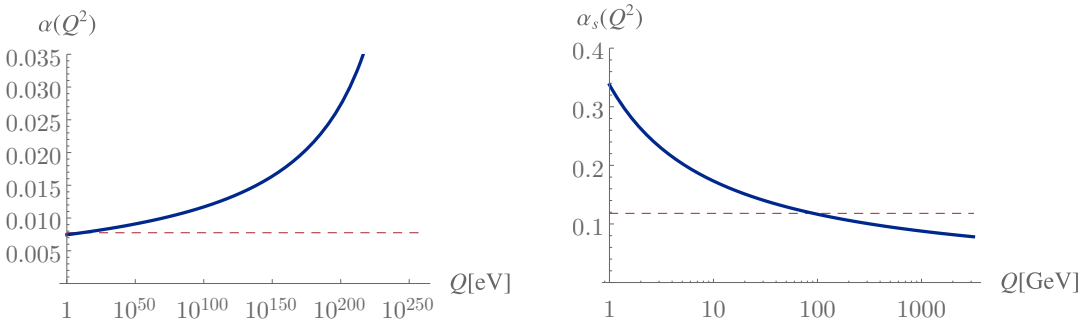

(a) Running coupling of QED.

(b) Running coupling of QCD.

Figure 2.1: Leading-order evolution of the QED and QCD running couplings as a function of the energy scale. The non-perturbative input for QED is $\alpha((1\text{eV})^2) = 1/137$ and for QCD is $\alpha_s\left(M_Z^2\right) = 0.1181$, they are marked by the dotted red lines. For QCD the number of active flavors is set to $N_f = 5$.

outgoing particles are hadrons.

To bridge the gap between perturbative calculations and experimental observations, QCD relies on factorization theorems [103]. These theorems separate the non-perturbative parts of a process, such as parton distributions inside hadrons and the hadronization of outgoing partons, from the hard scattering process, which is computable in perturbation theory. This concept is explored in more detail in Section 2.6.

2.3 Perturbative QCD

2.3.1 Cross Sections

The definition of cross sections in particle physics comes from a time when particles were thought of as small indestructible balls. Therefore, it was sensible to attempt to measure their size using scattering experiments and connect the probability of interaction directly to the cross section of the particles. The first divergence from this meaning of the geometrical cross section to the cross section in particle physics began in the early 20th century with the scattering experiments by Rutherford [6], where they scattered α and β particles off of gold foil to learn more about the inner structure of the atom. After the discovery of the Neutron by Chadwick [7], the final departure from the geometrical cross section came with the experiments by Fermi [104], which showed that the cross section of a neutron depends on its velocity, where slow-moving neutrons had a much higher probability to interact with nuclei than fast-moving neutrons. Now, the geometrical interpretation of the cross section was no longer viable because the size of a particle should not depend on its velocity. Nowadays, the term cross section is only used in its probabilistic interpretation

and has very little to do with the physical size of particles. It is now a measure for the likelihood of an interaction and, in the end, that is what is measured in experiments. This section starts with the classical definition of a cross section and connects it, in the end, to the perturbative calculation that will be presented in this thesis. This part of the thesis covers the basic principles necessary to understand the connection between perturbative calculations and cross sections. For a more detailed view on this topic see, for example, [64, 65, 105].

From Hard Spheres to Cross Sections

The first step is a brief recapitulation of the definition of a cross section in a classical sense. For this, consider the classical fixed-target scattering of hard spheres, where the beam size and the target are much larger than the scattering spheres. The only way to have a scattering in this setting is by getting a direct hit of a sphere from the beam with a sphere in the target. There are no other interactions. Assuming that the particles in the beam travel with the same constant velocity $\vec{v}$ towards the target and the experiment runs for a fixed time T, then all beam particles that are no farther away from the target than $T|\vec{v}|$ will have a chance to hit the target. Let ρ be the number density of the particles in the beam, then the total number of beam particles able to hit the target during the duration of the experiment per unit area is $T|\vec{v}|\rho$.[18] Let now N be the number of scattering events, then the classical cross section of the scattering of hard spheres is:

$$\sigma_{cl} = \frac{1}{T|\vec{v}|\rho} N = \frac{1}{T}\frac{1}{\Phi} N \ , \tag{2.47}$$

where $\Phi := |\vec{v}|\rho$ is the incoming flux of the beam.
This formula for the cross section can also be used as a definition. In that case, it can be applied to other interactions, such as the scattering of two charged particles, which can interact over much larger distances than their physical size. For an experiment with incoming flux Φ, runtime T and number of scattering events N, the effective cross section can be calculated using Equation (2.47). The effective cross section calculated in this way no longer is the actual geometric cross section of the particles interacting, but rather a measure for the range of the interaction of the particles in the experiment: the effective scattering cross section. Further details on these classical cross sections can be found in [106].

[18] For a real beam ρ is not expected to be constant. In fact, there are generally more particles in the center of the beam than at the edge. However, because the assumed interaction range and the width of the particles are much smaller than the cross sectional area of the beam, it may safely be assumed that ρ is constant. For a real experiment, one would then simply have to integrate over the cross sectional area of the beam with the specific particle densities $\rho(x)$.

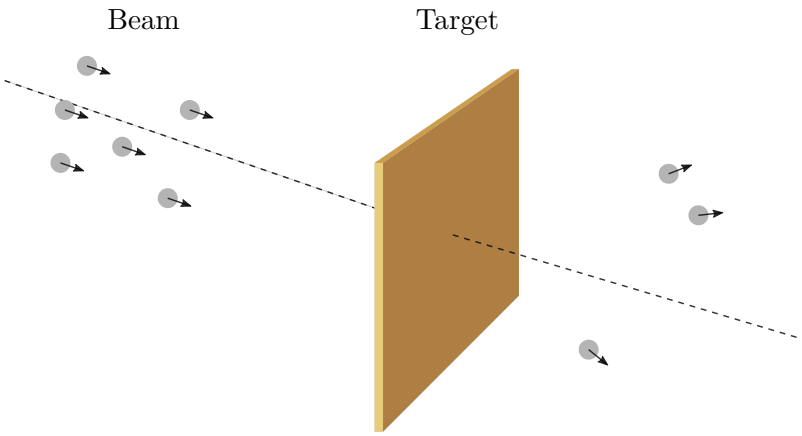

Figure 2.2: Schematical setup of a fixed target Experiment.

To apply this formula to quantum mechanical interactions, some adjustments must be made. In a quantum mechanical scattering, there is no longer a fixed number of particles that scatter, but rather a likelihood P, that scattering takes place. This likelihood, in a classical sense, would be the total number of scattering events divided by the total number of all incident particles N_{inc}, so $P = N/N_{inc}$. Therefore, if the incoming flux is normalized to one incoming particle and the number of scattering events is written as a probability, the cross section of a quantum mechanical scattering can be defined as:

$$\sigma := \frac{1}{T}\frac{1}{\Phi}P \ , \tag{2.48}$$

where P is the probability for scattering, and the Flux Φ is now normalized to just one particle, so $\rho = 1/V$ and therefore $\Phi = |\vec{v}|/V$. Note that this is true only for a fixed-target experiment in the lab frame. For a collider experiment or in the center-of-momentum frame, where the flux comes from both directions, the relative velocity of the incoming particles has to be used. This results in:

$$\Phi = \frac{|\vec{v}_1 - \vec{v}_2|}{V} \ , \tag{2.49}$$

where the velocities here are collinear.

From Cross Sections to the S-Matrix and the Scattering Amplitude

The next step is to find a way to calculate the scattering probability P. To do this, the Hamiltonian $\hat{H}$ is written as the sum of the free Hamiltonian $\hat{H}_0$, where there are no interactions between particles and the eigenstates are well known, and the interaction

Hamiltonian $\hat{H}_{int}$, which governs all interactions and will be handled by perturbation theory:

$$\hat{H} = \hat{H}_0 + \hat{H}_{int} \ . \tag{2.50}$$

Furthermore, the Dirac picture is employed here, where the time evolution of the operators is governed by the free Hamiltonian, and the time evolution of the states is determined by the interaction Hamiltonian via

$$|\psi(t)\rangle = \mathcal{T}\left[\exp\left(i\int_{t_0}^{t} \mathrm{d}t' \hat{H}_{int}(t')\right)\right]|\psi(t_0)\rangle =: \hat{U}(t,t_0)|\psi(t_0)\rangle \ , \tag{2.51}$$

where $\mathcal{T}$ is the time ordering operator (defined in [107] p. 143), and the time evolution operator $\hat{U}$ was introduced in the last step. To set up a scattering experiment, a definition for the initial state of the system is required. It is defined at a time long before the scattering takes place: $|i\rangle := |\psi(-\infty)\rangle$. By the time evolution given in (2.51), the state of the system will have evolved a long time after the scattering to

$$|f\rangle := |\psi(\infty)\rangle = \hat{U}(\infty,-\infty)|\psi(-\infty)\rangle \ . \tag{2.52}$$

The scattering Matrix or simply S-matrix is defined as

$$\hat{S} := \hat{U}(\infty,-\infty) \ , \tag{2.53}$$

so $|f\rangle = \hat{S}|i\rangle$. With this, the probability of observing the final state $|f\rangle$ can be written as:

$$P_{fi} = \frac{|\langle f|\hat{S}|i\rangle|^2}{\langle f|f\rangle\langle i|i\rangle} \ . \tag{2.54}$$

This procedure, involving the S-matrix, was first introduced by Wheeler [108] and independently developed by Heisenberg [109–111]. This derivation follows the one given in [65]. First, assume that all initial particles have fixed momentum and the initial state is just the product of the plane waves:

$$|i\rangle = \prod_{j=1}^{n_i} |p_j\rangle \ , \tag{2.55}$$

with p_j being the momenta of the n_i incident particles. The same holds for the final state particles

$$|f\rangle = \prod_{l=1}^{n_f} |k_l\rangle \ , \tag{2.56}$$

where the k_l are the momenta of the n_f outgoing particles. Here, it is immediately obvious that there will be a problem with the normalization of the states, since they are plane waves and therefore not normalizable. To mitigate this, the states are restricted to a finite volume V and a finite time T. In the end, it will be possible to safely take the limit to infinity for both. To do this with a bit more mathematical rigor, one would take the initial scattering particles as wave packets $|\phi\rangle = \int \frac{\mathrm{d}^3p}{(2\pi)^3} \frac{1}{\sqrt{2E_p}} \phi(p)|p\rangle$, instead of states with fixed momenta, and use product states of those as initial and final configurations. This would also fix the problem of normalization, but ultimately, it would yield the same result. Here the simpler, albeit less rigorous, derivation with a finite volume is performed. The derivation with wave packets is presented in [64, 112, 113].
To understand the normalization, it is a good starting point to take the original definition of a momentum eigenstate

$$|p\rangle = \sqrt{2E_p}\hat{a}_p^\dagger|0\rangle \ , \tag{2.57}$$

where $|0\rangle$ is the vacuum state of the free theory, which is normalized to $\langle 0|0\rangle = 1$ and $\hat{a}_p^\dagger$ the creation operator for a particle with momentum p. Taking the absolute value squared:

$$\begin{aligned} \langle p|p\rangle &= \langle 0|2E_p\hat{a}_p\hat{a}_p^\dagger|0\rangle \\ &= \langle 0|2E_p\left((2\pi)^3\delta^3(0) + \hat{a}_p^\dagger\hat{a}_p\right)|0\rangle \\ &= 2E_p(2\pi)^3\delta^3(0) \ , \end{aligned} \tag{2.58}$$

where the commutation relation of the creation operators: $[\hat{a}_p, \hat{a}_q^\dagger] = (2\pi)^3\delta^3(\vec{p}-\vec{q})$ is used. To make sense of the seemingly nonsensical delta function in the last expression, it is a good idea to examine the meaning of the delta function as the Fourier transform of unity:

$$(2\pi)^3\delta^3(p) = \int \mathrm{d}^3x \mathrm{e}^{\mathrm{i}\vec{p}\cdot\vec{x}} \ . \tag{2.59}$$

Therefore, in the finite volume, this results in

$$(2\pi)^3\delta^3(0) = \int_V \mathrm{d}^3x = V \ . \tag{2.60}$$

Since it is needed soon, the result for $\delta^4(0)$, which can be derived in the same way, is given already here:

$$\delta^4(0) = \frac{1}{(2\pi)^4} \int_{VT} \mathrm{d}^4x = \frac{VT}{(2\pi)^4} \ , \tag{2.61}$$

where, as mentioned above, T is the runtime of the experiment. So, in the finite volume, the normalization of the states evaluates to

$$\langle i|i\rangle = \prod_{j=1}^{n_i} (2E_j V) \quad \text{and} \quad \langle f|f\rangle = \prod_{l=1}^{n_f} (2E_l V) \ . \tag{2.62}$$

With this, the denominator of (2.54) is complete, and the focus can shift to the numerator. There are two cases for the scattering. In the first, trivial case, nothing happens, and the S-matrix is the identity. This would be the case for the free theory, but it is also a possibility in a theory with interaction: The particles can simply miss one another. The second case is the interesting one and the one that will be treated here. Therefore, the S-matrix is split into two parts by writing

$$\langle f|\hat{S}|i\rangle = \langle f|\mathbb{1}|i\rangle \ + \mathrm{i}\langle f|\hat{T}|i\rangle \ \ , \tag{2.63}$$

where $\hat{T}$ is called transfer matrix and the i is convention. As a general fact, the S-matrix has to obey physical conservation laws; therefore, it should vanish if the total momentum is not conserved. This allows the extraction of the delta function for the conservation of 4-momentum from the transfer matrix, thus obtaining

$$\langle f|\hat{T}|i\rangle \ = (2\pi)^4 \delta^4 \left(\sum\nolimits_j p_j - \sum\nolimits_l k_l \right) \mathcal{M}_{fi} \ , \tag{2.64}$$

where the matrix element $\mathcal{M}_{fi}$ was introduced, which is also often called scattering amplitude. So, for a true scattering event with $|i\rangle \neq |f\rangle$, this becomes

$$\begin{aligned} |\langle f|\hat{S}|i\rangle|^2 &= (2\pi)^8 \delta^4 \left(\sum\nolimits_j p_j - \sum\nolimits_l k_l \right) \delta^4(0) |\mathcal{M}_{fi}|^2 \\ &= (2\pi)^4 \delta^4 \left(\sum\nolimits_j p_j - \sum\nolimits_l k_l \right) VT |\mathcal{M}_{fi}|^2 \ , \end{aligned} \tag{2.65}$$

where the result for the four-dimensional delta function in a finite volume of Equation (2.61) was used in the second line. With that, the probability in (2.54) is

$$P_{fi} = VT \frac{(2\pi)^4 \delta^4 \left(\sum_{j=1}^{n_i} p_j - \sum_{l=1}^{n_f} k_l\right)}{\left(\prod_{j=1}^{n_i} 2E_j V\right)\left(\prod_{l=1}^{n_f} 2E_l V\right)} |\mathcal{M}_{fi}|^2 \ . \tag{2.66}$$

The next step is to abandon the requirement of a specific final state. In the continuous case, it would in fact be unphysical to demand final state particles with fixed momenta. Such a state could never be measured. It is more sensible to ask what the probability is that the final momenta of the particles are within a certain range. Therefore, it has to be summed/integrated over a range suited to the experimental setup. This results in:

$$P = \prod_{l=1}^{n_f} \sum_{\vec{k}_l} P_{fi} \ , \tag{2.67}$$

with a sum over all suitable momenta $\vec{k}_l$ for a finite volume V. In the continuous limit for large V this is

$$\sum_{\vec{k}} \to \int \frac{\mathrm{d}^3\vec{k}}{(2\pi/L)^3} = V \int \frac{\mathrm{d}^3\vec{k}}{(2\pi)^3} \ , \tag{2.68}$$

where the integral should be taken over the desired momenta that match the experimental setup. With that, the scattering probability is

$$P \to VT \int \prod_{l=1}^{n_f} \left(\frac{\mathrm{d}^3 k_l}{(2\pi)^3} \frac{1}{2E_l}\right) \frac{(2\pi)^4 \delta^4 \left(\sum_{j=1}^{n_i} p_j - \sum_{l=1}^{n_f} k_l\right)}{\left(\prod_{j=1}^{n_i} 2E_j V\right)} |\mathcal{M}_{fi}|^2 \tag{2.69}$$

and for the cross section:

$$\sigma = \frac{1}{\Phi} V \int \prod_{l=1}^{n_f} \left(\frac{\mathrm{d}^3 k_l}{(2\pi)^3} \frac{1}{2E_l}\right) \frac{(2\pi)^4 \delta^4 \left(\sum_{j=1}^{n_i} p_j - \sum_{l=1}^{n_f} k_l\right)}{\left(\prod_{j=1}^{n_i} 2E_j V\right)} |\mathcal{M}_{fi}|^2 \ . \tag{2.70}$$

In this thesis, the interest lies in the case with two initial state particles, i.e., $n_i = 2$. For this the cross section can be written as

$$\sigma = \frac{1}{4E_1 E_2 |\vec{v}_1 - \vec{v}_2|} \int \prod_{l=1}^{n_f} \left(\frac{\mathrm{d}^3 k_l}{(2\pi)^3} \frac{1}{2E_l}\right) (2\pi)^4 \delta^4 \left(p_1 + p_2 - \sum_{l=1}^{n_f} k_l\right) |\mathcal{M}_{fi}|^2 \ . \tag{2.71}$$

With the shorthand notation for $F := 4E_1E_2|\vec{v}_1 - \vec{v_2}|$, the Møller flux factor [114], and the n_f-particle Lorentz-invariant phase space integral becomes:

$$\begin{aligned}\int \mathrm{PS}_{n_f} :&= \int \prod_{l=1}^{n_f} \left(\frac{\mathrm{d}^3 k_l}{(2\pi)^3} \frac{1}{2E_l} \right) (2\pi)^4 \delta^4 \left(p_1 + p_2 - \sum\nolimits_{l=1}^{n_f} k_l \right) \\ &= \int \prod_{l=1}^{n_f} \left(\frac{\mathrm{d}^4 k_l}{(2\pi)^4} \delta^+(k_l^2) \right) (2\pi)^4 \delta^4 \left(p_1 + p_2 - \sum\nolimits_{l=1}^{n_f} k_l \right) \ ,\end{aligned} \tag{2.72}$$

with the δ^+-distribution defined as

$$\delta^+(k^2) := \delta(k^2)\theta(k^0) \ , \tag{2.73}$$

and the Heaviside theta function enforcing the energy constraint. Therefore, the cross section can be written as the following compact expression:

$$\sigma = \frac{1}{F} \int \mathrm{dPS}_{n_f} |\mathcal{M}_{fi}|^2 \ . \tag{2.74}$$

Here it is evident, that all dependence on the finite volume and time has canceled and the limits $V, T \to \infty$ can be taken safely. In a similar manner, all dependence on the form of the narrow wave packets would have dropped out if this case would have been considered here. Furthermore, it is clear that the phase space integral is Lorentz invariant, as is the matrix element. Only the flux factor is not Lorentz invariant. It is, in fact, invariant under boosts along the beam axis of the incoming particles, but not for a general Lorentz transformation. This is exactly the transformation behavior of a cross section. Nevertheless it is possible to write the Møller flux factor for collinear velocities $F = 4E_1E_2|\vec{v}_1 - \vec{v}_2|$ in covariant form as:

$$F = 4\sqrt{(p_1 \cdot p_2)^2 - m_1^2 m_2^2} \ , \tag{2.75}$$

with the relation between the velocities and the momenta given, as usual, by $\vec{v_i} = \vec{p_i}/E_i$. This is the form most often used in particle physics [115], since it is covariant and therefore not restricted to collinear momenta. To check this form of the flux factor start from the

covariant form and write it explicitly [116]:

$$\begin{aligned}\frac{F}{4} &= \sqrt{(p_1 \cdot p_2)^2 - m_1^2 m_2^2} = \sqrt{(E_1 E_2 - \vec{p_1} \cdot \vec{p_2})^2 - m_1^2 m_2^2} \\ &= \sqrt{E_1^2 E_2^2 - 2E_1 E_2 \vec{p_1} \cdot \vec{p_2} + (\vec{p_1} \cdot \vec{p_2})^2 - m_1^2 m_2^2} \\ &= \sqrt{m_2^2 \vec{p_1}^2 + m_2^2 \vec{p_2}^2 + \vec{p_1}^2 \vec{p_2}^2 - 2E_1 E_2 \vec{p_1} \cdot \vec{p_2} + (\vec{p_1} \cdot \vec{p_2})^2} \\ &= \sqrt{m_2^2 \vec{p_1}^2 + m_1^2 \vec{p_2}^2 - 2E_1 E_2 \vec{p_1} \cdot \vec{p_2} + 2\vec{p_1}^2 \vec{p_2}^2} \ ,\end{aligned} \tag{2.76}$$

where $E_i^2 = m_i^2 + \vec{p}_i^2$ is used in the third line, and the fact that the momenta $\vec{p}_1$ and $\vec{p}_2$ are collinear in the last line. On the other hand, the difference of velocities can be written as

$$|\vec{v}_1 - \vec{v}_2| = \left| \frac{\vec{p_1}}{E_1} - \frac{\vec{p_2}}{E_2} \right| = \frac{|E_2 \vec{p_1} - E_1 \vec{p_2}|}{E_1 E_2} \ . \tag{2.77}$$

The numerator evaluates to

$$|E_2 \vec{p_1} - E_1 \vec{p_2}| = \sqrt{m_2^2 \vec{p_1}^2 + m_1^2 \vec{p_2}^2 - 2E_1 E_2 \vec{p_1} \cdot \vec{p_2} + 2\vec{p_1}^2 \vec{p_2}^2} \ , \tag{2.78}$$

again using $E_i^2 = m_i^2 + \vec{p}_i^2$, getting the desired result from (2.76), proving the relation.

2.4 Feynman Rules

In the regime of perturbative QCD, cross sections can be calculated with arbitrary high precision by including more and more terms in the perturbative expansion. The coupling constant serves as the expansion parameter. When this coupling is sufficiently small, as it is at high momentum transfers owing to asymptotic freedom, it is expected that the first few terms yield an accurate approximation of the full result.

Because each power of the coupling constant corresponds to an additional interaction vertex, the terms in the expansion are sorted according to the number of interactions. The resulting expressions in the perturbative expansion have a diagrammatic representation introduced by Richard Feynman [117]. These Feynman diagrams offer a visual shorthand for the mathematical expressions describing each process. The Feynman rules translate these diagrams back into concrete mathematical expressions.

The following Feynman rules for massless fermions are taken from [118]. The Greek letters $\mu, \nu, \rho, \sigma \in \{0, ..., 3\}$ are spacetime indices, the Latin letters from the beginning of the alphabet $a, b, c, d \in \{1, ..., 8\}$ index the fundamental representation of SU(3), the letters $i, j \in \{1, ..., 3\}$ are color indices, p, k are momenta, s the spins, λ the polarizations, e the electric charge of the fermion, and g_s the strong coupling constant.

As in the case of pure QED, fermions are represented by Dirac spinors and gluons, being vector bosons, are described by polarization vectors as follows:

incoming particles		outgoing particles	
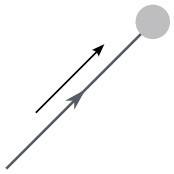	$u(p,s)$	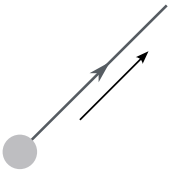	$\bar{u}(k,s)$
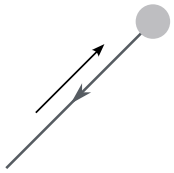	$\bar{v}(p,s)$	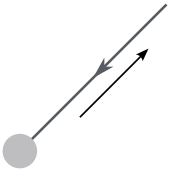	$v(k,s)$
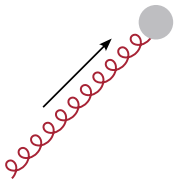	$\epsilon_\mu(p,\lambda)$	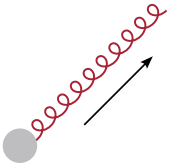	$\epsilon^*_\mu(k,\lambda)$.

For the internal lines, the photon-, quark-, gluon- and ghost-propagators are given by

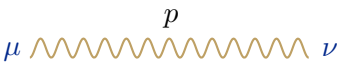

$$\frac{-\mathrm{i}g_{\mu\nu}}{p^2+\mathrm{i}\eta}$$

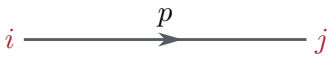

$$\mathrm{i}\delta_{ij}\frac{\not{p}}{p^2+\mathrm{i}\eta}$$

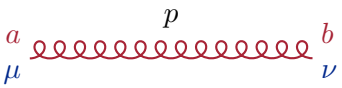

$$\frac{-\mathrm{i}\delta_{ab}g_{\mu\nu}}{p^2+\mathrm{i}\eta}$$

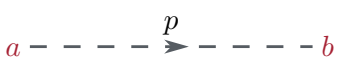

$$\frac{\mathrm{i}\delta_{ab}}{p^2+\mathrm{i}\eta}\ .$$

The QED vertex and the four fundamental vertices in QCD, the quark-gluon, three-gluon, ghost-gluon, and four-gluon vertex, are given by

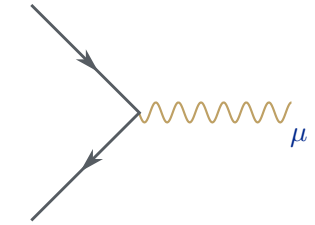

$$-\mathrm{i}e\gamma_\mu$$

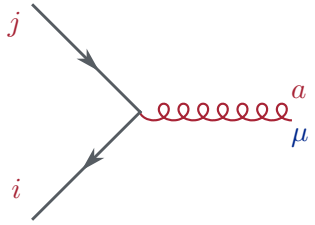

$$\mathrm{i}g_s\gamma_\mu T^a_{ij}$$

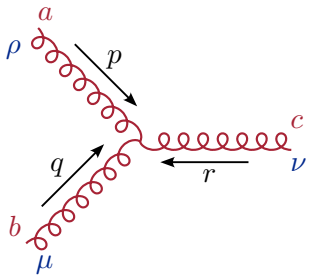

$$g_s f_{abc}[g_{\rho\mu}(p-q)_\nu + g_{\mu\nu}(q-r)_\rho + g_{\nu\rho}(r-p)_\mu]$$

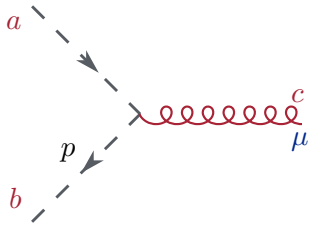

$$-g_s f_{abc} p_\mu$$

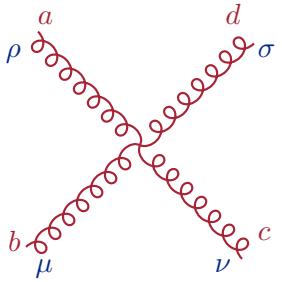

$$\begin{aligned}-\mathrm{i}g_s^2[&f_{abe}f_{cde}(g_{\rho\nu}g_{\mu\sigma} - g_{\rho\sigma}g_{\mu\nu})\\ &+f_{ace}f_{bde}(g_{\rho\mu}g_{\nu\sigma} - g_{\rho\sigma}g_{\mu\nu})\\ &+f_{ade}f_{cbe}(g_{\rho\nu}g_{\mu\sigma} - g_{\rho\mu}g_{\sigma\nu})]\end{aligned}$$

respectively. Four-momentum is conserved at each vertex. Furthermore, over every momentum in a closed loop must be integrated, and each closed quark or ghost loop must be multiplied by a factor of (-1). These rules can be derived from the Lagrangian [119, 120].

2.5 The Origin of Divergences

A prominent feature of higher-order perturbative calculations in quantum field theory is the appearance of divergences. While these singularities manifest in intermediate steps of the computation, they must not persist in the final, physical observable. Understanding the origin of these divergences is crucial for identifying how they cancel or are absorbed into non-perturbative aspects of the theory. Divergences in quantum field theory can be categorized into two categories, ultraviolet (UV) and infrared (IR) divergences. Infrared divergences are further subdivided into soft and collinear types:

Ultraviolet divergences arise in loop integrals, for example in virtual corrections. Loop diagrams require an integration over all possible internal momenta, including arbitrarily large ones. An example of such a divergence is the quark self-energy correction shown in Figure 2.3a. This Feynman diagram results in the loop integral

$$I = \int \frac{\mathrm{d}^4 l}{(2\pi)^4} \frac{f(l)}{l^2 (p-l)^2} \ , \tag{2.79}$$

where $f(l)$ is a polynomial of degree 1 in the loop momentum l and captures all other arising factors. This integral diverges for large loop momenta l, because the integrand only drops off as l^{-3}, which indicates a linear divergence for a 4-dimensional integral. This simple way of power counting can be expanded by writing the superficial degree of divergence as

$$D = 4L - 2I_b - I_f \ , \tag{2.80}$$

with L being the number of loops, I_b the number of internal boson lines, and I_f the number of internal fermion lines. This means, if $D \geq 0$ the diagram might diverge, depending on the numerator. An explicit calculation for the Feynman diagram in Figure 2.3a shows a logarithmic divergence in this case.

Soft divergences stem from the other end of the energy spectrum. They arise in theories with massless particles, such as gluons or, in a massless approximation of QCD, quarks. In virtual corrections, they are typically associated with massless bosons connecting two external fermions. This can be seen in the example above. This diagram in Figure 2.3a is also divergent for $l \to 0$. So, if the superficial degree of divergence is non-positive, the diagram can also be divergent, but in this case, it is an infrared divergence.

Infrared divergences do not only occur in loop integrals; they are also present in real emission processes. Here, soft divergences arise if a massless particle is emitted with

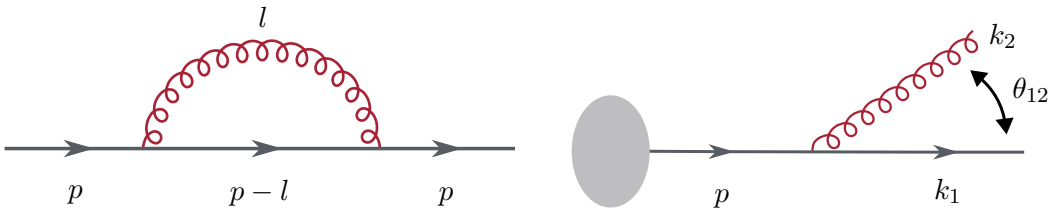

(a) Quark self-energy correction.

(b) Gluon emission.

Figure 2.3: Two examples of divergent Feynman diagrams. The loop diagram from the quark self-energy correction is UV- and IR-divergent, while the gluon emission diagram is solely IR-divergent.

vanishing energy from an external on-shell particle. An example is shown in Figure 2.3b. The internal propagator of this diagram can be written as

$$\frac{1}{p^2} = \frac{1}{(k_1 + k_2)^2} = \frac{1}{E_1 E_2 (1 - \cos\theta_{12})} \,, \tag{2.81}$$

where E_i is the energy of the particle with momentum k_1 and θ_{12} is the angle between the three momenta of k_1 and k_2. It is evident that this propagator diverges if either $E_1 \to 0$ or $E_2 \to 0$. This is a soft divergence.

Collinear divergences occur when two massless particles become collinear in their three-momenta. The emitted particle can either be collinear to an incoming or an outgoing particle. This can also be seen in Equation (2.81), where the propagator also diverges for $\theta_{12} \to 0$.

Each class of divergence requires specific handling. UV divergences are removed through a renormalization procedure. This procedure redefines the parameters of the theory (such as masses, fields, and coupling constants) in a way that absorbs these infinities, yielding finite predictions. Renormalization is discussed in Section 2.5.3.

Soft divergences originating from loop integrals cancel in sufficiently inclusive observables with infrared divergences coming from phase space integrations due to the soft emission of massless particles. This fact was proven by Felix Bloch and Arnold Nordsieck for QED in 1937 [121] and for the standard model by Toichiro Kinoshita in 1962 [122] and independently by Tsung-Dao Lee and Michael Nauenberg in 1964 [123]. The theorem is called Kinoshita-Lee-Nauenberg theorem. The same is true for singularities that are simultaneously soft and collinear. They will cancel in the sum of all contributing virtual and real corrections.

Pure collinear divergences, on the other hand have to be handled differently. They do not

have a counterpart in virtual contributions. They are connected to the collinear emission of massless particles to external ones. Therefore, these divergences can be attributed to a more complex behavior of the external particles. In QCD, those external particles are strongly interacting hadrons. We already know that the inner low-energy dynamics of those hadrons cannot be described by perturbative calculations. The goal is to attribute the collinear divergences to those hadrons. This is done by absorbing the divergences into parton distribution functions (PDFs) or fragmentation functions (FFs), depending on whether they stem from emissions that are collinear to initial or final state particles. This procedure is called factorization and is described in a bit more detail in Section 2.6. Factorization allows the cross section to be separated into long-distance (non-perturbative) and short-distance (perturbative) parts.
Before divergences can be renormalized, canceled, or absorbed, they must first be regularized, i.e., made mathematically well-defined. There are various ways to achieve this. The next section will cover some of these possibilities.

2.5.1 Regularization

Various types of divergences inevitably appear in the next-to-leading order calculations in QCD. These divergences originate from several sources: loop integrals involving arbitrarily large momenta that are unconstrained by external momenta, collinear emissions of particles, and soft radiation of massless particles. While some of these infinities cancel each other in physical observables, others require independent treatment. To make sense of the intermediate steps and isolate the divergent contributions, it is essential to introduce a regularization scheme that renders all expressions finite before the cancellation or subtraction procedures.
Regularization is implemented by introducing a regulator that modifies divergent expressions such that their singular behavior becomes explicit and isolates the parts of the function that diverge once the regulator is removed. Several methods exist for regularizing UV divergences, each with its own advantages and limitations.

Cut-off regularization is one of the most intuitive methods of regularization, where loop integrals are restricted to a finite range by imposing an upper limit Λ on the loop momentum. For example, the radial part of an integral like in (2.79) in spherical coordinates, will have an upper limit:

$$\int_0^\infty \mathrm{d}|l| \frac{|l|^3 f(l)}{l^2(p-l)^2} \to \int_0^\Lambda \mathrm{d}|l| \frac{|l|^3 f(l)}{l^2(p-l)^2} \,. \tag{2.82}$$

This approach has a seemingly physical motivation: because QCD is expected to

break down at extremely high energy scales, one might reasonably impose an upper energy bound. However, this method has significant drawbacks. First, there is no clearly defined energy scale that can serve as an universal cutoff. Second, and more importantly, it breaks Lorentz invariance because a fixed cutoff in momentum space is not invariant under Lorentz boosts. Consequently, cutoff regularization is rarely used in practical QCD calculations.

Lattice regularization is more sophisticated and primarily used in non-perturbative QCD. Here, a finite spacing is introduced between points in spacetime, effectively turning the continuous spacetime into a discrete lattice. This discretization introduces a natural cutoff in momentum space due to the finite first Brillouin zone of the lattice, thus regulating all loop integrals. Lattice regularization preserves gauge invariance and is well-suited for numerical studies of strongly interacting systems. It forms the foundation of Lattice QCD, a field devoted to solving non-perturbative QCD phenomena using Monte Carlo simulations. However, in perturbative computations, the presence of a non-zero lattice spacing complicates analytical calculations, making the method less useful for analytical higher-order computations.

Pauli-Villars regularization is another classic method, introduced by Wolfgang Pauli and Felix Villars in 1949 [124]. In this approach, additional auxiliary massive particles are introduced into the theory. These particles are designed to cancel the divergent parts of loop integrals by contributing terms with opposite sign and high-mass suppression.

While Pauli-Villars regularization preserves Lorentz invariance, it significantly increases the complexity of calculations. Furthermore, in non-abelian gauge theories, such as QCD, the method breaks gauge invariance. Consequently, although historically important, this method is not widely used in modern QCD perturbation theory.

Dimensional regularization preserves gauge invariance and Lorentz symmetry, making it the most widely used regularization in quantum field theory, and particularly in perturbative QCD. It was first introduced by Carlos Guido Bollini and Juan José Giambiagi [125] and independently by Gerard 't Hooft and Martinus Veltman [126] in 1972. This is the method that will be used throughout this thesis. In dimensional regularization, the number of spacetime dimensions becomes the regulator. This is explained in the next section.

2.5.2 Dimensional Regularization

The regularization techniques discussed earlier were primarily developed to address UV divergences. A key advantage of dimensional regularization is its ability to simultaneously handle both UV and IR divergences. Despite being somewhat abstract, this method is widely favored for its conceptual simplicity and compatibility with gauge and Lorentz invariance.

Unlike other regularization procedures that rely on introducing a momentum cutoff or a minimum distance in spacetime, dimensional regularization uses the number of spacetime dimensions as a regulator for divergent integrals. Rather than integrating over four-dimensional spacetime, the divergent integral is extended to d-dimensional spacetime, with one time and $d-1$ spatial dimensions. The change of dimensions alters the convergence behavior of the integral. Expressions that are UV divergent in four dimensions might no longer be divergent in lower dimensions.

For instance, the integral

$$\int \mathrm{d}^4x \frac{1}{x^4} \tag{2.83}$$

is divergent for large x, i.e., UV-divergent. However, it is no longer divergent in fewer than four dimensions:

$$\int \mathrm{d}^3x \frac{1}{x^4} \ , \tag{2.84}$$

which is convergent for large x. Similarly, IR-divergent integrals may become convergent when considered in higher dimensions.

The loop integral of the previous section, Equation (2.79), is then replaced by

$$\int \frac{\mathrm{d}^4l}{(2\pi)^4} \frac{f(l)}{l^2(p-l)^2} \to \int \frac{\mathrm{d}^dl}{(2\pi)^d} \frac{f(l)}{l^2(p-l)^2} \ . \tag{2.85}$$

These integrals are usually evaluated in spherical coordinates, starting with integer values of d, and then extended to arbitrary (non-integer) values through analytic continuation. A more detailed discussion on integration in d dimensions and the associated special functions can be found in Section 4.6.

It is common practice to write the dimension as the deviation from the physical four

dimensions[19]:

$$d = 4 - 2\epsilon, \quad \text{with } \epsilon \in \mathbb{R} \ . \tag{2.86}$$

With this convention, divergences in four-dimensional integrals manifest as poles of the form $1/\epsilon^n$, where $n \in \mathbb{N}$.
Changing the spacetime dimension has some additional consequences. First, the metric tensor is now a $d \times d$ matrix satisfying

$$g^{\mu\nu} g_{\mu\nu} = d \ . \tag{2.87}$$

This is relevant for the anticommutation relation of the Dirac matrices ($\{\gamma^\mu, \gamma^\nu\} = 2g^{\mu\nu}$), leading to modified identities such as:

$$\begin{aligned}
\gamma^\mu \gamma^\nu \gamma_\mu &= -2(1-\epsilon)\gamma^\nu \\
\gamma^\mu \gamma^\nu \gamma^\rho \gamma_\mu &= 4g^{\nu\rho} - 2\epsilon \gamma^\nu \gamma^\rho \\
\gamma^\mu \gamma^\nu \gamma^\rho \gamma^\sigma \gamma_\mu &= -2(\gamma^\sigma \gamma^\rho \gamma^\nu - \epsilon \gamma^\nu \gamma^\rho \gamma^\sigma) \\
\mathrm{Tr}[\gamma^\mu \gamma^\nu] &= (4-2\epsilon) g^{\mu\nu} \\
\mathrm{Tr}[\gamma^\mu \gamma^\nu \gamma^\rho \gamma^\sigma] &= (4-2\epsilon)(g^{\mu\nu} g^{\rho\sigma} - g^{\mu\rho} g^{\sigma\nu} - g^{\mu\sigma} g^{\nu\rho}) \ .
\end{aligned} \tag{2.88}$$

Terms proportional to ϵ can produce finite contributions when multiplied by divergent terms proportional to $1/\epsilon$, and therefore must be retained.
Another critical consequence is the change in the gluon spin sum and averaging. In four dimensions, gluons have two physical polarizations, but in d dimensions, the number of polarization states becomes $d-2$. This modifies the average over gluon polarization states, introducing a factor of

$$\frac{1}{d-2} = \frac{1}{2(1-\epsilon)} \tag{2.89}$$

for all incoming gluons.
Finally, it is worth emphasizing that, like other regularization methods, dimensional regularization introduces a new mass scale. While cutoff, lattice, and Pauli-Villars regularizations introduce this scale explicitly - through a momentum cut-off, lattice spacing, or particle mass - dimensional regularization introduces it indirectly through dimensional consistency.
Since the action must remain dimensionless, the Lagrangian density must have mass di-

[19] Other conventions are $d = 4 - \epsilon$ or $d = 4 + \epsilon$.

mension d. This leads to the following mass dimension:

$$[A_\mu^a] = \frac{d-2}{2}, \quad [\Psi_f] = \frac{d-1}{2}, \quad [m_f] = 1, \quad [g_s] = \frac{4-d}{2} \ . \tag{2.90}$$

To ensure that the coupling constant remains dimensionless, an arbitrary renormalization scale μ is introduced, such that

$$g_s \to \mu^{\frac{4-d}{2}} g_s = \mu^\epsilon g_s \ . \tag{2.91}$$

This scale μ, sometimes also μ_R, to make the origin in renormalization apparent, played a central role in the renormalization group and is the one that appears in the running coupling $\alpha_s(\mu_R)$.

2.5.3 Renormalization

The primary objective of this section is to eliminate ultraviolet divergences. In a renormalizable quantum field theory, such as QCD [9, 10], this is achieved by adding a finite number of counterterms to the Lagrangian. The original, unrenormalized Lagrangian contains all the interactions as described above, while the counterterms are constructed specifically to cancel out UV divergences that arise in loop corrections.
The ansatz for the renormalization of the QCD Lagrangian is

$$\mathcal{L}_{\text{QCD}}(g_{s,0}, \Psi_0, A_0^\mu, c_0, m_0, \xi_0) = \mathcal{L}_{\text{QCD}}(g_s\mu^\epsilon, \Psi, A^\mu, c, m, \xi) + \mathcal{L}_{\text{c}}(g_s\mu^\epsilon, \Psi, A^\mu, c, m, \xi) \ ,$$

where $\mathcal{L}_{\text{c}}$ is the Lagrangian of the counterterms, defined as[20]:

$$\begin{aligned}
\mathcal{L}_{\text{counter}} = &(Z_\Psi - 1)\mathrm{i}\overline{\Psi}\gamma^\mu\partial_\mu\Psi - (Z_V - 1)g_s\mu^\epsilon\overline{\Psi}A_\mu^a T^a\Psi - (Z_m - 1)\overline{\Psi}m\Psi \\
&- (Z_A - 1)\frac{1}{4}(\partial_\mu A_\nu^a - \partial_\nu A_\mu^a)^2 + (Z_{3g} - 1)\frac{1}{2}g_s\mu^\epsilon f_{abc}(\partial_\mu A_\nu^a - \partial_\nu A_\mu^a)A_b^\mu A_c^\nu \\
&- (Z_{4g} - 1)\frac{1}{4}g_s^2\mu^{2\epsilon} f_{abc}f_{ade}A_b^\mu A_c^\nu A_\mu^d A_\nu^e \\
&+ (Z_c - 1)\partial_\mu\overline{c}_a\partial^\mu c^a + (Z_{Vc} - 1)g_s\mu^\epsilon f_{abc}(\partial^\mu\overline{c}^a)A_\mu^b c^c \ ,
\end{aligned} \tag{2.92}$$

where the flavor index is omitted to make the equation more readable. The counterterms effectively amount to rescaling the quark, gluon, and ghost fields, as well as the gauge-

[20] In the literature, the renormalization constants are often named differently. A common naming scheme is: $Z_V = Z_1^F$, $Z_\Psi = Z_2$, $Z_A = Z_3$, $Z_{3g} = Z_1$, $Z_{4g} = Z_4$, $Z_c = \tilde{Z}_3$, $Z_{Vc} = \tilde{Z}_1$.

fixing parameter. These parameters are redefined as follows:

$$\begin{aligned} \Psi &\to Z_\Psi^{-1/2}\Psi_0 \\ A_\mu^a &\to Z_A^{-1/2}A_{\mu,0}^a \\ c^a &\to Z_c^{-1/2}c_0^a \\ \xi &\to Z_A\,\xi_0 \ , \end{aligned} \tag{2.93}$$

where Z_Ψ, Z_A and Z_c are the quark, gluon, and ghost field renormalization constants, respectively. The renormalization constants for the gauge fixing parameter and the gluon field are both Z_A, to keep the form of the gauge fixing term in the Lagrangian invariant. This rescaling also introduces the renormalized coupling constant

$$g_{s,0} = Z_g g_s \mu^\epsilon \tag{2.94}$$

and the renormalized mass

$$m_0 = Z_m Z_\Psi^{-1} m \ . \tag{2.95}$$

The coupling renormalization constant Z_g can be related to the other field renormalization constants using the following identities:

$$Z_g = \frac{Z_V}{Z_\Psi Z_A^{1/2}} = \frac{Z_{3g}}{Z_A^{3/2}} = \frac{Z_{4g}^{1/2}}{Z_A} = \frac{Z_{Vc}}{Z_c Z_A^{1/2}} \tag{2.96}$$

Additionally the renormalization constants are also related by the Slavnov-Taylor identities [127–129]

$$\frac{Z_{3g}}{Z_A} = \frac{Z_{Vc}}{Z_c} = \frac{Z_V}{Z_\Psi} = \frac{Z_{4g}}{Z_{3g}} \ , \tag{2.97}$$

which generalizes the Ward identity $Z_V = Z_\Psi$ from QED.
To determine the full set of renormalization constants, it suffices to compute the quark, gluon, and vertex renormalization constants. This can be achieved by calculating the UV divergences of the quark and gluon self-energies and the vertex correction at one loop order. For example, the quark self-energy diagram of Figure 2.4 gives

$$-\mathrm{i}\Sigma^{ab}(p) = \mathrm{i}g_s^2 (T_c)^{ad}(T_c)^{db} \int \frac{\mathrm{d}^d l}{(2\pi)^d} \frac{\gamma_\mu(\not{p} - \not{l} + m)\gamma^\mu}{l^2((p-l)^2 - m^2)} \ . \tag{2.98}$$

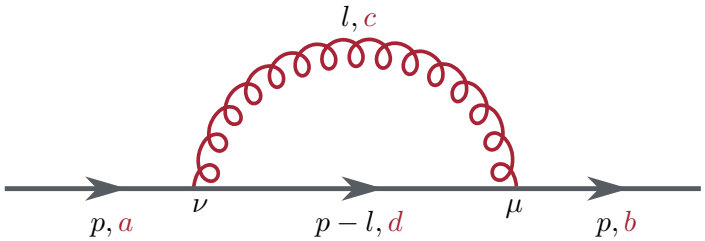

Figure 2.4: Quark self-energy contribution. The particles are labeled with their momenta (black) and color indices (red), and the vertices are label by their Lorentz index.

The color factor evaluates to $(T_c)^{ad}(T_c)^{db} = C_F\delta^{ab}$ (see Section 4.1), and the integral is known from the electron self-energy contribution. A systematic way to calculate these integrals is provided in Section 4. Finally, the quark self-energy is evaluated as follows:

$$-\mathrm{i}\Sigma^{ab}(p) = \mathrm{i}\frac{g_s^2 C_F \delta^{ab}}{16\pi^2\epsilon}(\not{p} - 4m) + \mathcal{O}(\epsilon^0) \ . \tag{2.99}$$

The Feynman diagram for the counterterm evaluates to

$$-\mathrm{i}\Sigma^{ab}_{\text{counter}}(p) = \mathrm{i}\delta^{ab}(Z_\Psi - 1)\not{p} - \mathrm{i}\delta^{ab}(Z_m - 1)m \ . \tag{2.100}$$

To make this combination finite the quark wave function renormalization is

$$Z_\Psi - 1 = -\frac{g_s^2 C_F}{16\pi^2\epsilon} + \mathcal{O}(\epsilon^0) \ , \tag{2.101}$$

and the quark mass renormalization is

$$Z_m - 1 = -\frac{g_s^2 C_F}{4\pi^2\epsilon} + \mathcal{O}(\epsilon^0) \ . \tag{2.102}$$

Similar considerations for the gluon self energy diagrams of Figure 2.5 give

$$Z_A - 1 = \frac{g_s^2}{16\pi^2\epsilon}\left(\frac{5C_A}{3} - \frac{4N_f T_F}{3}\right) + \mathcal{O}(\epsilon^0) \ . \tag{2.103}$$

And from the vertex correction of Figure 2.6

$$Z_V - 1 = -\frac{g_s^2}{16\pi^2\epsilon}(C_A + C_F) \tag{2.104}$$

can be derived. The detailed calculations can be found in Section 7 of [130].

Figure 2.5: Gluon self-energy contributions from a gluon loop, fermion loops, ghost loops, and a loop generated by a four-gluon vertex.

Figure 2.6: The two vertex corrections to the quark-gluon vertex in QCD.

Renormalization Schemes

Once the divergences are isolated, it has to be decided what to do with the remaining finite parts. This is the role of the renormalization scheme. While the divergent terms must be removed to make sense of the theory, the finite parts can, in principle, be subtracted in various ways. A renormalization scheme imposes a condition on how this subtraction is performed.

One physically motivated scheme is the on-shell scheme, often used in QED, where parameters are fixed at physical values (e.g., the physical mass or coupling at a specific energy). However, in QCD, this approach is problematic due to confinement: quarks and gluons are never observed as free particles and cannot be truly on-shell in the physical sense.

Instead, a practical choice in QCD is the minimal subtraction (MS) scheme introduced by Gerard 't Hooft and Steven Weinberg in 1973 [131, 132]. In this scheme, only the divergent $1/\epsilon$ poles from dimensional regularization are subtracted, and the finite parts are left untouched. The pole terms in dimensional regularization always come in tandem with two other terms

$$\frac{1}{\epsilon} - \gamma_E + \log(4\pi) \ , \tag{2.105}$$

where $\gamma_E \approx 0.577$ is the Euler-Mascheroni constant. Therefore, it is sensible to also absorb these common constants into the subtraction term. This is done in the widely used modified minimal subtraction scheme (denoted $\overline{\text{MS}}$) [133]. This version of the scheme simplifies many calculations and is the default scheme in modern QCD computations.

In practical calculations, implementing the $\overline{\text{MS}}$ scheme is done by replacing the renormal-

ization scale

$$\mu^2 \to \overline{\mu}^2 = \mu^2 \frac{\mathrm{e}^{\gamma_E}}{4\pi} \tag{2.106}$$

and only subtracting the $1/\epsilon$ poles. This shift does not affect the renormalization group equation (RGE), since it is defined in terms of the logarithmic derivative

$$\frac{\mathrm{d}}{\mathrm{d}\log\mu} = \mu \frac{\mathrm{d}}{\mathrm{d}\mu} \ , \tag{2.107}$$

which is invariant under such a change.
The resulting renormalization constants at one-loop in the MS scheme are

$$\begin{aligned} Z_\Psi &= 1 - \frac{g_s^2 C_F}{16\pi^2\epsilon} \\ Z_m &= 1 - \frac{g_s^2 C_F}{4\pi\epsilon} \\ Z_A &= 1 + \frac{g_s^2}{16\pi^2\epsilon}\left(\frac{5C_A}{3} - \frac{4N_f T_F}{3}\right) \\ Z_V &= 1 - \frac{g_s^2}{16\pi^2\epsilon}(C_A + C_F) \ . \end{aligned} \tag{2.108}$$

From Equation (2.94), it is possible to determine the scale dependence of the coupling constant using (2.96) and the renormalization constants from (2.108):

$$g_{s,0} = g_s \mu^\epsilon \frac{Z_V}{Z_\Psi Z_A^{1/2}} = g_s \mu^\epsilon \left(1 - \frac{g_s^2}{32\pi^2\epsilon}\left(\frac{11}{3}C_A - \frac{4}{3}T_F N_f\right) + \mathcal{O}(g_s^4)\right) \ . \tag{2.109}$$

Using the already suggestive short hand notation

$$\beta_0 = \frac{11}{3}C_A - \frac{4}{3}T_F N_f \tag{2.110}$$

this becomes:

$$g_{s,0} = \mu^\epsilon \left(g_s - \frac{g_s^3}{32\pi^2\epsilon}\beta_0\right) + \mathcal{O}(g_s^5) \ . \tag{2.111}$$

Taking the derivative with respect to μ on both sides results in

$$0 = \epsilon\mu^{\epsilon-1}\left(g_s - \frac{g_s^3}{32\pi^2\epsilon}\beta_0\right) + \mu^\epsilon \left(1 - \frac{3g_s^2}{32\pi^2\epsilon}\beta_0\right)\frac{\mathrm{d}g_s}{\mathrm{d}\mu} + \mathcal{O}(g_s^4) \ . \tag{2.112}$$

Solving this for $\mu\frac{\mathrm{d}g_s}{\mathrm{d}\mu}$ gives

$$\mu\frac{\mathrm{d}g_s}{\mathrm{d}\mu} = -\epsilon\left(g_s - \frac{g_s^3}{32\pi^2\epsilon}\beta_0\right)\left(1 + \frac{3g_s^2}{32\pi^2\epsilon}\beta_0\right) + \mathcal{O}(g_s^4) \ , \tag{2.113}$$

which results at leading-order in ϵ and g_s in the renormalization group equation

$$\mu\frac{\mathrm{d}g_s}{\mathrm{d}\mu} = -\frac{g_s^3}{16\pi^2}\beta_0 \ . \tag{2.114}$$

The renormalization group equation can be solved analytically to obtain the running of the coupling:

$$g_s^2(\mu^2) = \frac{g_s^2(\mu_0^2)}{1 + \frac{\beta_0}{16\pi^2}g_s^2(\mu_0^2)\ln\left(\frac{\mu^2}{\mu_0^2}\right)} \ . \tag{2.115}$$

This result matches the known expression for the QCD coupling evolution, as previously given in Equation (2.46) for $\alpha_s = g_s^2/(4\pi)$.
It is important to emphasize that the effect of counterterms in the Lagrangian (2.92) is mirrored in the rescaling of the fields (2.93) and redefinition of the coupling constant (2.94). Subtracting UV divergences via counterterms is equivalent to redefining the strong coupling as follows:

$$\frac{\alpha_{s,0}}{4\pi} = \frac{\alpha_s(\mu)}{4\pi}\left(1 - \frac{1}{\epsilon}\frac{\alpha_s(\mu)}{4\pi}\beta_0\left(\frac{\mathrm{e}^{\gamma_E}}{4\pi}\right)^{\epsilon}\right) \ . \tag{2.116}$$

This is the method through which ultraviolet divergences are handled throughout this thesis.

2.6 Factorization in QCD

So far, UV divergences have been addressed through renormalization, and soft divergences cancel when all contributions to the same observable are summed. The remaining source of divergences are collinear divergences.
To recall, collinear divergences stem from the collinear emission of massless particles from massless external legs. These external particles either originate from hadrons or eventually hadronize into observable final-state hadrons. Given that hadrons are intrinsically non-perturbative objects, it is natural to expect that these collinear divergences can be absorbed into the complex non-perturbative dynamics associated with the external hadrons.

Therefore, the goal is to find a systematic way to identify, characterize, and isolate collinear divergences and assign them to the non-perturbative structure of the initial or final state hadrons. For this to be viable in practice, it is crucial that the way collinear divergences arise does not depend on the specific hard scattering process. Otherwise, the separation between long-distance (non-perturbative) and short-distance (perturbative) physics would have to be redefined for each individual process, eliminating the predictive power.
However, if this separation is universal, then the non-perturbative components, once measured in one process, can be applied to others. This principle is formalized in the so-called factorization theorems. For a number of processes, these theorems have been rigorously proven (see [134–149]), while for others, factorization remains an assumption. A broad overview is provided in [103].
To make the structure explicit, consider a generic process in which an incoming hadron A scatters into an outgoing hadron B. The details of the scattering are irrelevant for this argument. The factorization theorems establish that the hadronic cross section σ_{AB} can be factorized into a convolution of:

A hard partonic cross section $\hat{\sigma}_{ab}$, computable in perturbative QCD, where a and b are partons of the hadron A and B respectively

a non-perturbative parton distribution function (PDF) $f_{a/A}$, which describes the probability distribution for finding a parton a inside the initial-state hadron A, and

a non-perturbative fragmentation function (FF) $d_{B/b}$, which encodes how an outgoing parton b hadronize into the detected final-state hadron B.

This is symbolically written as

$$\sigma_{AB} = f_{a/A} \otimes \hat{\sigma}_{ab} \otimes d_{B/a} \ , \tag{2.117}$$

where the convolutions are over the relevant momentum fractions. For an explicit example, see Section 3.4.
Each component in this equation is renormalized and finite, free of all UV and IR singularities. The central statement of the factorization theorems is that all low-energy phenomena are captured by the parton distribution functions and fragmentation functions, which are universal and do not depend on the specifics of the hard scattering. They depend only on the specific hadron and the parton. While all high-energy phenomena are captured by the hard partonic cross section, which does not depend on the specific hadrons but only on the partons that participate in the hard scattering. This formula serves as the starting point for the analysis of any physical observable in perturbative QCD.

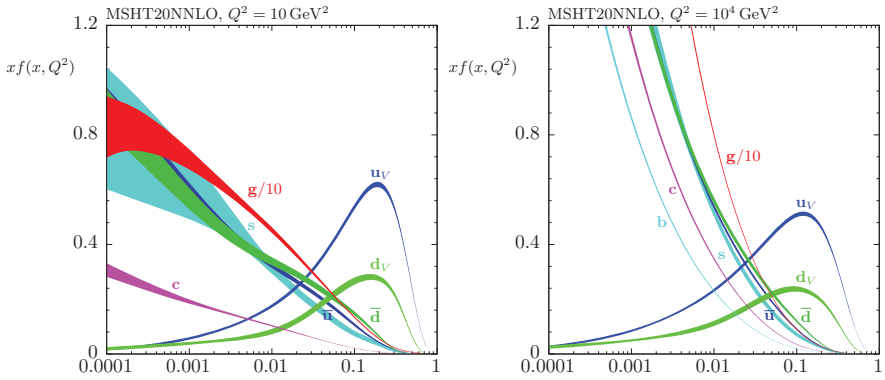

Figure 2.7: Parton distribution functions from the NNLO MSHT20 global analysis, shown at two different scales: $Q^2 = 10$ GeV^2 (left) and $Q^2 = 10^4$ GeV^2 (right). The bands represent one-σ confidence intervals. The figure is taken from [150].

From a physical standpoint, this factorization makes intuitive sense. The internal dynamics of a hadron with mass M take place over time scales of the order of $\sim 1/M$, whereas hard interactions involving a large momentum transfer Q happen on time scales $\sim 1/Q$, which are significantly shorter. Consequently, during the hard scattering, the internal structure of the hadron appears frozen, justifying the assumption that the partons can be treated as quasi-free particles. Typically, only a single parton from each hadron participates in the hard scattering, moving collinearly with the parent hadron and carrying a certain fraction of its momentum. This method of separating long- and short-distance interactions is called collinear factorization.

At leading order, PDFs can be interpreted probabilistically: they represent the probability of finding a parton with a specific longitudinal momentum fraction inside the hadron. Similarly, FFs describe the probability that a parton will fragment into a particular hadron with a given momentum. However, at higher orders in perturbation theory, this probabilistic interpretation breaks down. PDFs and FFs acquire scheme- and scale-dependence, and only the convolution with the hard cross section in the same factorization scheme yields a physical quantity.

Parton distribution functions are inherently non-perturbative and are determined from global fits to experimental data. One fit is presented in Figure 2.7.

While collinear factorization is a powerful framework, it is based on an approximation. In reality, partons can possess intrinsic transverse momentum, i.e., momentum perpendicular to the beam direction, even prior to the hard interaction. This transverse momentum contributes to the final-state kinematics without requiring recoil against another particle.

To model such effects, one introduces transverse momentum dependent PDFs (TMDs). These functions provide a more detailed description of parton dynamics by encoding both the longitudinal momentum fraction and transverse momentum of partons inside hadrons [151, 152].
TMDs are particularly useful for describing processes involving low transverse momentum. However, this approach has its limitations, they are not valid across the entire kinematic range. For large transverse momentum, a fully perturbative treatment is required. The intermediate region, where both non-perturbative and perturbative contributions are significant, is the subject of active theoretical research. Notably, the matching between the TMD and collinear descriptions in this regime remains imperfect, and inconsistencies have been identified, as discussed in [24].
Returning to collinear factorization, one of the key challenges in proving factorization theorems lies in demonstrating that the leading contribution to the observable comes from Feynman diagrams that resemble Figure 2.8, where all regions (initial state, hard scattering, final state) are separated and only connected by single lines representing partons. However, the picture shown in Figure 2.8 can not be exact. For instance, the proton starts off as color neutral, yet when a colored quark is extracted for the hard process, the proton remnant must again become color neutral, without the one quark. This implies, at the very least, that soft interactions between the regions exist to exchange color. Thus, the goal of factorization theorems is not to show that the splitting holds exactly, but that all other contributions to the observable, such as multiple connections between regions, are suppressed by a factor of M/Q. The strategy of factorization proofs is outlined in great detail in [103, 153].
Accepting that the leading-power contributions take the simplified, factorized form of Figure 2.8, the next task is to determine how to systematically rearrange the collinear divergences in order to arrive at the factorized structure of Equation (2.117).

2.6.1 From Bare Distribution Functions to PDFs

At this stage, it is not yet clear how to isolate the partonic hard cross section $\hat{\sigma}_{ab}$ appearing in the factorization formula (2.117). The issue is that the collinear divergences still remain in the partonic cross section; let us denote this unrenormalized cross section by $\tilde{\sigma}_{ab}$. These divergences must be systematically extracted and attributed to the distribution and fragmentation functions. This situation can be represented symbolically as

$$\sigma_{AB} = f_{a/A}^{\text{bare}} \otimes \tilde{\sigma}_{ab} \otimes d_{B/b}^{\text{bare}} \,, \tag{2.118}$$

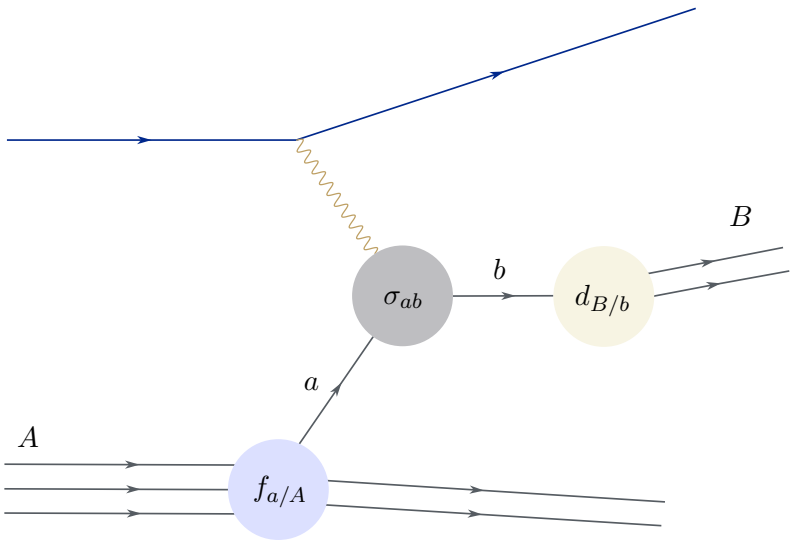

Figure 2.8: Schematical illustration of the factorization of the SIDIS process. The incident lepton (blue) scatters off particle A, represented by the three incident lines at the bottom, via a virtual photon (yellow). The shaded areas represent the three ingredients for the factorization formula. The light blue area represents the PDF $f_{a/A}$, the light yellow area the FF $d_{B/b}$ and the gray area the hard scattering σ_{ab}.

where $f_{a/A}^{\text{bare}}$ and $d_{B/b}^{\text{bare}}$ are the bare, unrenormalized, parton distribution and fragmentation functions, respectively. The partonic cross section $\tilde{\sigma}_{ab}$, as well as the bare parton distribution and fragmentation functions, contain collinear divergences, but these divergences cancel exactly to give a finite hadronic cross section σ_{AB} with no divergences.
The next step in the factorization procedure is to separate the collinear divergences from the cross section $\tilde{\sigma}_{ab}$. Divergences associated with initial-state partons are extracted at a scale μ_f and denoted by $\hat{\sigma}_{ab}^{\text{coll}}$. Similarly, divergences from final-state partons are extracted at a scale μ_f' and are denoted by $\hat{\sigma}_{ab}^{\text{coll}'}$. These scales μ_f and μ_f', the factorization scales, are typically chosen to be of the order of the hard scale Q of the process to avoid large logarithms. Thus, the cross-section can be written as

$$\sigma_{AB} = f_{a/A}^{\text{bare}} \otimes \hat{\sigma}_{ab}^{\text{coll}}(\mu_f) \otimes \hat{\sigma}_{ab}(\mu_f, \mu_f') \otimes \hat{\sigma}_{ab}^{\text{coll}'}(\mu_f') \otimes d_{B/b}^{\text{bare}} \ . \tag{2.119}$$

The exact form of the terms $\hat{\sigma}_{ab}^{\text{coll}}$ and $\hat{\sigma}_{ab}^{\text{coll}'}$ depends on the factorization scheme used. Analogous to the renormalization procedure, where in different schemes different finite parts can be subtracted alongside the divergences, different factorization schemes define different finite subtractions. This work adopts the same scheme as for the renormalization: the $\overline{\text{MS}}$ scheme, where alongside the divergences, also the accompanying terms $\log(4\pi) - \gamma_E$

are subtracted.
These divergences are then absorbed into the parton distribution functions and fragmentation functions:

$$f_{a/A}(\mu_f) = f_{a/A}^{\text{bare}} \otimes \hat{\sigma}_{ab}^{\text{coll}}(\mu_f) \tag{2.120}$$

$$d_{B/b}(\mu'_f) = \hat{\sigma}_{ab}^{\text{coll}'}(\mu'_f) \otimes d_{B/b}^{\text{bare}} \ . \tag{2.121}$$

In doing so, the renormalized PDFs $f_{a/A}(\mu_f)$ and FFs $d_{B/b}(\mu'_f)$ inherit the dependence on the factorization scale. They are now completely finite. In principle, the full hadronic cross section σ_{AB} should be independent of the factorization scale when computed to all orders in perturbation theory. However, at a finite order in α_s the cross-section is left with some residual dependence on the scale. As is the case with the renormalization scale μ, varying the scale provides a useful means for estimating theoretical uncertainties in predictions.
The scale dependence of PDFs and FFs is governed by evolution equations, which allow one to relate their values at different factorization scales. These are known as the DGLAP equations [154–157]:

$$\mu_f^2 \frac{\partial f_{a/A}(\eta, \mu_f)}{\partial \mu_f^2} = \int_\eta^1 \frac{\mathrm{d}\xi}{\xi} P_{aa'}(\xi, \alpha_s(\mu_f)) f_{a'/A}(\eta/\xi, \mu_f) \tag{2.122}$$

$$\mu_f'^2 \frac{\partial d_{B/b}(\eta, \mu'_f)}{\partial \mu_f'^2} = \int_\eta^1 \frac{\mathrm{d}\xi}{\xi} P'_{bb'}(\xi, \alpha_s(\mu'_f)) d_{B/b'}(\eta/\xi, \mu_f) \ . \tag{2.123}$$

Here, η is the momentum fraction carried by partons a or b relative to their parent particles A and B. A sum over the intermediate partons a' and b' is implied. The functions $P_{aa'}(\xi, \alpha_s(\mu_f))$ and $P'_{bb'}(\xi, \alpha_s(\mu'_f))$ are the Altarelli-Parisi splitting functions, also known as DGLAP kernels. The Altarelli-Parisi splitting functions can be expanded in a perturbative series in the strong coupling constant:

$$P_{aa'}(\xi, \alpha_s) = \left(\frac{\alpha_s}{2\pi}\right) P_{aa'}^{(0)}(\xi) + \left(\frac{\alpha_s}{2\pi}\right)^2 P_{aa'}^{(1)}(\xi) + \mathcal{O}(\alpha_s^3) \ , \tag{2.124}$$

with a similar expansion for $P'_{bb'}(\xi, \alpha_s(\mu'_f))$. The coefficients $P_{aa'}^{(i)}(\xi)$ and $P_{bb'}^{\prime(i)}(\xi)$ can be calculated in perturbative QCD. The coefficients $P_{aa'}^{(0)}(\xi)$ were first calculated in [154, 156]. They are given by:

$$
\begin{aligned}
P_{qq}^{(0)}(\xi) &= C_F \left(\frac{1+\xi^2}{(1-\xi)_+} + \frac{3}{2}\delta(1-\xi) \right) \\
P_{qg}^{(0)}(\xi) &= T_f \left(\xi^2 + (1-\xi)^2 \right) \\
P_{gq}^{(0)}(\xi) &= C_F \left(\frac{1+(1-\xi)^2}{\xi} \right) \\
P_{gg}^{(0)}(\xi) &= 2C_A \left(\frac{\xi}{(1-\xi)_+} + \frac{1-\xi}{\xi} + \xi(1-\xi) \right) \\
&\quad + \frac{11C_A - 4N_f T_f}{6} \delta(1-\xi) \ ,
\end{aligned}
\tag{2.125}
$$

where the plus distribution $(1-\xi)_+^{-1}$ is, for any sufficiently regular test function $f(\xi)$, defined as:

$$
\int_0^1 \mathrm{d}\xi \frac{f(\xi)}{(1-\xi)_+} = \int_0^1 \mathrm{d}\xi \frac{f(\xi) - f(1)}{1-\xi} \ . \tag{2.126}
$$

The two loop [158–171] and three loop results [172–176] are also known, while in recent years progress has been made towards four loop results [177–183]. For the fragmentation functions the leading-order coefficients coincide with those for initial state partons [154–156, 184–187]. However, from next-to-leading order onward, the evolution of the factorization functions differs. Next-to-leading order results were calculated in [158, 163, 167, 188, 189] and third order results can be found in [190–193].
To avoid large logarithms and ensure reliable predictions, the factorization scales μ_f and μ'_f are typically chosen to be of the same order as the hard scale of the process. The final form of the factorized cross-section is as follows:

$$
\sigma_{AB}(\mu_f, \mu'_f) = f_{a/A}(\mu_f) \otimes \hat{\sigma}_{ab}(\mu_f, \mu'_f) \otimes d_{B/a}(\mu'_f) \ . \tag{2.127}
$$

As guaranteed by the factorization theorem, the parton distribution functions $f_{a/A}$ and fragmentation functions $d_{B/b}$ are universal: they do not depend on the specifics of the hard process $\hat{\sigma}_{ab}$, and the hard process is independent of the external hadrons. This universality will be exploited in the next section, where a procedure to extract the collinear divergences from the unrenormalized partonic cross section $\tilde{\sigma}_{ab}$ is developed.

2.6.2 The Hard Partonic Cross Section

The perturbative calculation of a partonic process using Feynman rules yields a renormalized but infrared-divergent cross section, denoted $\tilde{\sigma}_{ab}$. To arrive at the desired finite hard partonic cross section $\hat{\sigma}_{ab}$, the collinear divergences must be systematically removed. This procedure is guided by the factorization theorem. A key implication of the factorization theorem is that the factorization formula holds regardless of the initial or final state with the correct density functions f and d. This means that the factorization formula can also be applied when partons themselves are in the initial and final state. This allows to apply the factorization structure directly to partonic scattering, relating the divergent cross section $\tilde{\sigma}_{ab}$ to the finite hard cross section $\hat{\sigma}_{ab}$ through

$$\tilde{\sigma}_{ab} = f_{i/a} \otimes \hat{\sigma}_{ij} \otimes d_{b/j} \ , \tag{2.128}$$

where $f_{i/a}$ and $d_{b/j}$ are the parton-in-parton distribution and fragmentation functions, respectively. The parton-in-parton distribution function $f_{i/a}(\xi)$ encodes the probability of a parton a splitting into a parton i with momentum fraction ξ of the parent parton. The language of a parton splitting into a different particle (or the same) is already suggestive of how these functions $f_{i/a}$ and $d_{b/j}$ can be calculated. In fact, the advantage of this approach is that the parton-in-parton functions are calculable in perturbation theory. For the explicit calculation of $f_{i/a}$ and $d_{b/j}$ see [153] Chapters 9 and 12, respectively. One finds that the parton-in-parton distribution function can be expressed by the Altarelli-Parisi splitting functions P_{ia}, introduced earlier in the context of DGLAP evolution (2.122). These kernels are calculable using a perturbative expansion:

$$P_{ia}(\xi) = \left(\frac{\alpha_s}{2\pi}\right) P_{ia}^{(0)}(\xi) + \left(\frac{\alpha_s}{2\pi}\right)^2 P_{ia}^{(1)}(\xi) + \mathcal{O}(\alpha_s^3) \ . \tag{2.129}$$

The parton-in-parton distribution function can then be expressed as follows:

$$f_{i/a}(\xi) = \delta_{ia}\delta(1-\xi) - \frac{S_\epsilon}{\epsilon}\frac{\alpha_s}{2\pi} P_{ia}^{(0)}(\xi) + \mathcal{O}(\alpha_s^2) \ , \tag{2.130}$$

where factor S_ϵ corresponds to the choice of renormalization scheme. In the $\overline{\text{MS}}$ scheme, used throughout this thesis, it is given by

$$S_\epsilon = \frac{4\pi}{\Gamma(1-\epsilon)} \ . \tag{2.131}$$

Analogous expressions exist for the fragmentation functions ([153] Chapter 12), which,

while structurally similar, generally involve different splitting functions beyond leading order. Both can be written as a perturbative series in α_s:

$$f_{i/a}(\xi) = \sum_{n=0}^{\infty} \left(\frac{\alpha_s}{2\pi}\right)^n f_{i/a}^{(n)}(\xi) \tag{2.132}$$

$$d_{b/j}(\zeta) = \sum_{n=0}^{\infty} \left(\frac{\alpha_s}{2\pi}\right)^n d_{b/j}^{(n)}(\zeta) \ . \tag{2.133}$$

The trivial contributions are given by

$$f_{i/a}^{(0)}(\xi) = \delta_{ia}\delta(1-\xi) \qquad \text{and} \qquad d_{b/j}^{(0)}(\zeta) = \delta_{bj}\delta(1-\zeta) \ . \tag{2.134}$$

The leading contributions also coincide:

$$f_{i/a}^{(1)}(\xi) = -\frac{S_\epsilon}{\epsilon} P_{ia}^{(0)}(\xi) \ , \qquad d_{b/j}^{(1)}(\zeta) = -\frac{S_\epsilon}{\epsilon} P_{bj}^{(0)}(\zeta) \ . \tag{2.135}$$

The cross section $\tilde{\sigma}_{ab}$, that is calculated from the Feynman rules and still has collinear divergences can also be written as the perturbative expansion:

$$\tilde{\sigma}_{ab} = \sum_{n=0}^{\infty} \left(\frac{\alpha_s}{2\pi}\right)^n \tilde{\sigma}_{ab}^{(n)} \ . \tag{2.136}$$

The desired hard cross section $\hat{\sigma}_{ab}$ can be expressed similarly:

$$\hat{\sigma}_{ab} = \sum_{n=0}^{\infty} \left(\frac{\alpha_s}{2\pi}\right)^n \hat{\sigma}_{ab}^{(n)} \ . \tag{2.137}$$

Inserting these expansions into the factorization formula for partonic states (2.128) and comparing order by order yields, for the leading-order:

$$\hat{\sigma}_{ab}^{(0)} = \tilde{\sigma}_{ab}^{(0)} \tag{2.138}$$

and at next-to-leading order:

$$\begin{aligned} \hat{\sigma}_{ab}^{(1)} &= \tilde{\sigma}_{ab}^{(1)} - f_{i/a}^{(1)} \otimes \hat{\sigma}_{ib}^{(0)} - \hat{\sigma}_{aj}^{(0)} \otimes d_{b/j}^{(1)} \\ \hat{\sigma}_{ab}^{(1)} &= \tilde{\sigma}_{ab}^{(1)} + \frac{S_\epsilon}{\epsilon} P_{ia}^{(0)} \otimes \hat{\sigma}_{ib}^{(0)} + \frac{S_\epsilon}{\epsilon} \hat{\sigma}_{aj}^{(0)} \otimes P_{bj}^{(0)} . \end{aligned} \tag{2.139}$$

Thus, at one loop level, obtaining the finite hard cross section $\hat{\sigma}_{ab}^{(1)}$ is straightforward: it amounts to subtracting the collinear divergences, expressed as convolutions of the splitting functions with the Born-level cross sections from the perturbatively calculated cross section at parton level $\tilde{\sigma}_{ab}^{(1)}$. It is crucial that the Born cross sections $\hat{\sigma}_{ib}^{(0)}$ and $\hat{\sigma}_{aj}^{(0)}$ are evaluated at $\epsilon \neq 0$ at least to order ϵ^1, since they are multiplied by explicit $1/\epsilon$ poles. The final result $\hat{\sigma}_{ab}^{(1)}$ is then guaranteed to be free of divergences and suitable for insertion into the hadronic factorization formula (2.117) to obtain results for hadrons. A more detailed application of this procedure to the specific process studied in this thesis - semi-inclusive deep inelastic scattering - will be given in 3.4. This completes the general framework for systematically extracting the finite partonic hard cross section, which is central to perturbative QCD predictions and provides the theoretical foundation for the remainder of this thesis.

Chapter 3

Semi-Inclusive Deep Inelastic Scattering

The central aim of this thesis is to contribute to a deeper understanding of the internal structure of hadrons, with a particular focus on the proton and the origin of the transverse momentum of its constituent particles. One of the most informative processes regarding the inner workings of protons is deep inelastic scattering (DIS), which played a pivotal role in understanding the quark content of the proton. The groundbreaking experiments at the Stanford Linear Accelerator Center (SLAC) in the late 1960s [52, 53], which provided the first experimental evidence for the existence of partons, led to the awarding of the 1990 Nobel Price in physics to Jerome I. Friedman, Henry W. Kendall and Richard E. Taylor. DIS is conceptually similar to Rutherford scattering [6], but takes place at much higher energies, where the interaction is no longer elastic; the incident lepton transfers enough energy to the hadron to break it apart. The process is coined "deep" due to the high momentum transfer, and "inelastic" because the final state no longer contains the intact hadron. In the language of perturbative QCD, this is described as the exchange of a highly virtual photon between the lepton and the hadron. Using QCD factorization, the virtual photon can be interpreted as scattering off a single parton inside the proton. At leading order in perturbative QCD, this process is illustrated in Figure 3.1.

A major strength of DIS lies in its clean theoretical structure. There is only one proton in the initial state, and only the scattered lepton is measured in the final state. The minimal involvement of non-perturbative dynamics makes DIS a powerful tool for determining parton distribution functions (PDFs). In fact, alongside hadron-hadron collisions, DIS is one of the primary experimental sources for global PDF fits [194–199].

While PDFs provide an excellent description of the longitudinal momentum distribution of partons within the proton, this one-dimensional picture is incomplete. The inner work-

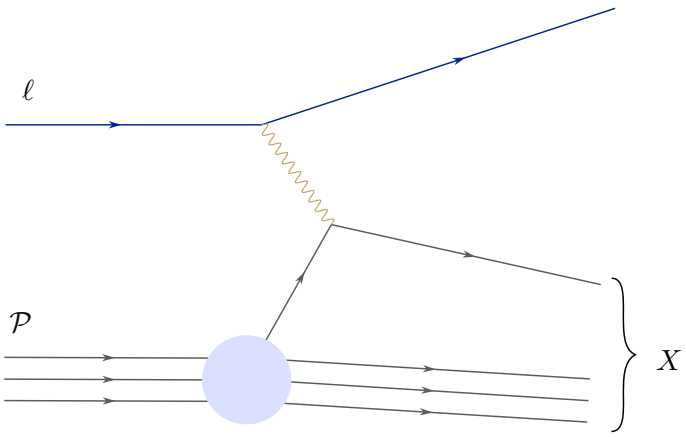

Figure 3.1: DIS at leading order. The lepton ℓ (blue) scatters off a proton $\mathcal{P}$, via exchange of a photon (yellow). The outgoing particles are the scattered lepton ℓ and the remnants of the proton, denoted by X. The light blue shaded region represents the PDF, capturing the long-distance dynamics.

ings of hadrons are more complicated than just being comprised of collinearly moving partons that all share the same position. A more comprehensive understanding of the proton requires probing its three-dimensional structure. This includes the transverse spatial distribution of partons, described by the generalized parton distribution (GPD) (for an introduction, see for example [200, 201]) as well as their transverse momentum distribution, encoded in the transverse momentum dependent PDF (TMD) (see Section 2.6 and [151, 152]). However, standard DIS is insufficient for accessing this information because all information about the three-dimensional structure of the proton is encoded in the final state hadrons, which are not measured in a pure DIS process.

To overcome this limitation, DIS must be modified to also include measurements of one hadron in the final state. Since a specific hadron in the final state is observed, this process is no longer fully inclusive. This modified process is known as semi-inclusive deep inelastic scattering (SIDIS). Notably, measuring the hadron in the final state enables the study of TMDs, as the transverse momentum of the detected hadron reflects the transverse motion of the original parton.

An additional benefit of SIDIS is its sensitivity to the flavor structure of the proton. By analyzing the flavor composition of the observed hadron, one can infer the flavor of the struck parton, thus gaining insight into flavor-separated parton distribution functions.

In recent years, SIDIS has gained renewed attention owing to the advent of the Electron-Ion Collider (EIC) at Brookhaven National Laboratory [12–15]. The EIC is designed to perform high-precision measurements of deep inelastic scattering, with a major scientific

goal being the three-dimensional imaging of the proton, particularly through the extraction of TMDs. This has spurred significant theoretical advances in SIDIS. The next-to-leading order corrections have long been known [202–204], but in recent years, the next-to-next-to-leading order contributions have also been calculated [205–214].
A precise determination of TMDs requires an understanding of the full range of transverse momentum scales. At low transverse momentum, TMDs provide a valid, non-perturbative description. However, at high transverse momentum, fixed-order perturbative QCD becomes applicable. This thesis focuses specifically on the perturbative regime, which corresponds to large transverse momentum.
The next section introduces SIDIS in greater technical detail, with the goal of developing a theoretical framework suited for describing transverse momentum in the process, particularly in the region of high transverse momentum. This will serve as the basis for the calculations and results presented in the following chapters.

3.1 Kinematics of the SIDIS Process

Semi-inclusive deep inelastic scattering describes the scattering of a lepton off a proton, where the scattered lepton and a final-state hadron are measured. The process is illustrated schematically in Figure 3.2 and can be written as

$$\ell(l) + \mathcal{P}(P) \to \ell(l') + h(P_h) + X \ , \tag{3.1}$$

where ℓ denotes the leptons, $\mathcal{P}$ the proton, h the observed hadron ,and X the remaining unobserved particles resulting from the collision. The four-momenta of the respective particles are indicated in parentheses. Unlike fully inclusive DIS, SIDIS involves tagging a specific hadron h in the final state. Assuming the interaction proceeds via the exchange of a single photon from the lepton beam to the target proton, the momentum transfer is defined as $q := l - l'$ and the virtuality as

$$Q^2 := -q^2 \ . \tag{3.2}$$

This assumption is justified because each photon must couple to the lepton, resulting in an additional factor of α due to the electromagnetic coupling constant. Therefore, additional photons lead to suppressed contributions.
The following Lorentz-invariant variables are commonly introduced in the analysis of SIDIS:

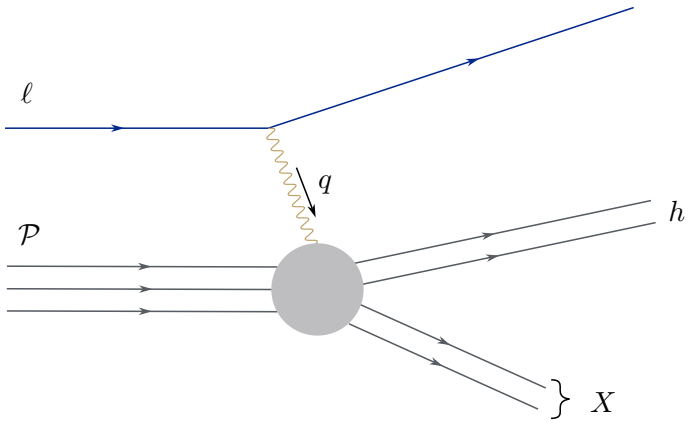

Figure 3.2: Diagram for the SIDIS process, where an incident lepton ℓ (blue) scatters off a proton $\mathcal{P}$ via the exchange of a photon with momentum q (yellow). The resulting particles in the final state are the initial lepton ℓ, a hadron h and the unobserved remnants, collectively called X. The gray shaded area represents the scattering, which can be evaluated via factorization and perturbative QCD.

$$x = \frac{Q^2}{2\ P \cdot q} \qquad y = \frac{P \cdot q}{P \cdot l} \qquad z = \frac{P \cdot P_h}{P \cdot q}\ . \tag{3.3}$$

Here x is the Bjorken x [215], the variable y is called the inelasticity of the reaction, because in the rest frame of the initial proton it describes the energy fraction of the initial lepton that is transferred to the hadron, and the variable z is a new addition to the otherwise standard DIS variables, due to the availability of the final state hadron's momentum.
Throughout this thesis, the hard scattering limit is assumed, i. e., Q^2 is considered to be large with respect to all involved masses, even for fixed x, y and z. Therefore it is justified to neglect all corrections that would be due to the masses of the hadrons or the lepton. The variables x and z can be interpreted at lowest order in perturbative QCD in the following way. If the photon scatters elastically off a single massless parton inside the proton with momentum ξP, then $x = \xi$. This also means that at $x = 1$ the scattering off the proton would be elastic, since the scattering would involve the entire proton and not break it apart. The variable z is the final state analogon; if the momentum fraction of the final state hadron carried by the final state parton is called ζ, i.e., the momentum of the final state parton is P_h/ζ, then $z = \zeta$.
Until now, the standard SIDIS process has been described. The next step is to introduce a central concept in this thesis: transverse momentum. There is one observed parton in the final state, and it is its transverse momentum that is measured. The transverse momentum

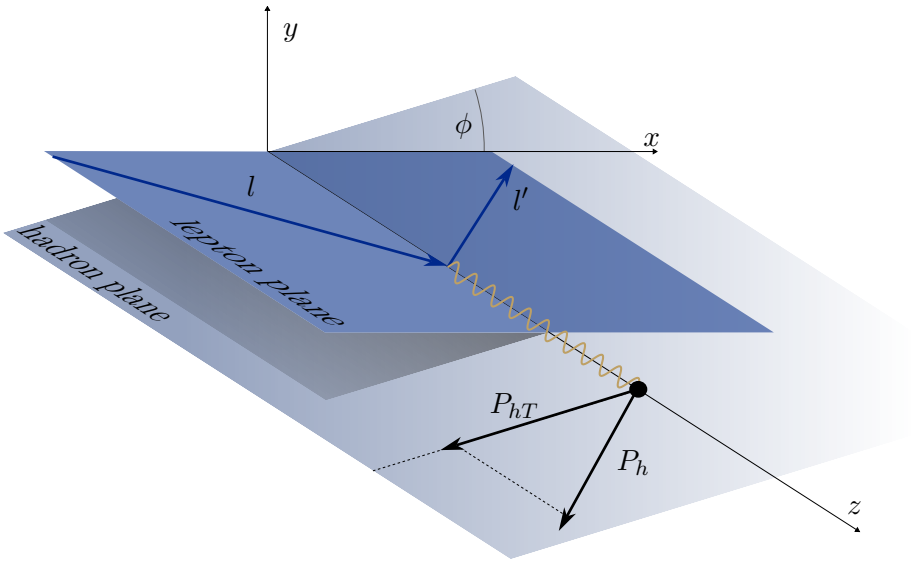

Figure 3.3: Kinematics in the target rest frame. The lepton plane is aligned with the xz-plane, the virtual photon moves along the z-axis, and the initial proton is at rest, signified by the black dot. The hadron plane is tilted with respect to the lepton plane by the angle ϕ. The transverse momentum of P_h is also marked as the part of P_h perpendicular to the virtual photon.

is the part of P_h that is transverse with respect to the photon momentum q in the target rest frame, as shown in Figure 3.3. In this frame, the transverse momentum of P_h is transverse with respect to both the momentum of the initial proton and the photon. In the simplest consideration of SIDIS at leading order, momentum conservation implies that the photon and final state hadron are collinear if there is nothing to push off of, and thus the transverse momentum vanishes. This changes if either intrinsic transverse momentum of the proton is considered, which naturally leads to the concept of transverse momentum dependent parton distribution functions (TMDs) or, the goal of this thesis, the recoil off an additional particle is considered. The latter can result in significantly larger transverse momenta and is therefore mostly relevant for the region of large transverse momenta, the so-called "high p_T" region.

For this thesis, it is convenient to choose a frame in which the momentum of the proton P and the virtual photon q are collinear. In this frame, the transverse momentum P_{hT} is defined as the component of P_h orthogonal to both the momentum of the proton P and the momenta of the exchanged photon q.

Another key variable to introduce is the azimuthal angle ϕ of the resulting hadron with respect to the lepton plane (see Figure 3.3). In accordance with the Trento conventions

[216], it is defined as

$$\begin{aligned} \cos\phi &= \frac{\hat{q}\times\vec{l}}{|\hat{q}\times\vec{l}|}\cdot\frac{\hat{q}\times\vec{P}_h}{|\hat{q}\times\vec{P}_h|}\ , \\ \sin\phi &= \frac{\left(\vec{l}\times\vec{P}_h\right)\cdot\hat{q}}{|\hat{q}\times\vec{l}||\hat{q}\times\vec{P}_h|}\ , \end{aligned} \tag{3.4}$$

where $\hat{q} := \vec{q}/|\vec{q}|$. All vectors are given in the proton rest frame or in a frame that is boosted from the proton rest frame along $\hat{q}$, for example, the hadron frame, which will be defined in the next section.
By introducing the perpendicular projection tensors [216]

$$g_\perp^{\mu\nu} = g^{\mu\nu} - \frac{q^\mu P^\nu + P^\mu q^\nu}{P\cdot q\ (1+\gamma^2)} + \frac{\gamma^2}{1+\gamma^2}\left(\frac{q^\mu q^\nu}{Q^2} - \frac{P^\mu P^\nu}{M^2}\right) \tag{3.5}$$

$$\epsilon_\perp^{\mu\nu} = \epsilon^{\mu\nu\rho\sigma}\frac{P_\mu q_\nu}{P\cdot q\ \sqrt{1+\gamma^2}}\ , \tag{3.6}$$

where $\gamma = 2xM/Q$ and M is the mass of the proton, it is possible to write Equation (3.4) in covariant form as

$$\begin{aligned} \cos\phi &= -\frac{g_\perp^{\mu\nu}l_\mu P_{h\nu}}{|l_\perp||P_{hT}|}\ , \\ \sin\phi &= -\frac{\epsilon_\perp^{\mu\nu}l_\mu P_{h\nu}}{|l_\perp||P_{hT}|}\ , \end{aligned} \tag{3.7}$$

with $|l_\perp| = \sqrt{-g_\perp^{\mu\nu}l_\mu l_\nu}$ and $|P_{hT}| = \sqrt{-g_\perp^{\mu\nu}P_{h\mu}P_{h\nu}}$. The mass M of the proton will be neglected in the following.
Another way to characterize the off-collinearity of the process is through the transverse momentum of the virtual photon with respect to the incoming proton and the produced hadron [217]:

$$q_t^\mu = q^\mu - \frac{q\cdot P_h}{P\cdot P_h}P^\mu - \frac{q\cdot P}{P\cdot P_h}P_h^\mu\ . \tag{3.8}$$

This vector is space-like. For easier notation, the magnitude of the transverse momentum of the photon is denoted by

$$q_T := \sqrt{-q_t^\mu q_{t\mu}}\ , \tag{3.9}$$

which makes q_T positive. An alternative way to write the transverse momentum of the

photon is [24]:

$$q_t^\mu = q^\mu + (1-r)xP^\mu - P_h^\mu/z \ , \tag{3.10}$$

with $r = q_T^2/Q^2$.
The relation between the transverse momentum of the hadron with respect to the photon and proton, the transverse momentum of the photon with respect to the proton and hadron, and the momentum of the proton is given by

$$P_{hT}^\mu = -zq_t^\mu - 2rzxP^\mu \ . \tag{3.11}$$

From this relation, it is easy to go from a differential cross section in q_T^2 to one differential in P_{hT}^2. This change of variable will result in an additional factor of z^2 due to the Jacobian.

3.1.1 Hadron Frame

To make the kinematics more explicit, a specific frame, the hadron frame [217] (also see [218]), is chosen. The hadron frame is the Breit frame of the initial proton and the exchanged photon, where additionally the direction of the x-axis is specified. It is depicted in Figure 3.4. This frame is defined as follows: first, the energy component of the photon momentum is zero, and the three-dimensional part of the momentum points along the z axis. Therefore, the photon momentum is given by

$$q^\mu = (0, 0, 0, -Q) \ . \tag{3.12}$$

The spatial part of the momentum of the incoming proton is also aligned with the z-axis, giving

$$P^\mu = \left(\frac{Q}{2x}, 0, 0, \frac{Q}{2x}\right) \ , \tag{3.13}$$

and lastly the x-axis is chosen such that the spatial component of the outgoing hadron lies in the xz-plane,

$$P_h^\mu = \left(\frac{zQ}{2}\left(1 + \frac{q_T^2}{Q^2}\right), zq_T, 0, \frac{zQ}{2}\left(\frac{q_T^2}{Q^2} - 1\right)\right) \ , \tag{3.14}$$

with q_T from above in Equation (3.8). This is well defined as long as q_T is non-zero. If q_T is zero, the momenta P^μ and P_h^μ are collinear, and the x-axis can be chosen freely. One can see that in this frame, the magnitude of the transverse momentum of the final state

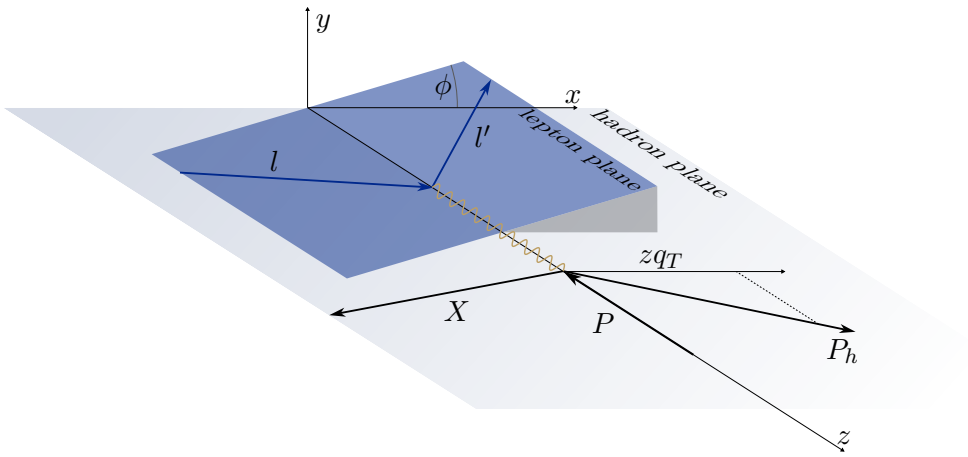

Figure 3.4: Kinematics in the hadron frame. The virtual photon and the proton are moving back-to-back along the z-axis. The x-axis is aligned with the hadron plane. The lepton plane is tilted with respect to the hadron plane by the angle ϕ.

hadron P_{hT} is related to the transverse momentum of the photon via

$$P_{hT} = zq_T \ . \tag{3.15}$$

In fact, this is true in all frames that can be reached by boosting this frame along the z-axis, i.e., all frames in which the initial quark and the photon are collinear. In the hadron frame, the transverse momentum of the virtual photon q_t^μ has the simple form

$$q_t^\mu = \left(-\frac{q_T^2}{Q^2}, -q_T, 0, -\frac{q_T^2}{Q^2} \right) \ . \tag{3.16}$$

Next is the parametrization of the incoming and outgoing lepton momenta. Using the azimuthal angle ϕ between the hadron and lepton plane, defined in (3.7), the lepton momenta can be written as

$$\begin{aligned} l^\mu &= \frac{Q}{2} \left(\cosh\psi, \sinh\psi\cos\phi, \sinh\psi\sin\phi, -1 \right) \ , \\ l'^\mu &= \frac{Q}{2} \left(\cosh\psi, \sinh\psi\cos\phi, \sinh\psi\sin\phi, +1 \right) \ , \end{aligned} \tag{3.17}$$

where ψ is the boost parameter that relates the hadron frame to the electron Breit frame, in which $l^\mu = \frac{Q}{2}(1,0,0,-1)$. In the hadron frame, equations (3.3) and (3.17) fix the boost

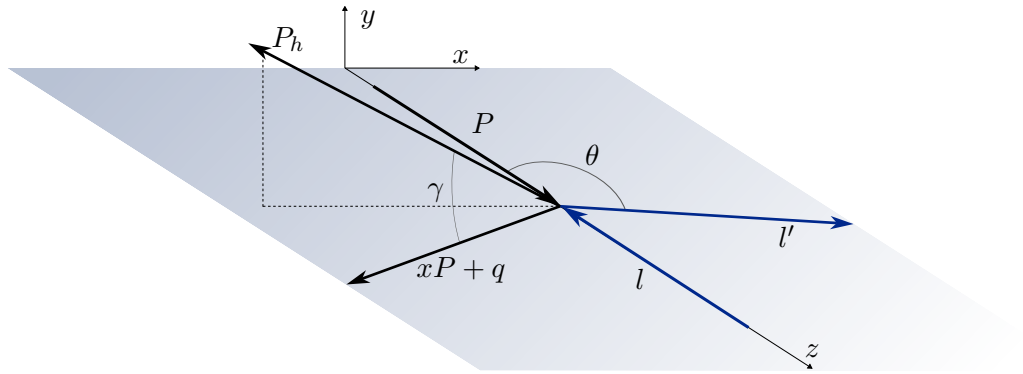

Figure 3.5: Kinematics in the lab frame. The proton and the lepton are colliding along the z-axis. The x-axis is aligned with the lepton plane. The outgoing hadron with momentum P_h moves out of the xz-plane.

parameter as

$$\cosh\psi = \frac{2}{y} - 1 \ . \tag{3.18}$$

Having fixed the hadron frame, it will be useful later to have expressions for the unit vectors along the axis of the hadron frame in terms of the momenta P^μ, P_h^μ and q^μ. The unit coordinate vectors are

$$T^\mu = \frac{1}{Q}\left(q^\mu + 2xP^\mu\right) \ , \tag{3.19}$$

$$X^\mu = \frac{1}{q_T}\left(\frac{P_h^\mu}{z} - q^\mu - \left(1 + \frac{q_T^2}{Q^2}\right) xP^\mu\right) \ , \tag{3.20}$$

$$Y^\mu = \epsilon^{\mu\nu\rho\sigma} Z_\nu T_\rho X_\sigma \ , \tag{3.21}$$

$$Z^\mu = -\frac{q^\mu}{Q} \ . \tag{3.22}$$

It can be checked easily that those vectors are mutually orthogonal and normalized to $T^\mu T_\mu = 1$ and $X^\mu X_\mu = Y^\mu Y_\mu = Z^\mu Z_\mu = -1$. When inserting the parametrizations of the momenta in the hadron frame one finds that the vectors T^μ, X^μ, Y^μ and Z^μ are $(1,0,0,0)$, $(0,1,0,0)$, $(0,0,1,0)$ and $(0,0,0,1)$ respectively. Note that Y^μ is an axial vector.

3.1.2 Lab Frame

In experimental setups, measurements are made in the lab frame, where the incoming lepton and proton travel in opposite directions (see [217–219]). The goal here is to relate the variables defined in the hadron frame to the equivalent ones in the lab frame. In the latter, the momenta are parametrized as follows:

$$P^\mu = (E_p, 0, 0, E_p) \ , \tag{3.23}$$

$$P_h^\mu = (E_h, E_h \sin\theta_h \cos\phi_h, E_h \sin\theta_h \sin\phi_h, E_h \cos\theta_h) \ , \tag{3.24}$$

$$l^\mu = (E, 0, 0, -E) \ , \tag{3.25}$$

$$l'^\mu = (E', -E' \sin\theta, 0, -E' \cos\theta) \ . \tag{3.26}$$

The momenta are illustrated in Figure 3.5. The photon momentum is

$$q^\mu = l^\mu - l'^\mu = (E - E', E' \sin\theta, 0, E' \cos\theta - E) \ . \tag{3.27}$$

The DIS variables Q^2, x of equations (3.2), (3.3) and $s_{lP} = (l+P)^2$ are fully determined by the energies of the incoming beams and the energy and direction of the outgoing lepton. In the lab frame, they are

$$Q^2 = 2EE' (1 - \cos\theta) \ , \tag{3.28}$$

$$x = \frac{EE' (1 - \cos\theta)}{E_p (2E - E' (1 + \cos\theta))} \ , \tag{3.29}$$

$$s_{lP} = 4EE_p \ . \tag{3.30}$$

The inelasticity y of Equation (3.3) is given by

$$y = \frac{Q^2}{x s_{lP}} = \frac{2E - E' (1 + \cos\theta)}{2E} \ . \tag{3.31}$$

The variable z of (3.3) additionally depends on the momentum of the final-state hadron. In the lab frame, it can be written as

$$z = \frac{2x}{Q^2} P \cdot P_h = \frac{2x E_p E_h (1 - \cos\theta_h)}{Q^2} \ . \tag{3.32}$$

For the transverse momentum of the photon q_T and the angle ϕ, the azimuthal angle between the lepton and hadron planes in the hadron frame, it is useful to introduce the

shorthand notation

$$\beta = \frac{2xE_p}{Q} = \frac{\sqrt{2EE'(1-\cos\theta)}}{2E - E'(1+\cos\theta)} \ , \tag{3.33}$$

and to parametrize the momentum $xP^\mu + q^\mu$ as:

$$xP^\mu + q^\mu = E_0 \left(1, \sin\theta_*, 0, \cos\theta_*\right) \ , \tag{3.34}$$

where the energy component is given by

$$E_0 = \frac{Q(1+(1-y)\beta^2)}{2\beta} \ , \tag{3.35}$$

and the polar angle θ_* evaluates to

$$\cot\left(\frac{\theta_*}{2}\right) = \beta\sqrt{1-y} \ . \tag{3.36}$$

If the observed hadron travels exactly along the direction of $x\vec{P}+\vec{q}$, i.e., if $(\theta_h, \phi_h) = (\theta_*, 0)$, then the transverse momentum of the photon vanishes, $q_T = 0$. In general, the transverse momentum can be expressed in the lab frame as

$$q_T^2 = \frac{2E_hE_0}{z}\left(1-\cos\gamma\right) \ , \tag{3.37}$$

where γ is the angle between $\vec{P}_h$ and $x\vec{P}+\vec{q}$. In terms of the angles θ_*, θ_h and ϕ_h, the angle γ can be expressed as

$$\cos\gamma = \cos\theta_*\cos\theta_h + \sin\theta_*\sin\theta_h\cos\phi_h \ . \tag{3.38}$$

This formula for q_T^2 makes it clear that q_T^2 is a measure of how far the observed hadron is away from the naive parton model direction, where the transverse momentum of the photon is zero. Using some trigonometric identities, this matches the result given in [217]. Finally, the angle ϕ can be expressed in terms of lab frame variables as[1]

$$\cos\phi = \frac{Q}{2q_T}\frac{1}{\sqrt{1-y}}\left(1-y+\frac{q_T^2}{Q^2} - \frac{1}{\beta^2}\cot^2\left(\frac{\theta_h}{2}\right)\right) \ . \tag{3.39}$$

These relations also allow for a change of variables from the lab frame variables of the outgoing particles $E', \theta, E_h, \theta_h$ and ϕ_h to the variables x, Q^2, z, q_T and ϕ. The Jacobians

[1] There are misprints in [218, 219].

for these transformations are given by [217]

$$E' \mathrm{d}E' \mathrm{d}\cos\theta = \frac{Q^2}{2x^2 s_{lP}} \mathrm{d}Q^2 \mathrm{d}x \tag{3.40}$$

and

$$E_h \mathrm{d}E_h \mathrm{d}\cos\theta_h \mathrm{d}\phi_h = \frac{z}{2} \mathrm{d}z \mathrm{d}q_T^2 \mathrm{d}\phi \ . \tag{3.41}$$

3.2 Differential Cross-Section of SIDIS

The next step is to turn the attention to the cross section of the semi-inclusive deep inelastic scattering process

$$\ell(l) + \mathcal{P}(P) \to \ell(l') + h(P_h) + X \ , \tag{3.42}$$

where ℓ is the incoming lepton, $\mathcal{P}$ the proton, h the observed final-state hadron, and X the unobserved remnants. The momenta of the respective particles are given in parentheses. The starting point is the expression for the cross section introduced in (2.74),

$$\sigma_{\ell\mathcal{P}\to\ell h X} = \frac{1}{2s_{lP}} \int \mathrm{dPS} |\overline{\mathcal{M}}_{\ell\mathcal{P}\to\ell h X}|^2 \ , \tag{3.43}$$

with $s_{lP} = (l + P)^2$ denoting the squared center-of-mass energy of the lepton-proton system. The scattering discussed in this thesis is unpolarized; therefore, the matrix element squared must be averaged over all initial spin states and summed over all final spin states. This is indicated by the bar over the matrix element $|\overline{\mathcal{M}}_{\ell\mathcal{P}\to\ell h X}|^2$.
As discussed, the SIDIS cross section will be evaluated in the one-photon exchange approximation, which is well justified because the exchange of additional photons is suppressed by additional factors of the QED coupling α. With this approximation, the leptonic part of the process is well understood, and all the complexity is captured by the hadronic part. The hadronic part involves, in addition to the QED vertex, higher-order corrections of strong interactions. To proceed, the squared matrix element $|\overline{\mathcal{M}}_{\ell\mathcal{P}\to\ell h X}|^2$ is factorized at the photon line (see Figure 3.6). This allows for a clean separation between leptonic and hadronic components. Additionally, the integration over the phase space of the unobserved hadronic particles is absorbed into the definition of the hadronic tensor, whereas the integrals over the observed particles are written explicitly. The cross-section becomes

$$\sigma_{\ell\mathcal{P}\to\ell h X} = \frac{(2\pi)^4}{2s_{lP}} \int \frac{\mathrm{d}^3\vec{l'}}{(2\pi)^3 2l'^0} \frac{\mathrm{d}^3\vec{P}_h}{(2\pi)^3 2P_h^0} \frac{e^4}{Q^4} L_{\mu\nu}(l, l') W^{\mu\nu}(P, q, P_h) \ . \tag{3.44}$$

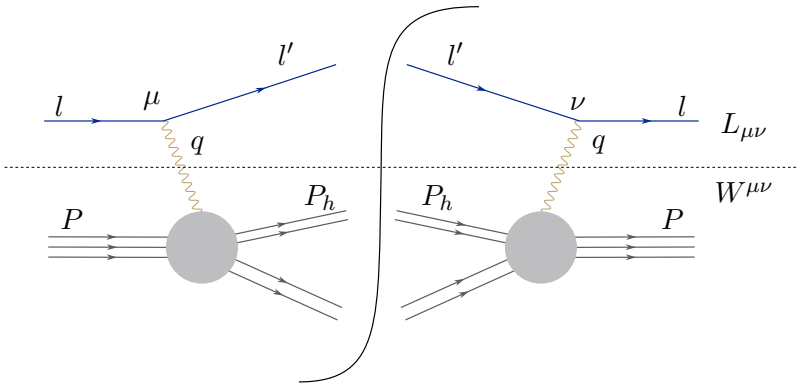

Figure 3.6: Diagram of the squared SIDIS amplitude. The parts to the right of the curved line represent the complex conjugate of the amplitude, where the Lorentz index of the photon vertex is changed to ν. The gray areas represent the scattering of the virtual photon off the proton. The squared amplitude can be split along the dotted line: the upper part contributes to the leptonic tensor $L_{\mu\nu}$, while the lower part contributes to the hadronic tensor $W^{\mu\nu}$.

The $(2\pi)^4$ is conventional and will be absorbed in the hadronic tensor. The lepton charge e and momentum transfer Q are kept explicit and do not become part of the tensors. In differential form, the cross section reads

$$4l'^0 P_h^0 \frac{\mathrm{d}\sigma_{\ell\mathcal{P}\to\ell hX}}{\mathrm{d}^3\vec{l}'\mathrm{d}^3\vec{P}_h} = \frac{2\alpha^2}{s_{lP}Q^4} L_{\mu\nu}(l,l')W^{\mu\nu}(P,q,P_h) \ , \tag{3.45}$$

with the fine-structure constant $\alpha = e^2/(4\pi)$.
Transforming to the SIDIS variables x, Q^2, z, q_T^2 and ϕ, the cross section can be written as

$$\frac{\mathrm{d}\sigma_{\ell\mathcal{P}\to\ell hX}}{\mathrm{d}x\mathrm{d}Q^2\mathrm{d}z\mathrm{d}q_T^2\mathrm{d}\phi} = \frac{\alpha^2}{Q^2x^2s_{lP}^2} L_{\mu\nu}W^{\mu\nu} \ . \tag{3.46}$$

The leptonic tensor $L_{\mu\nu}$ describes the interaction of the lepton with the virtual photon. It is given by:

$$\begin{aligned} L_{\mu\nu}(l,l') &= \frac{1}{2}\sum_{s,s'} \overline{u}(l',s')\gamma_\mu u(l,s)\overline{u}(l,s)\gamma_\nu u(l',s') \\ &= \frac{1}{2}\mathrm{Tr}\left(\gamma_\mu \not{l} \gamma_\nu \not{l}'\right) \\ &= 2(l_\mu l'_\nu + l'_\mu l_\nu - g_{\mu\nu} l\cdot l') \ , \end{aligned} \tag{3.47}$$

where the factor 1/2 from the spin average of the initial lepton, and the sum over the final leptons spin states are taken into account.
The hadronic tensor encodes all strong interactions relevant to the scattering process. It is given by:

$$W^{\mu\nu}(P,q,P_h) = \frac{1}{(2\pi)^4}\sum_X \int \mathrm{d}^4 z \mathrm{e}^{\mathrm{i}q\cdot z}\langle P|J^\mu(z)|P_h,X\rangle\langle P_h,X|J^\nu(0)|P\rangle \ , \tag{3.48}$$

where $J^\mu(x) = e_q\overline{\Psi}(x)\gamma^\mu\Psi(x)$ is the electromagnetic current. An average over the spins of the initial proton and the sum over spin of the final hadron are implied, but not shown. The same is true for the sums over the flavor of the final-state parton and the unobserved final-state particles.
The hadronic tensor captures both perturbative and non-perturbative QCD effects. The perturbative component describes the short-distance hard scattering of the photon with a parton of the proton, while the non-perturbative component includes the structure of the proton via parton distribution functions and the hadronization process via fragmentation functions.
This completes the derivation of the differential SIDIS cross section in terms of the leptonic and hadronic tensors. The next step is to analyze the structure of the hadronic tensor in more detail.

3.3 Decomposition of the Hadronic Tensor

After separating the cross section into leptonic and hadronic parts, the focus is now on the more complicated hadronic tensor. The central aim of this thesis is to obtain angular-dependent expressions for the SIDIS cross-section at high transverse momentum. To achieve this, the hadronic tensor must be decomposed in a way that clearly isolates different angular structures.
Historically, early forms of this decomposition appeared in 1970 [220–222]. The full angular decomposition was developed later that decade [223–226]. This thesis focuses on the decomposition and notation given in 1991 by Ruibin Meng, Fredrick I. Olness and Davidson E. Soper [217].
To decompose the hadronic tensor $W^{\mu\nu}(P,q,P_h)$ two general properties are used. First,

$$W^{\mu\nu}(P,q,P_h) = (W^{\nu\mu}(P,q,P_h))^* \ , \tag{3.49}$$

and second, due to the conservation of the electromagnetic current, the hadronic tensor $W^{\mu\nu}$ satisfies

$$\begin{aligned} q_\mu W^{\mu\nu}(P,q,P_h) &= 0 \\ q_\nu W^{\mu\nu}(P,q,P_h) &= 0 \ . \end{aligned} \tag{3.50}$$

These constraints restrict the possible tensor structure. As a result the hadronic tensor can be expressed as a linear combination of nine independent tensors built from the available four-vectors P^μ, q^μ, P_h^μ, the Levi-Civita tensor $\epsilon^{\mu\nu\rho\sigma}$, and the metric tensor $g^{\mu\nu}$. These nine tensors are called $\mathcal{V}_1^{\mu\nu}, ..., \mathcal{V}_9^{\mu\nu}$ and the decomposition can be written as

$$W^{\mu\nu} = \sum_{k=1}^{9} \mathcal{V}_k^{\mu\nu} S_k \ , \tag{3.51}$$

with the structure functions S_k capturing the information about the hadrons. Note that the structure functions S_k are Lorentz scalar functions of the momenta P^μ, q^μ and P_h^μ. Therefore, they can only be functions of the Lorentz invariant combinations x, z, Q^2 and q_T^2.
To define the nine independent tensors $\mathcal{V}_k^{\mu\nu}$, the coordinate basis vectors of the hadron frame (3.19) are employed. The tensors are chosen as follows:

$$\begin{aligned} \mathcal{V}_1^{\mu\nu} &= X^\mu X^\nu + Y^\mu Y^\nu & \mathcal{V}_2^{\mu\nu} &= g^{\mu\nu} + Z^\mu Z^\nu & \mathcal{V}_3^{\mu\nu} &= T^\mu X^\nu + X^\mu T^\nu \\ \mathcal{V}_4^{\mu\nu} &= X^\mu X^\nu - Y^\mu Y^\nu & \mathcal{V}_5^{\mu\nu} &= \mathrm{i}\,(T^\mu X^\nu - X^\mu T^\nu) & \mathcal{V}_6^{\mu\nu} &= \mathrm{i}\,(X^\mu Y^\nu - Y^\mu X^\nu) \\ \mathcal{V}_7^{\mu\nu} &= \mathrm{i}\,(T^\mu Y^\nu - Y^\mu T^\nu) & \mathcal{V}_8^{\mu\nu} &= T^\mu Y^\nu + Y^\mu T^\nu & \mathcal{V}_9^{\mu\nu} &= X^\mu Y^\nu + Y^\mu X^\nu \ . \end{aligned} \tag{3.52}$$

The inverses of these tensors will be necessary to find the structure functions S_k by projecting the hadronic tensor onto them. They are given by:

$$\begin{aligned} \tilde{\mathcal{V}}_1^{\mu\nu} &= \frac{1}{2}(2T^\mu T^\nu + X^\mu X^\nu + Y^\mu Y^\nu) & \tilde{\mathcal{V}}_2^{\mu\nu} &= T^\mu T^\nu & \tilde{\mathcal{V}}_3^{\mu\nu} &= -\frac{1}{2}\,(T^\mu X^\nu + X^\mu T^\nu) \\ \tilde{\mathcal{V}}_4^{\mu\nu} &= \frac{1}{2}\,(X^\mu X^\nu - Y^\mu Y^\nu) & \tilde{\mathcal{V}}_5^{\mu\nu} &= \frac{\mathrm{i}}{2}\,(T^\mu X^\nu - X^\mu T^\nu) & \tilde{\mathcal{V}}_6^{\mu\nu} &= -\frac{\mathrm{i}}{2}\,(X^\mu Y^\nu - Y^\mu X^\nu) \\ \tilde{\mathcal{V}}_7^{\mu\nu} &= \frac{\mathrm{i}}{2}\,(T^\mu Y^\nu - Y^\mu T^\nu) & \tilde{\mathcal{V}}_8^{\mu\nu} &= -\frac{1}{2}\,(T^\mu Y^\nu + Y^\mu T^\nu) & \tilde{\mathcal{V}}_9^{\mu\nu} &= \frac{1}{2}\,(X^\mu Y^\nu + Y^\mu X^\nu) \ . \end{aligned} \tag{3.53}$$

With these inverses, the structure functions S_k can be calculated as

$$S_k = W_{\mu\nu}\tilde{\mathcal{V}}_k^{\mu\nu} \ . \tag{3.54}$$

Note that the tensors $\mathcal{V}_1^{\mu\nu}, ..., \mathcal{V}_4^{\mu\nu}, \mathcal{V}_8^{\mu\nu}, \mathcal{V}_9^{\mu\nu}$ are symmetric under the exchange of μ and ν, while the rest are antisymmetric. The first five tensors $\mathcal{V}_1^{\mu\nu}, ..., \mathcal{V}_5^{\mu\nu}$ are even under parity transformation, whereas the rest are parity-odd due to the axial vector Y^μ.
For a process with unpolarized leptons, unpolarized initial protons, and unpolarized final state hadrons, as in this thesis, both leptonic and hadronic tensors are symmetric tensors. Therefore, only the structure functions $S_1, ..., S_4$ contribute.
To provide the full picture about the angular structure of the cross section, the totally antisymmetric term $2\mathrm{i}\epsilon_{\mu\nu\rho\sigma}l^\rho l'^\sigma$, which might arise from the polarization of the lepton, is added to the leptonic tensor that is considered for the rest of this chapter:

$$L_{\mu\nu}(l, l') = 2(l_\mu l'_\nu + l'_\mu l_\nu - g_{\mu\nu} l \cdot l' + \mathrm{i}\epsilon_{\mu\nu\rho\sigma} l^\rho l'^\sigma) \ . \tag{3.55}$$

To express the cross section in terms of the structure functions S_k, the decomposition tensors $\mathcal{V}_k^{\mu\nu}$ are applied to the leptonic tensor. In doing so, the angular dependence of the cross section will become explicit by introducing

$$\mathcal{A}_k = \frac{1}{Q^2} L_{\mu\nu}\mathcal{V}_k^{\mu\nu} \ . \tag{3.56}$$

This contraction can easily be evaluated in the hadron frame, giving:

$$\begin{aligned}
&\mathcal{A}_1 = 1 + \cosh^2\psi && \mathcal{A}_2 = -2 && \mathcal{A}_3 = -\cos\phi \sinh 2\psi \\
&\mathcal{A}_4 = \cos 2\phi \sinh^2\psi && \mathcal{A}_5 = 2\sin\phi\sinh\psi && \mathcal{A}_6 = 2\cosh\psi \\
&\mathcal{A}_7 = -2\cos\phi\sinh\psi && \mathcal{A}_8 = -\sin\phi\sinh 2\psi && \mathcal{A}_9 = \sin 2\phi \sinh^2\psi \ ,
\end{aligned} \tag{3.57}$$

where, as mentioned above, the functions $\mathcal{A}_1, ..., \mathcal{A}_4, \mathcal{A}_8, \mathcal{A}_9$ are non-zero due to the symmetric part of the leptonic tensor, while the rest are only non-zero for a leptonic tensor with an antisymmetric component.
With (3.51) and (3.56) the combination $L_{\mu\nu}W^{\mu\nu}$ can be written as

$$\begin{aligned}
L_{\mu\nu}W^{\mu\nu} &= \sum_{k=1}^{9} L_{\mu\nu}\mathcal{V}_k^{\mu\nu} S_k \\
&= Q^2 \sum_{k=1}^{9} \mathcal{A}_k(\psi, \phi) S_k(x, z, Q^2, q_T^2) \ .
\end{aligned} \tag{3.58}$$

The benefits of this decomposition are evident. All dependence on the angles ψ and ϕ is captured by the functions $\mathcal{A}_k$, while the dependence on the Lorentz scalars x, z, Q^2 and q_T^2 is fully captured by the structure functions S_k. Therefore, if the structure functions are known, the entire cross section is also known. But even more, every single structure function provides insights into the angular distributions of the cross section, without having to deal with open indices in the calculation.
For the process relevant to this thesis, only the structure functions $S_1, ..., S_4$ contribute to the cross section. However, calculating these structure functions is quite involved. This is the task for the remainder of this thesis.
Since only the structure functions $S_1, ..., S_4$ contribute, the cross section can be decomposed into three parts with different angular ϕ dependence, according to the respective angular functions $\mathcal{A}_1, ..., \mathcal{A}_4$:

$$\frac{\mathrm{d}\sigma_{\ell\mathcal{P}\to\ell hX}}{\mathrm{d}x\mathrm{d}Q^2\mathrm{d}z\mathrm{d}q_T^2\mathrm{d}\phi} = \sigma_0 + \sigma_1 \cos\phi + \sigma_2 \cos 2\phi \ , \tag{3.59}$$

where σ_0 receives contributions from S_1 and S_2, σ_1 stems from S_3 and the $\cos 2\phi$ part comes from the structure function S_4.

3.4 Factorization Formula for the Differential Cross-Section

The general principles of factorization were introduced in Section 2.6. In this section, these principles will be applied to semi-inclusive deep inelastic scattering, aiming to derive an explicit formula for the calculation of the cross section, and, in the end, for the structure functions. The factorization procedure is explained in detail in [153], while this section closely follows the approach presented in [31]. The factorization formula in Equation (2.127) expresses the hadronic cross section as a convolution of three components: the collinear parton distribution function $f_{i/\mathcal{P}}(\xi)$, the hard partonic cross section $\hat{\sigma}_{\ell i\to\ell jX}$, and the collinear fragmentation functions $d_{h/j}(\zeta)$. It reads:

$$\begin{aligned}\sigma_{\ell\mathcal{P}\to\ell hX}(P,q,P_h) &= f_{i/\mathcal{P}} \otimes \hat{\sigma}_{\ell i\to\ell jX} \otimes d_{h/j} \\ &= \int_{\xi_{\min}}^1 \mathrm{d}\xi \int_{\zeta_{\min}}^1 \mathrm{d}\zeta \ f_{i/\mathcal{P}}(\xi)\ \hat{\sigma}_{\ell i\to\ell jX}(p=\xi P, q, k_1 = P_h/\zeta)\ d_{h/j}(\zeta) \ ,\end{aligned} \tag{3.60}$$

where a sum over all possible parton species i and j is implicitly understood. The momentum p of parton i is given by a fraction of the momentum of its parent particle, the proton. In formulas, it is given by $p = \xi P$, with P being the momentum of the proton.

Likewise for the momentum k_1 of the parton j that subsequently fragments to give rise to the observed hadron. Its momentum is given by $k_1 = P_h/\zeta$, where P_h is the momentum of the observed hadron. The indices i and j for the incoming and outgoing partonic momenta p_i and k_{1j} are omitted for clarity but are implicitly understood.
The limits of integration are dictated by the overall momentum conservation and the fact that the virtuality of the spectator parton system $s_{23} = (q + p - k_1)^2$ can reach zero, to give

$$\xi_{\min} = x\left(1 + \frac{z}{1-z}\frac{q_T^2}{Q^2}\right) , \qquad \zeta_{\min} = z\left(1 + \frac{x}{1-x}\frac{q_T^2}{Q^2}\right) , \tag{3.61}$$

where the hadronic variables x and z are defined in Equation (3.3).
In differential form, the factorization formula reads:

$$4l'^0 P_h^0 \frac{\mathrm{d}\sigma_{\ell\mathcal{P}\to\ell hX}}{\mathrm{d}^3\vec{l}'\mathrm{d}^3\vec{P}_h} = \int_{\xi_{\min}}^1 \frac{\mathrm{d}\xi}{\xi}\int_{\zeta_{\min}}^1 \frac{\mathrm{d}\zeta}{\zeta^2} f_{i/\mathcal{P}}(\xi) 4l'^0 k_1^0 \frac{\mathrm{d}\hat{\sigma}_{\ell i\to\ell jX}}{\mathrm{d}^3\vec{l}'\mathrm{d}^3\vec{k}_1} d_{h/j}(\zeta) , \tag{3.62}$$

where the differential partonic cross section is defined in analogy to its hadronic counterpart,

$$4l'^0 k_1^0 \frac{\mathrm{d}\hat{\sigma}_{\ell i\to\ell jX}}{\mathrm{d}^3\vec{l}'\mathrm{d}^3\vec{k}_1} = \frac{2\alpha^2}{\hat{s}Q^4} L_{\mu\nu}\hat{W}_{ij}^{\mu\nu} . \tag{3.63}$$

Note that the definition of the partonic cross section differs from that of the hadronic cross section in Equation (3.45) in three ways:

Firstly, by the introduction of the partonic analog of the hadronic Mandelstam variable s_{lP}, namely, $\hat{s} = (l + p)^2$. The hadronic variable can be recovered through $\hat{s} = \xi s_{lP}$.

Secondly, by the change of variables for the outgoing particle. The hadronic momentum P_h is now replaced by its partonic counterpart k_1, with $k_1 = P_h/\zeta$. One power of ζ in the factorization formula (3.62) comes from the conversion of the explicit momentum, and a factor of $1/\zeta^3$ comes from the change of variables in the differential cross section, resulting in the factor $1/\zeta^2$ in (3.62).

Lastly, by the introduction of the partonic tensor $\hat{W}^{\mu\nu}$, which is also defined in complete analogy to its hadronic counterpart from Equation (3.48),

$$\hat{W}_{ij}^{\mu\nu}(p, q, k_1) = \frac{1}{(2\pi)^4}\sum_X \int \mathrm{d}^4 z \mathrm{e}^{\mathrm{i}q\cdot z}\langle p|J^\mu(z)|k_1, X\rangle\langle k_1, X|J^\nu(0)|p\rangle . \tag{3.64}$$

As stated in Section 2.6, the hard partonic cross section in Equation (3.62) is finite and can be calculated as a perturbative expansion in the strong coupling constant. For large transverse momenta, the perturbative expansion begins at order α_s. All soft interactions that can not be handled by perturbation theory are contained in the parton distribution functions f and fragmentation functions d.
The connection of the hard partonic tensor $\hat{W}_{ij}^{\mu\nu}$ to the hadronic tensor $W^{\mu\nu}$ can be directly inferred from Equation (3.62) by inserting (3.48) and (3.64) to get the factorization formula for the hadronic tensor as

$$W^{\mu\nu}(P,q,P_h) = \int_{\xi_{\min}}^{1} \frac{\mathrm{d}\xi}{\xi} \int_{\zeta_{\min}}^{1} \frac{\mathrm{d}\zeta}{\zeta^2} f_{i/\mathcal{P}}(\xi) \hat{W}_{ij}^{\mu\nu}(\xi P, q, P_h/\zeta) d_{h/j}(\zeta) \ . \tag{3.65}$$

The hard partonic tensor can be obtained from the full (unsubtracted) partonic tensor $\tilde{W}^{\mu\nu}$ by subtractions similar to those in (2.138) and (2.139). The full partonic tensor can be calculated as the phase space integral over the squared matrix element,

$$\tilde{W}^{\mu\nu} = \frac{1}{4\pi} \frac{1}{\mathrm{e}^2} \int \mathrm{dPS} \overline{\mathcal{M}^{\mu} \mathcal{M}^{\nu *}} \ , \tag{3.66}$$

where the matrix elements $\mathcal{M}$ describe the partonic process

$$\gamma^*(q) + i(p) \to j(k_1) + X \ , \tag{3.67}$$

with open Lorentz indices associated with the virtual photon.
Depending on the purpose, the open indices of the virtual photon can be contracted, for example, with the metric tensor or some combination of momenta. For our purpose, to access the angular structure, the open photon indices are contracted with the tensors $\tilde{\mathcal{V}}_k^{\mu\nu}$. This provides direct access to the structure functions at parton level. The decomposition of the hadronic tensor into components with different angular structures can be equally applied to $\hat{W}_{ij}^{\mu\nu}$. The challenge lies in calculating the partonic tensor, since here higher-order corrections come into play. To aid in this calculation, it is useful to define variables that are tailored to the task. This is discussed in the next section.

3.5 Partonic Kinematic Variables

While the hadronic kinematic variables were already defined in Section 3.1, this section collects the relevant definitions for clarity before adapting them to the partonic process. Subsequently, variables specialized for calculating the structure functions are introduced. First, the Mandelstam variables of the subprocess corresponding to the hadronic tensor

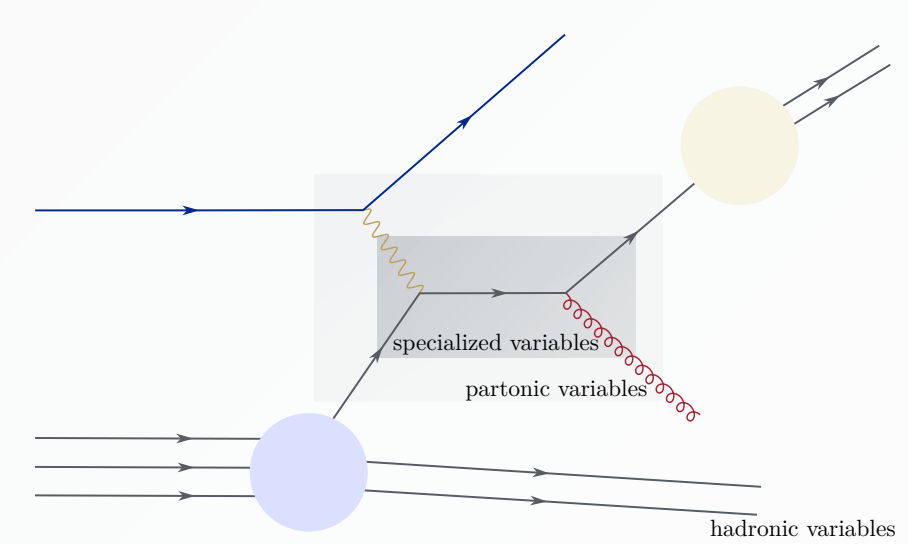

Figure 3.7: Leading order Feynman diagram for SIDIS at high transverse momentum. The blue area denotes the PDF, while the yellow area denotes the FF. The gray boxes indicate the domain the variables are useful in. The hadronic variables describe the overall interaction of the proton with the lepton, with an outgoing hadron. The partonic variables describe the process after a parton is split off the proton and before the outgoing parton hadronizes. The specialized variables, like the Mandelstam variables or the dimensionless variables, exclude the trivial leptonic interaction.

and then the dimensionless variables v and w, which streamline the analytic expressions, are introduced. A schematic overview of this increasingly zoomed-in kinematical process is illustrated for an example Feynman diagram at leading order for a high p_T process in Figure 3.7.
The SIDIS process at hadron level is given by

$$\ell(l) + \mathcal{P}(P) \to \ell(l') + h(P_h) + X \ , \tag{3.68}$$

where ℓ is the leptons, $\mathcal{P}$ the Proton, h the observed hadron and X stands for all unobserved particles. The four momenta of the respective particles are given in parentheses. The momentum transfer from the leptonic to the hadronic system is defined as

$$q := l - l' \ , \tag{3.69}$$

which is a space-like vector in SIDIS. Therefore the virtuality is defined as

$$Q^2 := -q^2 \ . \tag{3.70}$$

Virtuality is defined only via the leptonic system. Therefore, it is the same for hadronic and partonic variables.
Another important vector is the transverse momentum of the photon

$$q_t^\mu = q^\mu - \frac{q \cdot P_h}{P \cdot P_h} P^\mu - \frac{q \cdot P}{P \cdot P_h} P_h^\mu \ . \tag{3.71}$$

This vector is also space-like. So, as for the virtuality, the magnitude of the transverse momentum of the photon is denoted by

$$q_T := \sqrt{-q_t^\mu q_{t\mu}} \ , \tag{3.72}$$

which makes q_T positive.
The center-of-mass energy of the collision is

$$s_{lP} := (l + P)^2 = 2 \ l \cdot P \ . \tag{3.73}$$

Since it is common to split the hadronic and leptonic parts the standard variables used in SIDIS reflect this fact by incorporating the momentum transfer q prominently in the definition of the variables

$$x = \frac{Q^2}{2 \ P \cdot q} \ , \qquad y = \frac{P \cdot q}{P \cdot l} \ , \qquad z = \frac{P \cdot P_h}{P \cdot q} \ . \tag{3.74}$$

The variables x and y do not depend on the final state hadron and y is not an independent variable, as

$$y = \frac{Q^2}{x s_{lP}} \ . \tag{3.75}$$

The square of the transverse momentum of the photon can be defined via the scalar products

$$q_T^2 = Q^2 + \frac{2(q \cdot P_h)(P \cdot q)}{P \cdot P_h} \ , \tag{3.76}$$

which is only true in the massless approximation $P^2 = P_h^2 = 0$. The transverse momentum of the hadron squared can be expressed as

$$P_{hT}^2 = \frac{(P \cdot P_h) \left(Q^2 (P \cdot P_h) + 2(q \cdot P_h)(P \cdot q) \right)}{(P \cdot q)^2} = z^2 q_T^2 \ . \tag{3.77}$$

3.5.1 Partonic SIDIS Variables

Using collinear factorization, the same process can also be described at parton level. The process is then

$$\ell(l) + i(p) \to \ell(l') + j(k_1) + X \ , \tag{3.78}$$

where ℓ is the lepton, i is a parton of the incident proton, j is a parton of the outgoing hadron and X are the unobserved partons. The momenta are again given in the respective brackets, where the momenta of partons i and j are connected to the hadronic momenta P and P_h via the momentum fractions ξ and ζ,

$$p = \xi P \quad \text{and} \quad k_1 = \frac{P_h}{\zeta} \ . \tag{3.79}$$

The partonic center-of-mass energy is

$$\hat{s} = (p + l)^2 = 2\ p \cdot l = \xi s_{lP} \ . \tag{3.80}$$

The partonic SIDIS variables are defined in complete analogy to their hadronic counterparts as

$$\hat{x} = \frac{Q^2}{2\ p \cdot q} \ , \qquad \hat{y} = \frac{p \cdot q}{p \cdot l} \ , \qquad \hat{z} = \frac{p \cdot k_1}{p \cdot q} \ , \tag{3.81}$$

with the connection to the hadronic variables given by

$$\hat{x} = \frac{x}{\xi} \ , \qquad \hat{y} = y \ , \qquad \hat{z} = \frac{z}{\zeta} \ . \tag{3.82}$$

The partonic inelasticity can be written as

$$\hat{y} = \frac{Q^2}{\hat{x}\hat{s}} \ . \tag{3.83}$$

The square of the transverse momentum of the photon remains unchanged in the partonic variables,

$$q_T^2 = Q^2 + \frac{2(q \cdot k_1)(p \cdot q)}{p \cdot k_1} \ , \tag{3.84}$$

while the transverse momentum of the outgoing parton is

$$k_{1T}^2 = P_{hT}^2/\zeta^2 = \hat{z}^2 q_T^2 \ . \tag{3.85}$$

3.5.2 Mandelstam Variables

The SIDIS cross section is typically separated into a leptonic tensor and a hadronic tensor, as done in this thesis. The main challenge in calculating the cross section lies in evaluating the hadronic tensor. Therefore, it is common to introduce kinematic variables that are specialized for the subprocess that describes the hadronic tensor at parton level,

$$\gamma^*(q) + i(p) \to j(k_1) + X \ , \tag{3.86}$$

where γ^* is the highly virtual photon coming from the leptonic system, and i, j and X are the partons from above. Again, the momenta are given in the respective brackets. The Mandelstam variables are defined as follows:

$$\begin{aligned} s &= (p+q)^2 = 2\ p\cdot q - Q^2 \ , & t &= (q-k_1)^2 = 2\ q\cdot k_1 - Q^2 \ , \\ u &= (p-k_1)^2 = 2\ p\cdot k_1 \ , & s_{23} &= s+t+u+Q^2 \ . \end{aligned} \tag{3.87}$$

They can also be expressed in terms of the partonic variables $\hat{x}, \hat{z}$ and q_T^2,

$$\begin{aligned} s &= Q^2\left(\frac{1-\hat{x}}{\hat{x}}\right) & t &= -Q^2 + \hat{z}\left(Q^2 - q_T^2\right) \\ u &= -\frac{\hat{z}}{\hat{x}}Q^2 & s_{23} &= Q^2\hat{z}\left(\frac{(1-\hat{x})\,(1-\hat{z})}{\hat{x}\hat{z}} - \frac{q_T^2}{Q^2}\right) \ , \end{aligned} \tag{3.88}$$

with the inverse relations given by

$$\hat{x} = \frac{Q^2}{s+Q^2} \ , \qquad \hat{z} = \frac{-u}{s+Q^2} \ , \qquad q_T^2 = \frac{st + s_{23}Q^2}{u} \ . \tag{3.89}$$

This implies the Jacobian for the change of variables from t and u to $\hat{z}$ and q_T^2 is given by

$$\mathrm{d}t\,\mathrm{d}u = \frac{\hat{z}}{\hat{x}}Q^2\mathrm{d}\hat{z}\,\mathrm{d}q_T^2 \ . \tag{3.90}$$

At leading order, that is $\mathcal{O}(\alpha_s)$, the final state includes one unobserved parton in X, while at next-to-leading order in the real correction, there are two partons attributed to X. The momenta of these partons are denoted by k_2 at leading order or for virtual corrections, and k_2 and k_3 for the real corrections at next-to-leading order (see Figure 3.8). In intermediary steps of the calculation, it is useful to extend the Mandelstam variables

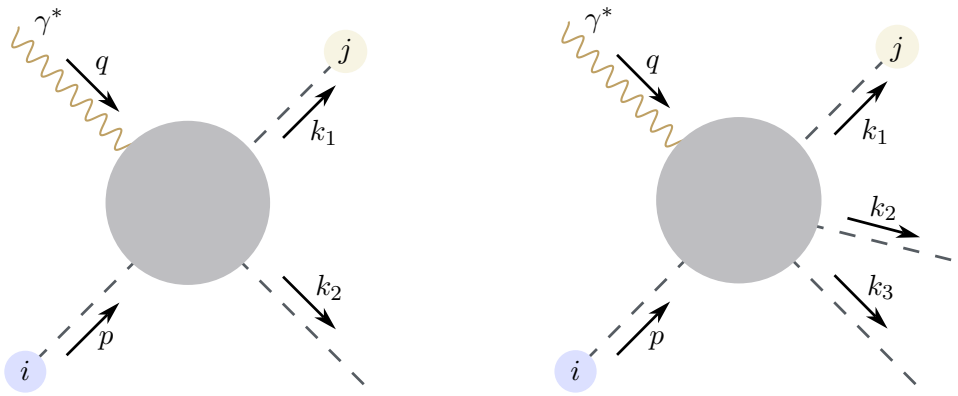

(a) $2 \to 2$ process. (b) $2 \to 3$ process.

Figure 3.8: Momentum labels for the partonic scattering. The dashed lines represent partons. The blue shaded area indicates that this parton comes from the proton, and the yellow area indicates that this parton fragments to become the observed hadron.

to include momenta k_2 and k_3. This is done by the definitions

$$\begin{aligned} t_2 &= (q-k_2)^2 = 2\,q\cdot k_2 - Q^2\,, & t_3 &= (q-k_3)^2 = 2\,q\cdot k_3 - Q^2\,, \\ u_2 &= (p-k_2)^2 = 2\,p\cdot k_2\,, & u_3 &= (p-k_3)^2 = 2\,p\cdot k_3\,, \\ s_{ij} &= (k_i+k_j)^2 = 2\,k_i\cdot k_j\,, \end{aligned} \tag{3.91}$$

for $i,j \in \{1,2,3\}$, and s_{23} coincides with the definition above.

3.5.3 The Dimensionless Variables v and w

For some aspects of the calculation, it is beneficial to change to dimensionless combinations of scalar products. Here, some expressions are also more concise for a shifted center-of-mass energy. These new variables are defined as

$$s' = 2\,p\cdot q\,, \qquad v = 1 + \frac{2\,q\cdot k_1 - Q^2}{2\,p\cdot q}\,, \qquad w = \frac{-2\,p\cdot k_1}{2\,p\cdot q + 2\,q\cdot k_1 - Q^2}\,. \tag{3.92}$$

Their relation to the Mandelstam variables is

$$s' = s + Q^2\,, \qquad v = 1 + \frac{t}{s+Q^2}\,, \qquad w = \frac{-u}{s+t+Q^2}\,. \tag{3.93}$$

The inverse relations are

$$s = s' - Q^2\,, \qquad t = -s'(1-v)\,, \qquad u = -s'vw\,, \qquad s_{23} = s'v(1-w)\,. \tag{3.94}$$

The relations to the partonic SIDIS variables are

$$s' = \frac{Q^2}{\hat{x}} \ , \qquad v = (1-\hat{x}) + \hat{x}\hat{z}\left(1 - \frac{q_T^2}{Q^2}\right) \ , \qquad w = \frac{\hat{z}}{(1-\hat{x}) + \hat{x}\hat{z}(1-\frac{q_T^2}{Q^2})} \ , \tag{3.95}$$

with the inverse relations

$$\hat{x} = \frac{Q^2}{s'} \ , \qquad \hat{z} = vw \ , \qquad q_T^2 = \frac{s'\,(1-v) + Q^2\,(1-vw)}{vw} \ . \tag{3.96}$$

Having established all necessary kinematic variables it is now time to proceed with the description of the more technical parts of the calculation of the hadronic tensor. This is the focus of the next section.

Chapter 4

Technicalities of the Calculation of Partonic Cross Sections

This chapter introduces the more technical aspects of the next-to-leading order calculation of the hadronic tensor. It involves the evaluation of Feynman diagrams, the difficulties introduced by loops in these diagrams, the evaluation of the angular integral, and the subtraction of collinear divergences. Parts of this chapter are based on the summary of the methods I laid out in my master's thesis [75]. The first part of this chapter addresses the computation of color factors, an integral part of Quantum Chromodynamics. The introduction of color as a quantum number was the key insight that led to the formulation of the theory of QCD. The concept of color was introduced to explain why only quark-antiquark pairs or combinations of three quarks are observed in nature and to allow for a symmetric ground state of baryons that obey the Fermi-Dirac statistics [227]. Greenberg [50] first proposed this quantum number, the color, which was implemented into a Yang-Mills theory by Fritzsch, Gell-Mann, and Leutwyler through the introduction of the SU(3) color gauge group [228].

4.1 Color Factors

A brief introduction to the Lie group SU(3) and some basic facts are provided in Section 2.1.1. The most essential properties and conventions used for the practical calculation of color factors are restated here for reference.
Although calculations are ultimately carried out for SU(3), it is instructive to formulate them in terms of a general SU(N) gauge group with an arbitrary number of colors. But for the specific case of SU(3) the generators of the fundamental representation are chosen

as

$$T_a = \frac{\lambda_a}{2} \ , \tag{4.1}$$

where λ_a are the Gell-Mann matrices of Equation (2.6). The following fact are necessary for the calculation and true for arbitrary N:
The generators are chosen to be orthogonal and normalized to

$$\mathrm{Tr}(T_a T_b) = \frac{1}{2}\delta_{ab} \ , \tag{4.2}$$

they are traceless

$$\mathrm{Tr}(T_a) = 0 \tag{4.3}$$

and the totally antisymmetric structure constants are given by

$$[T_a, T_b] = \mathrm{i} f_{abc} T_c \ , \tag{4.4}$$

which can also be expressed as

$$f_{abc} = -2\mathrm{i}\mathrm{Tr}([T_a, T_b]T_c) \ . \tag{4.5}$$

Because in a matrix representation multiplication is defined in addition to the Lie bracket, another set of structure functions can be introduced via the anticommutator as follows:

$$\{T_a, T_b\} = \frac{1}{N}\delta_{ab} + d_{abc} T_c \ , \tag{4.6}$$

where the structure functions d_{abc} are totally symmetric:

$$d_{abc} = 2\mathrm{Tr}(T_a\{T_b, T_c\}) \ . \tag{4.7}$$

With these totally symmetric structure functions, the product of two generators can be written as

$$T_a T_b = \frac{1}{2}\left(\frac{1}{N}\delta_{ab} + (d_{abc} + \mathrm{i} f_{abc})\, T_c\right) \ . \tag{4.8}$$

From these equations, the following relations can be derived [65, 118]:

$$
\begin{aligned}
\mathrm{Tr}(T_a T_b T_c) &= \frac{1}{4}\left(d_{abc} + \mathrm{i} f_{abc}\right) \ , \\
\mathrm{Tr}(T_a T_b T_a T_c) &= -\frac{1}{4N}\delta_{bc} \ , \\
\mathrm{Tr}(T_a T_b T_c T_d) &= \frac{1}{4N}\delta_{ab}\delta_{cd} + \frac{1}{8}\left(d_{abe} + \mathrm{i} f_{abe}\right)\left(d_{cde} + \mathrm{i} f_{cde}\right) \ , \\
f_{abb} &= 0 \ , \\
d_{abb} &= 0 \ , \\
f_{acd} f_{bcd} &= N\delta_{ab} \ , \\
f_{acd} d_{bcd} &= 0 \ , \\
f_{ade} f_{bef} f_{cfd} &= \frac{N}{2} f_{abc} \ .
\end{aligned}
\tag{4.9}
$$

These relations are sufficient for all color factor calculations required in this thesis. Additional relations can be found in [229].

When analyzing Feynman diagrams, color factors can be computed independently of the Lorentz structure, provided that no four-gluon vertices are involved. This condition holds for all next-to-leading order corrections considered in this work.

In squared matrix elements, each fermion line contributes a trace over color generators from the associated vertices as external color states are summed over. An additional averaging factor must be applied for initial-state color configurations. For quarks and gluons, which possess N and $N^2 - 1$ possible color states respectively, the appropriate normalization factors are

$$
\frac{1}{N} \text{ for quarks} \qquad \text{and} \qquad \frac{1}{N^2 - 1} \text{ for gluons.} \tag{4.10}
$$

The general procedure for computing the color factor of a Feynman diagram is as follows.

- Select a starting point on each fermion line.
- Traverse the fermion line in the direction opposite to the fermion flow and record the corresponding generator at each vertex in a trace.
- Once this process is completed for all fermion lines, the structure constants associated with the three-gluon vertices must be incorporated.[1]

[1] It is important to ensure that the order of indices in the structure constants matches the order of the Lorentz indices in the remaining contribution of the three-gluon vertex. To maintain consistency, it is generally advisable to traverse the vertex in a counterclockwise direction.

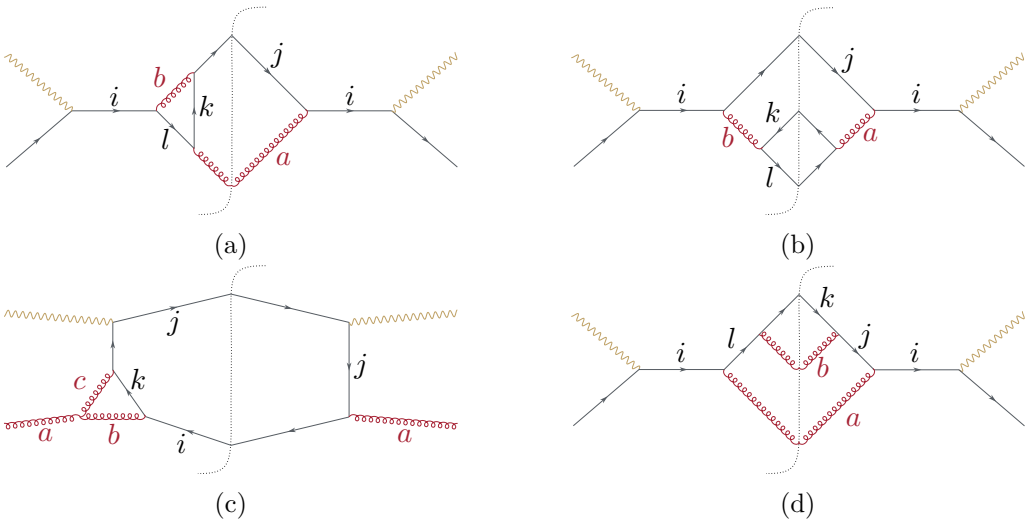

Figure 4.1: Example Feynman diagrams for the calculation of color factors.

- Apply the appropriate averaging factor for the color degree of freedom in the initial states.

By applying the previously established relations, the color factors can be systematically determined. These rules already take the summation over outgoing color states and averaging over initial color states into account.
Here are examples for the calculation of the color factor for four representative Feynman diagrams for the process in this work, where in the last steps the Casimir operators

$$C_A = N \ , \tag{4.11}$$

$$C_F = \frac{N^2 - 1}{2N} \tag{4.12}$$

are introduced. Diagram (a) of Figure 4.1 evaluates to

$$\begin{aligned} (T_a)_{ij}(T_b)_{jk}(T_a)_{kl}(T_b)_{li} &= \mathrm{Tr}(T_a T_b T_a T_b) \\ &= -\frac{1}{4N}\delta_{bb} = -\frac{N^2-1}{4N} = -\frac{C_F}{2} \ , \end{aligned} \tag{4.13}$$

with an averaging factor of $1/N = 1/C_A$ for the incoming quark, the overall color factor for this diagram is:

$$-\frac{N^2-1}{4N^2} = -\frac{1}{2}\frac{C_F}{C_A} \ . \tag{4.14}$$

The next diagram, Figure 4.1b, gives:

$$\begin{aligned}(T_a)_{ij}(T_b)_{ji}(T_a)_{kl}(T_b)_{lk} &= \mathrm{Tr}(T_aT_b)\mathrm{Tr}(T_aT_b) \\ &= \frac{1}{2}\delta_{ab}\frac{1}{2}\delta_{ab} \\ &= \frac{1}{4}\delta_{aa} = \frac{N^2-1}{4} = \frac{C_AC_F}{2}\ ,\end{aligned} \tag{4.15}$$

again, averaging over the quark color states yields $1/N = 1/C_A$. The final color factor for this diagram is

$$-\frac{N^2-1}{4N} = -\frac{C_F}{2}\ . \tag{4.16}$$

The third diagram, Figure 4.1c, results in

$$\begin{aligned}(T_a)_{ij}(T_c)_{jk}(T_b)_{ki}f_{abc} &= \mathrm{Tr}(T_aT_cT_b)f_{abc} \\ &= \frac{1}{4}\left(d_{acb} + \mathrm{i}f_{acb}\right)f_{abc} \\ &= \frac{1}{4}\left(d_{abc}f_{abc} - \mathrm{i}f_{abc}f_{abc}\right) \\ &= -\frac{\mathrm{i}}{4}N\delta_{aa} = -\frac{\mathrm{i}}{4}N\left(N^2-1\right) = -\frac{\mathrm{i}}{2}C_A^2C_F\ ,\end{aligned} \tag{4.17}$$

with an averaging factor of $1/(N^2-1) = 1/(2C_AC_F)$ for the incoming gluon, the resulting color factor is

$$-\frac{\mathrm{i}}{4}N = -\frac{\mathrm{i}}{4}C_A\ . \tag{4.18}$$

The diagram of the last example, Figure 4.1d, evaluates to

$$\begin{aligned}(T_a)_{ij}(T_a)_{jk}(T_b)_{kl}(T_b)_{li} &= \mathrm{Tr}(T_aT_aT_bT_b) \\ &= \frac{1}{4N}\delta_{aa}\delta_{bb} = \frac{1}{4N}\left(N^2-1\right)^2 = C_AC_F^2\ ,\end{aligned} \tag{4.19}$$

together with the averaging factor of $1/(N^2-1) = 2C_A/C_F$ this results in:

$$\frac{1}{4N}\left(N^2-1\right) = \frac{C_F}{2}\ . \tag{4.20}$$

In practical computations, the symbolic evaluation of the traces and structure constants are performed using the `FeynCalc` package [230–233]. The averaging factor must be implemented manually. From the above examples, it is clear that all closed fermion lines

yield traces over color generators. A similar treatment can be applied to the Dirac part of the Feynman diagrams. This is the topic of the next section.

4.2 Casimir's Trick

In order to compute cross sections, it is necessary to calculate squares of amplitudes. These squared amplitudes always result in closed loops of fermion lines, and it is often beneficial to use the completeness relation of the spinors to write the resulting matrix expression as a trace. This is known as Casimir's trick.
The completeness relation for Dirac spinors is given by

$$\sum_s u^s(p)\bar{u}^s(p) = \sum_s v^s(p)\bar{v}^s(p) = \not{p} \ , \tag{4.21}$$

for massless particles, with the sum over all possible spin states s, and $\not{p} = \gamma_\mu p^\mu$. A general expression for a fermion line in a squared matrix element with an incoming particle with with momentum p and an outgoing particle with momentum k can be written as

$$\sum_{s_1,s_2} (\bar{v}^{s_2}(k)\Gamma' u^{s_1}(p))(\bar{v}^{s_2}(k)\Gamma u^{s_1}(p))^* \ , \tag{4.22}$$

where Γ' and Γ are arbitrary 4×4 matrices, for example, combinations of gamma matrices, describing the interaction of the particles. Using the shorthand notation $\overline{\Gamma} := \gamma^0\Gamma^\dagger\gamma^0$ for the Dirac adjoint of the matrix Γ, this expression becomes

$$\begin{aligned}
\sum_{s_1,s_2} (\bar{v}^{s_2}(k)\Gamma' u^{s_1}(p))(\bar{v}^{s_2}(k)\Gamma u^{s_1}(p))^* &= \sum_{s_1,s_2} \bar{v}^{s_2}(k)\Gamma' u^{s_1}(p)\bar{u}^{s_1}(p)\overline{\Gamma} v^{s_2}(k) \\
&= \sum_{s_2} \bar{v}^{s_2}(k)\Gamma' \not{p} \overline{\Gamma} v^{s_2}(k) \\
&= \sum_{s_2} \bar{v}_\mu^{s_2}(k)\Gamma'^{\mu\nu} \not{p}_{\nu\rho} \overline{\Gamma}^{\rho\sigma} v_\sigma^{s_2}(k) \\
&= \Gamma'^{\mu\nu} \not{p}_{\nu\rho} \overline{\Gamma}^{\rho\sigma} \not{k}_{\sigma\mu} \\
&= \mathrm{Tr}(\Gamma' \not{p} \overline{\Gamma} \not{k}) \ ,
\end{aligned} \tag{4.23}$$

where the matrix multiplication is made explicit in the third equation by the reintroduction

of the Dirac spinor indices. The same is true for different combinations of Dirac spinors:

$$\begin{aligned}
&\sum_{s_1,s_2} (\bar{u}^{s_2}(k)\Gamma' v^{s_1}(p))(\bar{u}^{s_2}(k)\Gamma v^{s_1}(p))^* \\
&= \sum_{s_1,s_2} (\bar{v}^{s_2}(k)\Gamma' v^{s_1}(p))(\bar{v}^{s_2}(k)\Gamma v^{s_1}(p))^* \\
&= \sum_{s_1,s_2} (\bar{u}^{s_2}(k)\Gamma' u^{s_2}(p))(\bar{u}^{s_2}(k)\Gamma u^{s_2}(p))^* = \mathrm{Tr}(\Gamma' \not{p} \overline{\Gamma} \not{k}) \ .
\end{aligned}$$

As a small remark: If the sum over the spin is not taken, this trick can still by used by employing the projection

$$u^s(p)\bar{u}^s(p) = v^s(p)\bar{v}^s(p) = \frac{1}{2}\not{p}(1 + \gamma_5 \not{s}) \ . \tag{4.24}$$

This projection can be used to derive the leptonic tensor in Equation (3.59). For more details, see [234].

4.3 Feynman Parametrization

In next-to-leading order calculations, it will be necessary to evaluate integrals involving product of multiple propagators. To simplify such integrals, products of several potentially different propagators are combined into a single generalized propagator with a higher power. This merging of the propagators is done by virtue of Feynman parametrization [235, 236], which is explained in the following. The basic idea can be illustrated using two complex numbers, a_1 and a_2. It holds

$$\frac{1}{a_1 a_2} = \frac{1}{a_1 - a_2}\frac{a_1 - a_2}{a_1 a_2} = \frac{1}{a_1 - a_2}\left(\frac{1}{a_2} - \frac{1}{a_1}\right) = \frac{1}{a_1 - a_2}\int_{a_1}^{a_2} \mathrm{d}y \frac{1}{y^2} \ . \tag{4.25}$$

Substituting $y = a_1 x_1 + a_2(1 - x_1)$ gives, with $\frac{\mathrm{d}y}{\mathrm{d}x_1} = a_1 - a_2$:

$$\frac{1}{a_1 a_2} = \int_0^1 \mathrm{d}x_1 \frac{1}{(a_1 x_1 + a_2(1 - x_1))^2} \ , \tag{4.26}$$

which is the simplest form of the Feynman parametrization. The variable x_1 is called Feynman parameter.

As a concrete application, consider the product of two scalar propagators:

$$\begin{aligned}
&\frac{1}{l^2+\mathrm{i}\eta}\frac{1}{(l-k)^2+\mathrm{i}\eta} \\
&\qquad = \int_0^1 \mathrm{d}x_1 \frac{1}{((l^2+\mathrm{i}\eta)x_1+((l-k)^2+\mathrm{i}\eta)(1-x_1))^2} \\
&\qquad = \int_0^1 \mathrm{d}x_1 \frac{1}{(l^2-2l\cdot k(1-x_1)+k^2(1-x_1)+\mathrm{i}\eta)^2} \\
&\qquad = \int_0^1 \mathrm{d}x_1 \frac{1}{((l-k(1-x_1))^2+k^2x_1(1-x_1)+\mathrm{i}\eta)^2} \\
&\qquad = \int_0^1 \mathrm{d}x_1 \frac{1}{(\tilde{l}^2-\Delta+\mathrm{i}\eta)^2} \ ,
\end{aligned} \tag{4.27}$$

with the shifted loop momentum $\tilde{l}$ and Δ both being functions of x_1 with $\tilde{l} := l - k(1-x_1)$ and $\Delta := -k^2x_1(1-x_1)$. A first generalization of the Feynman parametrization arises by differentiating of the above relation with respect to a_1 and a_2

$$\partial_{a_1}^{\alpha_1-1}\partial_{a_2}^{\alpha_2-1}\frac{1}{a_1a_2} = (-1)^{\alpha_1-1}(-1)^{\alpha_2-1}\Gamma(\alpha_1)\Gamma(\alpha_2)\frac{1}{a_1^{\alpha_1}a_2^{\alpha_2}} \ , \tag{4.28}$$

where $\Gamma(x) := (x-1)!$ is the Gamma function. With that follows

$$\begin{aligned}
\frac{1}{a_1^{\alpha_1}a_2^{\alpha_2}} &= (-1)^{-(\alpha_1+\alpha_2-2)}\frac{1}{\Gamma(\alpha_1)\Gamma(\alpha_2)}\partial_{a_1}^{\alpha_1-1}\partial_{a_2}^{\alpha_2-1}\int_0^1 \mathrm{d}x_1 \frac{1}{(a_1x_1+a_2(1-x_1))^2} \\
&= \frac{\Gamma(\alpha_1+\alpha_2)}{\Gamma(\alpha_1)\Gamma(\alpha_2)}\int_0^1 \mathrm{d}x_1 \frac{x_1^{\alpha_1-1}(1-x_1)^{\alpha_2-1}}{(a_1x_1+a_2(1-x_1))^{\alpha_1+\alpha_2}} \ .
\end{aligned} \tag{4.29}$$

This method can be extended to an arbitrary number of terms. For n complex numbers $a_1, ..., a_n$ the Feynman parametrization yields

$$\frac{1}{a_1...a_n} = (n-1)!\int_0^1 \mathrm{d}x_1 \int_0^1 \mathrm{d}x_2 ... \int_0^1 \mathrm{d}x_n \frac{\delta(1-\sum_{i=1}^n x_i)}{(a_1x_1+...+a_nx_n)^n} \ , \tag{4.30}$$

provided that zero is not in the convex hull of $a_1, ..., a_n$. This identity can be proven by induction.

An alternative but closely related method was independently developed by Julian Schwinger [237]. Known as Schwinger parametrization, it is based on the fact that every complex number a with positive imaginary part can be written as

$$\mathrm{i}\frac{1}{a} = \int_0^\infty \mathrm{d}\tau \exp(-\mathrm{i}a\tau) \ . \tag{4.31}$$

with this, a product of n such terms can be expressed as:

$$\frac{1}{a_1 ... a_n} = \frac{1}{\mathrm{i}^n} \int_0^\infty \mathrm{d}\tau_1 ... \int_0^\infty \mathrm{d}\tau_n \exp\left(\mathrm{i} \sum_{j=1}^{n} \tau_j a_j\right) , \tag{4.32}$$

for $a_1, ..., a_n$ being complex numbers with positive imaginary part.
The Schwinger parametrization is already useful for calculating the integral over one propagator. This parametrization is readily transformed into the Feynman parametrization by the substitution $x_j = \tau_j / (\sum_{k=1}^{n} \tau_k)$. In this way, both approaches are complementary tools for simplifying multi-propagator integrals in next-to-leading order integrals.

4.4 Wick Rotation

Another challenge in next-to-leading order calculations is loop integration in virtual corrections. These loop momenta are not fixed by external kinematics and must be integrated over the whole d-dimensional Minkowski space. These integrals would be more straightforward if they were instead over d-dimensional Euclidean space. To simplify such integrals, it is common to perform a Wick rotation [238], which analytically continues the energy component to complex values and rotates the integration path from the real axis to the imaginary axis. This procedure eliminates the minus sign in the metric associated with the energy component.
Consider, for example, the product of two propagators in Equation (4.27) the integration over the loop momentum l or equivalently $\tilde{l}$ can be transformed as

$$\int \frac{\mathrm{d}^d \tilde{l}}{(2\pi)^4} \frac{1}{(\tilde{l}^2 - \Delta + \mathrm{i}\eta)^2} = -\mathrm{i} \int \frac{\mathrm{d}^d \tilde{l}_E}{(2\pi)^4} \frac{1}{(\tilde{l}_E^2 + \Delta - \mathrm{i}\eta)^2} , \tag{4.33}$$

where the subscript E indicates Euclidean variables.
To justify this transformation, consider the energy integration separately

$$\begin{aligned} \int \frac{\mathrm{d}^d \tilde{l}}{(2\pi)^4} \frac{1}{(\tilde{l}^2 - \Delta + \mathrm{i}\eta)^2} &= \int \frac{\mathrm{d}^{d-1} \vec{\tilde{l}}}{(2\pi)^4} \int_{-\infty}^{\infty} \mathrm{d}l^0 \frac{1}{\left((l^0)^2 - \vec{\tilde{l}}^2 - \Delta + \mathrm{i}\eta\right)^2} \\ &= \int \frac{\mathrm{d}^{d-1} \vec{\tilde{l}}}{(2\pi)^4} \int_{-\infty}^{\infty} \mathrm{d}l^0 \frac{1}{\left((l^0)^2 - a^2 + \mathrm{i}\eta\right)^2} , \end{aligned} \tag{4.34}$$

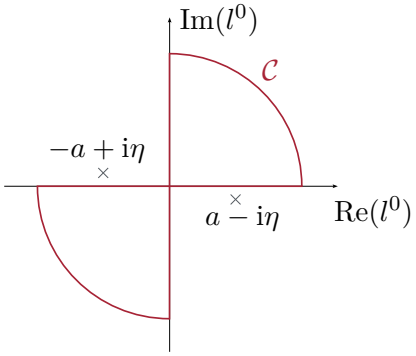

Figure 4.2: Contour $\mathcal{C}$ for the Wick rotation in the complex plane(red). The poles of the propagator are indicated by the gray crosses.

where the shorthand notation $a^2 = \vec{l}^2 + \Delta$ was introduced. The goal is to replace the integration along the real axis with one along the imaginary axis. To this end, consider the integration path along the close contour $\mathcal{C}$ shown in Figure 4.2. The integrand $\left(\left(l^0\right)^2 - a^2 + \mathrm{i}\eta\right)^{-n}$ is holomorphic in $\mathbb{C}\backslash\{a - \mathrm{i}\eta, -a + \mathrm{i}\eta\}$[2], therefore Cauchy's integral theorem applies[3] and the integral along $\mathcal{C}$ is zero. The integrals along the arcs at infinity vanish, and thus, the integrals along the real and imaginary axes must be equal:

$$\begin{aligned} I :&= \int_{-\infty}^{\infty} \mathrm{d}l^0 \frac{1}{\left((l^0)^2 - a^2 + \mathrm{i}\eta\right)^2} \\ &= \int_{-\mathrm{i}\infty}^{\mathrm{i}\infty} \mathrm{d}l^0 \frac{1}{\left((l^0)^2 - a^2 + \mathrm{i}\eta\right)^2} \ . \end{aligned} \tag{4.35}$$

Substituting $l_E^0 := -\mathrm{i}l^0$ and $\vec{l}_E := \vec{l}$ yields:

$$\begin{aligned} I &= \mathrm{i}\int_{-\infty}^{\infty} \mathrm{d}l_E^0 \frac{1}{\left(-(l_E^0)^2 - \vec{l}^2 - \Delta + \mathrm{i}\eta\right)^2} \\ &= -\mathrm{i}\int_{-\infty}^{\infty} \mathrm{d}l_E^0 \frac{1}{\left(l_E^2 + \Delta - \mathrm{i}\eta\right)^2} \ , \end{aligned} \tag{4.36}$$

where l_E now behaves like a vector in Euclidean space with Euclidean length $|l_E| = \sqrt{(l_E^0)^2 + \vec{l}_E^2}$.
The Wick rotation is possible since the poles of the generalized propagator are on the

[2]This in only true for infinity small η. For a finite η the poles are at $l^0 = \pm\sqrt{a^2 - \mathrm{i}\eta} = \pm(a - \frac{\mathrm{i}\eta}{2a} + \frac{a\eta^2}{8a^4} + \mathcal{O}(\eta^3))$.
[3]To be exact the path needs to be taken finite and then the limit has to be taken. This yields the same result.

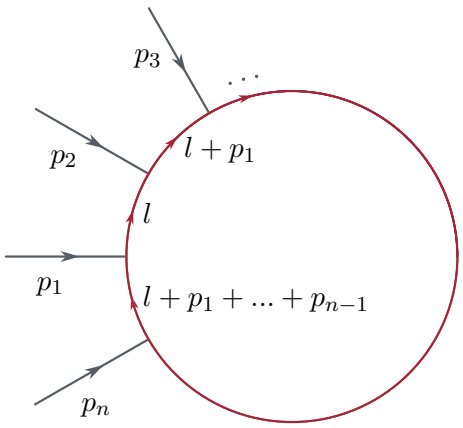

Figure 4.3: Schematic diagram of a n-point function as used in the Passarino-Veltman reduction, with all external momenta are flowing inwards.

outside of the curve due to the infinitesimal $i\eta$. The position of these poles originates from the time ordering of the propagator.
Since the integrand solely depends on the length of the Euclidean vector l_E, it is rotationally invariant. Consequently, the integration can be further simplified by switching to spherical coordinates.

4.5 Passarino-Veltman Reduction

Loop integrals in higher-order calculations often exhibit a common structure: they consist of products of propagators. For scalar particles, the propagator is of the form $((l+p)^2)^{-1}$ with the loop momentum l. A product of these propagators integrated over l is called a scalar integral. These are the only integrals that need to be solved. The more general integrals additionally involving fermion propagators are of the form $\frac{\gamma_\mu l^\mu}{(l+p)^2}$, which can be systematically reduced to a combination of scalar integrals. This procedure for reducing the integrals is called Passarino-Veltman reduction [239]. Here the technique developed by Bern, Dixon and Kosower [240] is presented. Although more recent approaches employ orthogonal momentum bases to simplify the reduction process [207, 241], the traditional method is presented here for its broader familiarity and well-established usage. The resulting decompositions are equivalent.
The gamma matrix γ_μ does not depend on the loop momentum and thus can be factored out of the integral. Consequently, it suffices to analyze integrals of the following form. The functions

$$I_n[\mathcal{N}(l)] := \int \frac{\mathrm{d}^d l}{(2\pi)^d} \mathcal{N}(l) \prod_{i=0}^{n-1} \frac{1}{(l+q_i)^2} \tag{4.37}$$

are called n-point loop integrals, where the numerator $\mathcal{N}(l)$ is a polynomial in the loop momentum l with degree $r \leq n$ and $q_i = \sum_{j=1}^{i} p_j$ is a shorthand notation for the sum over all previous incoming momenta. Due to momentum conservation it holds: $q_0 = q_n = \sum_{i=1}^{n} p_i = 0$. A schematic diagram of such an n-point function is shown in 4.3. In the special case $\mathcal{N}(l) = 1$ the resulting expression is referred to as a scalar n-point loop integral. Also define the reduced $(n-1)$-point integral as

$$I_{n-1}^{(j)}[\mathcal{N}(l)] := \int \frac{\mathrm{d}^d l}{(2\pi)^d} \mathcal{N}(l) \prod_{\substack{i=0 \\ i\neq j}}^{n-1} \frac{1}{(l+q_i)^2} \ , \tag{4.38}$$

where the j-th propagator is left out.
Starting with the vector valued n-point integral

$$I_n[l^\mu] = \int \frac{\mathrm{d}^d l}{(2\pi)^d} l^\mu \prod_{i=0}^{n-1} \frac{1}{(l+q_i)^2} \ , \tag{4.39}$$

the goal is to show that it can be written as a linear combination of scalar n- and $(n-1)$-point integrals. This is done by realizing that this integral is itself a Lorentz vector and can therefore be written as a linear combination of the only available external vectors $p_1, ..., p_{n-1}, p_n$. p_n is by conservation of momentum not independent of the other momenta $(p_1 + ... + p_{n-1} = -p_n)$ and therefore not needed. So, the integral can be written as

$$I_n[l^\mu] = \sum_{i=1}^{n-1} a_i p_i^\mu \ , \tag{4.40}$$

with some coefficients a_i. To determine the coefficients a_i both sides of the equation are contracted with a momentum p_j^μ. This results in:

$$I_n[l \cdot p_j] = \sum_{i=1}^{n-1} a_i (p_i \cdot p_j) = \sum_{i=1}^{n-1} a_i G_{ij} \ , \tag{4.41}$$

where $G_{ij} := p_i \cdot p_j$ is the Gram matrix. The crucial point in the reduction is the following identity concerning the numerator:

$$l \cdot p_j = \frac{1}{2}(((l+q_j)^2) - ((l+q_{j-1})^2) - q_j^2 + q_{j-1}^2) \ , \tag{4.42}$$

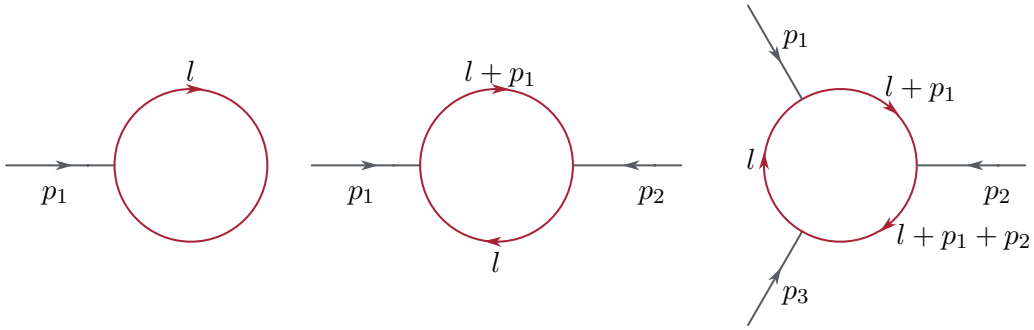

Figure 4.4: 1-, 2- and 3-point functions

which allows to cancel the first two terms with parts of the denominator and so get a sum of loop integrals with no loop momentum in the numerator. Doing this for all $n-1$ momenta, one obtains a set of $n-1$ linear equations:

$$\sum_{i=1}^{n-1} a_i G_{ij} = \frac{1}{2}(I_{n-1}^{(j)}[1] - I_{n-1}^{(j-1)}[1] + (-q_j^2 + q_{j-1}^2) I_n[1]) \ . \tag{4.43}$$

By inverting this relation, the coefficients are given by

$$a_i = \sum_{j=1}^{n-1} G_{ij}^{-1} \frac{1}{2}(I_{n-1}^{(j)}[1] - I_{n-1}^{(j-1)}[1] + (-q_j^2 + q_{j-1}^2) I_n[1]) \ . \tag{4.44}$$

Here, the Gram matrix needs to be inverted, which is only possible if its determinant is non-zero, that is, if the momenta $p_1, ..., p_{n-1}$ are linearly independent. This will lead to problems when dealing with $n > 4$ external momenta, since only four of the momenta can be linearly independent. However, because four linearly independent momenta already span the entire space, it is sufficient to choose four such vectors. In the calculations in this thesis, it is not necessary to go beyond 4-point functions.
By convention, the $1, 2, 3, 4$-point integrals are named A, B, C, D respectively. With the number of indices corresponding to the degree r of the numerator. The diagrams for the 1-, 2-, and 3-point functions are shown in Figure 4.4. Executing this procedure for the

one- and two-point functions yields

$$I_1[1] = \int \frac{\mathrm{d}^d l}{(2\pi)^d} \frac{1}{l^2} = A_0 \tag{4.45}$$

$$I_1[l^\mu] = \int \frac{\mathrm{d}^d l}{(2\pi)^d} \frac{l^\mu}{l^2} = 0 \tag{4.46}$$

$$I_2[1] = \int \frac{\mathrm{d}^d l}{(2\pi)^d} \frac{1}{l^2} \frac{1}{(l+p_1)^2} = B_0(p_1^2) \tag{4.47}$$

$$I_2[l^\mu] = \int \frac{\mathrm{d}^d l}{(2\pi)^d} l^\mu \frac{1}{l^2} \frac{1}{(l+p_1)^2} = B_1(p_1^2) p_1^\mu \tag{4.48}$$

$$\begin{aligned} I_2[l \cdot p_1] &= \int \frac{\mathrm{d}^d l}{(2\pi)^d} \frac{\frac{1}{2}((l+p_1)^2 - l^2 - p_1^2)}{l^2 (l+p_1)^2} \\ &= \frac{1}{2}(A_0 - A_0 - p_1^2 B_0(p_1^2)) \end{aligned} \tag{4.49}$$

$$\implies B_1(p_1^2) = -\frac{1}{2} B_0(p_1^2) \tag{4.50}$$

Higher-rank tensor integrals can be reduced recursively. So the starting point is to show that the tensorial n-point integral

$$I_n[l^\mu l^\nu] = \int \frac{\mathrm{d}^d l}{(2\pi)^d} l^\mu l^\nu \prod_{i=0}^{n-1} \frac{1}{(l+q_i)^2} \tag{4.51}$$

can be expressed as a linear combination of scalar n-,$(n-1)$-, and $(n-2)$-point integrals. The integral can be written as a linear combination of the metric tensor and dyadic products of two external momenta, as these are the only available tensor structures:

$$I_n[l^\mu l^\nu] = \int \frac{\mathrm{d}^d l}{(2\pi)^d} l^\mu l^\nu \prod_{i=0}^{n-1} \frac{1}{(l+q_i)^2} = a_{00} g^{\mu\nu} + \sum_{i,j=1}^{n-1} a_{ij} p_i^\mu p_j^\nu \ . \tag{4.52}$$

Contracting with the metric tensor gives

$$I_n[l^2] = \int \frac{\mathrm{d}^d l}{(2\pi)^d} l^2 \prod_{i=0}^{n-1} \frac{1}{(l+q_i)^2} = a_{00} d + \sum_{i,j=1}^{n-1} a_{ij} G_{ij} \ . \tag{4.53}$$

Therefore, the first equation for the coefficients is as follows:

$$I^0_{n-1}[1] = a_{00} d + \sum_{i,j=1}^{n-1} a_{ij} G_{ij} \ . \tag{4.54}$$

Contracting with $p_k^\mu p_h^\nu$ yields the remaining $4+3+2+1$ equations for $n > 4$ and $(n-1)+...+(n-n)$ equations for $n \leq 4$:

$$I_n[(p_k \cdot l)(p_h \cdot l)] = a_{00} G_{kh} + \sum_{i,j=1}^{n-1} a_{ij} G_{ik} G_{jh} \ . \tag{4.55}$$

The left-hand side can be reduced to already solved integrals using Equation (4.42). For $(p_h \cdot l)$ this yields

$$\begin{aligned} &\frac{1}{2}(I_{n-1}^{(h)}[p_k \cdot l] - I_{n-1}^{(h-1)}[p_k \cdot l] + (-q_h^2 + q_{h-1}^2) I_n[p_k \cdot l]) \\ &\quad = a_{00} G_{kh} + \sum_{i,j=1}^{n-1} a_{ij} G_{ik} G_{jh} \ . \end{aligned} \tag{4.56}$$

These integrals can be reduced to scalar integrals with the reduction of vector integrals above (4.39). Therefore, a system of $\frac{1}{2}n(n-1)$ linear equations for the $\frac{1}{2}n(n-1)$ coefficients (the coefficients are symmetric) is obtained. Solving this leads to the desired representation.
Applying this procedure to the 2-point integral leads to

$$\begin{aligned} I_2[l^\mu l^\nu] &= \int \frac{\mathrm{d}^d l}{(2\pi)^d} l^\mu l^\nu \frac{1}{l^2} \frac{1}{(l+p_1)^2} = B_{00} g^{\mu\nu} + B_{11} p_1^\mu p_1^\nu \\ I_2[l^2] &= \int \frac{\mathrm{d}^d l}{(2\pi)^d} \frac{l^2}{l^2 (l+p_1)^2} = B_{00} d + B_{11} p_1^2 = A_0 \\ I_2[(l \cdot p_1) l^\nu] &= \int \frac{\mathrm{d}^d l}{(2\pi)^d} \frac{(l \cdot p_1) l^\nu}{l^2 (l+p_1)^2} = B_{00} p_1^\nu + B_{11} p_1^2 p_1^\nu \\ I_2[(l \cdot p_1) l^\nu] &= \int \frac{\mathrm{d}^d l}{(2\pi)^d} \frac{\frac{1}{2}((l+p_1)^2 - l^2 - p_1^2) l^\nu}{l^2 (l+p_1)^2} \\ &= \int \frac{\mathrm{d}^d l}{(2\pi)^d} \frac{1}{2} \left(0 - \frac{(l-p_1)^\nu}{l^2} + \frac{-p_1^2 l^\nu}{l^2 (l+p_1)^2} \right) \\ &= \frac{1}{2}(0 - 0 + p_1^\nu A_0 + p_1^\nu (-p_1^2) B_1(p_1^2)) \\ \Longrightarrow \begin{pmatrix} 1 & p_1^2 \\ d & p_1^2 \end{pmatrix} &\begin{pmatrix} B_{00} \\ B_{11} \end{pmatrix} = \begin{pmatrix} \frac{1}{2}(A_0 + (-p_1^2) B_1(p_1^2)) \\ A_0 \end{pmatrix} \end{aligned} \tag{4.57}$$

Inserting $B_1(p_1^2)$ from Equation (4.45), using the definition $A_0 = 0$ and solving this equation yields the coefficients B_{00} and B_{11}.

$$B_{00} = -\frac{p_1^2}{4(d-1)} B_0(p_1^2) \qquad \text{and} \qquad B_{11} = \frac{d}{4(d-1)} B_0(p_1^2) \ . \tag{4.58}$$

Having seen the reduction explicitly for $r = 1, 2$ the general case follows easily. An n-point integral can be written as a linear combination of scalar n- to $(n-r)$-point functions, where r is the degree of the polynomial in l in the numerator. By the linearity of the integral, the only relevant integrals are

$$I_n[l^{\mu_1}...l^{\mu_s}] \,, \tag{4.59}$$

with $s \leq r$. The integral can be written as a linear combination of the external momenta and metric tensor. For an even s the combination is

$$\begin{aligned} I_n[l^{\mu_1}...l^{\mu_s}] = a_{0...0} g^{\{\mu_1\mu_2}...g^{\mu_{s-1}\mu_s\}} + \sum_{i_{s-1},i_s=1}^{n-1} a_{0...0i_{s-1}i_s} g^{\{\mu_1\mu_2}...g^{\mu_{s-3}\mu_{s-2}} p_{i_{s-1}}^{\mu_{s-1}} p_{i_s}^{\mu_s\}} \\ +... + \sum_{i_1,...,i_s=1}^{n-1} a_{i_1...i_s} p_{i_1}^{\{\mu_1}...p_{i_s}^{\mu_s\}} \,, \end{aligned} \tag{4.60}$$

where the brackets in the exponent means the symmetric combination of the tensors ($p_1^{\{\mu} p_2^{\nu\}} := p_1^\mu p_2^\nu + p_1^\nu p_2^\mu$). For odd s a similar formula can be found. Contracting with these tensors and using Equation (4.42) to get a system of linear equations for the coefficients. These coefficients are then a linear combination of n-point and $(n-1)$-point integrals, both with numerator degree $s-1$. Since the degree of the numerator is decreased by one, iterating this process s times will yield a linear combination of scalar n-,...,$(n-s)$-point integrals. Therefore, the original integral can be expressed as a linear combination of scalar n-,...,$(n-r)$-point integrals.

Although algebraically intensive, this procedure is algorithmic and needs to be performed only once per tensor structure. A full set of explicit reduction formulas can be found in [239], with a more modern treatment presented in [241]. These reduction formulas are also implemented in the `FeynCalc` package [230–233], which is employed in this work to apply the reduction.

The remaining scalar integrals, which serve as a basis for all reduced expressions, can be calculated using Feynman parameters. For a complete calculation, see [207]. The scalar integrals are also implemented in `FeynCalc`.

4.6 Spherical integration in d Dimensions

As introduced in previous sections, the divergences accruing in next-to-leading order calculations are regulated by dimensional regularization. This method requires the evaluation of integrals in non-integer spacetime dimensions. Such integrals arise in the evaluation

of loop diagrams and in the calculation of phase space integrals. This section presents a concise overview of integration in d-dimensional spherical coordinates, emphasizing a systematic approach applicable to both loop and phase space integrals. The treatment follows the presentations in [241, 242].

First, spherical coordinates at integer dimensions are introduced. Subsequently, integration in integer-dimensional spherical coordinates is discussed by simplifying the general integration with properties of the integrand. In the case at hand, the integrand only contains the dependence on at most two angles, which allows for a splitting of the angular integrals. This results in a method for integration without specifying the dimension d, creating a way to generalize the integration.

The starting point are the well-known two-dimensional spherical coordinates, the polar coordinates. In those, a vector $x^{(2)} \in \mathbb{R}^2$ can be expressed by its radial component r_2 and its polar angle $\theta_1 \in [0, 2\pi]$, by

$$x^{(2)} = r_2 u^{(2)}(\theta_1) \ , \tag{4.61}$$

where

$$u^{(2)}(\theta_1) = (\sin\theta_1, \cos\theta_1) \tag{4.62}$$

is a unit vector that describes the direction of $x^{(2)}$.

This formulation generalizes naturally to d-dimensions. In vector $x^{(d)} \in \mathbb{R}^d$ can be written in spherical coordinates as

$$x^{(d)} = r_d u^{(d)} \ , \tag{4.63}$$

with the length $r_d = |x^{(d)}|$ and a unit vector $u^{(d)}$ that depends on $d-1$ angles $\theta_1, ..., \theta_{d-1}$. To construct $u^{(d)}$ explicitly, an iterative procedure is used, starting from $u^{(2)}$ given above. If $u^{(d-1)}$ is known as a function of the $d-2$ angles $\theta_1, ..., \theta_{d-2}$, then the vector $x^{(d)}$ can be written in cylindrical coordinates as

$$x^{(d)} = \left(r_{d-1} u^{(d-1)}(\theta_1, ..., \theta_{d-2}), x_d\right) \ , \tag{4.64}$$

where x_d is the dth component of $x^{(d)}$. Introducing the angle $\theta_{d-1} \in [0, \pi]$ as the angle between $x^{(d)}$ and the x_d-axis, and r_d as the length of $x^{(d)}$ these variables can be written as:

$$r_{d-1} = r_d \sin\theta_{d-1} \ , \qquad x_d = r_d \cos\theta_{d-1} \ . \tag{4.65}$$

This yields the recursion relation for spherical coordinates in d dimensions, where d is an integer

$$x^{(d)} = r_d \left(\sin\theta_{d-1}\, u^{(d-1)}(\theta_1, ..., \theta_{d-2}), \cos\theta_{d-1} \right) \ . \tag{4.66}$$

The objective is to evaluate integrals in d dimensions without having to specify the dimension d. This can be achieved by using some features of the integrand. In loop integrals, the integrand only depends on the absolute square of the variable. This can be achieved by the Passarino-Veltman reduction of the previous Section 4.5. In contrast, phase space integrals can exhibit a more complex structure. It can also depend on up to two angles in the processes discussed in this thesis. For readers familiar with the standard procedure for angular integration of [243, 244], this is due to the ability to reduce all integrands in these angular integrations to two angular-dependent variables. For a more recent approach and a thorough explanation, see ([241], App. D). Therefore, the integrand can be assumed to take the form $f(r_d, \theta_{d-1}, \theta_{d-2})$.
To reflect this the vector $x^{(d)}$ is written with the two angles θ_{d-1} and θ_{d-2} explicit as

$$x^{(d)} = r_d \left(\sin\theta_{d-1}\, \sin\theta_{d-2}\, u^{(d-2)}(\theta_1, ..., \theta_{d-3}), \sin\theta_{d-1}\, \cos\theta_{d-2}, \cos\theta_{d-1} \right) \ . \tag{4.67}$$

The standard integral in spherical coordinates in d dimensions is

$$\int \mathrm{d}^d x^{(d)} = \int_0^\infty \mathrm{d}r_d r_d^{d-1} \int \mathrm{d}\Omega_{d-1} \ , \tag{4.68}$$

where Ω_{d-1} is the $d-1$ dimensional unit sphere. The integral $\int \mathrm{d}\Omega_{d-1}$ contains all angular integrations. In the case where the integrand only depends on the absolute square of the integration variable, these angular integrals can be evaluated by [64]

$$\begin{aligned}
(\sqrt{\pi})^d &= \left(\int \mathrm{d}x \exp\left(-x^2\right) \right)^d = \int \mathrm{d}^d x \exp\left(-\sum_{i=1}^d x_i^2 \right) \\
&= \int \mathrm{d}\Omega_{d-1} \int_0^\infty \mathrm{d}x x^{d-1} \exp\left(-x^2\right) \\
&= \left(\int \mathrm{d}\Omega_{d-1} \right) \frac{1}{2} \int_0^\infty \mathrm{d}(x^2)\ (x^2)^{n/2-1} \exp\left(-(x^2)\right) \\
&= \Omega_{d-1} \frac{1}{2} \Gamma\left(\frac{d}{2}\right) \ .
\end{aligned} \tag{4.69}$$

The calculation cannot be performed for non-integer values of d. Nonetheless, the result suggests the definition of the area of the unit sphere in an arbitrary dimension d as

$$\Omega_d = \int \mathrm{d}\Omega_d = \frac{2\pi^{\frac{d+1}{2}}}{\Gamma(\frac{d+1}{2})} \ . \tag{4.70}$$

If, on the other hand, the integrand is the function f from above, then the angular integration needs to be separated into the first $d-2$ angular integrals and the last two over θ_{d-2} and θ_{d-1}. By using the recursion relation (4.66) the angular integral can be written as

$$\int \mathrm{d}\Omega_{d-1} = \left(\prod_{i=2}^{d-1} \int_0^\pi \mathrm{d}\theta_i \sin^{i-1}\theta_i\right) \int_0^{2\pi} \mathrm{d}\theta_1 \ . \tag{4.71}$$

or writing only the last two integrations explicitly:

$$\int \mathrm{d}\Omega_{d-1} = \int_0^\pi \mathrm{d}\theta_{d-1} \sin^{d-2}\theta_{d-1} \int_0^\pi \mathrm{d}\theta_{d-2} \sin^{d-3}\theta_{d-2} \int \mathrm{d}\Omega_{d-3} \ . \tag{4.72}$$

This decomposition remains valid for arbitrary d using Equation (4.70) if the integrand only depends on the last two angles. If more angles were involved, more angular integrals must be made explicit before the area of the unit sphere can be used.
This means that the function f from above can be integrated as follows in an arbitrary dimension d by using (4.68) and (4.72):

$$\begin{aligned}&\int \mathrm{d}^d x^{(d)} f(r_d, \theta_{d-1}, \theta_{d-2}) \\ &\quad = \Omega_{d-3} \int_0^\infty r_d\, r_d^{d-1} \int_0^\pi \mathrm{d}\theta_{d-1} \sin^{d-2}\theta_{d-1} \int_0^\pi \mathrm{d}\theta_{d-2} \sin^{d-3}\theta_{d-2}\, f(r_d, \theta_{d-1}, \theta_{d-2}) \ .\end{aligned} \tag{4.73}$$

For notational convenience, it is customary to rename the angles $\theta_{d-1} \to \theta_1$ and $\theta_{d-2} \to \theta_2$ yielding the result:

$$\begin{aligned}&\int \mathrm{d}^d x^{(d)} f(r_d, \theta_1, \theta_2) \\ &\quad = \Omega_{d-3} \int_0^\infty r_d\, r_d^{d-1} \int_0^\pi \mathrm{d}\theta_1 \sin^{d-2}\theta_1 \int_0^\pi \mathrm{d}\theta_2 \sin^{d-3}\theta_2\, f(r_d, \theta_1, \theta_2) \ .\end{aligned} \tag{4.74}$$

This forms the foundation for the angular integrations required in subsequent sections.

The next section introduces the origin of those integrals, the phase space integration, followed by a section describing techniques to solve those integrals.

4.7 Phase Space

As seen above, the cross section comprises not only the squared matrix element but also contains the integral over all outgoing states of the squared matrix element. In practical calculations, one typically avoids integrating over the full phase space. Instead, results are often presented differentially with respect to some kinematic variables. Common choices include the Mandelstam variables, or for the SIDIS process, the kinematic variables x and z, and the dimensionless variables v and w. This work predominantly employs the latter two.

Notably, the leading-order calculation can be performed in four spacetime dimensions because no divergences arise at this order. However, beginning at next-to-leading order, the emerging divergences necessitate the use of a regularization scheme. Dimensional regularization is employed throughout this work (see Section 2.5.1). Consequently, even the two-particle phase space is derived in $d := 4 - 2\epsilon$ dimensions, anticipating the need for the results in the evaluation of virtual corrections.

The starting point is the general expression for the n-particle phase space [62, 64]

$$\int \mathrm{dPS}_n := \int \prod_{i=1}^{n} \left(\frac{\mathrm{d}^d k_i}{(2\pi)^{d-1}} \delta^+(k_i^2) \right) (2\pi)^d \, \delta^d \left(p + q - \sum_{i=1}^{n} k_i \right) \,, \tag{4.75}$$

where p and q denote the momenta of the initial-state parton and virtual photon, respectively, and k_i are the momenta of the final-state particles. Furthermore, the function $\delta^+(k_i^2) := \delta(k_i^2)\theta(k_i^0)$, where θ is the Heaviside step function, enforces on-shell conditions on the outgoing particles, while also including the positivity constraint on that particles energy. In our case, all outgoing particles are massless. The last delta function in Equation (4.75) imposes overall momentum conservation.

For the two-particle phase space ($n = 2$), the delta function is kept explicit, resulting in an additional integration that can, in principle, be carried out immediately. To be specific, this is the delta function $\delta(1-w)$ in the result. While in the next chapter, where the phase space for $n = 3$ is derived, the momentum conserving delta function will be evaluated in an integral. This yields an expression that is also differential in v and w, as is the case for the two-particle phase space.

4.7.1 The Two Particle Phase Space

To derive an expression for the two-particle phase space, set $n = 2$. In a physical setting, the momentum of the second outgoing particle k_2 is considered to be unmeasured. This is the justification for integrating over this momentum and obtaining

$$\begin{aligned}\int \mathrm{dPS}_2 &= \int \frac{\mathrm{d}^d k_1}{(2\pi)^{d-1}} \int \frac{\mathrm{d}^d k_2}{(2\pi)^{d-1}} (2\pi)^d \delta^+(k_1^2)\delta^+(k_2^2)\delta^d(p+q-k_1-k_2) \\ &= \int \frac{\mathrm{d}^d k_1}{(2\pi)^{d-2}} \delta^+(k_1^2)\delta^+((p+q-k_1)^2) \ ,\end{aligned} \tag{4.76}$$

where momentum conservation is used to eliminate the integral over k_2. Since the momentum k_2 is already fixed by the d-dimensional delta function to $k_2 \to q + p - k_1$, a measurement would not result in new information.
Due to Lorentz invariance, the phase space integral can be evaluated in any frame. A natural choice is the center-of-momentum (c.o.m.) frame of the initial-state system, where $\vec{p} + \vec{q} = 0$ and $p^0 + q^0 = \sqrt{(p+q)^2} = \sqrt{s}$, with the usual Mandelstam variable s defined in Section 3.5.2. In this frame, the delta function simplifies to

$$\begin{aligned}\delta((p+q-k_1)^2) &= \delta\left((q+p)^2 - 2k_1\cdot(p+q) + k_1^2\right) \\ &= \delta\left(s - 2k_1^0\sqrt{s}\right) \\ &= \frac{1}{2\sqrt{s}}\delta\left(k_1^0 - \frac{\sqrt{s}}{2}\right) \ .\end{aligned} \tag{4.77}$$

For later convenience, the delta function can also be written in terms of the Mandelstam variables to get

$$\delta((p+q-k_1)^2) = \delta(s+t+u+Q^2) = \delta(s_{23}) \ . \tag{4.78}$$

To proceed, the delta function of the momentum k_1 can be used to eliminate one additional integration. This delta function can be expressed as

$$\delta^+(k_1^2) = \delta\left((k_1^0)^2 - |\vec{k_1}|^2\right)\theta(k_1^0) = \frac{1}{2|\vec{k_1}|}\delta(k_1^0 - |\vec{k_1}|)\theta(k_1^0) \ , \tag{4.79}$$

where the Heaviside function θ is used to exclude the unphysical negative energy solution of the delta function. Splitting the k_1 integration into its energy and momentum components

$$\mathrm{d}^d k_1 = \mathrm{d}k_1^0 \mathrm{d}^{d-1}\vec{k_1} \tag{4.80}$$

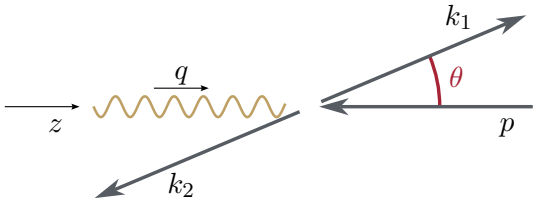

Figure 4.5: Illustration of the frame used in the two-particle phase space, with p and q aligned with the z-axis and the scattering angle θ (red).

and plugging those two transformations into the expression for the two-particle phase space, one gets, after integrating over k_1^0:

$$\int \mathrm{dPS}_2 = \int \frac{\mathrm{d}^{d-1}\vec{k_1}}{4\sqrt{s}|\vec{k_1}|(2\pi)^{d-2}} \delta\left(|\vec{k_1}| - \frac{\sqrt{s}}{2}\right) . \tag{4.81}$$

To simplify further, spherical coordinates for the spatial component of the momentum k_1 are introduced. Note that these spherical coordinates are needed in the non-integer dimension $d-1$. For this analytic continuation of the standard results for integer dimensions must be used. Specifically, the spatial component of k_1, i. e., $\vec{k_1}$ is parametrized by its magnitude $|\vec{k_1}|$ and the $d-2$ angles $\theta_1, ..., \theta_{d-2}$. To make it more explicit, the frame will be rotated such that the spatial components of p and, therefore, also of q are purely in z-direction. For easier notation, the polar angle θ_1 is renamed to θ. This momenta in this frame are illustrated in Figure 4.5. In formulas they are

$$\begin{aligned} p &= (p^0, \mathbf{0}_{d-2}, -p^0) , \\ q &= (q^0, \mathbf{0}_{d-2}, p^0) , \\ k_1 &= |\vec{k_1}|(1, \mathbf{k_1}_{d-2}, \cos\theta) , \end{aligned} \tag{4.82}$$

where $\mathbf{0}_{d-2}$ are the missing $d-2$ zero components of the d-dimensional vectors and $\mathbf{k_1}_{d-2}$ the first $d-2$ components of the spatial unit vector in $d-1$ dimensions, as shown in Section 4.6. By introducing spherical coordinates to rewrite the k_1 part of the phase space, one obtains

$$\int \frac{\mathrm{d}^{d-1}\vec{k_1}}{2|\vec{k_1}|} = \frac{1}{2} \int \mathrm{d}|\vec{k_1}||\vec{k_1}|^{d-3} \int \mathrm{d}\Omega_{d-2} . \tag{4.83}$$

The next step in the integration of the angular integral is to realize that only one angle is measured in the collision and all other $d-3$ azimuthal angles can be integrated, resulting

in

$$\begin{aligned}\int \frac{\mathrm{d}^{d-1}\vec{k_1}}{2|\vec{k_1}|} &= \frac{1}{2}\int \mathrm{d}|\vec{k_1}||\vec{k_1}|^{d-3}\int \mathrm{d}\theta \sin^{d-3}(\theta)\int \mathrm{d}\Omega_{d-3} \\ &= \frac{1}{2}\int \mathrm{d}|\vec{k_1}||\vec{k_1}|^{d-3}\int \mathrm{d}\cos\theta(1-\cos^2(\theta))^{d/2-2}\int \mathrm{d}\Omega_{d-3}\ .\end{aligned} \tag{4.84}$$

The area of the $d-3$-dimensional unit sphere is given by

$$\int \mathrm{d}\Omega_{d-3} = \frac{2\pi^{(d-2)/2}}{\Gamma((d-2)/2)}\ . \tag{4.85}$$

For more details, see Section 4.6.
The energy components of the incoming momenta p^0 and q^0 can be expressed in terms of the Mandelstam variables as

$$p^0 = \frac{s+Q^2}{2\sqrt{s}}\ , \tag{4.86}$$

$$q^0 = \frac{s-Q^2}{2\sqrt{s}}\ . \tag{4.87}$$

This can be seen readily by observing $s = (p+q)^2 = (p^0+q^0)^2$ and $s+Q^2 = 2p\cdot q = 2p^0(p^0+q^0)$, from which follows $p^0 = \frac{s+Q^2}{2\sqrt{s}}$ and $Q^2 = -q^2 = (p^0)^2 - (q^0)^2$ to get to $q^0 = \frac{s-Q^2}{2\sqrt{s}}$. The remaining variables that are still not integrated are $|\vec{k_1}|$ and θ, which can be related to the Mandelstam variables t and u by inserting their definitions

$$t = -2(q^0|\vec{k_1}| - p^0|\vec{k_1}|\cos\theta) - Q^2\ , \tag{4.88}$$

$$u = -2(p^0|\vec{k_1}| + p^0|\vec{k_1}|\cos\theta)\ . \tag{4.89}$$

This gives

$$|\vec{k_1}| = \frac{-Q^2-t-u}{2\sqrt{s}}\ , \tag{4.90}$$

$$\cos\theta = -\frac{s(t-u)+Q^2 s_{23}}{(s+Q^2)(t+u+Q^2)} \tag{4.91}$$

and together with the Jacobian

$$\left|\frac{\mathrm{d}(t,u)}{\mathrm{d}(|\vec{k_1}|,\cos\theta)}\right| = \frac{(s+Q^2)(t+u+Q^2)}{\sqrt{s}} \tag{4.92}$$

the following expression in terms of Mandelstam variables can be reached:

$$\int \frac{\mathrm{d}^{d-1}\vec{k_1}}{2|\vec{k_1}|} = \frac{1}{4}\frac{2\pi^{(d-2)/2}}{\Gamma((d-2)/2)} \int \mathrm{d}t\mathrm{d}u \frac{1}{s+Q^2} \left(\frac{(s+Q^2)^2}{u(st+Q^2 s_{23})}\right)^{2-d/2} . \tag{4.93}$$

This results in the following expression for the whole phase-space integral:

$$\begin{aligned} \int \mathrm{dPS}_2 &= \frac{1}{4}\frac{1}{(2\pi)^{d-2}}\frac{2\pi^{(d-2)/2}}{\Gamma((d-2)/2)} \int \mathrm{d}t\mathrm{d}u \frac{1}{s+Q^2} \left(\frac{(s+Q^2)^2}{u(st+Q^2 s_{23})}\right)^{2-d/2} \delta(s_{23}) \\ &= \frac{1}{8\pi}\frac{(4\pi)^\epsilon}{\Gamma(1-\epsilon)} \int \mathrm{d}t\mathrm{d}u \frac{1}{s+Q^2} \left(\frac{(s+Q^2)^2}{stu}\right)^{\epsilon} \delta(s_{23}) , \end{aligned} \tag{4.94}$$

where in the second step, $d = 4-2\epsilon$ is replaced, all prefactors are collected, and the delta function is used to eliminate s_{23}. The delta function $\delta(s_{23})$ is a direct representation of the momentum conservation with two incoming and two outgoing particles. For more outgoing particles, this delta function is no longer present, and the more complicated structure from the first equation must be kept. This will become relevant in the next chapter.
In terms of the SIDIS variables $\hat{z}$ and q_T^2, with the transitions provided in Section 3.5.2, the two particle phase space is

$$\int \mathrm{dPS}_2 = \frac{1}{8\pi}\frac{(4\pi)^\epsilon}{\Gamma(1-\epsilon)} \int \mathrm{d}\hat{z}\mathrm{d}q_T^2 \frac{1}{Q^2} \left(\hat{z}^2 q_T^2\right)^{-\epsilon} \delta\left(\frac{q_T^2}{Q^2} - \frac{(1-\hat{x})(1-\hat{z})}{\hat{x}\hat{z}}\right) . \tag{4.95}$$

Transitioning to the dimensionless variables $v = 1 + t/(s+Q^2)$ and $w = -u/(s+t+Q^2)$ one gets:

$$\int \mathrm{dPS}_2 = \frac{1}{8\pi}\frac{(4\pi)^\epsilon}{\Gamma(1-\epsilon)} \int \mathrm{d}v\mathrm{d}w \left(sv(1-v)\right)^{-\epsilon} \delta(1-w) , \tag{4.96}$$

where $\delta(s_{23}) = \delta((s+Q^2)v(1-w)) = \frac{1}{(s+Q^2)v}\delta(1-w)$ and the Jacobian $\left|\frac{\mathrm{d}(t,u)}{\mathrm{d}(v,w)}\right| = (s+Q^2)^2 v$ were used. One might realize the striking similarity to the fully massless case, as in [245]. This is in no way obvious, as can be seen in the phase-space expression in terms of Mandelstam variables. This is in fact only true due to the clever choice of variables s, v and w, which carry the mass Q^2 implicitly.

4.7.2 The Three Particle Phase Space

For the three-particle phase space, it is often advantageous to factor out a known contribution, namely, the two-particle phase space. This can be done by grouping two of

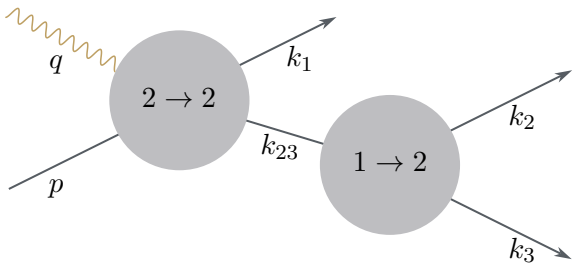

Figure 4.6: Graphical illustration of the factorization of the three-particle phase space into a two-to-two-particle phase space and a one-to-two-particle decay.

the outgoing particles together as "unobserved" particles, leaving the third particle as the "observed" particle[4], see Figure 4.6. This results in a convenient factorization of the three-particle phase space into a two-particle phase space contribution and a subsequent $1 \to 2$ decay. The general expression for the three-particle phase space in d dimensions is:

$$\int \mathrm{dPS}_3 := \int \frac{\mathrm{d}^d k_1}{(2\pi)^{d-1}} \frac{\mathrm{d}^d k_2}{(2\pi)^{d-1}} \frac{\mathrm{d}^d k_3}{(2\pi)^{d-1}} \delta^+(k_1^2)\delta^+(k_2^2)\delta^+(k_3^2)(2\pi)^d \delta^d(p+q-k_1-k_2-k_3) \ . \tag{4.97}$$

With $\delta^+(k_i^2) := \delta(k_i^2)\theta(k_i^0)$, where θ is the Heaviside step function, from above.
Two particles need to be grouped together to split off the two-particle phase space. Here, the two unobserved particles with momenta k_2 and k_3 are grouped together by introducing a new variable $k_{23} := k_2 + k_3$. By additionally inserting a one $1 = \int \frac{\mathrm{d}^d k_{23}}{(2\pi)^d}(2\pi)^d \delta^d(k_{23} - k_2 - k_3)$, the three-particle phase space can be written as:

$$\begin{aligned} \int \mathrm{dPS}_3 = \int \frac{\mathrm{d}^d k_1}{(2\pi)^{d-1}} \frac{\mathrm{d}^d k_{23}}{(2\pi)^d} \delta^+(k_1^2)(2\pi)^d \delta^d(p+q-k_1-k_{23}) \\ \times \int \frac{\mathrm{d}^d k_2}{(2\pi)^{d-1}} \frac{\mathrm{d}^d k_3}{(2\pi)^{d-1}} \delta^+(k_2^2)\delta^+(k_3^2)(2\pi)^d \delta^d(k_{23}-k_2-k_3) \ . \end{aligned} \tag{4.98}$$

Both factors in (4.98) are Lorentz invariants and resemble the standard two-particle phase space integral from above. Due to Lorentz invariance, the reference frame of both factors can be chosen freely. For the second factor, the rest frame of $k_{23} = (k_{23}^0, \vec{0})$ is chosen. The first integral to be integrated is the one over the momentum k_2, taking the delta function

[4]Quarks and Gluons are never directly observed, regardless of what they are called. This particle is called "observed" because its remnants after recombination into colorless hadrons can be observed.

in k_2 with the relation given in Equation (4.79) into account, to obtain

$$\begin{aligned}\int \mathrm{d}^d k_2 \delta^+(k_2^2) &= \int \mathrm{d}^d k_2 \delta((k_2^0)^2 - \vec{k_2}^2)\theta(k_2^0) \\ &= \int \mathrm{d}^d k_2 \frac{1}{2|\vec{k_2}|}\delta(k_2^0 - |\vec{k_2}|) \\ &= \int \frac{\mathrm{d}^{d-1}k_2}{2|\vec{k_2}|} \ .\end{aligned} \tag{4.99}$$

Next, the d-dimensional delta function is used to integrate over the momentum k_3, resulting in

$$\begin{aligned}\int \mathrm{d}k_3 \delta^+(k_3^2)\delta^d(k_{23} - k_2 - k_3) &= \delta^+((k_{23} - k_2)^2) \\ &= \delta((k_{23} - k_2)^2)\theta\left((k_{23} - k_2)^0\right) \\ &= \delta((k_{23}^0)^2 - 2k_{23}^0 k_2^0)\theta\left((k_{23} - k_2)^0\right) \\ &= \frac{1}{2|k_{23}^0|}\delta\left(k_2^0 - \frac{k_{23}^0}{2}\right)\theta\left((k_{23} - k_2)^0\right) \\ &= \frac{1}{2|k_{23}^0|}\delta\left(|\vec{k_2}| - \frac{k_{23}^0}{2}\right)\theta(k_{23}^0 - |\vec{k_2}|) \ ,\end{aligned} \tag{4.100}$$

where, in the last line, the delta function resulting from the k_2 integration, that is, the fact that k_2 is on-shell, was used. Therefore, the second factor of (4.98) becomes

$$\begin{aligned}&\int \frac{\mathrm{d}^d k_2}{(2\pi)^{d-1}} \frac{\mathrm{d}^d k_3}{(2\pi)^{d-1}} \delta^+(k_2^2)\delta^+(k_3^2)(2\pi)^d \delta^d(k_{23} - k_2 - k_3) \\ &\qquad = \frac{1}{2|k_{23}^0|(2\pi)^{d-2}} \int \frac{\mathrm{d}^{d-1}k_2}{2|\vec{k_2}|}\delta\left(|\vec{k_2}| - \frac{k_{23}^0}{2}\right)\theta(k_{23}^0 - |\vec{k_2}|) \ .\end{aligned} \tag{4.101}$$

From here on, the derivation proceeds analogously to the two-particle phase space, and spherical coordinates for the spatial part of k_2 are introduced via

$$\int \frac{\mathrm{d}^{d-1}\vec{k_2}}{2|\vec{k_2}|} = \frac{1}{2}\int \mathrm{d}|\vec{k_2}||\vec{k_2}|^{d-3} \int \mathrm{d}\Omega_{d-2} \ . \tag{4.102}$$

Now, the integral over the magnitude of $\vec{k_2}$ is evaluated, which is trivial with the delta function and results in

$$\frac{1}{2}\int \mathrm{d}|\vec{k_2}||\vec{k_2}|^{d-3}\delta\left(|\vec{k_2}| - \frac{k_{23}^0}{2}\right)\theta(k_{23}^0 - |\vec{k_2}|) = \frac{(k_{23}^0)^{d-3}}{2^{d-2}}\theta(k_{23}^0) \ . \tag{4.103}$$

At this stage, the only thing left is the integral over the $d-2$ angles in spherical coordinates. Because the functions that need to be integrated over the phase space only depend on two angles, the trivial remaining $d-4$ dimensional spherical integrals can be integrated. By Section 4.6, the angular integral can be written as

$$\int \mathrm{d}\Omega_{d-2} = \int \mathrm{d}\theta_1 \sin^{d-3}\theta_1 \int \mathrm{d}\theta_2 \sin^{d-4}\theta_2 \int \mathrm{d}\Omega_{d-4} \ . \tag{4.104}$$

The trivial integration over $\mathrm{d}\Omega_{d-4}$ can be calculated to give the area of the $d-4$-dimensional sphere

$$\Omega_{d-4} := \int \mathrm{d}\Omega_{d-4} = \frac{2\pi^{(d-3)/2}}{\Gamma((d-3)/2)} = 2^{d-4}\pi^{d/2-2}\frac{\Gamma(d/2-2)}{\Gamma(d-4)} = 2^{d-3}\pi^{d/2-2}\frac{\Gamma(d/2-1)}{\Gamma(d-3)} \ , \tag{4.105}$$

where the Legendre duplication formula

$$\frac{\Gamma(z)}{\Gamma(2z)} = \frac{\sqrt{\pi}}{2^{2z-1}}\frac{1}{\Gamma(z+1/2)} \tag{4.106}$$

and the relation $z\Gamma(z) = \Gamma(z+1)$ is used.
To summarize, the second factor in (4.98) becomes

$$\begin{aligned}
&\int \frac{\mathrm{d}^d k_2}{(2\pi)^{d-1}} \frac{\mathrm{d}^d k_3}{(2\pi)^{d-1}} \delta^+(k_2^2)\delta^+(k_3^2)(2\pi)^d \delta^d(k_{23}-k_2-k_3) \\
&\qquad = \frac{1}{2(4\pi)^{d-2}}(k_{23}^0)^{d-4}\theta(k_{23}^0)\Omega_{d-4}\int \mathrm{d}\theta_1 \sin^{d-3}\theta_1 \int \mathrm{d}\theta_2 \sin^{d-4}\theta_2 \\
&\qquad = \frac{1}{2(4\pi)^{d-2}}(k_{23}^0)^{d-4}\theta(k_{23}^0)\Omega_{d-4}\int \mathrm{d}\Omega_{\theta_1\theta_2} \ ,
\end{aligned} \tag{4.107}$$

where the shorthand notation

$$\int \mathrm{d}\Omega_{\theta_1\theta_2} := \int \mathrm{d}\theta_1 \sin^{d-3}\theta_1 \int \mathrm{d}\theta_2 \sin^{d-4}\theta_2 \tag{4.108}$$

was introduced in the last step.
All integrations involving the auxiliary variable k_{23} have been performed in the second factor. Moreover, all integrations that do not explicitly depend on the form of the matrix element were evaluated. The remaining factor, depending on the form of the matrix element, is left to be computed later in conjunction with the matrix element.
For now, the first factor of the phase space integral will become the center of attention.

Here, it must be realized that the k_{23} integration is now trivial, since the dependence on this variable in the second factor is explicit and the momentum-conserving delta function remains to be used. The remaining integral over k_1 should also be familiar from the two-particle phase space. Indeed, it is integrated in the same way, extracting the desired two degrees of freedom from this integration. It should be noted that the delta function $\delta^+((p+q+k_1)^2)$ from (4.76) is not present. This delta function resulted in the delta function for the Born kinematics. Because of the additional particle that can carry away some momentum, there cannot be such a delta function in this case. So, the kinematics must be different.
By keeping the k_{23} integration for last, the focus is now on the k_1 integration. The equations (4.79) and (4.80) are used to integrate the energy component, and in the next steps, (4.83) and (4.84) are employed to introduce spherical coordinates:

$$\begin{aligned}\int \frac{\mathrm{d}^d k_1}{(2\pi)^{d-1}}\delta^+(k_1^2) &= \frac{1}{(2\pi)^{d-1}}\int \frac{\mathrm{d}^{d-1}\vec{k_1}}{2|\vec{k_1}|} \\ &= \frac{1}{2(2\pi)^{d-1}}\int \mathrm{d}|\vec{k_1}||\vec{k_1}|^{d-3}\int \mathrm{d}\Omega_{d-2} \\ &= \frac{1}{2(2\pi)^{d-1}}\int \mathrm{d}|\vec{k_1}||\vec{k_1}|^{d-3}\int \mathrm{d}\cos\theta(1-\cos^2(\theta))^{d/2-2}\int \mathrm{d}\Omega_{d-3} \\ &= \frac{\Omega_{d-3}}{2(2\pi)^{d-1}}\int \mathrm{d}|\vec{k_1}||\vec{k_1}|^{d-3}\int \mathrm{d}\cos\theta(1-\cos^2(\theta))^{d/2-2}\ ,\end{aligned} \tag{4.109}$$

where in the last step the trivial angular integrals were computed and the notation

$$\Omega_{d-3} := \int \mathrm{d}\Omega_{d-3} = \frac{2\pi^{(d-2)/2}}{\Gamma((d-2)/2)} \tag{4.110}$$

for the surface of the $n-3$-dimensional sphere was introduced.
Now, the Lorentz invariance of the integral over k_1 is used to choose the center-of-mass frame of all three outgoing particles (i.e., the com frame of the incident particles) as the reference frame. This frame is again rotated to align the momenta of p and q with the z-axis. The scattering angle is again identified with the angle θ and the following parametrization of k_1 is chosen:

$$\begin{aligned}p &= (p^0, \mathbf{0}_{d-2}, -p^0)\ , \\ q &= (q^0, \mathbf{0}_{d-2}, p^0)\ , \\ k_1 &= |\vec{k_1}|(1, \mathbf{k_1}_{d-2}, \cos\theta)\ ,\end{aligned} \tag{4.111}$$

with $\mathbf{0}_{d-2}$ the $d-2$ zero components of p and q, and $\mathbf{k_1}_{d-2}$ the first $d-2$ components of the spatial unit vector in $d-1$ dimensions. This is the same frame as in Section 4.7.1 in Equation (4.82). As explained in Section 4.7.1, the variables p^0 and q^0 can be expressed as

$$p^0 = \frac{s+Q^2}{2\sqrt{s}} \,, \tag{4.112}$$

$$q^0 = \frac{s-Q^2}{2\sqrt{s}} \,. \tag{4.113}$$

Continuing by rewriting $|\vec{k_1}|$ and $\cos(\theta)$ in terms of the variables v and w yields:

$$v = 1 + \frac{2\ q\cdot k_1 - Q^2}{2\ p\cdot q} = \frac{s}{s+Q^2} - \frac{|\vec{k_1}|\left(s\left(1-\cos\theta\right) - Q^2\left(1+\cos\theta\right)\right)}{\sqrt{s}\left(s+Q^2\right)} \tag{4.114}$$

$$w = \frac{-2\ p\cdot k_1}{2\ p\cdot q + 2\ q\cdot k_1 - Q^2} = \frac{|\vec{k_1}|\left(1+\cos\theta\right)\left(s+Q^2\right)}{s^{3/2} - |\vec{k_1}|\left(s\left(1-\cos\theta\right) - Q^2\left(1+\cos\theta\right)\right)} \,. \tag{4.115}$$

Inverting these relations gives expressions for the magnitude of the momentum and the scattering angle:

$$|\vec{k_1}| = \frac{\sqrt{s}}{2}\left(1 - \frac{\left(s+Q^2\right)v(1-w)}{s}\right) \tag{4.116}$$

$$\cos\theta = -\frac{s\left(1-v-vw\right) - Q^2 v\left(1-w\right)}{s - (s+Q^2)v\left(1-w\right)} \,. \tag{4.117}$$

And the Jacobian of this transformation evaluates to

$$\left|\frac{\mathrm{d}(v,w)}{\mathrm{d}(|\vec{k_1}|,\cos\theta)}\right| = -\frac{s(1-v+vw) - Q^2 v\left(1-w\right)}{\sqrt{s}\left(s+Q^2\right)v} \,. \tag{4.118}$$

This gives:

$$\begin{aligned}\int \mathrm{d}|\vec{k_1}||\vec{k_1}|^{d-3} \int \mathrm{d}\cos\theta (1-\cos^2(\theta))^{d/2-2} \\ = \frac{1}{2}\int \mathrm{d}v\mathrm{d}w\left(s+Q^2\right)v\left[vw\left(s(1-v) - Q^2 v(1-w)\right)\right]^{d/2-2} \,.\end{aligned} \tag{4.119}$$

The same calculation was given in Section 4.7.1 in terms of the Mandelstam variables,

where an equivalent result (4.93) was derived:

$$\begin{aligned}\int \mathrm{d}|\vec{k_1}||\vec{k_1}|^{d-3} \int \mathrm{d}\cos\theta (1-\cos^2(\theta))^{d/2-2} \\ = \frac{1}{2}\int \mathrm{d}t\mathrm{d}u \frac{1}{s+Q^2}\left(\frac{(s+Q^2)^2}{u(st+Q^2\left(s+t+u+Q^2\right))}\right)^{2-d/2} .\end{aligned} \tag{4.120}$$

Now, the two calculations diverge again, because k_{23} still has to be integrated. This integral was not present in the two-particle phase space. The remaining integral is

$$\int \mathrm{d}^d k_{23} \delta^d(p+q-k_1-k_{23})(k_{23}^0)^{d-4}\theta(k_{23}^0) = \left(p^0+q^0-k_1^0\right)^{d-4}\theta\left(p^0+q^0-k_1^0\right) , \tag{4.121}$$

where the frame was already fixed to be the center-of-momentum frame for k_2+k_3, or equivalently the center-of-momentum frame of $p+q-k_1$. To write this in terms of Mandelstam variables or the dimensionless variables v and w, the invariant squared momentum is used:

$$\begin{aligned}(p+q-k_1)^2 &= 2\left(p\cdot q - p\cdot k_1 - q\cdot k_1\right) - Q^2 = s+t+u+Q^2 \\ &= (s+Q^2)v(1-w) ,\end{aligned} \tag{4.122}$$

to get, in the center-of-momentum frame of $p+q+k_1$, by taking the square root on both sides:

$$\begin{aligned}\sqrt{(p+q-k_1)^2} = \sqrt{\left(p^0+q^0-k_1^0\right)^2} = \left|p^0+q^0-k_1^0\right| \\ = \sqrt{s+t+u+Q^2} = \sqrt{(s+Q^2)\,v\,(1-w)} ,\end{aligned} \tag{4.123}$$

where the sign is fixed by the Heaviside theta function $\theta\left(p^0+q^0-k_1^0\right)$. This results in the expression

$$\begin{aligned}\int \mathrm{d}^d k_{23} \delta^d(p+q-k_1-k_{23})(k_{23}^0)^{d-4}\theta(k_{23}^0) = \left(s+t+u+Q^2\right)^{d/2-2} \\ = \left(\left(s+Q^2\right)v(1-w)\right)^{d/2-2} .\end{aligned} \tag{4.124}$$

Putting everything together, the three-particle phase space is

$$\begin{aligned}\int \mathrm{dPS}_3 = &\frac{\Omega_{d-3}\Omega_{d-4}}{2^{3d-2}\pi^{2d-3}} \\ &\times \int \mathrm{d}v\mathrm{d}w \left(s+Q^2\right)^{d/2-1} v^{d-3} \left[w(1-w)\left(s(1-v)-Q^2v(1-w)\right)\right]^{d/2-2} \\ &\times \int \mathrm{d}\Omega_{\theta_1\theta_2} \ .\end{aligned} \tag{4.125}$$

Inserting the area of the $(d-3)$- and $(d-4)$-dimensional spheres from (4.110) and (4.105), to get

$$\begin{aligned}\Omega_{d-3}\Omega_{d-4} &= 2\frac{(2\pi)^{d-3}}{\Gamma(d-3)} \\ &= \frac{1}{(2\pi)^{2\epsilon}}\frac{4\pi}{\Gamma(1-2\epsilon)} \ ,\end{aligned} \tag{4.126}$$

where the parameter ϵ with $d = 4-2\epsilon$ was introduced in the second line. Inserting this in the expression for the three-particle phase space and switching to the variable ϵ yields

$$\int \mathrm{dPS}_3 = \int \mathrm{d}v\mathrm{d}w \frac{\left(s+Q^2\right)^{1-\epsilon} v^{1-2\epsilon}}{(4\pi)^{4-2\epsilon}\Gamma(1-2\epsilon)} \left[w(1-w)\left(s(1-v)-Q^2v(1-w)\right)\right]^{-\epsilon} \int \mathrm{d}\Omega_{\theta_1\theta_2} \tag{4.127}$$

or in terms of the Mandelstam variables:

$$\int \mathrm{dPS}_3 = \int \mathrm{d}t\mathrm{d}u \frac{1}{(4\pi)^{4-2\epsilon}\Gamma(1-2\epsilon)} \frac{1}{s+Q^2} \left(s_{23}\right)^{-\epsilon} \left(\frac{u\left(st+Q^2s_{23}\right)}{\left(s+Q^2\right)^2}\right)^{-\epsilon} \int \mathrm{d}\Omega_{\theta_1\theta_2} \ . \tag{4.128}$$

4.8 Angular Integration

This section addresses the angular integrals arising in the real-emission diagrams, i. e., in the process

$$\gamma^*(q) + i(p) \to j(k_1) + j'(k_2) + j''(k_3) \ , \tag{4.129}$$

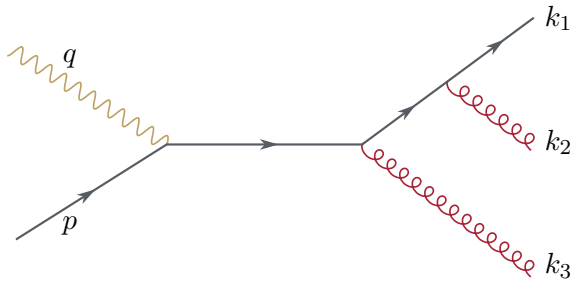

Figure 4.7: Example for a real-emission Feynman diagram, with an incident photon with momentum q, an incident quark with momentum p, a fragmenting quark with momentum k_1, and two spectator gluons with momenta k_2 and k_3.

where γ^* denotes the virtual photon, i is the incident parton, and j, j', j'' are outgoing partons. Among the final-state particles, the parton j is considered the fragmenting parton, and its remnants after hadronization are ultimately observed. The corresponding momenta are indicated in parentheses. An example of such a process is illustrated in Figure 4.7.

A common method for evaluating phase space integrals in this setting was established in 1986 [243, 244]. Although this technique is effective and widely adopted, it requires nontrivial partial fractioning of the integrand to cast it into a suitable form for integration. More recently, a modern and streamlined method for calculating angular integrals was introduced in [241], offering a conceptually cleaner approach with fewer algebraic complications. The results obtained using both methods are identical. The new method will be adopted here, following its applications to the Drell-Yan process as presented in [241], with modifications where necessary.

To begin, a convenient reference frame is chosen: the center-of-momentum frame of p, q and k_1, or equivalently the center-of-momentum frame of k_2 and k_3. This is the same frame used in the derivation of the three-particle phase space in Section 4.7.2. In this frame, the spatial components of the momenta satisfy

$$\vec{p} + \vec{q} - \vec{k_1} = 0 \ . \tag{4.130}$$

The coordinate system is rotated in such a way that these three vectors lie in the (x_{d-1}, x_d)-plane and p points along the x_d-axis. Using the Mandelstam variables introduced in Section

3.5.2, the momenta are parametrized as follows

$$\begin{aligned} p &= \frac{s_{23}-t}{2\sqrt{s_{23}}}\,(1,\mathbf{0}_{d-3},0,1) \\ k_1 &= \frac{s-s_{23}}{2\sqrt{s_{23}}}\,(1,\mathbf{0}_{d-3},\sin\vartheta,\cos\vartheta) \\ q &= \frac{s+t}{2\sqrt{s_{23}}}\left(1,\mathbf{0}_{d-3},\frac{s-s_{23}}{s+t}\sin\vartheta,\frac{t-s_{23}}{s+t}+\frac{s-s_{23}}{s+t}\cos\vartheta\right) \\ k_2 &= \frac{\sqrt{s_{23}}}{2}\,(1,\boldsymbol{k_2}_{d-3},\sin\theta_1\cos\theta_2,\cos\theta_1) \\ k_3 &= \frac{\sqrt{s_{23}}}{2}\,(1,\boldsymbol{k_3}_{d-3},-\sin\theta_1\cos\theta_2,-\cos\theta_1)\ , \end{aligned} \tag{4.131}$$

where $\mathbf{0}_{d-3}$ denotes $d-3$ vanishing components and $\boldsymbol{k_2}_{d-3}, \boldsymbol{k_3}_{d-3}$ are first $d-3$ components of the spatial part of k_2, k_3 respectively. These components are irrelevant because all other momenta are contained within the (x_{d-1}, x_d)-plane, and only scalar products of the momenta appear.
The coefficients of the energy components are calculated in the same way as in Section 4.7.1. They can be derived from

$$\begin{aligned} t = (q-k_1)^2 = (k_2+k_3-p)^2 &= s_{23} - 2p^0\sqrt{s_{23}} \\ s = (q+p)^2 = (k_1+k_2+k_3)^2 &= s_{23} + 2k_1^0\sqrt{s_{23}} \\ u = (p-k_1)^2 = (k_2+k_3-q)^2 &= s_{23} - 2q^0\sqrt{s_{23}} - Q^2 \\ &= s+t+u-2q^0\sqrt{s_{23}}\ . \end{aligned} \tag{4.132}$$

The angle ϑ is determined from

$$\begin{aligned} u = (p-k_1)^2 = -2p\cdot k_1 &= -\frac{(s_{23}-t)(s-s_{23})}{2s_{23}}(1-\cos\vartheta) \\ \Rightarrow \cos\vartheta &= 1 - \frac{2s_{23}u}{(s_{23}-t)(s_{23}-s)}\ . \end{aligned} \tag{4.133}$$

To simplify the propagators in the integrand, the normalized momenta are introduced

$$\begin{aligned} v_p &= \frac{p}{p^0} = (1,\vec{v}_p) \qquad & v_{k_1} &= \frac{k_1}{k_1^0} = (1,\vec{v}_{k_1}) \qquad & v_{k_2} &= \frac{k_2}{k_2^0} = (1,\vec{v}_{k_2}) \\ v_q &= \frac{q}{q^0} = (1,\vec{v}_q) \qquad & v_{\bar{q}} &= (1,\vec{v}_{\bar{q}})\ , \end{aligned} \tag{4.134}$$

where

$$\vec{v}_{\bar{q}} = \frac{s+t}{s+t+2Q^2}\vec{v}_q\ . \tag{4.135}$$

To further simplify the expression the shorthand notation

$$\Delta_{\vec{k}_2}(\vec{v}) = \frac{1}{1 - \vec{v}_{k_2} \cdot \vec{v}} \tag{4.136}$$

is introduced.
Since only the variables k_2 and k_3 depend on the angles θ_1 and θ_2, the rest of the momenta can be treated as constants in the angular integration. In general, an angular dependent propagator appearing in the integrand can have the following form

$$\frac{1}{(c \pm k_{2,3})^2} \ , \tag{4.137}$$

where c is one of the constant momenta p, q or k_1. These are precisely the angular-dependent Mandelstam variables introduced in (3.91). They can be written using the Δ-function notation as follows:

$$\begin{aligned}
\frac{1}{u_{2,3}} &= \frac{1}{(p - k_{2,3})^2} = \frac{-1}{2p \cdot k_{2,3}} = \frac{-2}{s_{23} - t} \frac{1}{1 \mp \vec{v}_{k_2} \cdot \vec{v}_p} = \frac{-2}{s_{23} - t} \Delta_{\vec{k}_2}(\pm \vec{v}_p) \\
\frac{1}{s_{12,13}} &= \frac{1}{(k_1 + k_{2,3})^2} = \frac{1}{2k_1 \cdot k_{2,3}} = \frac{2}{s - s_{23}} \frac{1}{1 \mp \vec{v}_{k_2} \cdot \vec{k}_1} = \frac{2}{s - s_{23}} \Delta_{\vec{k}_2}(\pm \vec{v}_{k_1}) \\
\frac{1}{t_{2,3}} &= \frac{1}{(q - k_{2,3})^2} = \frac{1}{-2q \cdot k_{2,3} - Q^2} = \frac{1}{-\frac{s+t}{2}(1 \mp \vec{v}_{k_2} \cdot \vec{v}_q) - Q^2} \\
&= \frac{1}{-\frac{s+t+2Q^2}{2} \pm \frac{s+t}{2}(\vec{v}_{k_2} \cdot \vec{v}_q)} = \frac{1}{-\frac{s+t+2Q^2}{2}(1 \mp \vec{v}_{k_2} \cdot \vec{v}_{\bar{q}})} = \frac{-2}{s + t + 2Q^2} \Delta_{\vec{k}_2}(\pm \vec{v}_{\bar{q}}) \ .
\end{aligned} \tag{4.138}$$

The most general angular-dependent denominator arising in real-emission corrections is a product of such propagators. It can be written as

$$\begin{aligned}
\frac{1}{s_{13}^{n_1} s_{23}^{n_2} t_2^{n_3} t_3^{n_4} u_2^{n_5} u_3^{n_6}} = &\left(\frac{2}{s - s_{23}}\right)^{n_1+n_2} \left(\frac{-2}{s + t + 2Q^2}\right)^{n_3+n_4} \left(\frac{-2}{s_{23} - t}\right)^{n_5+n_6} \\
&\times \Delta_{\vec{k}_2}^{n_1}(\vec{v}_{k_1}) \Delta_{\vec{k}_2}^{n_2}(-\vec{v}_{k_1}) \Delta_{\vec{k}_2}^{n_3}(\vec{v}_{\bar{q}}) \Delta_{\vec{k}_2}^{n_4}(-\vec{v}_{\bar{q}}) \Delta_{\vec{k}_2}^{n_5}(\vec{v}_p) \Delta_{\vec{k}_2}^{n_6}(-\vec{v}_p) \ .
\end{aligned} \tag{4.139}$$

These vectors are depicted in Figure 4.8 in the $x_0 = 1$ hyperplane.
To apply the angular integrations provided in [241], it is necessary to decompose the general denominator in Equation (4.139) into a sum of simpler terms, each containing at most two linearly independent vectors. This is done following the general procedure given in [241] by first applying two-point partial fractioning for the pairs of linear dependent vectors in the general denominator and then three-point partial fractioning for the remain-

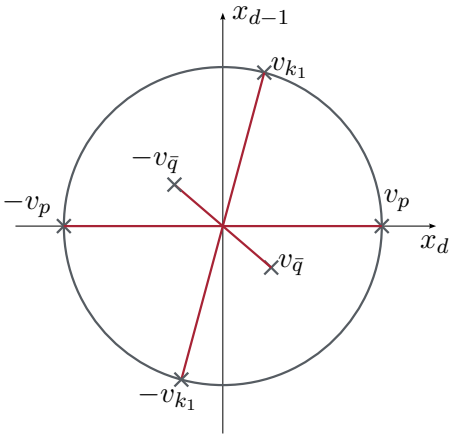

Figure 4.8: Normalized vectors in the $x_0 = 1$ hyperplane. The gray circle has radius one and the red lines connect pairs of linearly dependent vectors.

ing three vectors. Details on these fractioning procedures are provided in the next two sections, which are based on [241].

4.8.1 Two Point Partial Fractioning

The purpose of the two-point partial fractioning is to express the product of two propagators, where the vectors defining those propagators are linearly dependent, as a linear combination of individual propagators:

$$\Delta_{\vec{k}_2}(\vec{v}_1)\Delta_{\vec{k}_2}(\vec{v}_2) = \alpha\ \Delta_{\vec{k}_2}(\vec{v}_1) + \beta\ \Delta_{\vec{k}_2}(\vec{v}_2)\ , \tag{4.140}$$

where v_1 and v_2 are linearly dependent. The goal is to determine the coefficients α and β. To streamline the notation, a shorthand for the product of propagators is introduced as

$$\Delta_{\vec{k}_2}(\vec{v}_1, ..., \vec{v}_n) = \Delta_{\vec{k}_2}(\vec{v}_1)...\Delta_{\vec{k}_2}(\vec{v}_n)\ . \tag{4.141}$$

In anticipation of the more general three-point partial fractioning (discussed in the next subsection), a more versatile version of the two-point splitting is introduced here, even if it will only be fully needed for the three-point partial fractioning. Rather than directly reducing the expression to a sum of individual propagators, the product of two arbitrary propagators is expressed as a linear combination involving a third auxiliary propagator

$$\Delta_{\vec{k}_2}(\vec{v}_1, \vec{v}_2) = \lambda\ \Delta_{\vec{k}_2}(\vec{v}_1, \vec{v}_3) + \mu\ \Delta_{\vec{k}_2}(\vec{v}_2, \vec{v}_3)\ , \tag{4.142}$$

where λ and μ are real parameters, and $\vec{v}_3$ is a third vector defining a propagator. Some conditions to fix the parameters and the third vector need to be found. The right hand side of Equation (4.142) can be rewritten as

$$\begin{aligned}\lambda\ \Delta_{\vec{k}_2}(\vec{v}_1,\vec{v}_3)+\mu\ \Delta_{\vec{k}_2}(\vec{v}_2,\vec{v}_3) &= \left(\lambda\ \Delta^{-1}_{\vec{k}_2}(\vec{v}_2)+\mu\ \Delta^{-1}_{\vec{k}_2}(\vec{v}_1)\right)\Delta_{\vec{k}_2}(\vec{v}_1,\vec{v}_2,\vec{v}_3)\\ &= \left(\lambda\ \Delta^{-1}_{\vec{k}_2}(\vec{v}_2)+\mu\ \Delta^{-1}_{\vec{k}_2}(\vec{v}_1)\right)\Delta_{\vec{k}_2}(\vec{v}_3)\Delta_{\vec{k}_2}(\vec{v}_1,\vec{v}_2)\ .\end{aligned} \tag{4.143}$$

Plugging this in to Equation (4.142) gives the condition

$$\left(\lambda\ \Delta^{-1}_{\vec{k}_2}(\vec{v}_2)+\mu\ \Delta^{-1}_{\vec{k}_2}(\vec{v}_1)\right)\Delta_{\vec{k}_2}(\vec{v}_3)=1\ , \tag{4.144}$$

resulting in two equations for the two parameters λ,μ and the additional vector $\vec{v}_3$:

$$\begin{aligned}\lambda+\mu&=1\\ \mu\vec{v}_1+\lambda\vec{v}_2&=\vec{v}_3\ .\end{aligned} \tag{4.145}$$

Solving this system of equations while choosing λ as the free parameter yields the two-point splitting lemma:

$$\Delta_{\vec{k}_2}(\vec{v}_1,\vec{v}_2)=\lambda\ \Delta_{\vec{k}_2}(\vec{v}_1,\vec{v}_3)+(1-\lambda)\ \Delta_{\vec{k}_2}(\vec{v}_2,\vec{v}_3)\ , \tag{4.146}$$

where $\vec{v}_3=(1-\lambda)\vec{v}_1+\lambda\vec{v}_2$. Thus, the vector $\vec{v}_3$ lies on the line connecting $\vec{v}_1$ and $\vec{v}_2$, and the choice of λ determines its position along that line. Notably, λ is not restricted to the interval $[0,1]$; the vector $\vec{v}_3$ can also be outside the line segment between $\vec{v}_1$ and $\vec{v}_2$. A graphical representation of the situation is shown in Figure 4.9a.
The case of linearly dependent vectors $\vec{v}_1$ and $\vec{v}_2$ arises as a special case of the two-point splitting lemma (4.146). If the vectors $\vec{v}_1$ and $\vec{v}_2$ are linearly dependent, then the origin lies on the straight line connecting the two vectors. That is, there exists a λ such that

$$0=(1-\lambda)\vec{v}_1+\lambda\vec{v}_2\ , \tag{4.147}$$

which implies that the auxiliary vector $\vec{v}_3$ can be simply chosen as the origin. Since for this special vector $\Delta_{\vec{k}_2}(0)=1$, the two-point splitting lemma results in the desired reduction in the number of propagators, the two-point partial fractioning

$$\Delta_{\vec{k}_2}(\vec{v}_1,\vec{v}_2)=\lambda\ \Delta_{\vec{k}_2}(\vec{v}_1)+(1-\lambda)\ \Delta_{\vec{k}_2}(\vec{v}_2)\ , \tag{4.148}$$

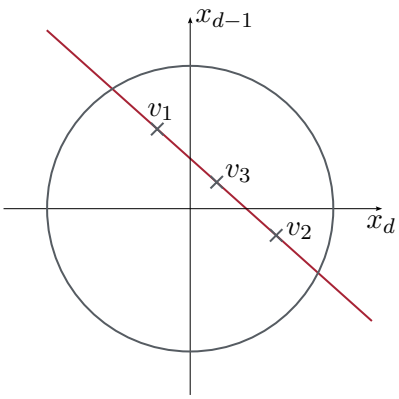

(a) Two-point splitting.

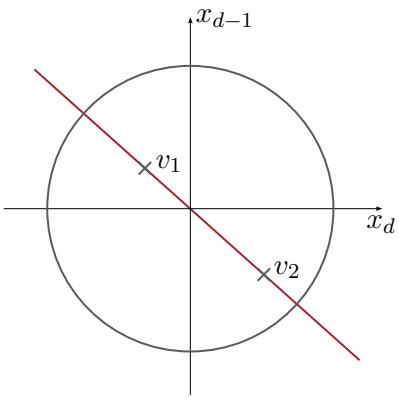

(b) Two-point partial fractioning.

Figure 4.9: For the two-point splitting (a) the vectors v_1 and v_2 are not necessarily linearly dependent. The vector v_3 can be chosen anywhere on the connecting red line. For two-point partial fractioning (b) the vectors v_1 and v_2 are linearly dependent and the origin lies on the connecting red line.

where the vectors $\vec{v}_1$ and $\vec{v}_2$ are linearly dependent and λ is such that $(1-\lambda)\vec{v}_1 + \lambda\vec{v}_2 = 0$. This situation is illustrated in Figure 4.9b.
The special case needed in the first step of the partial fractioning of the general propagator (4.139) is $\vec{v}_2 = -\vec{v}_1$. In this case $\lambda = 1/2$ and the formula simplifies further to

$$\Delta_{\vec{k}_2}(\vec{v}_1, -\vec{v}_1) = \frac{1}{2}\left(\Delta_{\vec{k}_2}(\vec{v}_1) + \Delta_{\vec{k}_2}(-\vec{v}_1)\right) \ . \tag{4.149}$$

4.8.2 Three Point Partial Fractioning

Having established a procedure to reduce the product of two propagators of linearly dependent vectors to one, it is time to turn to the product of three propagators with linearly dependent vectors. For the decomposition of the product of three propagators, the two-point splitting lemma (4.146) from the last section will be used. The three-point partial fractioning aims to reduce the number of propagators in a product from three to two. To set the stage, start with three pairwise linearly independent vectors $\vec{v}_1, \vec{v}_2$ and $\vec{v}_3$. These three vectors span a plane

$$\lambda_1\vec{v}_1 + \lambda_2\vec{v}_2 + \lambda_3\vec{v}_3 = 0 \ , \tag{4.150}$$

where $\lambda_1 + \lambda_2 + \lambda_3 \neq 0$. Then the objective is to find a reduction formula of the form

$$\Delta_{\vec{k}_2}(\vec{v}_1, \vec{v}_2, \vec{v}_3) = \alpha_1 \ \Delta_{\vec{k}_2}(\vec{v}_1, \vec{v}_2) + \alpha_2 \ \Delta_{\vec{k}_2}(\vec{v}_1, \vec{v}_3) + \alpha_3 \ \Delta_{\vec{k}_2}(\vec{v}_2, \vec{v}_3) \ , \tag{4.151}$$

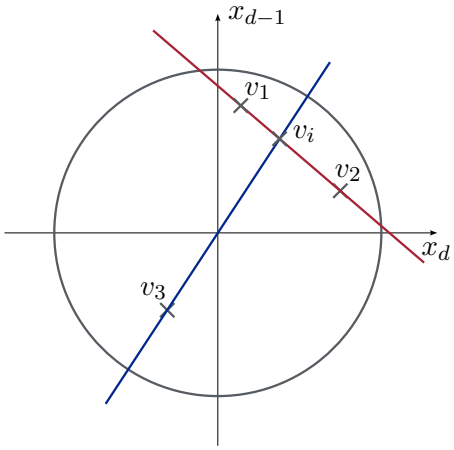

Figure 4.10: Vectors for the three-point partial fractioning. The red line connects v_1 and v_2, while the blue line connects v_3 and the origin. The auxiliary vector v_i lies on the intersection of these two lines.

where the parameters α_1, α_2 and α_3 need to be determined.
The derivation proceeds in three steps:

First the two-point splitting lemma is applied to rewrite the product

$$\Delta_{\vec{k}_2}(\vec{v}_1, \vec{v}_2) = \lambda\ \Delta_{\vec{k}_2}(\vec{v}_1, \vec{v}_i) + (1-\lambda)\ \Delta_{\vec{k}_2}(\vec{v}_2, \vec{v}_i)\ , \tag{4.152}$$

where $\vec{v}_i$ lies on the intersection of the lines connecting $\vec{v}_1$ and $\vec{v}_2$, and $\vec{v}_3$ and the origin. This constraint fixes λ and

$$\vec{v}_i = (1-\lambda)\vec{v}_1 + \lambda\vec{v}_2\ , \tag{4.153}$$

see Figure 4.10. To achieve such a configuration, it might be necessary to change the order of the three vectors $\vec{v}_1, \vec{v}_2$ and $\vec{v}_3$. By reintroducing the third propagator the product becomes

$$\Delta_{\vec{k}_2}(\vec{v}_1, \vec{v}_2, \vec{v}_3) = \lambda\ \Delta_{\vec{k}_2}(\vec{v}_1, \vec{v}_i, \vec{v}_3) + (1-\lambda)\ \Delta_{\vec{k}_2}(\vec{v}_2, \vec{v}_i, \vec{v}_3)\ . \tag{4.154}$$

The second step is to use the two-point partial fractioning on the linearly dependent vectors $\vec{v}_i$ and $\vec{v}_3$. Since they are linearly dependent there exists a μ such that

$$\vec{v}_i = \mu\vec{v}_3\ , \tag{4.155}$$

so the two-point partial fractioning becomes

$$\Delta_{\vec{k}_2}(\vec{v}_i,\vec{v}_3) = \frac{1}{1-\mu}\,\Delta_{\vec{k}_2}(\vec{v}_3) - \frac{\mu}{1-\mu}\,\Delta_{\vec{k}_2}(\vec{v}_i)\ . \tag{4.156}$$

Plugging this reduction in to Equation (4.154) gives

$$\begin{aligned}\Delta_{\vec{k}_2}(\vec{v}_1,\vec{v}_2,\vec{v}_3) = \frac{1-\lambda}{1-\mu}\,\Delta_{\vec{k}_2}(\vec{v}_1,\vec{v}_3) - \frac{(1-\lambda)\mu}{1-\mu}\,\Delta_{\vec{k}_2}(\vec{v}_1,\vec{v}_i)\\ + \frac{\lambda}{1-\mu}\,\Delta_{\vec{k}_2}(\vec{v}_2,\vec{v}_3) - \frac{\lambda\mu}{1-\mu}\,\Delta_{\vec{k}_2}(\vec{v}_2,\vec{v}_i)\ .\end{aligned} \tag{4.157}$$

The last step is to eliminate the auxiliary vector $\vec{v}_i$. To do this, the two terms containing the auxiliary vector $\vec{v}_i$ are combined into one with the help of the inverse two-point splitting lemma. This finally results in

$$\Delta_{\vec{k}_2}(\vec{v}_1,\vec{v}_2,\vec{v}_3) = -\frac{\mu}{1-\mu}\,\Delta_{\vec{k}_2}(\vec{v}_1,\vec{v}_2) + \frac{1-\lambda}{1-\mu}\,\Delta_{\vec{k}_2}(\vec{v}_1,\vec{v}_3) + \frac{\lambda}{1-\mu}\,\Delta_{\vec{k}_2}(\vec{v}_2,\vec{v}_3)\ . \tag{4.158}$$

To fix the parameters μ and λ the two equations (4.153) and (4.155) are used to get

$$\mu\vec{v}_3 = (1-\lambda)\vec{v}_1 + \lambda\vec{v}_2 \tag{4.159}$$

and (4.150) to get

$$\lambda = \frac{\lambda_1}{\lambda_1+\lambda_2} \qquad \mu = -\frac{\lambda_3}{\lambda_1+\lambda_2}\ . \tag{4.160}$$

Inserting these parameters into (4.158) gives the three-point partial fractioning formula:

$$\Delta_{\vec{k}_2}(\vec{v}_1,\vec{v}_2,\vec{v}_3) = \frac{1}{\lambda_1+\lambda_2+\lambda_3}\Big(\lambda_3\,\Delta_{\vec{k}_2}(\vec{v}_1,\vec{v}_2) + \lambda_2\,\Delta_{\vec{k}_2}(\vec{v}_1,\vec{v}_3) + \lambda_1\,\Delta_{\vec{k}_2}(\vec{v}_2,\vec{v}_3)\Big)\ , \tag{4.161}$$

with the parameters λ_1, λ_2 and λ_3 given by $\lambda_1\vec{v}_1+\lambda_2\vec{v}_2+\lambda_3\vec{v}_3 = 0$, where $\lambda_1+\lambda_2+\lambda_3 \neq 0$.

4.8.3 Back to the Angular Integrals

By applying the two- and three-point partial fractioning techniques, the general angular denominator in (4.139) can be decomposed into a sum of terms, where each term contains

only two linearly independent vectors. This decomposition simplifies the angular integrals to a small set of standard integrals. The resulting integrals take the following form:

$$I^{(0)}_{j,l}(u^{\pm}_{pk_1};\epsilon) = \int \mathrm{d}\Omega_{\theta_1\theta_2}\Delta^{j}_{\vec{k}_2}(\vec{v}_p)\Delta^{l}_{\vec{k}_2}(\mp\vec{v}_{k_1}) = \int \mathrm{d}\Omega_{\theta_1\theta_2}\Delta^{j}_{\vec{k}_2}(-\vec{v}_p)\Delta^{l}_{\vec{k}_2}(\pm\vec{v}_{k_1}) \tag{4.162}$$

$$I^{(1)}_{j,l}(u^{\pm}_{i\bar{q}}, v_{\bar{q}q};\epsilon) = \int \mathrm{d}\Omega_{\theta_1\theta_2}\Delta^{j}_{\vec{k}_2}(\vec{v}_{\bar{q}})\Delta^{l}_{\vec{k}_2}(\mp\vec{v}_{i}) = \int \mathrm{d}\Omega_{\theta_1\theta_2}\Delta^{j}_{\vec{k}_2}(-\vec{v}_{\bar{q}})\Delta^{l}_{\vec{k}_2}(\pm\vec{v}_{i}) \ , \tag{4.163}$$

where $i = p, k_1$,

$$u^{\pm}_{ab} = 1 \pm (1 - v_{ab}) \qquad \text{and} \qquad v_{ab} = v_a v_b = 1 - \vec{v}_a \cdot \vec{v}_b \ , \tag{4.164}$$

for $a, b = p, k_1, \bar{q}$. These variables can be explicitly expressed in Mandelstam variables as

$$\begin{aligned}
v_{pk_1} &= 1 - \cos\vartheta = \frac{2s_{23}u}{(s_{23}-t)(s_{23}-s)} \\
v_{\bar{q}\bar{q}} &= 1 - \left(\frac{s+t}{s+t+2Q^2}\right)^2 (\vec{v}_q \cdot \vec{v}_q) = \frac{-4Q^2u}{(Q^2+s_{23}-u)^2} \\
v_{p\bar{q}} &= 1 - \frac{s+t}{s+t+2Q^2}(\vec{v}_p \cdot \vec{v}_q) = 2 + \frac{2tu}{(t-s_{23})(Q^2+s_{23}-u)} \\
v_{k_1\bar{q}} &= 1 - \frac{s+t}{s+t+2Q^2}(\vec{v}_{k_1} \cdot \vec{v}_q) = 2 + \frac{2su}{(s-s_{23})(Q^2+s_{23}-u)} \ .
\end{aligned} \tag{4.165}$$

These results have been verified against the definitions and identities presented in Appendix D.6 of [241] by applying the crossing relation $s \to u, Q^2 \to -Q^2, s_2 \to s_{23}, u \to t, t \to s$.

The naming convention of the integrals $I^{(0)}_{j,l}(u^{\pm}_{pk_1};\epsilon)$ and $I^{(1)}_{j,l}(u^{\pm}_{i\bar{q}}, v_{\bar{q}q};\epsilon)$ follow the notation introduced in [241]. The explicit analytical results for these integrals can be found in Appendix G of the same reference.

4.9 The Hard Part of the Cross Section

At this stage, the computation of the scattering cross section at next-to-leading order becomes possible. This includes both virtual and real corrections, each of which presents its own set of technical challenges. However, a common feature is the appearance of divergences.

One kind being UV-divergences, which are systematically removed through renormalization (see Section 2.5.3). In this thesis, the $\overline{\text{MS}}$ renormalization scheme is employed for this purpose.

In addition to UV-divergences, next-to-leading order corrections also exhibit IR-divergences,

including both soft and collinear types. According to the Kinoshita-Lee-Nauenberg theorem [122, 123], soft divergences cancel when one considers a sufficiently inclusive sum over real and virtual corrections. Nevertheless, collinear divergences remain and must be addressed explicitly.
Collinear divergences arise from special configurations in a $2 \to 3$ scattering, where one of the unobserved massless particles is emitted collinearly to an external particle. This section presents explicit formulas for the calculation of these collinear divergences and shows how to subtract them in the specific case of semi-inclusive deep inelastic scattering.

First, the goal is to derive an explicit formula for the subtraction of collinear divergences in SIDIS. This is achieved by factorizing the collinear divergences into bare parton distributions or fragmentation functions. To do this, the general principle for subtracting the collinear divergences from the full partonic cross section, described in Section 2.6.2, is followed. By these general considerations, it is possible to perform the calculation of the scattering at the level of free, massless partons in initial and final states. This simplification of the calculation only involves the parton-in-parton splitting functions, which can be calculated in perturbation theory.
To calculate the hard part of the scattering, the convolution with the splitting functions needs to be taken. For the partonic tensor the factorization theorem at parton level reads

$$\tilde{W}_{ab}^{\mu\nu}(p,q,k_1) = \int_0^1 \frac{\mathrm{d}\xi}{\xi} \int_0^1 \frac{\mathrm{d}\zeta}{\zeta^2} f_{i/a}(\xi) \hat{W}_{ij}^{\mu\nu}(\xi p, q, k_1/\zeta) d_{b/j}(\zeta) \ , \tag{4.166}$$

where $\tilde{W}_{ab}^{\mu\nu}$ is the partonic tensor calculated from the Feynman diagrams, including collinear divergences, and $\hat{W}_{ij}^{\mu\nu}$ is the hard part of the partonic tensor, free of collinear divergences and the goal of the calculation (see Equations (2.128) and (3.65) for reference). The parton-in-parton distribution and fragmentation functions are defined in Equations (2.130) to (2.135). Expanding the partonic tensors, the distribution functions and the fragmentation functions in orders of α_s up to next-to-leading order results in [31]

$$\begin{aligned} &\tilde{W}_{ab}^{(\mathrm{LO})\mu\nu}(p,q,k_1) + \tilde{W}_{ab}^{(\mathrm{NLO})\mu\nu}(p,q,k_1) \\ &\qquad = \int_0^1 \frac{\mathrm{d}\xi}{\xi} \int_0^1 \frac{\mathrm{d}\zeta}{\zeta^2} \left(f_{i/a}^{(0)}(\xi) + f_{i/a}^{(1)}(\xi) \right) \\ &\qquad\qquad \times \left(\hat{W}_{ij}^{(\mathrm{LO})\mu\nu}(\xi p, q, k_1/\zeta) + \hat{W}_{ij}^{(\mathrm{NLO})\mu\nu}(\xi p, q, k_1/\zeta) \right) \\ &\qquad\qquad \times \left(d_{b/j}^{(0)}(\zeta) + d_{b/j}^{(1)}(\zeta) \right) \ . \end{aligned} \tag{4.167}$$

By comparing coefficients, the only contributions to the leading order come from the trivial

parts of the distribution and fragmentation functions:

$$\tilde{W}_{ab}^{(\mathrm{LO})\mu\nu}(p,q,k_1) = \int_0^1 \frac{\mathrm{d}\xi}{\xi} \int_0^1 \frac{\mathrm{d}\zeta}{\zeta^2} f_{i/a}^{(0)}(\xi) \hat{W}_{ij}^{(\mathrm{LO})\mu\nu}(\xi p, q, k_1/\zeta) d_{b/j}^{(0)}(\zeta) \ , \tag{4.168}$$

and by inserting the trivial part of the parton-in-parton functions

$$f_{i/a}^{(0)}(\xi) = \delta_{ia}\delta(1-\xi) \qquad \text{and} \qquad d_{b/j}^{(0)}(\zeta) = \delta_{bj}\delta(1-\zeta) \tag{4.169}$$

this becomes:

$$\tilde{W}_{ab}^{(\mathrm{LO})\mu\nu}(p,q,k_1) = \hat{W}_{ab}^{(\mathrm{LO})\mu\nu}(p,q,k_1) \ , \tag{4.170}$$

capturing the fact that the leading-order calculation is free of collinear divergences.
A more interesting result is reached at next-to-leading order, where $\hat{W}_{ij}^{(\mathrm{NLO})\mu\nu}$ is convoluted with the trivial parts of the parton-in-parton functions, but the leading-order part $\hat{W}_{ij}^{(\mathrm{LO})\mu\nu}$ is convoluted with the leading-order part of the parton-in-parton functions to gain the same order in α_s. This results in

$$\begin{aligned} \hat{W}_{ab}^{(\mathrm{NLO})\mu\nu}(p,q,k_1) = \tilde{W}_{ab}^{(\mathrm{NLO})\mu\nu}(p,q,k_1) \\ - \int_0^1 \frac{\mathrm{d}\xi}{\xi} \int_0^1 \frac{\mathrm{d}\zeta}{\zeta^2} f_{i/a}^{(1)}(\xi) \hat{W}_{ij}^{(\mathrm{LO})\mu\nu}(\xi p, q, k_1/\zeta) d_{b/j}^{(0)}(\zeta) \\ - \int_0^1 \frac{\mathrm{d}\xi}{\xi} \int_0^1 \frac{\mathrm{d}\zeta}{\zeta^2} f_{i/a}^{(0)}(\xi) \hat{W}_{ij}^{(\mathrm{LO})\mu\nu}(\xi p, q, k_1/\zeta) d_{b/j}^{(1)}(\zeta) \ . \end{aligned} \tag{4.171}$$

Inserting the expansion of the parton-in-parton functions (2.134) and (2.135) gives:

$$\begin{aligned} \hat{W}_{ab}^{(\mathrm{NLO})\mu\nu}(p,q,k_1) = \tilde{W}_{ab}^{(\mathrm{NLO})\mu\nu}(p,q,k_1) \\ + \frac{\alpha_s}{2\pi}\frac{S_\epsilon}{\epsilon} \int_0^1 \frac{\mathrm{d}\xi}{\xi} P_{ia}^{(0)}(\xi) \hat{W}_{ib}^{(\mathrm{LO})\mu\nu}(\xi p, q, k_1) \\ + \frac{\alpha_s}{2\pi}\frac{S_\epsilon}{\epsilon} \int_0^1 \frac{\mathrm{d}\zeta}{\zeta^2} \hat{W}_{aj}^{(\mathrm{LO})\mu\nu}(p, q, k_1/\zeta) P_{bj}^{(0)}(\zeta) \ , \end{aligned} \tag{4.172}$$

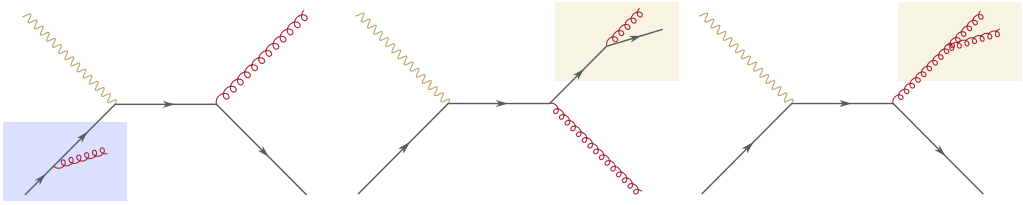

Figure 4.11: Splittings in the qg-channel. The splitting of the incident particle is marked by the blue box. The splittings of the outgoing partons are marked by the yellow boxes. The remaining parts of the diagrams are born-level diagrams.

with the one loop splitting functions of (2.125):

$$\begin{aligned}
P_{qq}^{(0)}(\xi) &= C_F \left(\frac{1+\xi^2}{(1-\xi)_+} + \frac{3}{2}\delta(1-\xi) \right) \\
P_{qg}^{(0)}(\xi) &= T_f \left(\xi^2 + (1-\xi)^2 \right) \\
P_{gq}^{(0)}(\xi) &= C_F \left(\frac{1+(1-\xi)^2}{\xi} \right) \\
P_{gg}^{(0)}(\xi) &= 2C_A \left(\frac{\xi}{(1-\xi)_+} + \frac{1-\xi}{\xi} + \xi(1-\xi) \right) \\
&\quad + \frac{11C_A - 4N_f T_f}{6} \delta(1-\xi) \ .
\end{aligned} \tag{4.173}$$

The calculation in this thesis requires a contraction with the tensors given in (3.53), to project the partonic tensor onto the angular distributions. This projection can equally be carried out before or after the subtraction. In this thesis the contraction is performed prior to the subtraction.
As an explicit example for the subtraction, one of the channels contributing to SIDIS is discussed in the following. For this the "qg"-process

$$\gamma^* q \to gX \tag{4.174}$$

is chosen here to illustrate the procedure of eliminating collinear divergences. At next-to-leading order, virtual corrections to the process $\gamma^* q \to gq$ and real corrections in the form of $\gamma^* q \to gqg$ contribute to the cross section. Both types exhibit divergences. The UV-divergences are removed by $\overline{\text{MS}}$ renormalization of the vertex and the self-energy corrections. By combining real and virtual contributions to the same channel, some divergences cancel after phase space integration. Namely, the soft divergences and divergences that are simultaneously soft and collinear, that is, ϵ^{-2} poles.

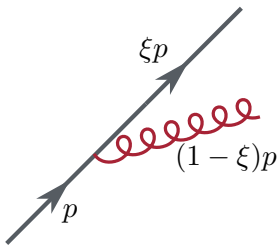

(a) Splitting of incident parton.

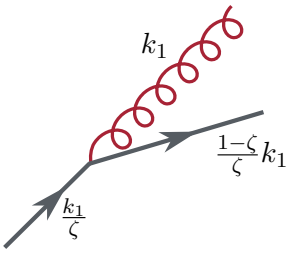

(b) Splitting of outgoing particle.

Figure 4.12: Momenta of the particles for the splittings. Quark-to-quark splitting of an incident quark on the left and a quark-to-gluon splitting of an outgoing quark on the right.

The remaining poles are collinear poles, which come from the collinear splitting of massless external particles. In the qg-process, there is one possible splitting for the incoming quark and two for the observed outgoing gluon. These are depicted in Figure 4.11. There is no splitting for the unobserved X particles, since these are already handled by the real emission diagrams and the associated phase-space integration. Additionally, although electron splitting functions exist [246], these splittings are irrelevant in this thesis, as they would lead to an additional order in α which is negligible with respect to the higher order in α_s considered here. Likewise, there is no collinear splitting from the incident virtual photon, since it originates from the interaction with the electron and is neither external nor on-shell.

As an example for the splitting, take the first splitting in Figure 4.11, marked by the blue box. The splitting functions can be viewed as follows. The incoming quark with momentum p splits off collinearly into a quark and a gluon. The resulting quark, with momentum ξp, will partake in the scattering and acts as the incident quark for the Born-level process. The gluon, with momentum $(1-\xi)p$, will no longer contribute to the scattering and will carry the remaining momentum away as one of the undetected particles.

The splitting of the outgoing particle in the yellow boxes in Figure 4.11 describes the following situation. A quark that participated in the scattering has momentum $\frac{k_1}{\zeta}$ after the scattering. It subsequently splits into a gluon with momentum k_1 that later fragments into the detected hadron and a quark with momentum $\frac{1-\zeta}{\zeta}k_1$ that carries that momentum away as part of the undetected particles contributing to X. This is illustrated in Figure 4.12. A priori, the momentum fractions ξ and ζ can take any value $0 \leq \xi \leq 1$ and $0 \leq \zeta \leq 1$, but will be limited by the kinematics of the process.

The procedure can be thought of as splitting the cross section in a collinear splitting of a particle with a subsequent scattering at one order lower. In this thesis, the scattering at one order lower is the leading-order only with changed kinematics. The fact that the

kinematics are changed by the splittings is captured by the convolution in the factorization theorem.

The leading-order expressions include a momentum-conserving delta function $\delta(s+t+u+Q^2)$, or in the case of the dimensionless variables $\delta(1-w)$. For the true Born cross section, the Mandelstam variables are $s=(q+p)^2$, $t=(q-k_1)^2$ and $u=(p-k_1)^2$, as defined above in Section 3.5.2. In the presence of a splitting, these kinematics are modified. For the new kinematics, there are two possible cases: the splitting happens on the incident particle (either a quark or a gluon), i.e., $p \to \xi p$, or the splitting happens on the outgoing detected particle, i.e., $k_1 \to k_1/\zeta$. This leads to the following new kinematic Mandelstam variables:

$$\tilde{s}_\xi = (q+\xi p)^2 = \xi s - (1-\xi)Q^2 \tag{4.175}$$

$$\tilde{t}_\zeta = (q - \frac{k_1}{\zeta})^2 = \frac{t}{\zeta} - (1-\frac{1}{\zeta})Q^2 \tag{4.176}$$

$$\tilde{u}_{\xi,\zeta} = (\xi p - \frac{k_1}{\zeta})^2 = \frac{\xi}{\zeta}u\ . \tag{4.177}$$

For the dimensionless variables this results in

$$\tilde{s}'_\xi = \xi s' \tag{4.178}$$

$$\tilde{v}_{\xi,\zeta} = 1 + \frac{\tilde{t}}{\tilde{s}+Q^2} = \frac{Q^2(1-\zeta) - s'(1-v-\xi\zeta)}{\xi\zeta s'} \tag{4.179}$$

$$\tilde{w}_{\xi,\zeta} = \frac{-\tilde{u}}{\tilde{s}+\tilde{t}+Q^2} = \frac{\xi s' v w}{Q^2(1-\zeta) - s'(1-v-\xi\zeta)}\ . \tag{4.180}$$

As required by Equation (4.172), the leading-order terms must be evaluated at the shifted momenta. The delta function, which always comes with the leading-order cross section, is evaluated for a splitting on the incident particle, i.e., $\zeta = 1$, as follows:

$$\delta\left(\tilde{s}_\xi + \tilde{t}_1 + \tilde{u}_{\xi,1} + Q^2\right) = \delta\left(\xi(s+u+Q^2)+t\right) \tag{4.181}$$

$$= \frac{1}{s+u+Q^2}\delta\left(\xi + \frac{t}{s+u+Q^2}\right)\ . \tag{4.182}$$

For a splitting on the outgoing particle, $\xi = 1$, the delta function becomes

$$\delta\left(\tilde{s}_1 + \tilde{t}_\zeta + \tilde{u}_{1,\zeta} + Q^2\right) = \delta\left(s + \frac{t+u+Q^2}{\zeta}\right) \tag{4.183}$$

$$= \frac{t+u+Q^2}{s^2}\delta\left(\zeta + \frac{t+u+Q^2}{s}\right)\ . \tag{4.184}$$

In terms of the dimensionless variables

$$\delta\left(1-\tilde{w}_{\xi,1}\right)=\delta\left(1+\frac{\xi vw}{1-v-\xi}\right)=\frac{vw(1-v)}{(1-vw)^2}\delta\left(\xi-\frac{1-v}{1-vw}\right) \tag{4.185}$$

$$\begin{aligned}\delta\left(1-\tilde{w}_{1,\zeta}\right)&=\delta\left(1-\frac{s'vw}{Q^2(1-\zeta)-s'(1-v-\zeta)}\right)\\&=\frac{s'vw}{s'-Q^2}\delta\left(\zeta-\frac{Q^2-s'\left(1-v+vw\right)}{Q^2-s'}\right)\,.\end{aligned} \tag{4.186}$$

The results of the leading-order and next-to-leading order cross sections will be expressed in terms of the dimensionless variables v and w and will be differential in v and w. However, after collinear splitting, the leading-order cross sections in the integrand will, a priori, be differential in the shifted variables $\tilde{v}$ and $\tilde{w}$. To express these contributions in terms of the original variables v and w, a Jacobian for the transformation must be applied to the terms. The Jacobian is

$$J_{\xi,\zeta}=\det\left(\frac{\partial(\tilde{v}_{\xi,\zeta},\tilde{w}_{\xi,\zeta})}{\partial(v,w)}\right)=\frac{s'v}{\zeta\left(Q^2(1-\zeta)-s'(1-v-\xi\zeta)\right)}\,. \tag{4.187}$$

This results in the factors for a splitting on an incident and outgoing leg, respectively

$$J_{\xi,1}=\frac{v}{\xi-(1-v)}\to\frac{1-vw}{w(1-v)} \tag{4.188}$$

$$J_{1,\zeta}=\frac{s'v}{\zeta\left(Q^2(1-\zeta)-s'(1-v-\zeta)\right)}\to\frac{s'-Q^2}{w\left(s'\left(1-v+vw\right)-Q^2\right)}\,, \tag{4.189}$$

where the arrow indicates, that the variable momentum fractions ξ and ζ were replaced by the constraint given by the delta functions at leading-order (4.185) and (4.186), i.e.,

$$\xi\to\frac{1-v}{1-vw}\qquad\text{and}\qquad\zeta\to\frac{Q^2-s'\left(1-v+vw\right)}{Q^2-s'}\,. \tag{4.190}$$

Additionally the splitting functions needs to be calculated at the specific values given by the leading-order delta function (4.185) and (4.186). The splitting functions contain terms of the form

$$\delta\left(1-\xi\right),\ \left(\frac{1}{1-\xi}\right)_+,\ \delta\left(1-\zeta\right)\ \text{and}\ \left(\frac{1}{1-\zeta}\right)_+\,, \tag{4.191}$$

where ξ and ζ need to be set to the values defined by the momentum-conserving delta function (4.190). To simplify the plus distribution, its origin needs to be considered and expanded in a power series in ϵ. Subsequently, the method of equating the coefficients is

applied. For the case $\xi = (1-v)/(1-vw)$, with $a = 1-\xi$, this results in [247]:

$$a^{-1-\epsilon} = -\frac{1}{\epsilon}\delta(a) + \left(\frac{1}{a}\right)_+ - \epsilon\left(\frac{\log(a)}{a}\right)_+ + \mathcal{O}\left(\epsilon^2\right) \tag{4.192}$$

and on the other hand:

$$\begin{aligned}
a^{-1-\epsilon} &= (1-\xi)^{-1-\epsilon} = \left(\frac{v(1-w)}{1-vw}\right)^{-1-\epsilon} = \left(\frac{v}{1-vw}\right)^{-1-\epsilon}(1-w)^{-1-\epsilon} \\
&= \left(\frac{1-vw}{v} + \epsilon\frac{1-vw}{v}\log\left(\frac{1-vw}{v}\right) - \epsilon^2\frac{1-vw}{2v}\log^2\left(\frac{1-vw}{v}\right) + \mathcal{O}\left(\epsilon^3\right)\right) \\
&\quad \left(-\frac{1}{\epsilon}\delta(1-w) + \left(\frac{1}{1-w}\right)_+ - \epsilon\left(\frac{\log(1-w)}{1-w}\right)_+ + \mathcal{O}\left(\epsilon^3\right)\right) \\
&= -\frac{1}{\epsilon}\frac{1-vw}{v}\delta(1-w) \\
&\quad + \frac{1-vw}{v}\left(\frac{1}{1-w}\right)_+ \frac{1-v}{v}\log\frac{v}{1-v}\delta(1-w) \\
&\quad + \epsilon\left[-\frac{1-vw}{v}\left(\frac{\log(1-w)}{1-w}\right)_+ + \frac{1-vw}{v}\log\left(\frac{v}{1-vw}\right)\left(\frac{1}{1-w}\right)_+ \right. \\
&\qquad \left. + \frac{1-v}{2v}\log^2\left(\frac{1-v}{v}\right)\delta(1-w)\right].
\end{aligned} \tag{4.193}$$

Therefore:

$$\delta(1-\xi) = \frac{1-v}{v}\delta(1-w) \tag{4.194}$$

$$\left(\frac{1}{1-\xi}\right)_+ = \frac{1-vw}{v}\left(\frac{1}{1-w}\right)_+ + \frac{v}{1-v}\log\left(\frac{1-v}{v}\right)\delta(1-w) \tag{4.195}$$

$$\begin{aligned}
\left(\frac{\log(1-\xi)}{1-\xi}\right)_+ &= \frac{1-vw}{v}\left(\frac{\log(1-w)}{1-w}\right)_+ + \frac{1-vw}{v}\log\left(\frac{v}{1-vw}\right)\left(\frac{1}{1-w}\right)_+ \\
&\quad + \frac{1-v}{2v}\log^2\left(\frac{1-v}{v}\right)\delta(1-w)\ .
\end{aligned} \tag{4.196}$$

Here, and everywhere else, log denotes the natural logarithm.

For $\zeta = Q^2 - s'\left(1 - v + vw\right)/(Q^2 - s')$ one gets:

$$\delta\left(1-\zeta\right) = \frac{s'-Q^2}{s'v}\delta\left(1-w\right) \tag{4.197}$$

$$\left(\frac{1}{1-\zeta}\right)_+ = \frac{s'-Q^2}{s'v}\left(\frac{1}{1-w}\right)_+ + \frac{s'-Q^2}{s'v}\log\left(\frac{s'v}{s'-Q^2}\right)\delta(1-w) \tag{4.198}$$

$$\begin{aligned}\left(\frac{\log\left(1-\zeta\right)}{1-\zeta}\right)_+ = {}& \frac{s'-Q^2}{s'v}\left(\frac{\log\left(1-w\right)}{1-w}\right)_+ + \frac{s'-Q^2}{s'v}\log\left(\frac{s'v}{s'-Q^2}\right)\left(\frac{1}{1-w}\right)_+ \\ & + \frac{s'-Q^2}{2s'v}\log^2\left(\frac{s'v}{s'-Q^2}\right)\delta\left(1-w\right)\ .\end{aligned} \tag{4.199}$$

This completes the ingredients necessary to continue with the example of the qg process. This process was already used in [248] for the factorization of mass singularities in prompt photon production. The results in [248] can be reproduced by the results in this thesis via crossing and taken the limit $Q^2 \to 0$. The leading-order cross sections differential in v and w for the two relevant processes are called

$$\frac{\mathrm{d}\hat{\sigma}^{\mathrm{LO}}_{\gamma^* q\to gq}}{\mathrm{d}v\mathrm{d}w} \qquad \text{and} \qquad \frac{\mathrm{d}\hat{\sigma}^{\mathrm{LO}}_{\gamma^* q\to qg}}{\mathrm{d}v\mathrm{d}w}\ . \tag{4.200}$$

The next-to-leading order cross section, still containing the collinear divergences is

$$\frac{\mathrm{d}\tilde{\sigma}^{\mathrm{NLO}}_{\gamma^* q\to gX}}{\mathrm{d}v\mathrm{d}w}\ . \tag{4.201}$$

To eliminate all collinear divergences, all possible splittings need to be subtracted. In diagrammatic form they are given in Figure 4.11. The formula for the subtraction is

$$\begin{aligned}\frac{\mathrm{d}\hat{\sigma}^{\mathrm{NLO}}_{\gamma^* q\to gX}}{\mathrm{d}v\mathrm{d}w}(s',v,w) = {}& \frac{\mathrm{d}\tilde{\sigma}^{\mathrm{NLO}}_{\gamma^* q\to gX}}{\mathrm{d}v\mathrm{d}w}(s',v,w) \\ & + \frac{\alpha_s}{2\pi}\frac{S_\epsilon}{\epsilon}\int_0^1 \mathrm{d}\xi J_\xi P^{(0)}_{qq}(\xi)\frac{\mathrm{d}\hat{\sigma}^{\mathrm{LO}}_{\gamma^* q\to gq}}{\mathrm{d}\tilde{v}\mathrm{d}\tilde{w}}(\tilde{s}'_\xi,\tilde{v}_{\xi,1},\tilde{w}_{\xi,1})\delta(1-\tilde{w}_{\xi,1}) \\ & + \frac{\alpha_s}{2\pi}\frac{S_\epsilon}{\epsilon}\int_0^1 \mathrm{d}\zeta J_\zeta P^{(0)}_{gq}(\zeta)\frac{\mathrm{d}\hat{\sigma}^{\mathrm{LO}}_{\gamma^* q\to qg}}{\mathrm{d}\tilde{v}\mathrm{d}\tilde{w}}(\tilde{s}'_1,\tilde{v}_{1,\zeta},\tilde{w}_{1,\zeta})\delta(1-\tilde{w}_{1,\zeta}) \\ & + \frac{\alpha_s}{2\pi}\frac{S_\epsilon}{\epsilon}\int_0^1 \mathrm{d}\zeta J_\zeta P^{(0)}_{gg}(\zeta)\frac{\mathrm{d}\hat{\sigma}^{\mathrm{LO}}_{\gamma^* q\to gq}}{\mathrm{d}\tilde{v}\mathrm{d}\tilde{w}}(\tilde{s}'_1,\tilde{v}_{1,\zeta},\tilde{w}_{1,\zeta})\delta(1-\tilde{w}_{1,\zeta})\ .\end{aligned} \tag{4.202}$$

The leading-order terms contain, of course, the leading-order phase space and the Møller flux factor. Only the delta function $\delta(1-w)$ of the leading-order terms is written explicitly. Furthermore, one might expect the factors $1/\xi$ and $1/\zeta^2$ to appear here, but they stem from the change of variables in the partonic tensor (see discussion after (3.62)). These

factors are effectively handled here by the Jacobians. The delta functions $\delta(1-\tilde{w}_{\xi,1})$ and $\delta(1-\tilde{w}_{1,\zeta})$ fix the integration variables ξ and ζ respectively, as can be seen in (4.185) and (4.186). To evaluate the splitting functions at fixed values of ξ and ζ, relations (4.194) to (4.199) are used. The resulting cross section $\frac{\mathrm{d}\hat{\sigma}^{\mathrm{NLO}}_{\gamma^* q\to gX}}{\mathrm{d}v\mathrm{d}w}$ is free of divergences, and the physical limit $\epsilon \to 0$ can safely be taken. The resulting hard part can now be convoluted with the appropriate parton distribution and fragmentation functions for the external particles to get results for the hadronic process, as explained in Section 2.6.

This concludes the technical introduction of the methods needed for the next-to-leading order calculation. The next chapter provides an overview of the explicit calculations performed in this thesis.

Chapter 5

The Born Cross Section

This chapter presents the perturbative calculation for SIDIS at high transverse momentum with an explicit dependency on the angular structure at leading order.
Starting with the factorization theorem (3.62), which expresses the hadronic differential cross section in terms of partonic subprocesses:

$$4l'^0 P_h^0 \frac{\mathrm{d}\sigma_{\ell\mathcal{P}\to\ell h X}}{\mathrm{d}^3\vec{l}'\mathrm{d}^3\vec{P}_h} = \int_{\xi_{\min}}^1 \frac{\mathrm{d}\xi}{\xi} \int_{\zeta_{\min}}^1 \frac{\mathrm{d}\zeta}{\zeta^2} f_{i/\mathcal{P}}(\xi) 4l'^0 k_1^0 \frac{\mathrm{d}\hat{\sigma}_{\ell i\to\ell j X}}{\mathrm{d}^3\vec{l}'\mathrm{d}^3\vec{k}_1} d_{h/j}(\zeta) \ . \tag{5.1}$$

The partonic cross sections are further factorized into a leptonic and a hadronic tensor, as (3.63):

$$4l'^0 k_1^0 \frac{\mathrm{d}\hat{\sigma}_{\ell i\to\ell j X}}{\mathrm{d}^3\vec{l}'\mathrm{d}^3\vec{k}_1} = \frac{2\alpha^2}{\hat{s}Q^4} L_{\mu\nu}\hat{W}_{ij}^{\mu\nu} \ . \tag{5.2}$$

The product of the leptonic and partonic hadronic tensor is decomposed into parts with different angular structures, to get the partonic analog of (3.58)

$$L_{\mu\nu}\hat{W}^{\mu\nu} = \sum_{k=1}^{9} L_{\mu\nu}\mathcal{V}_k^{\mu\nu}\hat{S}_k \tag{5.3}$$

$$= Q^2 \sum_{k=1}^{9} \mathcal{A}_k(\psi,\phi)\hat{S}_k(x,z,Q^2,q_T^2) \ , \tag{5.4}$$

where the functions $\mathcal{A}_k(\psi,\phi)$ capture the angular dependence, and $\hat{S}_k$ are the partonic equivalent of the hadronic structure functions

$$\hat{S}_k = \hat{W}_{\mu\nu}\tilde{\mathcal{V}}_k^{\mu\nu} \ , \tag{5.5}$$

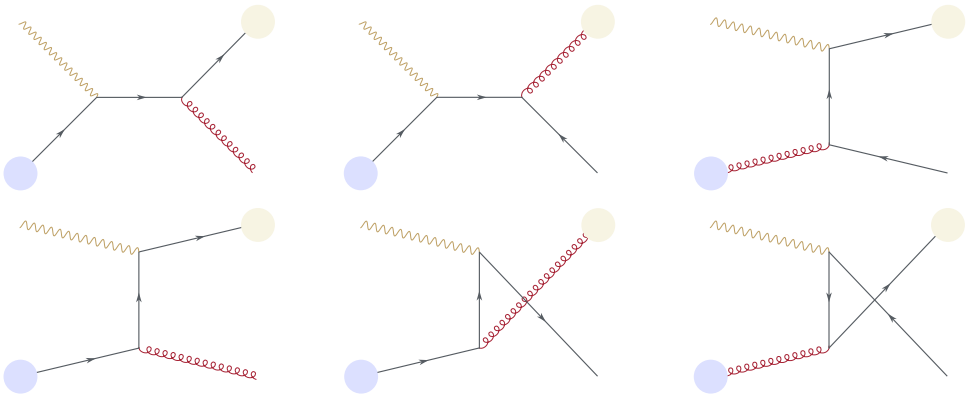

(a) qq-channel (b) qg-channel (c) gq-channel

Figure 5.1: Leading order Feynman diagrams, with the parton coming from the proton marked by the blue area and the fragmenting parton marked by the yellow area.

with the inverse tensors $\tilde{\mathcal{V}}_k^{\mu\nu}$ defined in (3.53).
This section covers the explicit calculation of $\hat{S}_k$ for the different channels contributing to the hadronic interaction. And provides the results in terms of the SIDS variables.
According to the factorization theorem, all possible partonic initial and final states must be included. At leading order the possible partonic contributions come from

$$\gamma^* + q(\bar{q}) \to q(\bar{q}) + g \quad , \tag{5.6}$$
$$\gamma^* + q(\bar{q}) \to g \quad + q(\bar{q}) \ , \tag{5.7}$$
$$\gamma^* + g \quad \to q(\bar{q}) + \bar{q}(q) \ , \tag{5.8}$$

where the first particle after the arrow is the observed (fragmenting) parton. Processes with antiparticles are also allowed and indicated in parentheses. Since all fermions in these processes are assumed to be massless, the change of charge flow does not change the Dirac structure. In addition, the electromagnetic coupling changes sign for antiparticles, and because the cross section contains squared matrix elements, this change of sign cancels. Therefore, the results for antiparticles are equal to those for particles.
The first process (5.6) is called qq-channel for the quark coming from the proton and the quark that will hadronize to be the observed final state hadron. Similarly, the second channel (5.7) is called qg- and the last one (5.8) is called gq-channel. Each of these channels has two leading-order Feynman diagrams. Those Feynman diagrams are shown in Figure 5.1.
The interaction gg is not allowed at leading order since the gluon and the photon do not interact directly. This channel will only open up at next-to-leading order.

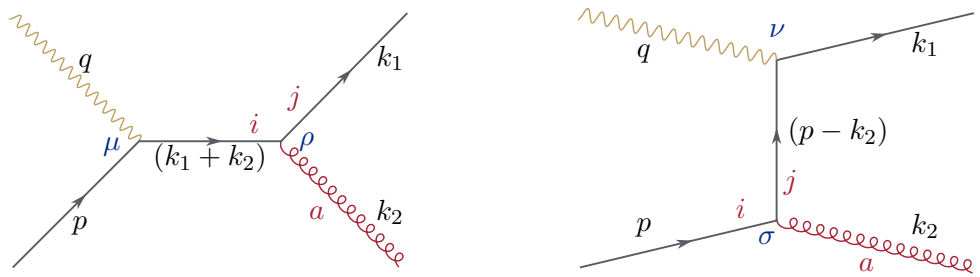

(a) s-channel (b) t-channel

Figure 5.2: Leading order Feynman diagrams of the qq-channel, with momenta (black), color indices (red), and Lorentz indices (blue).

While all channels are evaluated using the same methods, the calculation of the qq-channel is presented in the following. The results for the qg- and gq-channels are deferred to Sections 5.2 and 5.3.
Since the leading-order results are required in the next-to-leading order computation, both for the interference term in the virtual corrections and in the subtraction of collinear divergences, all calculations are performed in $d = 4 - 2\epsilon$ dimensions using dimensional regularization.
The practical implementations of the calculation uses the computational tool `Mathematica`, with the packages `FeynArts` [249] to automate the generation of Feynman diagrams and the package `FeynCalc` [230–233] for symbolic tensor algebra, contractions, and Dirac trace evaluations.

5.1 Calculation of the qq-Channel

The qq-channel, with its associated momenta and indices, is illustrated in Figure 5.2. Using the Feynman rules in Section 2.4 the matrix elements for the two diagrams are

$$\mathrm{i}\mathcal{M}_s^\mu = -\mathrm{i}\overline{u}_s'(k_1)\left(g_s\mu^\epsilon\gamma^\rho(T_a)^{ij}\right)\frac{\not{p}+\not{q}}{(p+q)^2}\left(e_q\gamma^\mu\right)u_s(p)\epsilon_\lambda^{*\rho}(k_2) \tag{5.9}$$

$$\mathrm{i}\mathcal{M}_t^\mu = -\mathrm{i}\overline{u}_s'(k_1)\left(e_q\gamma^\mu\right)\frac{\not{p}-\not{k}_2}{(p-k_2)^2}\left(g_s\mu^\epsilon\gamma^\sigma(T_a)^{ij}\right)u_s(p)\epsilon_\lambda^{*\sigma}(k_2)\ , \tag{5.10}$$

where e_q is the quarks fractional electric charge, g_s the strong coupling constant, $(T_a)^{ij}$ the color matrices and ϵ_λ describes the gluon polarization. The subscripts s and t indicate the respective channel, the spins of the fermions are signified by the indices s and s', and the color indices are as illustrated in Figure 5.2. The electromagnetic coupling constant

and the photon propagator are already taken care of by explicitly pulling them out in the definition of the hadronic tensor. The index μ at the matrix element is there to convey that the matrix element has an open index from the photon vertex. Squaring the amplitude results in

$$\overline{\sum}\left(\mathcal{M}_s^{\mu}+\mathcal{M}_t^{\mu}\right)\left(\mathcal{M}_s^{*\nu}+\mathcal{M}_t^{*\nu}\right)=\overline{\sum}\left(\mathcal{M}_s^{\mu}\mathcal{M}_s^{*\nu}+\mathcal{M}_t^{\mu}\mathcal{M}_t^{*\nu}+\mathcal{M}_s^{\mu}\mathcal{M}_t^{*\nu}+\mathcal{M}_t^{\mu}\mathcal{M}_s^{*\nu}\right)\ , \tag{5.11}$$

where the symbol $\overline{\sum}$ represents averaging and summation over spins, color, and polarization. As a shorthand notation

$$\overline{\mathcal{M}}^{\mu\nu}_{\gamma^* q\to qg}=\overline{\sum}\left(\mathcal{M}_s^{\mu}+\mathcal{M}_t^{\mu}\right)\left(\mathcal{M}_s^{*\nu}+\mathcal{M}_t^{*\nu}\right) \tag{5.12}$$

is introduced. Calculating the color factor with the methods described in Section 4.1 gives for all four contributions a color factor of

$$\mathrm{Tr}(T_a T_a)=\frac{\delta_{aa}}{2}=\frac{N^2-1}{2}=C_A C_F\ , \tag{5.13}$$

with the Casimir operators $C_F=\frac{N^2-1}{2N}$ and $C_A=N$ of Equations (2.22) and (2.23). Including the color averaging factor for the incident quark $(1/C_A)$ results in an overall color factor of C_F. The sum over all possible polarization states of the outgoing gluon yields

$$\sum_{\lambda}\epsilon_{\lambda}^{\rho}(k_2)\epsilon_{\lambda}^{*\sigma}(k_2)=-g^{\rho\sigma}\ . \tag{5.14}$$

The simple form of the polarization sum is valid, provided that ghost particles are properly included in the Lagrangian, ensuring the cancellation of unphysical polarization states. In approaches where ghost fields are not included, the polarization sum must be modified accordingly, see [64]. However, since ghost contributions are absent at leading-order in this calculation, the simple form of the polarization sum in (5.14) can be safely used without any modifications.

Averaging over the spins of the initial-state fermions and summing over those in the final state allows the use of Casimir's trick of Section 4.2 to write the Dirac matrices in a trace. Including the spin averaging factor of 1/2, the squared matrix element for the s-channel diagram becomes

$$\overline{\sum}\mathcal{M}_s^{\mu}\mathcal{M}_s^{*\nu}=-2\pi C_F\alpha_s e_q^2\frac{1}{s^2}\mu^{2\epsilon}\mathrm{Tr}\left(\not{p}\gamma^{\nu}\left(\not{p}+\not{q}\right)\gamma^{\rho}\not{k}_1\gamma_{\rho}\left(\not{p}+\not{q}\right)\gamma^{\mu}\right)\ , \tag{5.15}$$

where $\alpha_s = g_s^2/(4\pi)$ is introduced. With similar steps, the other terms yield

$$\overline{\sum}\mathcal{M}_t^{\mu}\mathcal{M}_t^{*\nu} = -2\pi C_F \alpha_s e_q^2 \frac{1}{t^2}\mu^{2\epsilon}\mathrm{Tr}\left(\not{p}\gamma^{\rho}\left(\not{p}-\not{k}_2\right)\gamma^{\nu}\not{k}_1\gamma^{\mu}\left(\not{p}-\not{k}_2\right)\gamma_{\rho}\right) \ , \tag{5.16}$$

$$\overline{\sum}\mathcal{M}_s^{\mu}\mathcal{M}_t^{*\nu} = \ 2\pi C_F \alpha_s e_q^2 \frac{1}{st}\mu^{2\epsilon}\mathrm{Tr}\left(\not{p}\gamma^{\nu}\left(\not{p}+\not{q}\right)\gamma^{\rho}\not{k}_1\gamma^{\mu}\left(\not{p}-\not{k}_2\right)\gamma_{\rho}\right) \ , \tag{5.17}$$

$$\overline{\sum}\mathcal{M}_t^{\mu}\mathcal{M}_s^{*\nu} = \ 2\pi C_F \alpha_s e_q^2 \frac{1}{st}\mu^{2\epsilon}\mathrm{Tr}\left(\not{p}\gamma^{\rho}\left(\not{p}-\not{k}_2\right)\gamma^{\nu}\not{k}_1\gamma_{\rho}\left(\not{p}+\not{q}\right)\gamma^{\mu}\right) \ . \tag{5.18}$$

The Lorentz indices of the photon remain uncontracted up to this point. While one could proceed by applying phase space integration and the normalization factor directly to the squared matrix element in order to construct the partonic tensor, as outlined in Equation (3.66), an alternative order of operation is adopted. Instead, the open indices are contracted with projection tensors that decompose the hadronic tensor into angular components. This contraction simplifies the expressions by eliminating the explicit Lorentz structures, reducing the dependence to scalar products of the external momenta. This operation can be performed either before or after phase space integration without changing the final result.

As the decomposition tensors were originally defined at the hadron level, a trivial modification is required to apply them at the parton level. This modification is explicitly shown to avoid confusion.

The vectors describing the hadron frame in Section 3.1.1 must be applied at parton level. With the Equations (3.79) and (3.82) one gets:

$$xP = \hat{x}p \qquad \text{and} \qquad \frac{P_h}{z} = \frac{k_1}{\hat{z}} \ . \tag{5.19}$$

With that the coordinate vectors of the hadron frame (3.19) can be written at parton level, without changing them as

$$\hat{T}^{\mu} = \frac{1}{Q}\left(q^{\mu} + 2\hat{x}p^{\mu}\right) \ , \tag{5.20}$$

$$\hat{X}^{\mu} = \frac{1}{q_T}\left(\frac{k_1^{\mu}}{\hat{z}} - q^{\mu} - \left(1+\frac{q_T^2}{Q^2}\right)\hat{x}p^{\mu}\right) \ , \tag{5.21}$$

$$\hat{Y}^{\mu} = \epsilon^{\mu\nu\rho\sigma}\hat{Z}_{\nu}\hat{T}_{\rho}\hat{X}_{\sigma} \ , \tag{5.22}$$

$$\hat{Z}^{\mu} = -\frac{q^{\mu}}{Q} \ . \tag{5.23}$$

This also leaves the projecting tensors (3.53) unchanged when applied at parton level:

$$\begin{aligned}
\tilde{\mathcal{V}}_1^{\mu\nu} &= \frac{1}{2}(2\hat{T}^\mu\hat{T}^\nu + \hat{X}^\mu\hat{X}^\nu + \hat{Y}^\mu\hat{Y}^\nu) \quad \tilde{\mathcal{V}}_2^{\mu\nu} = \hat{T}^\mu\hat{T}^\nu \qquad \tilde{\mathcal{V}}_3^{\mu\nu} = -\frac{1}{2}\left(\hat{T}^\mu\hat{X}^\nu + \hat{X}^\mu\hat{T}^\nu\right) \\
\tilde{\mathcal{V}}_4^{\mu\nu} &= \frac{1}{2}\left(\hat{X}^\mu\hat{X}^\nu - \hat{Y}^\mu\hat{Y}^\nu\right) \quad \tilde{\mathcal{V}}_5^{\mu\nu} = \frac{\mathrm{i}}{2}\left(\hat{T}^\mu\hat{X}^\nu - \hat{X}^\mu\hat{T}^\nu\right) \qquad \tilde{\mathcal{V}}_6^{\mu\nu} = -\frac{\mathrm{i}}{2}\left(\hat{X}^\mu\hat{Y}^\nu - \hat{Y}^\mu\hat{X}^\nu\right) \\
\tilde{\mathcal{V}}_7^{\mu\nu} &= \frac{\mathrm{i}}{2}\left(\hat{T}^\mu\hat{Y}^\nu - \hat{Y}^\mu\hat{T}^\nu\right) \quad \tilde{\mathcal{V}}_8^{\mu\nu} = -\frac{1}{2}\left(\hat{T}^\mu\hat{Y}^\nu + \hat{Y}^\mu\hat{T}^\nu\right) \qquad \tilde{\mathcal{V}}_9^{\mu\nu} = \frac{1}{2}\left(\hat{X}^\mu\hat{Y}^\nu + \hat{Y}^\mu\hat{X}^\nu\right) .
\end{aligned} \tag{5.24}$$

As discussed in Section 3.3 only the parity-even and symmetric tensors $\mathcal{V}_1^{\mu\nu}, ..., \mathcal{V}_4^{\mu\nu}$ contribute, since the sum of the squared matrix elements in (5.11) is symmetric and parity-even.[1]

These tensors are now used to contract the open photon indices in the squared matrix elements. This leads to lengthy expressions due to the numerous terms involving different combinations of momenta in the tensors. The contraction and subsequent evaluation of the Dirac traces are performed using the `Mathematica` package `FeynCalc` [230–233].

Once the Dirac traces are evaluated, the resulting expressions can be simplified significantly by applying momentum conservation ($p + q = k_1 + k_2$) and exploiting the fact that all particles, except the highly virtual photon, are massless.

For illustration purposes the metric tensor is introduced as

$$\tilde{\mathcal{V}}_0^{\mu\nu} = g^{\mu\nu} , \tag{5.25}$$

since the results using the projecting tensors from above are a bit cumbersome. After contracting with the metric tensor, introducing Mandelstam variables, and setting $\epsilon = 2 - d/2$, the terms are given by

$$g_{\mu\nu}\overline{\sum}\mathcal{M}_s^\mu\mathcal{M}_s^{*\nu} = 16\pi C_F\alpha_s e_q^2(1-\epsilon)^2\mu^{2\epsilon}\frac{t}{s} \tag{5.26}$$

$$g_{\mu\nu}\overline{\sum}\mathcal{M}_t^\mu\mathcal{M}_t^{*\nu} = 16\pi C_F\alpha_s e_q^2(1-\epsilon)^2\mu^{2\epsilon}\frac{s}{t} \tag{5.27}$$

$$g_{\mu\nu}\overline{\sum}\mathcal{M}_s^\mu\mathcal{M}_t^{*\nu} = g_{\mu\nu}\overline{\sum}\mathcal{M}_t^\mu\mathcal{M}_s^{*\nu} = -16\pi C_F\alpha_s e_q^2(1-\epsilon)\mu^{2\epsilon}\frac{Q^2u + \epsilon st}{st} . \tag{5.28}$$

The contraction with the more complex tensors $\tilde{\mathcal{V}}_1^{\mu\nu}, \tilde{\mathcal{V}}_2^{\mu\nu}, \tilde{\mathcal{V}}_3^{\mu\nu}, \tilde{\mathcal{V}}_4^{\mu\nu}$ is presented in Appendix A. The sum of all contributions to the qq-channel, contracted with the metric

[1] The last two terms in (5.11) are not symmetric on their own, but the combination of both terms is symmetric.

tensor is

$$\overline{\mathcal{M}}^{(0)}_{\gamma^* q\to qg} = g_{\mu\nu}\overline{\mathcal{M}}^{\mu\nu}_{\gamma^* q\to qg} = 16\pi C_F \alpha_s e_q^2 (1-\epsilon)\mu^{2\epsilon}\left((1-\epsilon)\left(\frac{t}{s}+\frac{s}{t}\right) - \frac{2Q^2 u}{st} - 2\epsilon\right) . \tag{5.29}$$

For the other contractions the same notation is used

$$\overline{\mathcal{M}}^{(k)}_{\gamma^* q\to qg} = \tilde{\mathcal{V}}_k^{\mu\nu}\overline{\mathcal{M}}^{\mu\nu}_{\gamma^* q\to qg} . \tag{5.30}$$

The next step is phase space integration. At leading order, the phase space is simple. It is the two-particle phase space derived in Section 4.7.1. Writing the cross section differential in the Mandelstam variables u and t yields

$$\frac{\mathrm{d}\hat{\sigma}^{\mathrm{LO}(k)}_{\gamma^* q\to qg}}{\mathrm{d}u\mathrm{d}t} = \frac{1}{8\pi}\frac{(4\pi)^\epsilon}{\Gamma(1-\epsilon)}\frac{1}{s+Q^2}\left(\frac{(s+Q^2)^2}{stu}\right)^\epsilon \overline{\mathcal{M}}^{(k)}_{\gamma^* q\to qg}\delta(s_{23}) . \tag{5.31}$$

To obtain the result differential in the SIDIS variables, the squared matrix element needs to be expressed in them too. This is done using the transformations provided in Section 3.5.2 to get

$$\frac{\overline{\mathcal{M}}^{(0)}_{\gamma^* q\to qg}}{4\pi} = -4C_F\alpha_s e_q^2(1-\epsilon)\mu^{2\epsilon}\left((1-\epsilon)\left(\frac{1-\hat{z}}{1-\hat{x}}+\frac{1-\hat{x}}{1-\hat{z}}\right)+2\frac{Q^2}{q_T^2}+2\epsilon\right) . \tag{5.32}$$

The other squared matrix elements are:

$$\begin{aligned}
\frac{\overline{\mathcal{M}}^{(1)}_{\gamma^* q\to qg}}{4\pi} &= 2C_F\alpha_s e_q^2(1-\epsilon)\mu^{2\epsilon}\frac{Q^2}{q_T^2}\frac{1}{\hat{x}\hat{z}}\big(\hat{x}^2(1-6\hat{z}(1-\hat{z})-\epsilon)+\hat{x}(2\hat{z}(4-3\hat{z}+\epsilon)-2)\\
&\qquad -\hat{z}(2-\hat{z}+\epsilon\hat{z})+2\big)\\
\frac{\overline{\mathcal{M}}^{(2)}_{\gamma^* q\to qg}}{4\pi} &= 8C_F\alpha_s e_q^2(1-\epsilon)\mu^{2\epsilon}\hat{x}\hat{z}\\
\frac{\overline{\mathcal{M}}^{(3)}_{\gamma^* q\to qg}}{4\pi} &= 4C_F\alpha_s e_q^2\mu^{2\epsilon}\left((1-\epsilon)\hat{x}\hat{z}\frac{Q^2+q_T^2}{Qq_T}+\epsilon\frac{Q}{q_T}\right)\\
\frac{\overline{\mathcal{M}}^{(4)}_{\gamma^* q\to qg}}{4\pi} &= 2C_F\alpha_s e_q^2\mu^{2\epsilon}\Bigg(2\hat{x}\hat{z}+\epsilon\frac{Q^2}{q_T^2}\frac{1}{\hat{x}\hat{z}}\big(2\hat{x}(\hat{z}(\hat{z}+\epsilon)-1)\\
&\qquad +\hat{x}^2(1+2(1-\hat{z})\hat{z}-\epsilon)-\hat{z}(2-\hat{z}+\epsilon\hat{z})+2\big)\Bigg) .
\end{aligned} \tag{5.33}$$

The factor $1/(4\pi)$ is convention in order to get the same normalization as for the hadronic tensor (3.66). These results match the result presented in [32–34], for $\epsilon \to 0$. When the squared matrix element is written in terms of the SIDIS variables, the partonic analog of the structure functions $\hat{S}_k$ of Equation (3.54) includes the phase space. Differential in $\hat{z}$ and q_T^2 they are

$$\hat{S}_k^{\gamma^* q\to qg} = \frac{\mathrm{d}\hat{\sigma}^{\mathrm{LO}(k)}_{\gamma^* q\to qg}}{\mathrm{d}\hat{z}\mathrm{d}q_T^2} = \frac{1}{8\pi}\frac{(4\pi)^\epsilon}{\Gamma(1-\epsilon)}\frac{1}{Q^2}\left(\hat{z}^2 q_T^2\right)^{-\epsilon}\overline{\mathcal{M}}^{(k)}_{\gamma^* q\to qg}\delta\left(\frac{q_T^2}{Q^2} - \frac{(1-\hat{x})(1-\hat{z})}{\hat{x}\hat{z}}\right) . \tag{5.34}$$

As seen in Section 4.9 the leading-order cross section is already the hard part, and there is no need for additional subtraction of collinear divergences.
The next step is to reintroduce the leptonic part of the interaction. Just as the hadronic tensor was decomposed according to its angular structure, the same decomposition must be applied to the leptonic part. This is accomplished using the projection defined in Equation (3.56):

$$\mathcal{A}_k = \frac{1}{Q^2} L_{\mu\nu}\mathcal{V}_k^{\mu\nu} . \tag{5.35}$$

Here the tensors $\mathcal{V}_1^{\mu\nu}, ..., \mathcal{V}_4^{\mu\nu}$ of Equation (3.52) are used for the decomposition and, additionally, a factor of $1/Q^2$ is included in the definition of $\mathcal{A}_k$. These functions can be evaluated with the leptonic tensor (3.47)

$$L_{\mu\nu}(l, l') = 2(l_\mu l'_\nu + l'_\mu l_\nu - g_{\mu\nu} l \cdot l') \tag{5.36}$$

to get:

$$\begin{aligned} \mathcal{A}_1 &= 1 + \cosh^2\psi & \mathcal{A}_2 &= -2 \\ \mathcal{A}_3 &= -\cos\phi \sinh 2\psi & \mathcal{A}_4 &= \cos 2\phi \sinh^2\psi . \end{aligned} \tag{5.37}$$

Resulting in the partonic differential cross section

$$\frac{\mathrm{d}\hat{\sigma}^{\mathrm{LO}}_{\ell q\to \ell qg}}{\mathrm{d}\hat{x}\mathrm{d}Q^2\mathrm{d}\hat{z}\mathrm{d}q_T^2\mathrm{d}\phi} = \frac{\alpha^2}{Q^2\hat{x}^2\hat{s}^2} Q^2 \sum_{k=1}^{4} \mathcal{A}_k \hat{S}_k^{\gamma^* q\to qg} \tag{5.38}$$

In practice, this sum is not evaluated explicitly, as the individual structure functions $\hat{S}_k$ are themselves the primary quantities of interest in this analysis.
This concludes the partonic part of the calculation for the qq-channel. To complete the transition to the hadronic interaction, the remaining partonic channels must be evaluated

and combined according to the factorization formula. This allows one to reconstruct the full hadronic cross section and its angular structure from the perturbative partonic subprocesses.

5.2 Results for the qg-Channel

The calculation of the qg-channel is analogous to the calculation of the qq-channel presented above. In terms of Mandelstam variables, the results are related by the crossing relation $t \leftrightarrow u$. The results in terms of the SIDIS variables for the averaged square matrix elements are

$$\begin{aligned}
\frac{\overline{\mathcal{M}}^{(0)}_{\gamma^* q\to gq}}{4\pi} &= -4C_F\alpha_s e_q^2\mu^{2\epsilon}\frac{1-\epsilon}{(1-\hat{x})\hat{z}}\left(1+(\hat{x}-\hat{z})^2-\epsilon-\epsilon(\hat{x}+\hat{z}-2)(\hat{x}+\hat{z})\right)\\
\frac{\overline{\mathcal{M}}^{(1)}_{\gamma^* q\to gq}}{4\pi} &= -2C_F\alpha_s e_q^2\mu^{2\epsilon}\frac{1-\epsilon}{(1-\hat{x})\hat{z}}\big(\hat{x}^2(6(1-\hat{z})\hat{z}-1)+\epsilon(\hat{x}+\hat{z}-1)^2\\
&\qquad +2\hat{x}(3\hat{z}-2)\hat{z}-\hat{z}^2-1\big)\\
\frac{\overline{\mathcal{M}}^{(2)}_{\gamma^* q\to gq}}{4\pi} &= 8C_F\alpha_s e_q^2\mu^{2\epsilon}(1-\epsilon)\hat{x}(1-\hat{z})\\
\frac{\overline{\mathcal{M}}^{(3)}_{\gamma^* q\to gq}}{4\pi} &= -4C_F\alpha_s e_q^2\mu^{2\epsilon}\frac{Q}{q_T}\frac{(1-\hat{z})}{\hat{z}}\left(\hat{z}+\epsilon+(1-\epsilon)\hat{x}(1-2\hat{z})-\epsilon\hat{z}\right)\\
\frac{\overline{\mathcal{M}}^{(4)}_{\gamma^* q\to gq}}{4\pi} &= -2C_F\alpha_s e_q^2\mu^{2\epsilon}\frac{1}{(1-\hat{x})\hat{z}}\big(\epsilon\left(\hat{x}^2(2(\hat{z}-1)\hat{z}-1)+2\hat{x}(2-\hat{z})\hat{z}-\hat{z}^2-1\right)\\
&\qquad +\epsilon^2(\hat{x}+\hat{z}-1)^2+2\hat{x}\hat{z}(-\hat{x}\hat{z}+\hat{x}+\hat{z}-1)\big)\ .
\end{aligned} \tag{5.39}$$

These results also match the results of [32, 33] and the ones in [34], when accounting for the labeling error. The remaining steps to get from the squared matrix elements to the structure functions and to the partonic differential cross sections are the same as in the qq-channel above.

5.3 Results for the gq-Channel

Also, the calculation for the gq-channel proceeds in close analogy to the previous channels. The primary difference arises from the nature of the incoming particle, which is now a gluon rather than a quark. Consequently, the averaging factors differ.
Once for the summation over all polarization states, which yields a factor of $1/(d-2) =$

$1/(2(1-\epsilon))$ in d dimension for the gluon, instead of the factor $1/2$ for the average over the spin of the incoming fermion above. The average of the color factor changes from the factor $1/C_A$ for an incident quark to $1/(2C_AC_F) = 1/(N^2-1)$ for the color average of the incoming gluon. Other than that, the calculations are analogous to those of the two channels above. The results for the squared matrix elements are as follows:

$$
\begin{aligned}
\frac{\overline{\mathcal{M}}^{(0)}_{\gamma^* g\to q\bar{q}}}{4\pi} &= -2\alpha_s e_q^2 \mu^{2\epsilon} \frac{1}{\hat{z}(1-\hat{z})} \left(1 - 2(1-\hat{x})\hat{x} - 2(1-\hat{z})\hat{z} - \epsilon\right) \\
\frac{\overline{\mathcal{M}}^{(1)}_{\gamma^* g\to q\bar{q}}}{4\pi} &= \alpha_s e_q^2 \mu^{2\epsilon} \frac{1}{1-\epsilon} \frac{1}{\hat{z}(1-\hat{z})} \big((2\hat{x}^2 - 2\hat{x})(1 - 6(1-\hat{z})\hat{z} - \epsilon) \\
&\quad + (1-\epsilon)(1 - 2(1-\hat{z})\hat{z} - \epsilon)\big) \\
\frac{\overline{\mathcal{M}}^{(2)}_{\gamma^* g\to q\bar{q}}}{4\pi} &= 8\alpha_s e_q^2 \mu^{2\epsilon} \frac{1}{1-\epsilon} \hat{x}(1-\hat{x}) \\
\frac{\overline{\mathcal{M}}^{(3)}_{\gamma^* g\to q\bar{q}}}{4\pi} &= 2\alpha_s e_q^2 \mu^{2\epsilon} \frac{q_T}{Q} \frac{1}{1-\epsilon} \frac{\hat{x}}{1-\hat{z}} (1-2\hat{z})(1-2\hat{x}) \\
\frac{\overline{\mathcal{M}}^{(4)}_{\gamma^* g\to q\bar{q}}}{4\pi} &= \alpha_s e_q^2 \mu^{2\epsilon} \frac{1}{1-\epsilon} \frac{1}{\hat{z}(1-\hat{z})} \big(4(1-\hat{x})\hat{x}(1-\hat{z})\hat{z} \\
&\quad + \epsilon - 2\epsilon(1-\hat{x})\hat{x} - 2\epsilon(1-\hat{z})\hat{z} - \epsilon^2\big) \,,
\end{aligned}
\tag{5.40}
$$

which are the same results as given in [32, 33] and [34], when accounting for the labeling error. As for the two cases above, the remaining steps to obtain the splitting functions and the differential cross section are the same.

5.4 The Hadronic Cross Section

The final step is to transition to the hadronic interaction, which is achieved via the factorization theorem explained in Section 3.4. In terms of the SIDIS variables, the factorized hadronic cross section reads:

$$
\frac{\mathrm{d}\sigma_{\ell\mathcal{P}\to\ell h X}}{\mathrm{d}x\mathrm{d}Q^2\mathrm{d}z\mathrm{d}q_T^2\mathrm{d}\phi} = \int_{\xi_{\min}}^1 \frac{\mathrm{d}\xi}{\xi} \int_{\zeta_{\min}}^1 \frac{\mathrm{d}\zeta}{\zeta} f_{i/\mathcal{P}}(\xi) \frac{\mathrm{d}\hat{\sigma}_{\ell i\to\ell j X}}{\mathrm{d}\hat{x}\mathrm{d}Q^2\mathrm{d}\hat{z}\mathrm{d}q_T^2\mathrm{d}\phi} d_{h/j}(\zeta) \,, \tag{5.41}
$$

where the terms $1/\xi$ and $1/\zeta$ arise from the change of variables between the hadronic and partonic SIDIS variables. It includes a sum over all partonic channels, by the twice appearing indices i for the incoming parton and j for the outgoing parton. By inserting the formula for the partonic differential cross sections (5.38) for all channels this can be written as

$$\frac{\mathrm{d}\sigma_{\ell\mathcal{P}\to\ell hX}}{\mathrm{d}x\mathrm{d}Q^2\mathrm{d}z\mathrm{d}q_T^2\mathrm{d}\phi} = \frac{\alpha^2}{Q^2x^2s_{lP}^2}Q^2\sum_{k=1}^{4}\mathcal{A}_k\int_{\xi_{\min}}^{1}\frac{\mathrm{d}\xi}{\xi}\int_{\zeta_{\min}}^{1}\frac{\mathrm{d}\zeta}{\zeta}f_{i/\mathcal{P}}(\xi)\hat{S}_k^{\gamma^*i\to jX}d_{h/j}(\zeta)\ , \tag{5.42}$$

giving the result for the hadronic SIDIS interaction at leading-order in dimensional regularization, where the terms for different angular dependencies are still separated, by leaving the sum over k explicit.

If the interest is only in the leading-order, then the limit $\epsilon \to 0$ can be safely taken. However, for the next-to-leading order, the leading-order results are required in d dimensions. The next-to-leading order calculations are the subject of the next section.

Chapter 6

Next-to-Leading Order Calculation

The transition from hadronic to partonic interactions follows the same procedure at next-to-leading order as it does at leading order. The key difference lies in the increased complexity of the partonic subprocesses. This complexity arises not only from the larger number of Feynman diagrams that contribute at next-to-leading order, but also from the appearance of UV and IR divergences that require careful regularization and subtraction to ensure a finite and physically meaningful result.

The next-to-leading order contributions are accompanied by a larger exponent of the strong coupling constant g_s. In terms of Feynman diagrams, this corresponds to the presence of an additional strong vertex, which in turn implies an additional particle in the final state. Since the initial state is fixed, a virtual photon and a parton originating from the proton, the extra vertex necessitates a three-particle final state. The third particle in the final state is unobserved and therefore contributes to the inclusive sum over unmeasured particles, denoted collectively by X.

When squaring the sum of all diagrams with the same three particles in the final state, the resulting matrix elements acquire a factor of g_s^2.[1] These are known as real emission corrections, reflecting the emission of an additional "real" parton.[2] Real emission is not the only possible way to create Feynman diagrams that result in an additional factor of g_s^2. Virtual corrections also appear at this order. These involve diagrams in which an internal line is added to a Born-level diagram, effectively introducing two new vertices but

[1] Corrections with only one additional factor of g_s would have to come from the interference of the born term with Feynman diagrams with three outgoing particles. However, these contributions cannot interfere because they have distinct external states.

[2] In the theory of strong interactions, the external particles are not the ones that are finally observed. The name "real" is a remnant QED, where the additionally radiated particles are real observable particles.

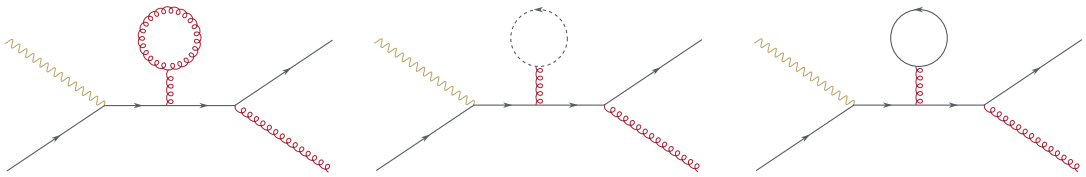

Figure 6.1: The three virtual tadpole corrections to the s-channel of the qq-channel.

no additional final-state particle. These diagrams can interfere with the Born term and also contribute at $\mathcal{O}(g_s^4)$. Interference among purely virtual diagrams would contribute at $\mathcal{O}(g_s^6)$ and thus are beyond the scope of next-to-leading order calculations. Virtual corrections are the subject of the following section.

Both real and virtual corrections come with their own challenges and both contain divergences. For virtual corrections, these divergences originate from internal loops created by the additional internal line. The momenta in these loops are not constrained by the external momenta, and their integration leads to divergences. For the real emission diagrams, the divergences originate from singularities in phase space integrations. All these integrals are typically divergent in four spacetime dimensions but can be regularized by dimensional regularization, which is used throughout this thesis to keep track of the divergences.

Given the increasing algebraic complexity of next-to-leading order expressions, symbolic computation tools are essential. All calculations were performed using Wolfram `Mathematica` with the help of several specialized packages:

`FeynArts` [249] is used to automatically generate Feynman diagrams in a machine readable format.

`FeynCalc` [230–233] handles algebraic manipulations such as Dirac traces and tensor contractions.

`FeynHelpers` [250] serves as an interface to loop integral libraries and provides access to the analytic forms of scalar loop integrals, formerly available via the now no longer supported `PackageX` [251].

These tools form the computational backbone of the next-to-leading order calculations presented in the following sections.

6.1 Virtual Contributions

The next-to-leading order virtual corrections share the same kinematics as the corresponding leading-order processes. Thus, the $\mathcal{O}(\alpha_s^2)$ contributions arise from the interference of

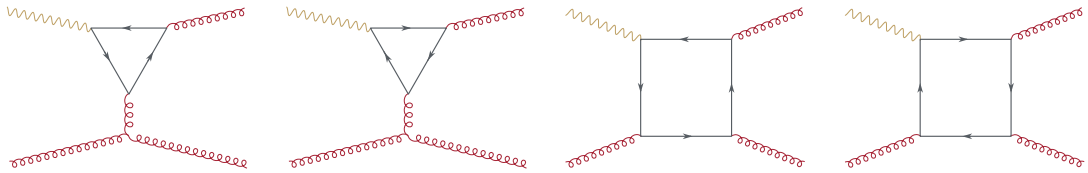

Figure 6.2: Example Feynman diagrams of the gg-channel one-loop level.

one-loop diagrams and the Born-level diagrams depicted in Figure 5.1.
The central task in evaluating these virtual corrections is the computation of one-loop amplitudes. In principle, there are four topologies of one-loop diagrams that could contribute: tadpole, bubble, triangle, and box diagrams. Among these, the tadpole contributions are the simplest to calculate. However, they do not contribute, as their color factors vanish. For completeness, the tadpole contributions to the s-channel diagram of the qq-channel are shown in Figure 6.1.
The remaining topologies, namely, bubble, triangle, and box diagrams, all yield nonzero contributions and must be accounted for. These are more involved and are discussed in the next section.
In general, one-loop corrections possess non-trivial tensor structure in the numerator of the loop integrals due to fermions in the loop. These tensorial loop integrals must be systematically reduced to scalar loop integrals using the Passarino-Veltman reduction method, as discussed in Section 4.5.
The next section focuses on the explicit calculation of virtual corrections in the qq-channel. In addition, it is worth noting that, at one-loop level, Feynman diagrams for the process $\gamma^* g \to gg$ exist. They all contain a closed fermion loop that couples to the virtual photon. These diagrams do not contribute for two reasons: The flow of momentum of these diagrams is not fixed by external parameters; thus, the sum of one diagram with one, where the fermion momentum is reversed, cancels. Furthermore, there is no leading-order diagram for this channel; therefore, they cannot contribute to the order $\mathcal{O}(\alpha_s^2)$ anyways. Some example diagrams are shown in Figure 6.2.
A final note regarding the inversion of charge flow, i.e., for the processes in parentheses in Eqs.(5.6), (5.7), and (5.8). These give the same results as the original processes not in parentheses, since the quarks are massless and all contributions come with the square of the electric charge of the quark, which does not change when switching to antiquarks:

$$e_q^2 = (-e_q)^2 \ . \tag{6.1}$$

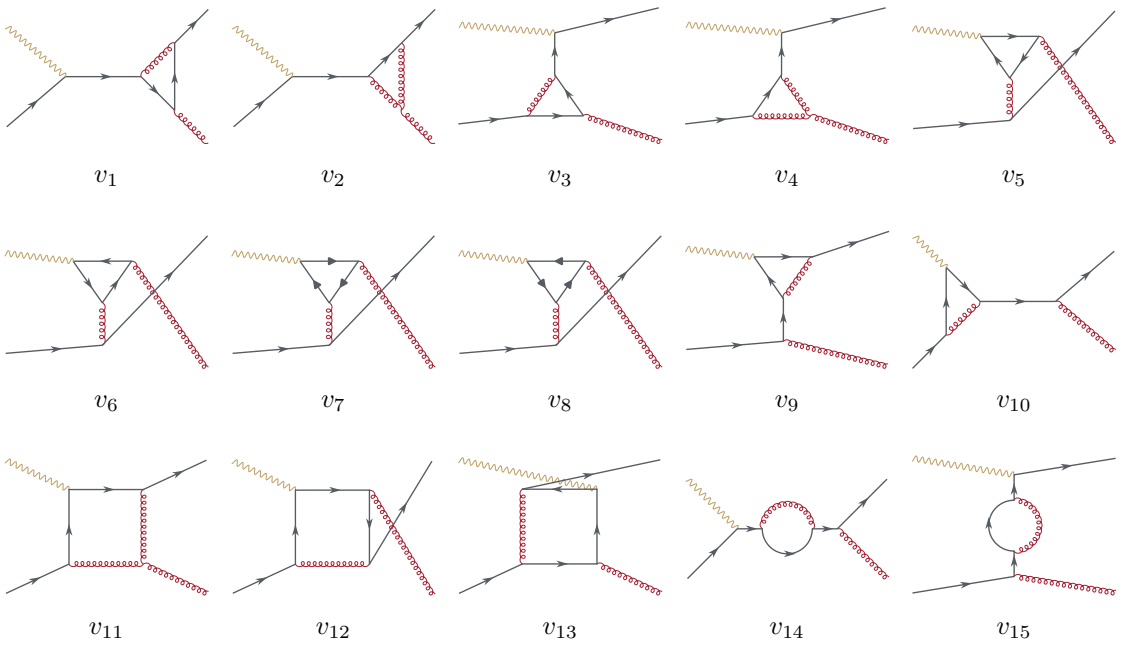

Figure 6.3: Feynman diagrams for the virtual corrections of the qq-channel. Fermions of different flavor are indicated by different arrow heads.

This statement might seem trivial here, but for real emission corrections, the charge conjugation must be handled with care.

6.1.1 Virtual Corrections to the qq-Channel

The virtual corrections to the qq-channel arise from the interference between the one-loop diagrams shown in Figure 6.3 and the two Born-level diagrams of Figure 5.1a. All diagrams are evaluated using a consistent set of techniques. The first four diagrams, labeled v_1 through v_4, correspond to vertex corrections: v_1 and v_2 are corrections to the strong coupling vertex of the leading-order s-channel, while v_3 and v_4 are analogous corrections to the t-channel diagrams. The diagrams $v_5, ..., v_8$ feature closed fermion loops with both flow directions. Since the theory is considered in the massless approximation, where particles and antiparticles have identical structures, these sums, $v_5 + v_6$ and $v_7 + v_8$ vanish and do not contribute.
Diagrams v_9 and v_{10} represent the QCD vertex correction to the QED vertex of the leading-order t- and s-channels, respectively. Diagrams v_{11}, v_{12} and v_{13} are box diagrams, which are algebraically the most complicated ones due to the larger number of propagators in the loop integrals. The final two diagrams represent quark self-energy corrections to the propagators in the leading-order s- and t-channels.

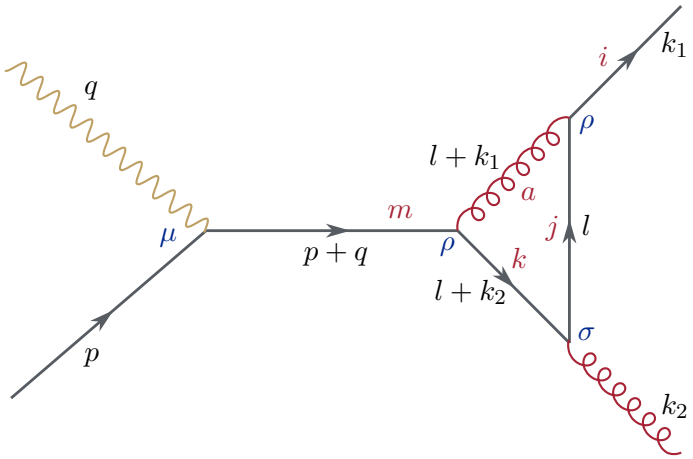

Figure 6.4: Feynman diagram v_1 of the qq-channel, with momenta (black), color indices (red) and Lorentz indices (blue).

The detailed calculation process is illustrated here using the diagram v_1, shown in Figure 6.3. This diagram is shown again in Figure 6.4, with the labels for the momenta, color indices, and Lorentz indices. The matrix element corresponding to this diagram is given by

$$\mathrm{i}\mathcal{M}^{\mu}_{v_1} = e_q g_s^3 \int \frac{\mathrm{d}^d l}{(2\pi)^d} \frac{\bar{u}(k_1)\gamma^\rho \not{l} \gamma_\sigma (\not{l} + \not{k}_2)\gamma_\rho (\not{p} + \not{q}) u(p)}{(p+q)^2 l^2 (l+k_2)^2 (l+k_1)^2} T^a_{ij} T^b_{jk} T^a_{kl} \epsilon^{*\sigma}_\lambda(k_2) \ . \tag{6.2}$$

This expression contains both vector and rank-2 tensor three-point integrals. These need to be reduced using Passarino-Veltman reduction of Section 4.5 to the scalar two-point integral B_0 and the scalar three-point integral C_0. In this case, only one of the particles attached to the loop, the quark propagator, has an effective mass, simplifying the reduction process. This reduction was performed using `FeynCalc`.
In contrast, diagrams v_9 and v_{10} involve two particles with an effective mass connected to the loop integral, leading to a more complicated structure of the reduced integrals.
After contractions and simplifications the matrix element takes the form

$$\begin{aligned}\mathrm{i}\mathcal{M}^{\mu}_{v_1} = \mathrm{i}\pi^2 e_q g_s^3 B_0((p+q)^2) \frac{1}{(p+q)^2} \big(&3(\bar{u}(k_1)\gamma_\sigma \not{k}_2 \gamma^\mu u(p)) + (d-2)(\bar{u}(k_1)\not{k}_2 \gamma_\sigma \gamma^\mu u(p)) \\ &- (d-2)(\bar{u}(k_1)\gamma^\mu u(p))(k_1+k_2)_\sigma\big) T^a_{ij} T^b_{jk} T^a_{kl}\, \epsilon^{*\sigma}_\lambda(k_2) \ .\end{aligned} \tag{6.3}$$

The matrix element for the second diagram includes contributions from both scalar two- and three-point functions. The scalar four-point function comes into play for the box

diagrams v_{11}, v_{12} and v_{13}, where the reduction is computationally more intensive due to the large number of terms introduced.
The next step is looking at the interference with the leading-order terms. For this, the complex conjugate of the leading-order terms is multiplied with the matrix element for the diagram v_1. The free photon index of the born level diagrams is changed to ν. This yields an interference term with two open photon indices, μ from the virtual correction and ν from the leading-order diagram, which contributes to the partonic tensor. In this example, the interference of v_1 with the s-channel diagram of the leading order is presented.
After constructing the interference, the standard procedure is as follows:

The spin average of the incident quark introduces a factor of 1/2. Casimir's trick is then applied to the Dirac structure as a trace over gamma matrices.

Executing the polarization sum over the gluon polarization. As for the leading-order case the simple form of the polarization sum (5.14) can be used. Additionally, there are no ghost terms that need to be considered for virtual corrections.

Evaluating the color algebra, while introducing the color averaging factor $1/C_A$ for the incoming quark. The color factor is the one form the first example in Section 4.1, the Equation (4.13), and evaluates to

$$\frac{1}{C_A}\mathrm{Tr}(T_a T_b T_a T_b) = -\frac{1}{2}\frac{C_F}{C_A} \ . \tag{6.4}$$

Following this procedure, one obtains for the interference of the diagram v_1 with the s-channel of the leading order:

$$\begin{aligned} 2\overline{\mathrm{Re}(\mathcal{M}^{\mu}_{v_1}\mathcal{M}^{*\nu}_{s})} = \frac{\pi^2}{2}e_q^2 g_s^4 B_0((p+q)^2)\frac{C_F}{C_A}\frac{1}{(p+q)^4}\big(&3\mathrm{Tr}(\not{p}\gamma^{\nu}(\not{k}_1+\not{k}_2)\gamma_{\sigma}\not{k}_1\gamma^{\sigma}\not{k}_2\gamma^{\mu}) \\ &+ (d-2)\mathrm{Tr}(\not{k}_1\gamma^{\mu}\not{p}\gamma^{\nu}(\not{k}_1+\not{k}_2)(\not{k}_1+\not{k}_2)) \\ &- (d-2)\mathrm{Tr}(\not{p}\gamma^{\nu}(\not{k}_1+\not{k}_2)\gamma_{\sigma}\not{k}_1\not{k}_2\gamma^{\sigma}\gamma^{\mu})\big) \ . \end{aligned} \tag{6.5}$$

Once all possible simplifications are made, the Dirac traces are evaluated using `FeynCalc`, followed by contraction with the projection tensors $\tilde{\mathcal{V}}_k^{\mu\nu}$ of Equations (5.24) and (5.25). In terms of the Mandelstam variables, with $\epsilon = (4-d)/2$ and $\alpha_s = g_s^2/(4\pi)$, the contraction with the metric tensor yields

$$2\tilde{\mathcal{V}}_0^{\mu\nu}\overline{\mathrm{Re}(\mathcal{M}^{\mu}_{v_1}\mathcal{M}^{*\nu}_{s})} = 64\pi^4(1-\epsilon)^2 e_q^2\alpha_s^2\frac{C_F}{C_A}B_0(s)\frac{1}{s}\left(t-u+2\epsilon t\right) \ . \tag{6.6}$$

The two expressions $2\tilde{\mathcal{V}}_k^{\mu\nu}\overline{\mathrm{Re}(\mathcal{M}_{v_1}^{\mu}\mathcal{M}_s^{*\nu})}$ and $2\tilde{\mathcal{V}}_k^{\mu\nu}\overline{\mathrm{Re}(\mathcal{M}_{v_1}^{\mu}\mathcal{M}_t^{*\nu})}$ for any tensor $\tilde{\mathcal{V}}_k^{\mu\nu}$ with $k = 0, ..., 4$ are grouped together to include both leading-order terms. The resulting squared matrix element is called

$$\overline{\mathcal{M}}_{v_1}^{(k)} = 2\tilde{\mathcal{V}}_k^{\mu\nu}\left(\overline{\mathrm{Re}(\mathcal{M}_{v_1}^{\mu}\mathcal{M}_s^{*\nu})} + \overline{\mathrm{Re}(\mathcal{M}_{v1}^{\mu}\mathcal{M}_t^{*\nu})}\right) . \tag{6.7}$$

The same procedure can be executed for all 15 virtual correction diagrams to get

$$\overline{\mathcal{M}}_{v_i}^{(k)} = 2\tilde{\mathcal{V}}_k^{\mu\nu}\left(\overline{\mathrm{Re}(\mathcal{M}_{v_i}^{\mu}\mathcal{M}_s^{*\nu})} + \overline{\mathrm{Re}(\mathcal{M}_{v_i}^{\mu}\mathcal{M}_t^{*\nu})}\right) , \tag{6.8}$$

with $i \in \{1, ..., 15\}$. The corrections corresponding to the diagrams $v_5, ..., v_8$ vanish due to symmetry considerations; therefore, they are omitted. The resulting 55 expressions are provided in separate files[3]. Some of the `Mathematica` code used to calculate these 55 terms is presented in Appendix B.1[4].

The subsequent steps are the evaluation of the scalar integrals using the built-in library of scalar integrals from the package `PackageX` [251] and applying phase space integration. The library of scalar integrals is accessed through the tool `FeynHelpers` [250] with the function "PaXEvaluate". At this stage, the squared matrix elements contain the full set of divergences. All UV, soft, and collinear divergences are present in the expressions and are regularized consistently by dimensional regularization.

To prepare the virtual corrections for combination with the real emission terms, the phase space integration is carried out in terms of the dimensionless variables v and w, as defined in Section 3.5.3. This choice facilitates a direct comparison and eventual merger with the real corrections, which will be expressed in the same variables. The $2 \to 2$ phase space in $d = 4 - 2\epsilon$ dimensions in terms of the dimensionless variables is given in Equation (4.96) as

$$\int \mathrm{dPS}_2 = \frac{1}{8\pi}\frac{(4\pi)^{\epsilon}}{\Gamma(1-\epsilon)}\int \mathrm{d}v\mathrm{d}w\,(sv(1-v))^{-\epsilon}\,\delta(1-w) . \tag{6.9}$$

Additionally, the Møller flux factor $F = 2s'$ (2.75) is included.

Before combining the virtual corrections with the real emission terms, the UV divergences must be removed by renormalization. The procedure is explained in Section 2.5.3 and amount to a redefinition of the strong coupling constant given in Equation (2.116) as

$$\frac{\alpha_{s,0}}{4\pi} = \frac{\alpha_s(\mu)}{4\pi}\left(1 - \frac{1}{\epsilon}\frac{\alpha_s(\mu)}{4\pi}\beta_0\left(\frac{\mathrm{e}^{\gamma_E}}{4\pi}\right)^{\epsilon}\right) , \tag{6.10}$$

[3]They are also available, upon request, at `https://github.com/DissKunzelmann/PhD`.
[4]The full code is also available at the above link.

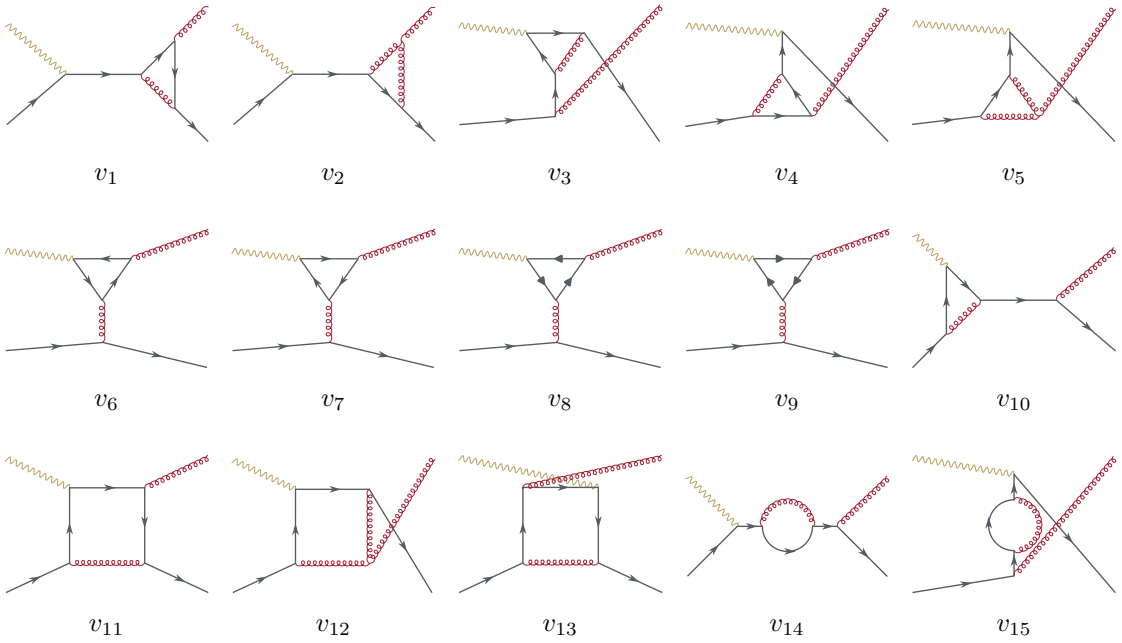

Figure 6.5: Feynman diagrams for the virtual corrections of the qg-channel. Fermions of different flavor are indicated by different arrow heads.

where $\beta_0 = \frac{11}{3}C_A - \frac{4}{3}T_F N_f$ is the one-loop QCD beta function.
Due to this formula, the renormalization terms come from the redefinition of the strong coupling in the leading-order term. These get an additional α_s via the renormalized strong coupling and therefore contribute to the next-to-leading order virtual corrections as $1/\epsilon$ poles.
After renormalization, the resulting terms are still IR divergent. Both soft and collinear divergences are still present. The soft divergences and the soft-collinear double divergences cancel in the appropriate sum with the real corrections, whereas pure collinear divergences need to be subtracted, as shown in Section 4.9. This is all that can be done with the virtual corrections to the qq-channel for now. The remaining virtual corrections to the partonic channels follow an analogous strategy. Differences and subtleties unique to each will be discussed in the following sections.

6.1.2 Virtual Corrections to the qg-Channel

The virtual corrections to the qg-channel are calculated in close analogy to those of the qq-channel. The Feynman diagrams for the virtual correction to the qg-channel are depicted in Figure 6.5. The first two diagrams are vertex corrections to the strong vertex of the leading-order s-channel, followed by the vertex correction to the QED vertex, and the

two QCD vertex corrections to the t-channel.
As for the qq-channel, the diagrams with closed fermion loops do not contribute in their sum because the diagrams with reversed fermion flow cancel each other for massless particles. Therefore, the diagrams $v_6, ..., v_9$ can be ignored in the following.
Diagram v_{10} is the correction to the QED vertex of the leading-order s-channel, followed by the three box diagrams. The last two diagrams are the propagator corrections to the leading-order s- and t-channels, respectively.
The methodology developed for the calculation of the virtual corrections to the qq-channel carries over seamlessly to the qg-channel. The computational strategy remains the same:

- Reduce tensor loop integrals using Passarino-Veltaman reduction,
- construct the interference with the Born-level terms,
- apply Casimir's trick, perform the polarization sum and evaluate the color algebra,
- contract with the decomposition tensors $\tilde{\mathcal{V}}_k^{\mu\nu}$ to isolate the structure functions,
- evaluate the scalar integrals by employing the `PackageX` library via `FeynHelpers`,
- integrate over phase space,
- transition to the variables v and w and finally
- renormalize the UV divergences in the $\overline{\text{MS}}$ scheme.

Although the general steps are unchanged, the Dirac structure and color factors differ because the starting Feynman diagrams differ. Furthermore, the hadronizing particle, which becomes the observed hadron, changes. The averaging factors remain the same since the incoming and outgoing particles are the same. Care must be taken when applying the polarization sum of the gluon, since its momentum, relative to the qq-channel, changes.
When comparing the Feynman diagrams of the qq- and qg-channels, it is clear that they are related by the same crossing relation as the corresponding leading-order channels.
The results for the 55 relevant expressions after the contraction but before the evaluation of the scalar integrals are provided in separate files[5].

6.1.3 Virtual Corrections to the qg-Channel

The calculation of the virtual corrections to the qg-channel follows the same conceptual approach as in the qq- and qg-channels, with a few key differences due to the gluon

[5]They are also available, together with the generating code, upon request, at `https://github.com/DissKunzelmann/PhD`.

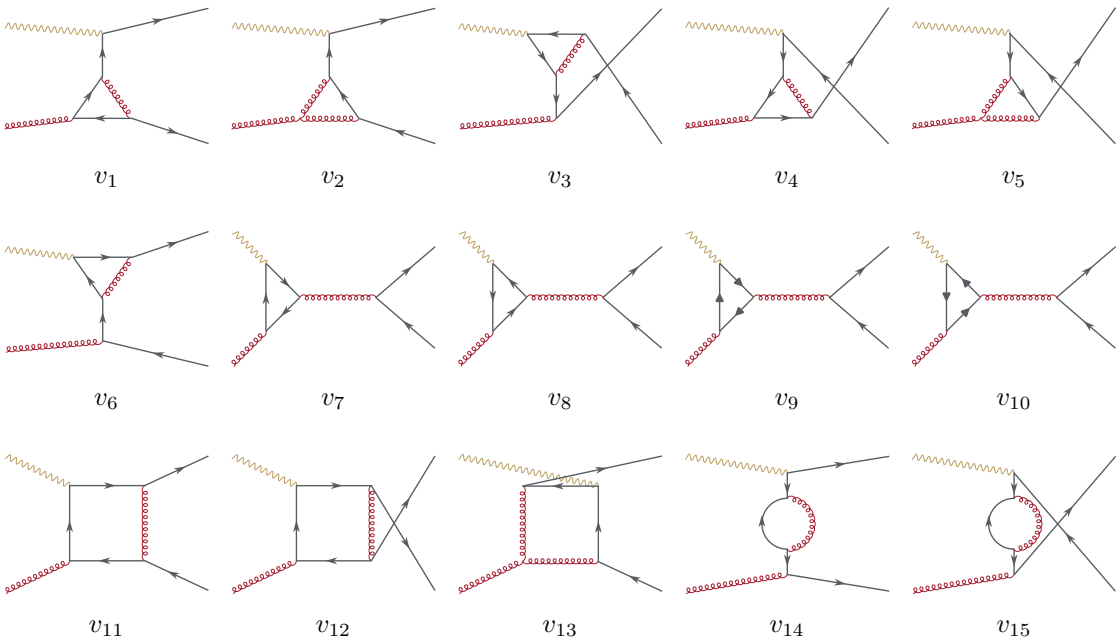

Figure 6.6: Feynman diagrams for the virtual corrections of the gq-channel. Fermions of different flavor are indicated by different arrow heads.

appearing in the initial state. These differences primarily affect the averaging factors.
As in the leading-order case, the average over the initial-state gluon polarization in d dimensions is given by

$$\frac{1}{d-2} = \frac{1}{2(1-\epsilon)} \,, \tag{6.11}$$

replacing the $1/2$ spin average used for initial-state fermions in the previous channels. Additionally, the color averaging factor changes to

$$\frac{1}{2C_A C_F} = \frac{1}{N^2-1} \tag{6.12}$$

for the color states of the incoming gluon.
The relevant one-loop Feynman diagrams contributing to the virtual corrections of the gq-channel are shown in Figure 6.6. The first two are QCD vertex corrections to the leading-order t-channel, followed by the correction to the QCD vertex and the two QCD vertex corrections to the u-channel, with the correction to the QED vertex for the t-channel being diagram v_6.
The following four diagrams $v_7, ..., v_{10}$ are the diagrams with closed fermion loops. The sum of these diagrams vanishes. Diagrams v_{11}, v_{12} and v_{13} are box diagrams, and the final

two diagrams give the next-to-leading order correction to the fermion propagator of the leading-order t- and u-channels, respectively.
The computational procedure mirrors that of the qq- and qg-channels. Tensor loop integrals are reduced using Passarino-Veltman techniques, interference terms between one-loop diagrams and the corresponding leading-order diagrams are constructed, Dirac traces, color factors, and polarization sums are performed, and the contraction with the tensors $\tilde{\mathcal{V}}_k^{\mu\nu}$ for $k = 0, ..., 4$ is made.
Care is required due to the different naming of the momenta of the particles and the changed averaging factors.
The complete set of 55 contributions is again provided in separate files, containing 11 contributions for a single projecting tensor, with all five different tensors[6].
As in the previous channels, the remaining steps, that is, the evaluation of the scalar integrals using the library for scalar integrals in `PackageX`, the change of variables to the dimensionless variables v and w, phase space integration, and the renormalization, remain analogous to the previous channel.
With the virtual contributions from all three partonic channels fully computed and renormalized, the calculation proceeds to the real emission contributions, which are essential for canceling infrared divergences and completing the next-to-leading order calculation.

6.2 Real Emission Diagrams

As alluded to in the introduction to the next-to-leading order, virtual corrections are not the only contributions at next-to-leading order. Real emission diagrams, characterized by the presence of one additional particle in the final state, must also be considered. These processes are essential not only for capturing the full interaction at next-to-leading order, but also for the cancellation of IR-divergences present in the virtual corrections.
The inclusion of an additional final-state particle increases the number of possible partonic processes that contribute at this order. The full list of contributing real emission channels is:

$$\begin{aligned}
&(qq_1) \quad \gamma^* q \to qgg && (qq_2) \quad \gamma^* q \to qq\bar{q} \\
&(qq_3) \quad \gamma^* q \to qq'\bar{q}' && (qq') \quad \gamma^* q \to q'q\bar{q}' \\
&(q\bar{q}) \quad \gamma^* q \to \bar{q}qq && (qg) \quad \gamma^* q \to gqg \\
&(gq) \quad \gamma^* g \to q\bar{q}g && (gg) \quad \gamma^* g \to gq\bar{q}\ ,
\end{aligned} \tag{6.13}$$

[6]The complete code and the results are also available, upon request, at `https://github.com/DissKunzelmann/PhD`.

where each channel label, given in parentheses, is used to refer to the corresponding subprocess in the discussion below.
The notation is as follows: γ^* is the virtual photon, g a gluon, q a quark, $\bar{q}$ an antiquark, and q' and $\bar{q}'$ a quark and an antiquark of a different flavor. The fragmenting parton is, as always, the first parton after the arrow.
These eight channels all have different external states and therefore do not interfere with each other. However, each channel contributes to the hadronic interaction. Six of the channels come from a quark, and two from the gluon, as the interacting parton of the proton. The first three channels qq_1, qq_2 and qq_3 also have a quark as the fragmenting parton. These channels need to be considered together, since they all contribute to the interaction $\gamma^* q \to qX$. This is the channel coming from the leading-order qq-channel that, at next-to-leading order, also has contributions due to virtual corrections.
The channels qq' and $q\bar{q}$ also have an initial quark and fragmenting quark, but the outgoing measured quark is of a different nature than the incoming quark. Due to this difference, they do not contribute to the same interaction. The channel qq' contributes to the interaction $\gamma^* q \to q'X$, which does not have a lower-order equivalent and no virtual contributions. The same holds for the channel $q\bar{q}$, which contributes to $\gamma^* q \to \bar{q}X$ as the only channel at this order.
The channels qg and gq, however, contribute to $\gamma^* q \to gX$ and $\gamma^* g \to qX$, respectively, which both have contributions from lower-order terms and from virtual corrections.
The last channel gg contributes to $\gamma^* g \to gX$, which does not appear at lower order and does not receive contributions from virtual corrections.
This section provides a systematic overview of the explicit calculation of the real corrections, beginning with the most complex case, the qq-channel, which includes multiple subprocesses with identical initial and fragmenting partons but different spectator partons.
The subsequent sections address the remaining channels and highlight their unique features.

6.2.1 Real Corrections to the qq-Channel

The Feynman diagrams contributing to the interaction $\gamma^* q \to qX$ are split into three distinct channels that do not interfere with each other. These channels were described above; they are the qq_1-, qq_2-, and qq_3-channels. The Feynman diagrams for these channels are shown in Figures 6.7, 6.9, and 6.10, respectively. An additional complication arises as a consequence of the gluon polarization. To be able to use the simple polarization sum for the gluons given in Equation (5.14), the need to subtract the unphysical polarizations

included in this sum arises. This is done throughout this thesis by introducing ghost terms. These will exactly cancel the unphysical terms that are included in the polarization sum. The Feynman diagrams for the ghost contributions are shown in Figure 6.8, and must be supplemented with their counterparts, where the direction of the ghost lines is reverted. Since these diagrams yield identical results, they result in a factor of two.
A equivalent approach would be to use the full polarization sum

$$\sum_{\lambda} \epsilon_{\lambda}^{\rho}(k)\epsilon_{\lambda}^{*\sigma}(k) = -g^{\rho\sigma} + \frac{k^{\rho}n^{\sigma}}{k\cdot n} + \frac{k^{\sigma}n^{\rho}}{k\cdot n} - \frac{n^2 k^{\rho}k^{\sigma}}{(k\cdot n)^2} \ , \tag{6.14}$$

with the auxiliary vector n satisfying $k_2 \cdot n \neq 0$. Although the final result is independent of the choice of n, it is beneficial to select a vector that is already present in the calculation. A common choice is the momentum of the other outgoing gluon. When using this polarization sum, unphysical polarization directions are excluded automatically, and ghost contributions become unnecessary.
Although using the full polarization sum provides a formally complete and theoretically elegant method, it leads to significantly more complex expressions for the squared matrix amplitudes. Given the already substantial computational cost of evaluating the diagrams with the simplified polarization sum, using the full form would result in prohibitively long calculation times.
Thus, the approach in this thesis, namely, using the simplified polarization sum combined with explicit ghost contributions, offers a simple and computationally efficient strategy. Moreover, the ghost diagrams do not interfere with diagrams that do not contain ghosts and can be calculated independently.

Calculation of the qq_1-Channel

The general procedure for computing real emission corrections is similar for all diagrams. To illustrate this approach, consider the first diagram in the qq_1-channel. Using Feynman Rules, its matrix element is given by

$$\mathrm{i}\mathcal{M}_1^{\mu} = -\mathrm{i}e_q g_s^2 \frac{\bar{u}(k_1)\gamma_{\sigma}(\not{k}_1+\not{k}_2)\gamma_{\rho}(\not{k}_1+\not{k}_2+\not{k}_3)\gamma^{\mu}u(p)}{(k_1+k_2)^2(k_1+k_2+k_3)^2}\epsilon_{\lambda}^{*\sigma}(k_2)\epsilon_{\lambda}^{*\rho}(k_3)T_{ij}^{a}T_{jk}^{b} \ . \tag{6.15}$$

As in the leading-order calculation, the first step is to square the amplitude. In the qq_1-channel, there are eight contributing Feynman diagrams. Consequently, the squared

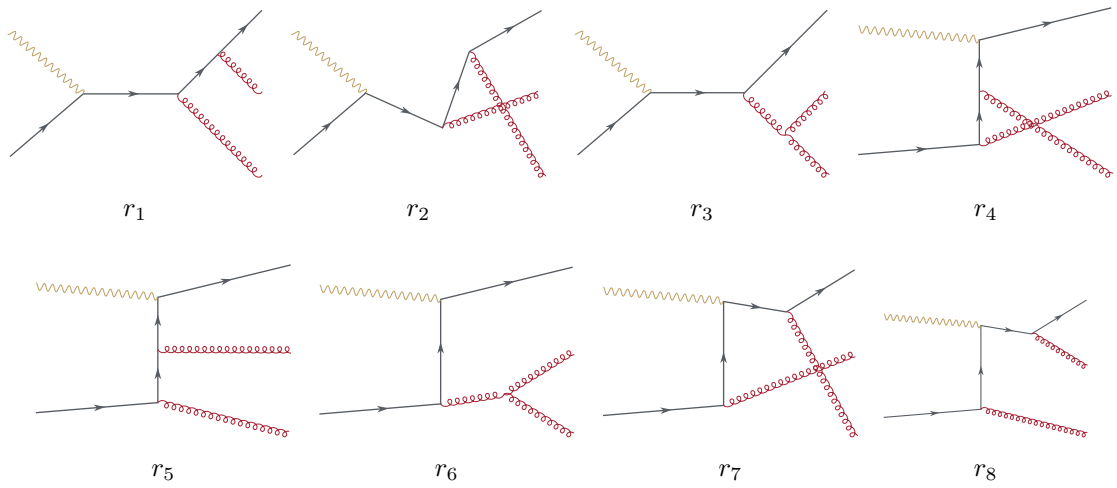

Figure 6.7: Feynman diagrams for the real corrections in the qq_1-channel.

matrix element includes all self- and cross-interference terms:

$$\left|\sum_{n=1}^{8}\mathcal{M}_n\right|^2 = \sum_{n=1}^{8}|\mathcal{M}_n|^2 + \sum_{n=1}^{8}\sum_{m=n+1}^{8}\left(\mathcal{M}_n\mathcal{M}_m^* + \mathcal{M}_m\mathcal{M}_n^*\right) \ . \tag{6.16}$$

This results in 36 distinct matrix elements, which are calculated separately. For each of these, contractions with all five projecting tensors $\tilde{\mathcal{V}}_0^{\mu\nu}, ..., \tilde{\mathcal{V}}_4^{\mu\nu}$ are performed, resulting in 180 contributions to the subchannel qq_1 alone. This clearly demonstrates the necessity of a fully automated computation workflow.

Continuing with the first diagram and considering the self-interference. The color factor for this interference is

$$\mathrm{Tr}(T_aT_bT_bT_a) = \frac{1}{4N}(N^2-1)^2 = C_AC_F^2 \ , \tag{6.17}$$

with the Casimir operators $C_F = (N^2-1)/(2N)$ and $C_A = N$ from Equations (2.22) and (2.23). Including the averaging factor for the incoming color of the quark, $1/C_A$, the total color factor becomes C_F^2.

After contracting with $\tilde{\mathcal{V}}_0^{\mu\nu} = g^{\mu\nu}$, and averaging over the incoming spins and colors, while summing over all outgoing spins, colors, and polarizations of both outgoing gluons, the result is

$$g_{\mu\nu}\overline{\sum}\mathcal{M}_1^{\mu}\mathcal{M}_1^{*\nu} = 16\pi^2(d-2)^3e_q^2\alpha_s^2C_F^2\frac{\left(\left((q-k_2)^2+Q^2\right)\left((p+q)^2+Q^2\right)+Q^2\left(p-k_1\right)^2\right)}{(k_1+k_2)^2(p+q)^4} \tag{6.18}$$

where the momentum k_3 is replaced due to momentum conservation by $k_3 = p + q - k_1 - k_2$ and the fact that all external quarks and gluons are massless is used. Furthermore, the strong coupling constant $\alpha_s = g_s^2/(4\pi)$ was introduced. In terms of the expanded Mandelstam variables defined in Equation (3.91), it can be written as

$$g_{\mu\nu}\overline{\sum}\mathcal{M}_1^{\mu}\mathcal{M}_1^{*\nu} = 16\pi^2(d-2)^3 e_q^2\alpha_s^2 C_F^2 \frac{\left(\left(t_2+Q^2\right)\left(s+Q^2\right)+Q^2u\right)}{s_{12}s^2} \,. \tag{6.19}$$

The next step is to perform the phase space integration. The full derivation of the three-particle phase space is discussed in Section 4.7.2. In terms of the Mandelstam variables, the three-particle phase space in $d = 4 - 2\epsilon$ dimensions is (4.128):

$$\int \mathrm{dPS}_3 = \int \mathrm{d}t\mathrm{d}u \frac{1}{(4\pi)^{4-2\epsilon}\Gamma(1-2\epsilon)} \frac{1}{s+Q^2} \left(s_{23}\right)^{-\epsilon} \left(\frac{u\left(st+Q^2s_{23}\right)}{\left(s+Q^2\right)^2}\right)^{-\epsilon} \int \mathrm{d}\Omega_{\theta_1\theta_2} \,. \tag{6.20}$$

Together with the phase space, the Møller flux factor $F = 2s'$ (2.75) can be introduced here.

The projected and averaged square matrix element of (6.18) contains the angular-dependent momentum k_2. This results in a nontrivial angular integration for the phase space integral. The procedure for the angular integration is explained in detail in Section 4.8. The expression for the example contains only two angular-dependent Mandelstam variables. In this case, the angular integrals can be evaluated directly without the need for partial fraction decomposition. Keeping in mind, that the integral over a trivial constant function also has to be evaluated to give $2\pi/(1-2\epsilon)$. In contrast, many of the remaining interference terms are significantly more complex and do require careful partial fractioning before the angular integrals can be evaluated using the analytical solutions provided in [241].

In practice, both the partial fractioning and evaluation of the angular integrals are handled by a script provided by one of the authors of [241], Fabian Wunder, which automates the procedure described in Section 4.8 in `Mathematica`, providing a streamlined integration of three-particle phase space integration to the analytical evaluation of real corrections. It is important to choose the correct threshold conditions to allow terms that vanish in the limit to remain unexpanded. The relevant threshold in this case is $s_{23} \to 0$.

In this limit, the limit of soft radiation, an additional subtlety arises. It is best understood in terms of the dimensionless variables v and w. Some integrals behave like $1/(1-w)$, which can be traced back to a vanishing invariant mass of the unobserved particles $s_{23} = (k_2 + k_3)^2 = sv(1-w)$. This behavior is obvious for diagrams of the form of Diagrams r_3 and r_6 in Figure 6.7, but also arises in other combinations of diagrams,

Figure 6.8: Ghost diagrams contributing to the qq-channel.

where a propagator proportional to the virtuality of the unobserved particles appears. The factor $1/(1-w)$ diverges for $w \to 1$ and is combined with the factor $(1-w)^{-\epsilon}$ of the phase space (4.127) to become $(1-w)^{-1-\epsilon}$.
To render this divergence at $w \to 1$ explicit, this factor is expanded using the plus distribution

$$(1-w)^{-1-\epsilon} = -\frac{1}{\epsilon}\delta(1-w) + \frac{1}{(1-w)_+} - \epsilon \left(\frac{\ln(1-w)}{1-w}\right)_+ + \mathcal{O}(\epsilon^2) \,, \tag{6.21}$$

where the plus distribution is defined in Equation (2.126). In `Mathematica`, the implementation of this procedure first requires the isolation of all terms proportional to $1/(1-w)$. This is accomplished via a custom function "explicitW" presented in Appendix B.2. Having all divergent $1/(1-w)$ terms in the same form, they can be expanded using the plus distribution. For a significant speedup and the guarantee that all relevant terms are converted, a slightly modified version of the function "ToDistribution" is used. The modified version is also shown in Appendix B.2.
After this replacement is made, the cross section can be fully expanded in ϵ, since now all possibly divergent terms are explicit. The expansion is performed up to order $\mathcal{O}(\epsilon^0)$ and contains up to quadratic divergences that come with a factor $1/\epsilon^2$. The quadratic poles are soft and collinear poles that cancel with their counterparts in the virtual corrections upon building the appropriate sum of real and virtual corrections. Linear poles, which come with a factor of $1/\epsilon$, are either soft or collinear, where only some of those poles cancel in the sum of real and virtual corrections. The remaining collinear poles need to be factored into the collinear PDFs and FFs. This is done at a later stage.
To eliminate the unphysical polarizations introduced via the simple form of the gluon polarization sum (5.14), the ghost diagrams must be added to this subchannel. The matrix elements for the ghost diagrams in Figure 6.8 are given by

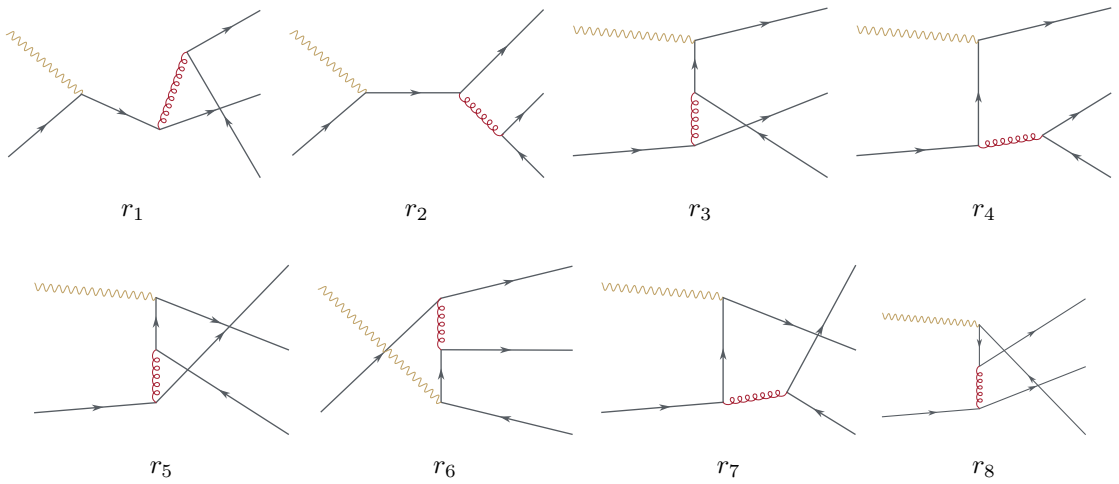

Figure 6.9: Feynman diagrams for the real corrections in the qq_2-channel.

$$\mathrm{i}\mathcal{M}^{\mu}_{1\mathrm{ghost}} = -e_q g_s^2 f_{abc} T^a_{ij} \frac{\bar{u}(k_1)\not{k}_2(\not{p}+\not{q})\gamma^{\mu}u(p)}{(k_2+k_3)^2(p+q)^2} \tag{6.22}$$

$$\mathrm{i}\mathcal{M}^{\mu}_{2\mathrm{ghost}} = -e_q g_s^2 f_{abc} T^a_{ij} \frac{\bar{u}(k_1)\gamma^{\mu}(\not{p}-\not{k}_2-\not{k}_3)\not{k}_1 u(p)}{(k_2+k_3)^2(p-k_2-k_3)^2} \ . \tag{6.23}$$

The evaluation of these ghost diagrams follows the same procedure as explained above. The two ghost diagrams only interfere with each other; therefore, there are only three different squared matrix elements to be accounted for.
After squaring the sum of the two diagrams and projecting via the tensors $\tilde{\mathcal{V}}_0^{\mu\nu}, ..., \tilde{\mathcal{V}}_4^{\mu\nu}$, Casimir's trick is used to generate a Dirac trace. The result is simplified and integrated using the same procedure as described above. After phase space integration, the poles for $w \to 1$ are made explicit with the introduction of the plus distribution, as for the other diagrams, and the result is expanded in ϵ up to order $\mathcal{O}(\epsilon^0)$. The results for the ghost diagrams with both ghost flow directions are then subtracted from the above-calculated rest of the subchannel qq_1. The diagrams with the inverse ghost flow are different to start with, but after phase space integration, they match the results for the original ghost flow direction, resulting in a factor of 2 for the inclusion of the other flow direction.
This completes the calculation of the qq_1-subchannel, and the remaining subchannels contributing to the qq-channel need to be evaluated.

The other subchannels of the qq-Channel

Subchannels qq_2 and qq_3 are evaluated using the same general methodology as the qq_1-channel discussed above. In these two channels, the outgoing gluon pair is replaced by a quark-antiquark pair. For qq_2 of the same flavor as the incoming quark and for qq_3 a

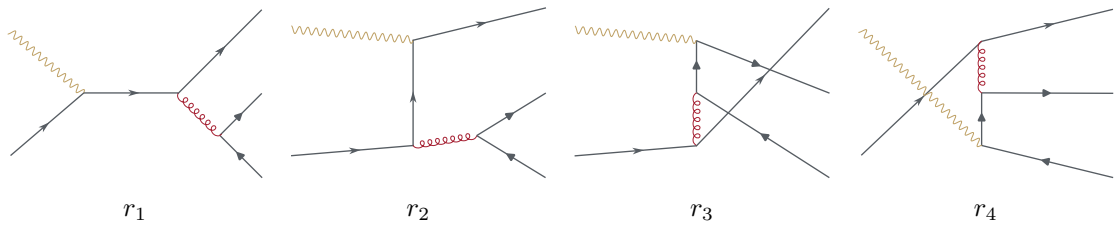

Figure 6.10: Feynman diagrams for the real corrections in the qq_3-channel. Fermions of a different flavor are symbolized by a different arrow head.

different flavor. This change in the final state means that the gluon polarization sum of the subchannel qq_1 is no longer present, and consequently, no accompanying ghost diagrams are required for the subchannels qq_2 and qq_3.
Due to the additional fermion, Casimir's trick results in up to two Dirac traces. In particular, for topologies shared between the subchannels qq_2 and qq_3, Casimir's trick does result in two traces due to the different flavors present in qq_3. The diagrams for these two subchannels, qq_2 and qq_3 are depicted in Figures 6.9 and 6.10, respectively.
The procedure is as follows:

- Construct interference term,
- contract them with the tensors $\tilde{\mathcal{V}}_0^{\mu\nu}, ..., \tilde{\mathcal{V}}_4^{\mu\nu}$,
- apply Casimir's trick and the averaging factors,
- perform Dirac and color simplifications,
- integrate over the three particle phase space using the procedure of Section 4.8,
- make the divergent terms for $w \to 1$ explicit via plus distributions, and finally
- expand the result in ϵ, and incorporate the Møller flux factor.

The averaging factors remain the same because the incident particle is still a quark.

Subtleties for the qq_3-Subchannel

In the subchannel qq_3, the flavor of the quark in the additional trace is different from that of the initial quark. This introduces several important subtleties in the calculation:

The contribution of the subchannel qq_3 must be multiplied by $N_f - 1$, the number of possible quark flavors of the unobserved quark, where N_f denotes the number of active quark flavors and the minus one accounts for the fact that contributions with

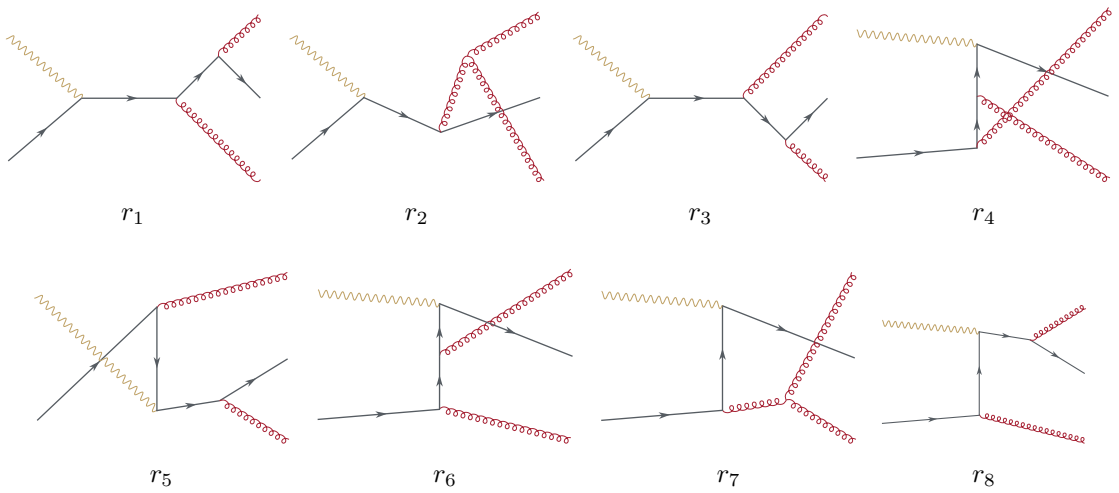

Figure 6.11: Feynman diagrams for the real corrections in the qg-channel.

the same quark flavor as for the incident quark are already included in the subchannel qq_2.

The virtual photon can couple to both the initial state quark and the unobserved final state pair with possibly different coupling strengths, e_q for the former and e'_q for the latter. The squared matrix element contains, a priori, three types of terms: one with e_q^2, one with $e_q e_{q'}$ and one with $e_{q'}^2$. However, due to the symmetry of the last two diagrams, contributions that would come with $e_q e_{q'}$ cancel after phase space integration. This is due to the fact that the phase space integration also includes the inversion of charge flow.

A consequence of this cancellation is that the contributions to the charge conjugated process $\gamma^* \bar{q} \to q q' \bar{q}'$ are equivalent to the results for the non charge conjugated process. Note that the charge of the second quark q' is not changed, since this is already handled by phase space integration. A separate inclusion of the process $\gamma^* \bar{q} \to q \bar{q}' q'$ would lead to double counting.

Adding the three subchannels qq_1, with the ghost contributions, qq_2, and qq_3 with the quark flavor factor $N_f - 1$ completes the real corrections to the qq-channel. The results for the three subchannels, qq_1, qq_2, and qq_3 are provided in a separate file[7].

Figure 6.12: Ghost diagrams contributing to the qg-channel.

6.2.2 Real Corrections to the qg-Channel

The real corrections to the qg-channel stem exclusively from the interaction $\gamma^* q \to gqg$, which features two gluons in the final state. The diagrams contributing to this channel are shown in Figure 6.11. As in the subchannel qq_1, the presence of two gluons in external states necessitates a careful treatment of the gluon polarization sum. To simplify the calculation and reduce the computational cost, the polarization sum is used in its simple form, which includes unphysical polarizations. Ghost contributions must be included to systematically cancel theses. The ghost contributions are shown in Figure 6.12. As before, diagrams with reversed ghost flow also contribute, and - unlike in the qq_1-case - these yield genuinely different results. Therefore, the contributions from both ghost flow directions to the qg-channel are calculated separately. Just like the leading-order and the virtual corrections terms, the expressions for this channel are closely related to those of the qq-channel. Specifically, they are related to the qq_1-channel via crossing relations.
The averaging factors remain the same since the incoming state did not change. And the general procedure for calculating the real corrections is also unchanged: the interference terms are generated using FeynArts and `FeynCalc` and contracted with the tensors $\tilde{\mathcal{V}}_0^{\mu\nu}, ..., \tilde{\mathcal{V}}_4^{\mu\nu}$. The polarization sum with (5.14) is executed for both gluons. Casimir's trick is applied, and the Dirac trace is simplified. Thereafter, the integration over three-particle phase space is performed using the procedure laid out in Sections 4.7.2 and 4.8, including the introduction of the flux factor. The divergent terms for $w \to 1$ are made explicit using the plus distribution, and the result is expanded in ϵ. Therefore, the standard procedure for calculating these corrections remains unchanged, albeit still computationally expensive.
The same procedure is followed to calculate the two ghost contributions with different flow directions. The results for the ghost contributions are subtracted from the $\gamma^* q \to gqg$ interaction terms to remove the unphysical polarizations. The results from this subtraction,

[7] Available, upon request, at `https://github.com/DissKunzelmann/PhD`.

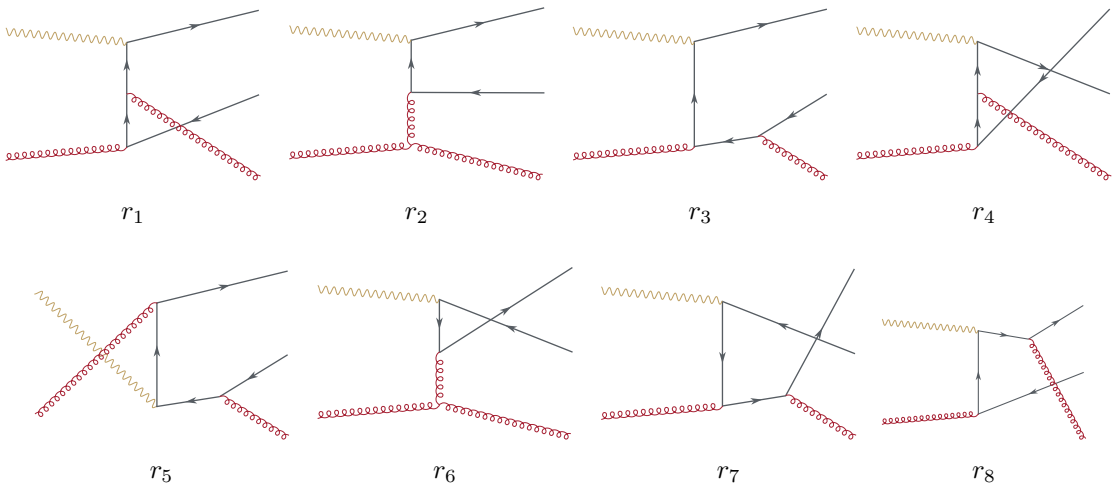

Figure 6.13: Feynman diagrams for the real corrections in the gq-channel.

Figure 6.14: Ghost diagrams contributing to the gq-channel.

and with that, the complete set of real corrections to the qg-channel for all five tensor projections are provided in a separate file[8].

6.2.3 Real Corrections to the gq-Channel

The corrections to the gq-channel due to emission of an additional gluon are depicted in Figure 6.13. In this channel, the incident particle is a gluon, changing the averaging factors from above. There is no longer an average over incident fermion spin, but rather an average over the $1/(d-2)$ polarization states of the incident gluon. In addition, the color averaging factor for an incident gluon, $1/(2C_A C_F)$, needs to be taken into account, as was the case for the born and virtual contributions.
Similar to the channels above, the simple polarization sum used for the gluon introduces unphysical polarization states, which need to be subtracted via ghost terms. These ghost contributions are shown in Figure 6.14, where the diagrams with inverted ghost flow are omitted but need to be calculated. For the ghost terms, the same averaging factors as

[8] Available, upon request, at `https://github.com/DissKunzelmann/PhD`.

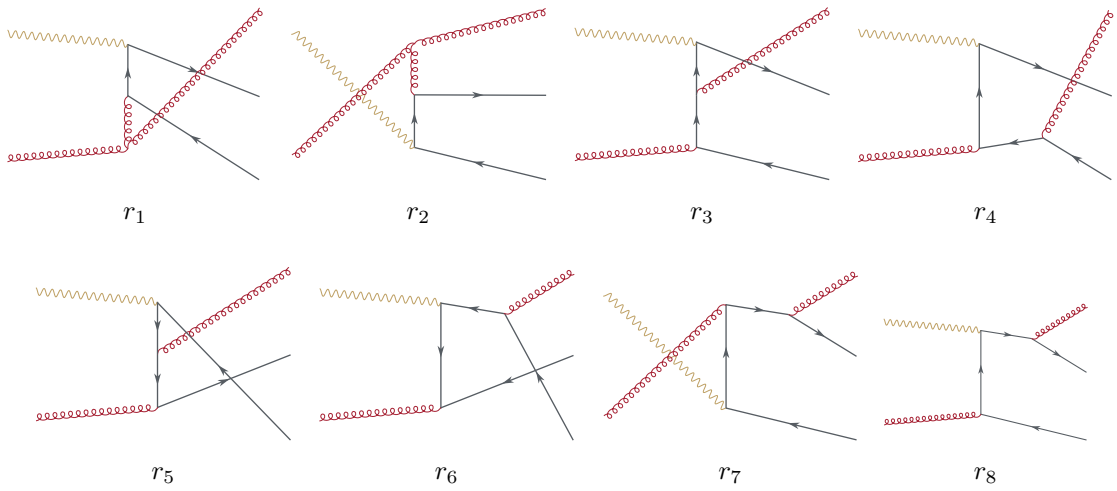

Figure 6.15: Feynman diagrams for the real corrections in the gg-channel.

Figure 6.16: Ghost diagrams contributing to the gg-channel.

for the rest of the channel need to be used to retain the corrective power of the ghost contributions.

Except for these differences, the standard, but computationally intensive, procedure is applied: Building the 36 interference terms, contracting them with the five tensors $\tilde{\mathcal{V}}_k^{\mu\nu}$, performing the polarization sum, and Casimir's trick, applying the averaging factors, simplifying color and Dirac expressions, integrating over three-particle phase space, expressing the $(1-w)^{-1-\epsilon}$ terms with distributions, and expanding the result in ϵ. From this result, the two ghost contributions are subtracted. This concludes the real corrections to the gq-channel, for which the results are presented for all five projection tensors in a dedicated file[9].

6.2.4 Real Emission Diagrams for the gg-Channel

The channel gg and all remaining channels are distinct in that they do not have lower-order counterparts. They first appear at order $\mathcal{O}(\alpha_s^2)$, which means that no virtual corrections

[9] Available, upon request, at `https://github.com/DissKunzelmann/PhD`.

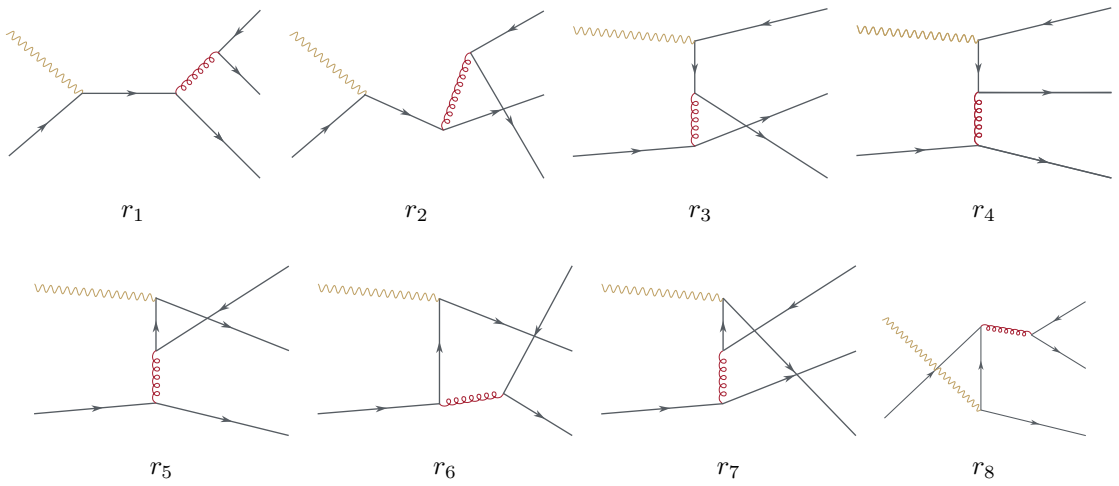

Figure 6.17: Feynman diagrams for the real corrections in the $q\bar{q}$-channel.

exist that could eliminate possible soft divergences. Nevertheless, these terms are still divergent. They exhibit collinear divergence, which must be accounted for by virtue of the splitting functions presented in Section 2.6.2.
The diagrams contributing to this channel are presented in Figure 6.15.
As for the channels above the ghost diagrams of Figure 6.16 need to be considered to eliminate the unphysical polarizations introduced by the simple polarization sum, which needs to be used for the real correction in order to achieve a manageable computing time. Figure 6.16 again only shows one ghost flow direction, but both directions contribute and need to be calculated.
The procedure for calculating these real corrections remains the same. The results are presented in the supplementary files[10].
Also note that there is no charge conjugation for this channel. The interaction $\gamma^* g \to g\bar{q}q$ is already taken care of via phase space integration. Therefore, it must not be included to avoid double counting.

6.2.5 Real Emission Diagrams for the $q\bar{q}$-Channel

As for the gg-channel above, the $q\bar{q}$-channel does not have a complementary contribution from a lower order in perturbation theory. Consequently, all divergences arising in the calculation of this channel need to be collinear divergences that can be subtracted by absorbing them into the distribution and fragmentation functions.
In this process, a quark from the proton participates in the interaction, and the observed final-state hadron originates from an antiquark. This setup requires the production of a

[10]Results and code are available, upon request, at `https://github.com/DissKunzelmann/PhD`.

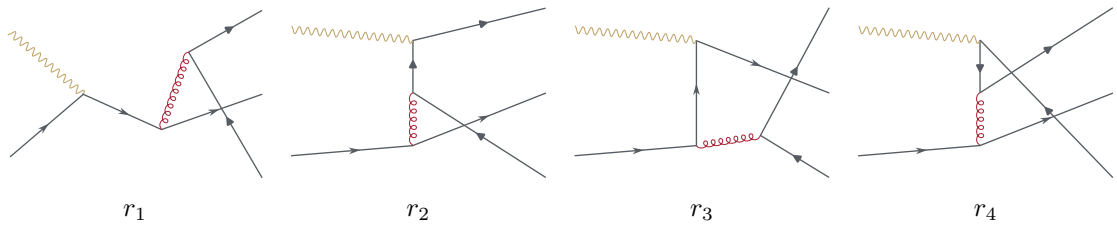

r_1 r_2 r_3 r_4

Figure 6.18: Feynman diagrams for the real corrections in the qq'-channel. Fermions of the flavor q' are symbolized by the rounded arrow head.

quark-antiquark pair in the final state, in addition to the quark coming from the proton. In this case, the two final state quarks are of the same flavor, which allows for a symmetry between the two unobserved final state quarks.
The diagrams contributing to the channel $q\bar{q}$ are shown in Figure 6.17.
Unlike all previous channels, the $q\bar{q}$-channel does not require the introduction of ghost diagrams. This is because all external particles are fermions, and no polarization sum has to be taken.
The incident particle is again a quark; therefore, the averaging factors need to be changed back to the average over the initial spin, which is $1/2$, and the average over the initial color of the quark $1/C_A$. The general steps for calculating the real emission diagrams of the $q\bar{q}$-channel remain unchanged. The results are provided in extra files[11].

6.2.6 Real Emission Diagrams for the qq'-Channel

The final channel to be considered is the channel qq'. As with the two previous channels, there is no equivalent channel at a lower order. The particular feature of this channel is that the fragmenting quark has a different flavor from the quark coming from the proton. As for the subchannel qq_3 this limits the possible contributing Feynman diagrams, which are depicted in Figure 6.18. There are no initial or final state gluons; therefore, no ghost contributions need to be considered. Due to the fact that there are always two different quarks present, there are two Dirac traces, which are both shorter than the single traces of all other channels, except for subchannel qq_3. These two are by far the computationally lightest channels, requiring the least amount of computation time. Nevertheless, this channel is quite interesting, since it is the only one where special care needs to be taken when applying charge conjugation.
The results for this channel contain terms proportional to e_q^2, $e_{q'}^2$ and contributions proportional to $e_q e_{q'}$. The latter change sign when switching to the process $\gamma^* \bar{q} \to q'\bar{q}\bar{q}'$ or $\gamma^* q \to \bar{q}' q q'$, making this the only channel with different results for charge-conjugated

[11] Results and code are available, upon request, at `https://github.com/DissKunzelmann/PhD`.

states. When both particles are simultaneously charge-conjugated, the result remains unchanged.
The results for the qq'-channel are given, as the results for the other channels in separate files[12].

6.3 Combining Channels and Subtracting Collinear Poles

The final stage of the next-to-leading order calculation involves combining the real and virtual corrections and subsequently subtracting the remaining collinear divergences to isolate the finite hard part of the partonic cross section. This hard part can then be used via the factorization theorem to get the result for the hadronic interaction.
With both the real and virtual contributions now expressed in terms of the dimensionless variables v and w, the initial combination is straightforward but provides a powerful first check for the correctness of the results. Specifically, in the sum of real and virtual corrections to the same channel, all quadratic poles in ϵ need to cancel. This was checked explicitly for each channel and all five tensor projections. For the qq-channel, only the virtual correction and the subchannel qq_1 have poles of the form $1/\epsilon^2$ and these cancel in the sum. All other subchannels, qq_2 and qq_3 contributing to the real corrections of the qq-channel only come with linear poles, i.e., poles in $1/\epsilon$. This is to be expected since there are no lower-order contributions to those subchannels. Yet, all subchannels and the contribution from the splitting functions, which will be discussed below, need to be combined to cancel the remaining linear divergences.
Similarly, the channels gg, $q\bar{q}$ and qq' also lack lower-order counterparts and therefore may not contain soft-collinear double poles. In fact, they do only contain linear poles and finite terms.
The qg- and gq-channels exhibit quadratic divergence, but these cancel completely once their respective real and virtual contributions are summed.
Another simple check is that all quadratic poles need to have the same structure in the variables v, w and s', as their leading-order counterparts. The coefficient will be different due to different color factors and coupling constants. This was explicitly checked for all channels and projectors.
After real and virtual corrections are combined, the resulting expressions only contain linear poles in ϵ. In fact, these are only collinear poles. All the linear soft poles did already cancel in the sum.
The remaining collinear poles need to be subtracted using the procedure detailed in Section 4.9. The qq-channel receives contributions from four different terms. There are two

[12] And are available, upon request, at `https://github.com/DissKunzelmann/PhD`.

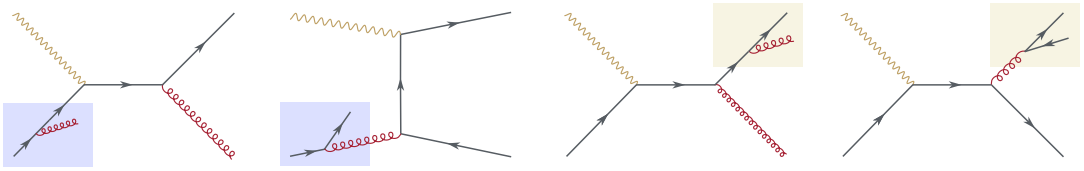

Figure 6.19: Splittings for the qq-channel.

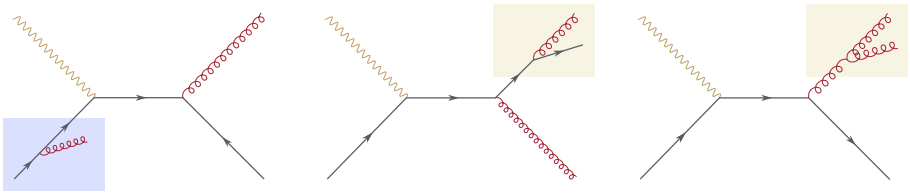

Figure 6.20: Splittings for the qg-channel.

splittings for the incident particle and two for the outgoing particles. For the incident quark, the possible splittings are $q \to qg$ and $q \to gq$, where the first particle on the right is the particle that contributes to the scattering. For both, it is possible to find born-level diagrams that result in a final quark. In the first case, the quark-quark splitting, the born level term is the interaction $\gamma^* q \to qg$, for a splitting quark into gluon the born level term is $\gamma^* g \to q\bar{q}$. The same procedure holds for the splitting of the outgoing quark. These contributions are depicted in Figure 6.19.

The qg-channel was described in detail in Section 4.9. In this case, only one splitting is possible for the incident particle and two for the outgoing particle. For completeness, the contributing diagrams are shown here again in Figure 6.20.

For the gq-channel, this is reversed, and there are two possible splittings for the incident particle and only one for the outgoing particle. This is again due to the fact that at $\mathcal{O}(\alpha_s)$ there is no gg-channel that could take the role of the leading order contribution. These diagrams are shown in Figure 6.21.

For channels that do not appear at $\mathcal{O}(\alpha_s)$, such as the gg-, $q\bar{q}$-, and qq'-channels, no soft

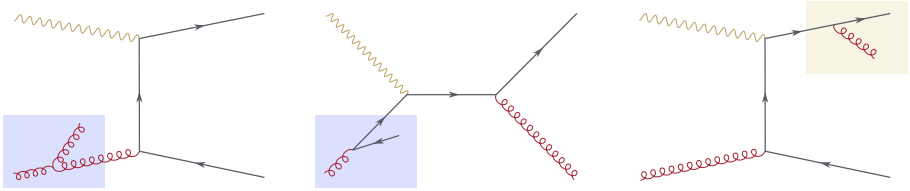

Figure 6.21: Splittings for the gq-channel.

Figure 6.22: Splittings for the gg-channel.

Figure 6.23: Splittings for the $q\bar{q}$-channel.

divergences are present. However, they still contain collinear divergences that need to be accounted for. This is also done using the splitting functions. For the gg-channel, the splitting cannot be a gluon-gluon splitting because, as mentioned above, there is no lower order gg interaction. Therefore, the only possibility for a splitting is a gluon to quark splitting for the incident gluon and a quark to gluon splitting on the outgoing gluon. These two contributions are depicted in Figure 6.22.
Similarly, the $q\bar{q}$-channel only receives two contributions because the outgoing particle needs to be an antiquark, which limits the choices. There is again one splitting, a quark to gluon splitting for the incident particle, and a gluon to quark splitting for the outgoing particle. The diagrams are illustrated in Figure 6.23.
The final channel, the qq'-channel, comes with a subtlety that is not present in the other cases. Here, the initial and final observed partons are of different flavors. This restricts the possible splittings. Additionally, the electromagnetic coupling of the two different quark flavors might be different, which needs to be taken into account. The possible splittings are the same as for the $q\bar{q}$-channel, a quark to gluon splitting for the incident quark, and a gluon to quark splitting at the outgoing leg. However, the contributions from the lower-order diagrams include the electric charge of the respective quarks. This means that the first diagram in Figure 6.24 comes with an electric coupling constant of e'_q, instead of e_q as in the $q\bar{q}$-channel. In the second diagram, the incident quark couples to the photon, which results in the coupling constant e_q, as before. This is reflected in the pole structure of the qq'-channel, where there is one contribution proportional to e_q^2 and one proportional

Figure 6.24: Splittings for the qq'-channel. Quarks of the flavor q' are indicated by rounded arrow heads.

to $e_{q'}^2$. Both of which cancel with the contributions from the splitting functions.
All contributions from the splitting functions are calculated for every projecting tensor $\tilde{\mathcal{V}}_k^{\mu\nu}$ using the procedure described in Section 4.9.
The resulting expressions include contributions involving the distributions $\delta(1-w)$ and $\left(\frac{1}{1-w}\right)_+$, with coefficients that also contain the variable w. To simplify the subtraction and facilitate the pole cancellation, the dependence on w for the coefficient functions is eliminated using the properties of the δ and $+$ distributions. It holds

$$\begin{aligned} & f(v,w) + g(v,w)\delta(1-w) + h(v,w)\left(\frac{1}{1-w}\right)_+ \\ =\, & f(v,w) + g(v,1)\delta(1-w) + h(v,1)\left(\frac{1}{1-w}\right)_+ - \frac{h(v,1)-h(v,w)}{1-w} \\ =\, & \tilde{f}(v,w) + g(v,1)\delta(1-w) + h(v,1)\left(\frac{1}{1-w}\right)_+ , \end{aligned} \tag{6.24}$$

where the functions $f, \tilde{f}, g$ and h do not contain the distributions $\delta(1-w)$ and $\left(\frac{1}{1-w}\right)_+$.
In the last line the function

$$\tilde{f}(v,w) = f(v,w) - \frac{h(v,1)-h(v,w)}{1-w} \tag{6.25}$$

was introduced.
Having simplified the distributions, the only remaining functions that hide the cancellation of the linear poles are the logarithms. The simplest way to get all of them in the same form is to expand the logarithms as far as possible using

$$\log(ab) = \log(a) + \log(b) \tag{6.26}$$

repeatedly, always keeping track of the sign of the factors. There is one combination of variables that must be handled with care; the combination $Q^2 - s'v$ can have both signs,

depending on the value of v. Here, the two cases $Q^2 > s'v$ and $Q^2 < s'v$ need to be calculated separately. For $Q^2 > s'v$ the critical functions become

$$\sqrt{\frac{(Q^2 - s'v)^2}{(Q^2 + s'v)^2}} = \frac{Q^2 - s'v}{Q^2 + s'v} \,, \tag{6.27}$$

$$\log\left(\frac{Q^2(\sqrt{1-(4Q^2s'v)/(Q^2+s'v)^2}+1)}{s'v(1-\sqrt{1-(4Q^2s'v)/(Q^2+s'v)^2})}\right) = 2\log Q^2 - 2\log s' - 2\log v \,. \tag{6.28}$$

For $Q^2 < s'v$ the sign in the first equation changes, and the logarithm in the second equation vanishes. In the end, both cases yield the same result, and they can be combined once more.

With all simplifications completed, the final step is to subtract the collinear divergences for each of the six channels and all five projecting tensors. This resulted in 30 final expressions, all free of divergences. The UV divergences were absorbed via renormalization, and the soft divergences were canceled through a careful sum of all contributions to the same channel, so all virtual and real corrections to the same order. Finally, the collinear divergences are subtracted using general considerations about the origin of these divergences.

The remaining expressions define the finite hard part of the partonic cross sections. These results retain the full dependence on the angular structure, which is encoded in the decomposition of the hadronic tensor presented in Section 3.3. Each result is labeled in the format "finalTermChannelProjector.m", where "Channel" refers to one of the partonic processes "qq", "qg" or "gq", and "Projector" is the number "k" associated with the projecting tensor $\tilde{\mathcal{V}}_k^{\mu\nu}$ used in the contraction. They are provided together with all the intermediary steps in separate organized data files[13].

These hard partonic results serve as the hard parts in the factorization formula to obtain the hadronic interaction, while still retaining the explicit dependence on the angular distributions.

[13] And made available, upon request, at `https://github.com/DissKunzelmann/PhD`.

Chapter 7

Summary and Outlook

The primary objective of this thesis was to perform a comprehensive, fully differential next-to-leading order calculation of semi-inclusive deep inelastic scattering at high transverse momentum. Using the formalism of QCD factorization and a careful treatment of all arising divergences, the analysis succeeded in deriving the hard partonic scattering coefficients for all relevant partonic channels contributing to the hadronic process. Crucially, through a systematic decomposition of the hadronic and leptonic tensors, this derivation retains the full angular structure of the cross section, an aspect not previously resolved at this level of precision.
A central motivation for this work was to enable precise theoretical predictions for angular modulations in SIDIS observables, which will be accessible at high precision in future experiments at the Electron-Ion Collider.

This thesis began with a general introduction to the fundamental concepts of Quantum Chromodynamics, with a particular emphasis on the perturbative regime in Chapter 2. The basic principles and formalism for cross section calculations were established, laying the foundation for more advanced treatments that follow. The discussion then shifted to the analytic computation of cross sections beyond leading order, where the proper handling of divergences was a central challenge. After outlining the theoretical tools required for higher-order calculations, the focus turned specifically to semi-inclusive deep inelastic scattering at high transverse momentum.
The theoretical treatment of SIDIS in Chapter 3 began with a detailed discussion of the kinematics and a derivation of the fully differential cross section. This was followed by a careful decomposition of the hadronic tensor, which was then adapted to unpolarized SIDIS. Explicit expressions for the factorization of short- and long-distance effects derived earlier were explicitly applied to SIDIS. Thereafter, specialized variables optimized for

next-to-leading order calculations were introduced to facilitate the forthcoming derivations.

Chapter 4 addressed the technical complexities inherent in next-to-leading order calculations. Beginning with a discussion of color algebra and Dirac structures, the chapter introduced systematic tools, such as Passarino-Veltman reduction for loop integrals and a more recent method for performing phase space integrals. Each step necessary for a full analytic calculation of the next-to-leading order corrections was presented in a structured manner.

In Chapter 5, the complete leading-order calculation was performed. Each partonic channel was treated individually, and all relevant differences were explained. These calculations were cross-checked against existing results in the literature, while providing a level of detail often absent from standard references. For the first time, the results were derived using dimensional regularization up to order $\mathcal{O}(\epsilon^1)$, which is required for the next-to-leading order calculation. The factorization formula was explicitly applied to link the partonic cross sections to the hadronic cross section.

Chapter 6 represented the culmination of the preceding work, presenting the full analytic NLO calculation of SIDIS at high transverse momentum. All techniques and tools developed earlier were brought together to handle the intricacies and computational intensity of this task. The calculation was split into two main components: virtual corrections and real emissions. For the virtual corrections, all three channels were considered separately, with a detailed explanation of the explicit calculation for the first channel and a comprehensive discussion of the differences for the other channels. Each contribution was projected according to the tensor decomposition of the hadron and leptonic tensors, ensuring that the explicit angular structure was fully retained.

The real emission corrections were presented for all three original channels and the additional three channels, which are only present at this higher level of precision. The focus was again on the detailed explanation of the intricacies connected with the next-to-leading order calculations, such as the multitude of possible interaction channels and the introduction of ghost terms to eliminate unphysical polarization states of external gluons. The explicit calculation was presented in detail for the qq-channel and all relevant differences for the other channels were discussed. In each contribution, the angular structure is retained, and all divergences arising in the real corrections are made explicit to prepare them for the subtraction steps.

This chapter concluded with the merger of real and virtual corrections, followed by the systematic subtraction of collinear divergences via splitting functions. This final step yielded the finite hard partonic structure functions at next-to-leading order, which is the crowning achievement of this thesis. This is the first time that the hard partonic cross section has

been calculated in a fully differential form, with the explicit dependency on the angular distribution given by the decomposition of the leptonic tensor retained.

The groundwork laid out in this thesis provides several promising avenues for future investigations. A natural and immediate extension of this work is the numerical study of phenomenological applications. The hard partonic structure functions derived in this thesis are formulated for direct use in the factorization theorem, where they can be convoluted with global fits of PDFs and FFs. This would allow for next-to-leading order predictions of angular-dependent observables in SIDIS, such as $\cos\phi$ and $\cos 2\phi$ modulations. These observables are of particular relevance for the upcoming Electron-Ion Collider, where high-precision angular measurements will be a key part of the physics program.
Another important direction in which the research can be extended is by including transverse momentum resummation. While the fixed-order results presented here are valid in the regime of large transverse momentum, they become unreliable at low transverse momentum due to large contributions of logarithms. Through resummation techniques, one can systematically account for these logarithms, thereby extending the validity of the predictions to lower transverse momenta. This provides the possibility to match the results for high transverse momenta in the regime of intermediate transverse momenta to the results obtained through the use of transverse momentum dependent PDFs, which best describe the regime of low transverse momentum.
Furthermore, the analysis presented in this work could be extended to include polarized particles. Expanding the presented calculation to include longitudinally or transversely polarized particles would allow for a more detailed exploration of spin asymmetries.

In conclusion, this thesis presents the first complete analytical calculation of angular-dependent SIDIS at high transverse momentum at next-to-leading order. The results are fully differential and ready to use for further studies. The technical challenges encountered, ranging from the overwhelming number of contributions to the tracking of divergences and the subtraction of collinear divergences, were met with a modular and automated computational strategy, which is not only easily reproducible but also extendable for future investigations.
The results obtained offer a solid foundation for both theoretical exploration and experimental comparison in the era of high-precision SIDIS at the Electron-Ion Collider.

Appendix A

Intermediate Results at Leading-Order

The matrix elements projected onto the tensor decomposition in term of Mandelstam variables are:

$$\tilde{\mathcal{V}}_{1\mu\nu}\overline{\sum}\mathcal{M}_s^{\mu}\mathcal{M}_s^{*\nu} = -8\pi C_F\alpha_s(1-\epsilon)\mu^{2\epsilon}\frac{Q^2t(1-\epsilon)-Q^2u-tu-u^2}{Q^2s} \tag{A.1}$$

$$\tilde{\mathcal{V}}_{2\mu\nu}\overline{\sum}\mathcal{M}_s^{\mu}\mathcal{M}_s^{*\nu} = -8\pi C_F\alpha_s(1-\epsilon)\mu^{2\epsilon}\frac{u}{Q^2} \tag{A.2}$$

$$\tilde{\mathcal{V}}_{3\mu\nu}\overline{\sum}\mathcal{M}_s^{\mu}\mathcal{M}_s^{*\nu} = 8\pi C_F\alpha_s(1-\epsilon)\mu^{2\epsilon}\frac{1}{Qs}\sqrt{\frac{st}{u}} \tag{A.3}$$

$$\tilde{\mathcal{V}}_{4\mu\nu}\overline{\sum}\mathcal{M}_s^{\mu}\mathcal{M}_s^{*\nu} = -8\pi C_F\alpha_s(1-\epsilon)\mu^{2\epsilon}\frac{t}{s} \tag{A.4}$$

$$\begin{aligned}\tilde{\mathcal{V}}_{1\mu\nu}\overline{\sum}\mathcal{M}_t^{\mu}\mathcal{M}_t^{*\nu} = {} & 8\pi C_F\alpha_s(1-\epsilon)\mu^{2\epsilon} \\ & \times\left(\frac{Q^2\left(t^2-4tu+u^2\right)}{t(t+u)^2}-\frac{u}{Q^2}+\frac{\epsilon st+\epsilon su+t^2-4tu+u^2}{t^2+tu}\right)\end{aligned} \tag{A.5}$$

$$\tilde{\mathcal{V}}_{2\mu\nu}\overline{\sum}\mathcal{M}_t^{\mu}\mathcal{M}_t^{*\nu} = -8\pi C_F\alpha_s(1-\epsilon)\mu^{2\epsilon}\frac{u(Q^2-s)^2}{Q^2(t+u)^2} \tag{A.6}$$

$$\tilde{\mathcal{V}}_{3\mu\nu}\overline{\sum}\mathcal{M}_t^{\mu}\mathcal{M}_t^{*\nu} = -8\pi C_F\alpha_s(1-\epsilon)\mu^{2\epsilon}\frac{(Q^2-s)(t-u)}{Qt(t+u)^2}\sqrt{\frac{st}{u}} \tag{A.7}$$

$$\tilde{\mathcal{V}}_{4\mu\nu}\overline{\sum}\mathcal{M}_t^{\mu}\mathcal{M}_t^{*\nu} = -8\pi C_F\alpha_s(1-\epsilon)\mu^{2\epsilon}\frac{s(\epsilon(t+u)^2-2tu)}{t(t+u)^2} \tag{A.8}$$

$$\tilde{\mathcal{V}}_{1\mu\nu}\overline{\sum}\mathcal{M}_s^{\mu}\mathcal{M}_t^{*\nu} = 8\pi C_F\alpha_s(1-\epsilon)\mu^{2\epsilon}\frac{\epsilon Q^2 st(t+u) - u\left(-2Q^2st + \left(Q^4\right)s + \left(Q^6\right) + s^2t\right)}{Q^2st(t+u)} \tag{A.9}$$

$$\tilde{\mathcal{V}}_{2\mu\nu}\overline{\sum}\mathcal{M}_s^{\mu}\mathcal{M}_t^{*\nu} = 8\pi C_F\alpha_s(1-\epsilon)\mu^{2\epsilon}\frac{u(Q^2-s)}{Q^2(t+u)} \tag{A.10}$$

$$\tilde{\mathcal{V}}_{3\mu\nu}\overline{\sum}\mathcal{M}_s^{\mu}\mathcal{M}_t^{*\nu} = -4\pi C_F\alpha_s\mu^{2\epsilon}\frac{Q^2(\epsilon s - \epsilon t + t - 3u) + \epsilon s^2 + t(3\epsilon s + u) + 2t^2 - u^2}{Q(t+u)}\sqrt{\frac{u}{st}} \tag{A.11}$$

$$\tilde{\mathcal{V}}_{4\mu\nu}\overline{\sum}\mathcal{M}_s^{\mu}\mathcal{M}_t^{*\nu} = 8\pi C_F\alpha_s\mu^{2\epsilon}\left(\epsilon^2 + \frac{\epsilon u\left(s(s+u) - Q^4\right)}{st(t+u)} + \frac{u}{t+u}\right) . \tag{A.12}$$

Since the first four projections are symmetric it holds $\tilde{\mathcal{V}}_{k\mu\nu}\overline{\sum}\mathcal{M}_s^{\mu}\mathcal{M}_t^{*\nu} = \tilde{\mathcal{V}}_{k\mu\nu}\overline{\sum}\mathcal{M}_t^{\mu}\mathcal{M}_s^{*\nu}$ for $k = 1, 2, 3, 4$. For $k = 5$ it is

$$\tilde{\mathcal{V}}_{5\mu\nu}\overline{\sum}\mathcal{M}_s^{\mu}\mathcal{M}_t^{*\nu} = -\tilde{\mathcal{V}}_{5\mu\nu}\overline{\sum}\mathcal{M}_t^{\mu}\mathcal{M}_s^{*\nu} = 4\pi\mathrm{i}C_F\alpha_s\sqrt{\frac{u}{st}}\frac{1}{Q}\left(Q^2(1-\epsilon) - u(1-\epsilon)\right) , \tag{A.13}$$

which vanishes in the sum of all leading-order contributions. All other projections vanish.

Appendix B

Selected Mathematica Code

B.1 Code for the Calculation of Virtual Corrections

The first function needs as an external variable the function SIDISqqVirtNLOAmplitude[[i]]. This is the virtual correction Feynman diagram *vi*, generated with FeynArts and translated to `FeynCalc` using the built-in function FCFAConvert, where the loop momentum is set to be l. Furthermore the replacement "rep" replaces scalar products of momenta with the respective squares, where the masslessness of the external particles is taken into account. Lastly the replacement "useMandelstam" replaces those squares by the correct Mandelstam variables.
The function for the simplification and the reduction due to Passarino-Veltman of the virtual corrections is given by:

SIDISqqVirtNLOAmplitudeIntegrated[*i*_] := Module[{amp, contractedAmp, diracSimplifiedAmp, tidAmp, paVeAmp, finalAmp},
(*Extract the amplitude*)
amp = SIDISqqVirtNLOAmplitude[[i]];
(*SUN and Dirac algebra simplifications*)
contractedAmp = Contract[DiracSimplify[SUNSimplify[amp, Expanding → False]]];
(*Trace and Dot simplifications*)
tidAmp = DotSimplify[FCTraceFactor[contractedAmp]];
(*Tensor Integral Decomposition*)
paVeAmp = TID[tidAmp, *l*, ToPaVe → True] /. rep /. useMandelstam;
(*Dirac algebra simplifications again if needed*)
diracSimplifiedAmp = DiracSimplify[Contract[paVeAmp]] /. rep /. useMandelstam;
(*Replace Mandelstam variables and factorize*)

finalAmp = diracSimplifiedAmp /. $(h$:A0|B0|C0|D0)[y___] :>
TrickMandelstam[$h[y], s, t, u, -Q^2$];
(*Collect and factorize final expression*)
Collect2[finalAmp, {A0, B0, C0, D0}, Factoring→
Function[z, Factor2[TrickMandelstam[$z, \{s, t, u, -Q^2\}$]]]]]

For the interference with the born level term, the summation over spins and polarizations, and projection onto the angular structure defined by the decomposition of the hadronic tensor in Section 3.3 the next function needs:
The integrated amplitude calculated above, the leading-order amplitudes SIDISqqLOAmplitude generated by FeynArts and translated to `FeynCalc`, written in a list, and the tensors $\tilde{\mathcal{V}}_k^{\mu\nu}$ written in the function "Proj".
The function is given by:

SIDISqqVirtNLOSquaredAmplitude[i_, $proj$_] := Module[ampLoop, ampTree, interference, spinSummedInterference, polarizationSummedInterference, sunSimplifiedInterference, diracSimplifiedInterference, projectedInterference, contractedInterference, mandelstamInterference, simplifiedInterference, finalSimplifiedInterference,
(*Calculate the one-loop amplitude and replace Mandelstam variables*)
ampLoop =Collect2[SIDISqqVirtNLOAmplitudeIntegrated[i], Spinor, LorentzIndex];
ampLoop = TrickMandelstam[ampLoop, $\{s, t, u, -Q^2\}$];
(*Calculate the interference with the tree-level amplitude*)
ampTree = Total[SIDISqqLOAmplitude] /. $\mu \to \nu$;
interference = ampLoop*ComplexConjugate[ampTree];
(*Perform fermion spin sum and polarization sums*)
spinSummedInterference = FermionSpinSum[interference, ExtraFactor → 1/2];
polarizationSummedInterference = DoPolarizationSums[spinSummedInterference, $k2, 0$, VirtualBoson → True];
(*Apply SUN simplifications*)
sunSimplifiedInterference = polarizationSummedInterference/SUNN;
sunSimplifiedInterference = SUNSimplify[sunSimplifiedInterference, Explicit → True, SUNNToCACF → True];
(*Contract and simplify Dirac algebra*)
diracSimplifiedInterference = Contract[DiracSimplify[sunSimplifiedInterference]] /. rep /. useMandelstam;
(*Apply the given projector and contract indices*)
projectedInterference = diracSimplifiedInterference*Proj[proj];

```
contractedInterference = Contract[projectedInterference] /. rep /. useMandelstam;
(*Replace Mandelstam variables again after contraction*)
mandelstamInterference = TrickMandelstam[contractedInterference, s, t, u, -Q^2];
(*Final collection and simplification*)
simplifiedInterference = Collect2[mandelstamInterference, B0, C0, D0];
finalSimplifiedInterference = Collect2[ FeynAmpDenominatorExplicit[simplifiedInterference] /. rep /. useMandelstam /. introducealphas /. D → 4 - 2 Epsilon, {B0,C0,D0}];
finalSimplifiedInterference]
```

where the replacement "introducealphas" replaces the strong coupling constant $g_s^2 \to 4\pi\alpha_s$. The full program for the calculation of virtual corrections to the qq-channel as well as the qg- and gq-channels is provided in an extra file[1].

B.2 Code for the Identification and Replacement of $1/(1-w)$ Poles

The real corrections contain terms that are divergent for $w \to 1$, after phase space integration. These terms need to be identified and the poles need to be made explicit by the introduction of plus distributions. The first function "explicitW" brings all the terms with a factor of $1/(1-w)$ in a standard form:

```
explictW[term_, w_] := ReplaceAll[
ReplaceAll[term, (x_)^(b_. + a_.Epsilon) :>Factor[x]^(b + a Epsilon)],
{((1 - w)c_)^(b_. + a_.Epsilon) :> (1 - w)^(b + aEpsilon) c^(b + aEpsilon),
((-1 + w)c_)^(b_. + a_.Epsilon) :> (1 - w)^(b + aEpsilon)(-c)^(b + aEpsilon)}];
```

Now that all divergent terms are in the same form they can be replaced. This is done by a slightly modified version of the built-in function "ToDistribution", which was not able to find all divergent terms and also often crashed due to extreme calculation times. The modified function is:

```
MyToDistribution[term,phaseSpaceFactor_, w_] := ReleaseHold[ReleaseHold[
Map2[Factor2,
Map2[(Times[phaseSpaceFactor, #1]&),
Collect2[
```

[1] And is available, upon request, at `https://github.com/DissKunzelmann/PhD`.

```
Apart1[term, w], w,IsolateNames → KK]] ]
/.{(1 − w)^(a_.Epsilon − 1) :>
(
1/(a Epsilon) DeltaFunction[1 − w]+
 PlusDistribution[1/(1 − w)]+
a Epsilon PlusDistribution[ Log[1 − w]/(1 − w)]+
1/2 a^2 Epsilon^2 PlusDistribution[Log[1 − w]^2/(1 − w)]+
1/6 a^3 Epsilon^3 PlusDistribution[Log[1 − w]^3/(1 − w)]
),
(1 − w)^(a_. Epsilon − 2) :>
−DeltaFunctionPrime[1 − w]/ Epsilon+
(
PlusDistribution[1/(1 − w)^2]+
(a Epsilon) PlusDistribution[Log[1 − w]/(1 − w)^2]+
1/2 a^2 Epsilon^2 PlusDistribution[Log[1 − w]^2/(1 − w)^2]+
1/6 a^3 Epsilon^3 PlusDistribution[Log[1 − w]^3/(1 − w)^2]
),
(1 − w)^(a_. Epsilon − 3) :>
DeltaFunctionDoublePrime[1 − w]/(2 Epsilon)+
PlusDistribution[(1 − w)^(−3)]+
(a Epsilon PlusDistribution[Log[1 − w]/(1 − w)^3])+
(a^2 Epsilon^2 PlusDistribution[Log[1 − w]^2/(1 − w)^3]/2)+
(a^3 Epsilon^3 PlusDistribution[Log[1 − w]^3/(1 − w)^3]/6)
}]];
```

The replacements for $(1-w)^{-2-\epsilon}$ and $(1-w)^{-3-\epsilon}$ are not needed in the calculation in this thesis.

Appendix C

Programs and Tools

This appendix collects programs and tools used during the course of the dissertation. In accordance with the "Eigenständigkeitserklärung" these are:

Mathematica by Wolfram Research was used as the backbone of the symbolic computation. It was used extensively throughout the calculation to simplify expressions and collect results. `Mathematica` also provided a excellent basis for the more specialized packages used in the calculation.

FeynCalc [230–233] is the most relevant package used in conjuction with `Mathematica`. It provides all manner of specialized functions for the analytical manipulation of expression. Most notably it is able to evaluate Dirac traces, calculate color factors, and simplify expressions.

FeynArts [249] provides an automated way of generating machine readable Feynman diagrams. It was used to generate all diagrams used in this thesis.

PackageX [251] provides a list of analytic expressions for the scalar Passarino-Veltman integrals, which were used in the calculation of the virtual corrections. The list provided by `PackageX` was used as the integrated function `PaXEvaluate` in `FeynCalc`.

FeynHelpers [250] is a package for `Mathematica`, which provided a seamless integration of `FeynCalc`, `FeynArts` and `PackageX` into `Mathematica`.

PaperPal is a generative AI tool, which was used to organize scientific papers and streamline the search for relevant information. In addition, it was used to correct spelling errors and improve the writing in this thesis.

ChatGPT is another generative AI tool, which was used to find relevant references, streamline the generation of `Mathematica` code, find bugs in that code, and to improve the writing in this thesis.

DeepL an AI-based translation software, used for the translation of the Abstract into German, and for the translation of scientific papers from foreign languages (non-german and non-english).
All generative AI tools were, in accordance with the guidelines of the University of Tübingen from the 30.04.2024, only used as tools and all generated output was critically reviewed (see "Erweiterte Erklärung zur Verwendung generativer Künstlicher Intelligenz").

GoogleScholar was as a great resource for finding scientific papers and the original journal publications.

OneDrive offered a way to store my work safely and allowed for remote access, which was of special importance during the shutdown time during Corona.

OneNote was used to keep notes, work through publications, and to make some calculations by hand.

GitHub was used to store and share code and results.

TexStudio provided a user friendly interface to typeset this thesis in LaTeX, where biblatex served as powerful tool to manage references.

InkScape is powerful tool for the creation of vector graphics. It was used to design all vector graphics in this thesis. (Figure 2.1 is a direct output from `Mathematica`.)

Turnitin was used to check the thesis for potentially missing citations.

Appendix D

Eigenständigkeitserklärung

Ich erkläre hiermit, dass ich die zur Promotion eingereichte Arbeit mit dem Titel: “Angular Structure of High Transverse Momentum Production in Semi-Inclusive Deep Inelastic Scattering at Next-to-Leading Order” selbständig verfasst, nur die angegebenen Quellen und Hilfsmittel benutzt und wörtlich oder inhaltlich übernommene Stellen (alternativ: Zitate) als solche gekennzeichnet habe. Ich erkläre, dass die Richtlinien zur Sicherung guter wissenschaftlicher Praxis der Universität Tübingen (Beschluss des Senats vom 26.02.2021) beachtet wurden. Ich versichere an Eides statt, dass diese Angaben wahr sind und dass ich nichts verschwiegen habe. Mir ist bekannt, dass die falsche Abgabe einer Versicherung an Eides statt mit Freiheitsstrafe bis zu drei Jahren oder mit Geldstrafe bestraft wird.

Datum, Unterschrift

Appendix E

Erweiterte Erklärung zur Verwendung generativer Künstlicher Intelligenz

Mir ist bewusst, dass die Nutzung mittels generativer KI erstellter Texte oder Inhalte keine Garantie für deren Qualität gewährleistet und ich die Verantwortung trage, falls es durch die Verwendung solcher Hilfsmittel zu fehlerhaften Inhalten, zu Verstößen gegen das Datenschutzrecht, Urheberrecht oder zu wissenschaftlichem Fehlverhalten (z.B. Plagiate) kommt.

Ich versichere außerdem,

- dass ich mich generativer KI-Tools lediglich als Hilfsmittel bedient habe und in der vorliegenden Arbeit mein gestalterischer Einfluss überwiegt,
- dass ich angegeben habe, welche generativen KI-Tools ich zu welchem Zweck und in welchem Umfang eingesetzt habe:
  Ich habe generative KI und KI-basierte Anwendungen (DeepL, GPT-4o, PaperPal) zum Zwecke der Übersetzung, Korrektur von Tippfehlern, Verbesserung der Lesbarkeit sowie Formulierungen dieser Dissertation verwendet. Zudem habe ich sie zur Übersetzung fremdsprachiger Fachartikel ins Englische und zur Suche nach und in Fachartikeln verwendet. Außerdem habe ich Sie zum finden von Tippfehlern und zur Aufbereitung von `Mathematica` Code verwendet. Nach der Nutzung dieser Dienste habe ich den Inhalt nach Bedarf überprüft und bearbeitet und übernehme die volle Verantwortung für den Inhalt der veröffentlichten Dissertation.

Die vorliegende Arbeit wurde bisher weder im In- noch im Ausland in gleicher oder ähnlicher Form einer anderen Prüfungsbehörde vorgelegt. Mir ist bekannt, dass ein Verstoß gegen die genannten Punkte prüfungsrechtliche Konsequenzen haben und insbesondere dazu führen kann, dass die Prüfungsleistung mit ”nicht ausreichend“ bzw. die Studienleistung mit ”nicht bestanden“ bewertet wird und bei mehrfachem oder schwerwiegendem Täuschungsversuch eine Exmatrikulation erfolgen bzw. ein Verfahren zur Entziehung eines eventuell verliehenen akademischen Titels eingeleitet werden kann.

Datum, Unterschrift

List of Figures

Bibliography

[1] T. McEvilley. *The Shape of Ancient Thought: Comparative Studies in Greek and Indian Philosophies*. Allworth, 2001. ISBN: 9781581152036.

[2] C. C. W. Taylor. *The Atomists: Leucippus and Democritus: Fragments*. University of Toronto Press, 1999. ISBN: 9781442612129.

[3] J. Dalton. "On the Absorption of Gases by Water and other Liquids". In: *Memoirs of the Literary and Philosophical Society of Manchester* 1.6 (1805), pp. 271–287.

[4] J. Dalton. *A New System of Chemical Philosophy*. Vol. 1. Printed by S. Russel for R. Bickerstaff, 1808.

[5] J. J. Thompson. "Cathode Rays". In: *The Electrician* 39 (1897), p. 104.

[6] E. Rutherford. "The scattering of α and β particles by matter and the structure of the atom". In: *The London, Edinburgh, and Dublin Philosophical Magazine and Journal of Science* 21.125 (1911), pp. 669–688.

[7] J. Chadwick. "Possible Existence of a Neutron". In: *Nature* 129.3252 (1932), p. 312.

[8] R. Hofstadter. "Electron Scattering and Nuclear Structure". In: *Rev. Mod. Phys.* 28 (3 July 1956), pp. 214–254.

[9] D. Gross and F. Wilczek. "Ultraviolet Behavior of Non-Abelian Gauge Theories". In: *Phys. Rev. Lett.* 30 (26 1973), pp. 1343–1346.

[10] H. D. Politzer. "Reliable Perturbative Results for Strong Interactions?" In: *Phys. Rev. Lett.* 30 (26 1973), pp. 1346–1349.

[11] H. D. Politzer. "Asymptotic freedom: An approach to strong interactions". In: *Physics Reports* 14.4 (1974), pp. 129–180. ISSN: 0370-1573.

[12] Engineering National Academies of Sciences and Medicine. *An Assessment of U.S.-Based Electron-Ion Collider Science*. Washington, DC: The National Academies Press, 2018. ISBN: 978-0-309-47856-4.

[13] D. Boer et al. *Gluons and the quark sea at high energies: distributions, polarization, tomography*. 2011.

[14] A. Accardi et al. *Electron Ion Collider: The Next QCD Frontier - Understanding the glue that binds us all*. 2014.

[15] R. Abdul Khalek et al. "Science Requirements and Detector Concepts for the Electron-Ion Collider". In: *Nuclear Physics A* 1026 (Oct. 2022), p. 122447. ISSN: 0375-9474.

[16] A. Airapetian et al. "Multiplicities of charged pions and kaons from semi-inclusive deep-inelastic scattering by the proton and the deuteron". In: *Physical Review D* 87.7 (Apr. 2013). ISSN: 1550-2368.

[17] M. Aghasyan et al. "Transverse-momentum-dependent multiplicities of charged hadrons in muon-deuteron deep inelastic scattering". In: *Phys. Rev. D* 97 (3 Feb. 2018), p. 032006.

[18] A. Bacchetta et al. "Extraction of partonic transverse momentum distributions from semi-inclusive deep-inelastic scattering, Drell-Yan and Z-boson production". In: *Journal of High Energy Physics* 2017.6 (June 2017). ISSN: 1029-8479.

[19] A. Bacchetta et al. "Erratum to: Extraction of partonic transverse momentum distributions from semi-inclusive deep-inelastic scattering, Drell-Yan and Z-boson production". In: *Journal of High Energy Physics* 2019.6 (June 2019). ISSN: 1029-8479.

[20] I. Scimemi and A. Vladimirov. "Non-perturbative structure of semi-inclusive deep-inelastic and Drell-Yan scattering at small transverse momentum". In: *Journal of High Energy Physics* 2020.6 (June 2020). ISSN: 1029-8479.

[21] M. Bury et al. "PDF bias and flavor dependence in TMD distributions". In: *Journal of High Energy Physics* 2022.10 (Oct. 2022). ISSN: 1029-8479.

[22] A. Bacchetta et al. "Unpolarized transverse momentum distributions from a global fit of Drell-Yan and semi-inclusive deep-inelastic scattering data". In: *Journal of High Energy Physics* 2022.10 (Oct. 2022). ISSN: 1029-8479.

[23] V. Moos, I. Scimemi, A. Vladimirov, and P. Zurita. "Extraction of unpolarized transverse momentum distributions from the fit of Drell-Yan data at N4LL". In: *Journal of High Energy Physics* 2024.5 (May 2024). ISSN: 1029-8479.

[24] A. Bacchetta, D. Boer, M. Diehl, and P. J. Mulders. "Matches and mismatches in the descriptions of semi-inclusive processes at low and high transverse momentum". In: *Journal of High Energy Physics* 2008.08 (Aug. 2008), pp. 023–023. ISSN: 1029-8479.

[25] M. Boglione, J. O. Gonzalez Hernandez, S. Melis, and A. Prokudin. "A study on the interplay between perturbative QCD and CSS/TMD formalism in SIDIS processes". In: *Journal of High Energy Physics* 2015.2 (Feb. 2015). ISSN: 1029-8479.

[26] J. Collins et al. "Relating transverse-momentum-dependent and collinear factorization theorems in a generalized formalism". In: *Phys. Rev. D* 94 (3 Aug. 2016), p. 034014.

[27] J. O. Gonzalez-Hernandez, T. C. Rogers, N. Sato, and B. Wang. "Challenges with large transverse momentum in semi-inclusive deeply inelastic scattering". In: *Phys. Rev. D* 98 (11 Dec. 2018), p. 114005.

[28] A. Daleo, D. de Florian, and R. Sassot. "$\mathcal{O}(\alpha_s^2)$ QCD corrections to the electroproduction of hadrons with high transverse momentum". In: *Phys. Rev. D* 71 (3 Feb. 2005), p. 034013.

[29] B.A. Kniehl, G. Kramer, and M. Maniatis. "Erratum to: "Inclusive production of single hadrons with finite transverse momenta in deep-inelastic scattering at next-to-leading order" [Nucl. Phys. B 711 (2005) 345]". In: *Nuclear Physics B* 720.1 (2005), p. 231. ISSN: 0550-3213.

[30] B.A. Kniehl, G. Kramer, and M. Maniatis. "Inclusive production of single hadrons with finite transverse momenta in deep-inelastic scattering at next-to-leading order". In: *Nuclear Physics B* 711.1 (2005), pp. 345–366. ISSN: 0550-3213.

[31] B. Wang, J. O. Gonzalez-Hernandez, T. C. Rogers, and N. Sato. "Large transverse momentum in semi-inclusive deeply inelastic scattering beyond lowest order". In: *Phys. Rev. D* 99 (9 May 2019), p. 094029.

[32] Y. Koike and J. Nagashima. "Double spin asymmetries for large-pT hadron production in semi-inclusive DIS". In: *Nuclear Physics B* 660.1 (2003), pp. 269–288. ISSN: 0550-3213.

[33] Y. Koike and J. Nagashima. "Erratum to: "Double spin asymmetries for large-pT hadron production in semi-inclusive DIS" [Nucl. Phys. B 660 (2003) 269]". In: *Nuclear Physics B* 742.1 (2006), pp. 312–316. ISSN: 0550-3213.

[34] Y. Koike, J. Nagashima, and W. Vogelsang. "Resummation for polarized semi-inclusive deep-inelastic scattering at small transverse momentum". In: *Nuclear Physics B* 744.1 (2006), pp. 59–79. ISSN: 0550-3213.

[35] D. A. Glaser. “Some Effects of Ionizing Radiation on the Formation of Bubbles in Liquids”. In: *Phys. Rev.* 87 (4 Aug. 1952), pp. 665–665.

[36] W. Heisenberg. “Über den Bau der Atomkerne. I”. de. In: *Eur. Phys. J. A* 77.1-2 (Jan. 1932), pp. 1–11.

[37] E. Wigner. “On the Consequences of the Symmetry of the Nuclear Hamiltonian on the Spectroscopy of Nuclei”. In: *Phys. Rev.* 51 (2 Jan. 1937), pp. 106–119.

[38] T. Nakano and K. Nishijima. “Charge Independence for V-particles*”. In: *Progress of Theoretical Physics* 10.5 (Nov. 1953), pp. 581–582. ISSN: 0033-068X.

[39] K. Nishijima. “Charge Independence Theory of V Particles*”. In: *Progress of Theoretical Physics* 13.3 (Mar. 1955), pp. 285–304. ISSN: 0033-068X.

[40] M. Gell-Mann. “The interpretation of the new particles as displaced charge multiplets”. en. In: *Il Nuovo Cimento* 4.S2 (Apr. 1956), pp. 848–866.

[41] M. Gell-Mann. “The Eightfold Way: A Theory of strong interaction symmetry”. In: (Mar. 1961).

[42] Y. Ne’eman. “Derivation of strong interactions from a gauge invariance”. In: *Nuclear Physics* 26.2 (1961), pp. 222–229. ISSN: 0029-5582.

[43] M. Gell-Mann. “A schematic model of baryons and mesons”. In: *Physics Letters* 8.3 (1964), pp. 214–215. ISSN: 0031-9163.

[44] G Zweig. “An SU_3 model for strong interaction symmetry and its breaking; Version 1”. In: (Jan. 1964).

[45] G Zweig. “An SU_3 model for strong interaction symmetry and its breaking; Version 2”. In: (Feb. 1964).

[46] V. E. Barnes et al. “Observation of a Hyperon with Strangeness Minus Three”. In: *Phys. Rev. Lett.* 12 (8 Feb. 1964), pp. 204–206.

[47] W. Pauli. “The Connection Between Spin and Statistics”. In: *Phys. Rev.* 58 (8 Oct. 1940), pp. 716–722.

[48] H. L. Anderson, E. Fermi, E. A. Long, and D. E. Nagle. “Total Cross Sections of Positive Pions in Hydrogen”. In: *Phys. Rev.* 85 (5 Mar. 1952), pp. 936–936.

[49] T. M. Hahn et al. “Neutrons and Gamma-Rays from the Proton Bombardment of Beryllium”. In: *Phys. Rev.* 85 (5 Mar. 1952), pp. 934–934.

[50] O. W. Greenberg. “Spin and Unitary-Spin Independence in a Paraquark Model of Baryons and Mesons”. In: *Phys. Rev. Lett.* 13 (20 1964), pp. 598–602.

[51] M. Y. Han and Y. Nambu. "Three-Triplet Model with Double SU(3) Symmetry". In: *Phys. Rev.* 139 (4B Aug. 1965), B1006–B1010.

[52] M. Breidenbach et al. "Observed Behavior of Highly Inelastic Electron-Proton Scattering". In: *Phys. Rev. Lett.* 23 (16 Oct. 1969), pp. 935–939.

[53] E. D. Bloom et al. "High-Energy Inelastic $e-p$ Scattering at 6° and 10°". In: *Phys. Rev. Lett.* 23 (16 Oct. 1969), pp. 930–934.

[54] S. L. Glashow, J. Iliopoulos, and L. Maiani. "Weak Interactions with Lepton-Hadron Symmetry". In: *Phys. Rev. D* 2 (7 Oct. 1970), pp. 1285–1292.

[55] M. Kobayashi and T. Maskawa. "CP-Violation in the Renormalizable Theory of Weak Interaction". In: *Progress of Theoretical Physics* 49.2 (Feb. 1973), pp. 652–657. ISSN: 0033-068X.

[56] J. -E. Augustin et al. "Discovery of a Narrow Resonance in e^+e^- Annihilation". In: *Phys. Rev. Lett.* 33 (23 Dec. 1974), pp. 1406–1408.

[57] J. J. Aubert et al. "Experimental Observation of a Heavy Particle J". In: *Phys. Rev. Lett.* 33 (23 Dec. 1974), pp. 1404–1406.

[58] S. W. Herb et al. "Observation of a Dimuon Resonance at 9.5 GeV in 400-GeV Proton-Nucleus Collisions". In: *Phys. Rev. Lett.* 39 (5 Aug. 1977), pp. 252–255.

[59] F. Abe et al. "Observation of Top Quark Production in $\overline{p}p$ Collisions with the Collider Detector at Fermilab". In: *Phys. Rev. Lett.* 74 (14 Apr. 1995), pp. 2626–2631.

[60] S. Abachi et al. "Observation of the Top Quark". In: *Phys. Rev. Lett.* 74 (14 Apr. 1995), pp. 2632–2637.

[61] C. N. Yang and R. L. Mills. "Conservation of Isotopic Spin and Isotopic Gauge Invariance". In: *Phys. Rev.* 96 (1 1954), pp. 191–195.

[62] R. K. Ellis, W. J. Stirling, and B. R. Webber. *QCD and Collider Physics*. Cambridge Monographs on Particle Physics, Nuclear Physics and Cosmology. Cambridge University Press, 1996.

[63] F. Halzen and A. D. Martin. *Quarks and Leptons: An Introductory Course in Modern Particle Physics*. Wiley, 1984. ISBN: 978-0-471-88741-6.

[64] M. Peskin and D. Schroeder. *An Introduction to quantum field theory*. Reading, USA: Addison-Wesley, 1995. ISBN: 978-0-201-50397-5.

[65] M. D. Schwartz. *Quantum Field Theory and the Standard Model*. Cambridge University Press, 2013. ISBN: 978-1-107-03473-0.

[66] H. Baum. *Eichfeldtheorie*. Springer Spektrum, 2009. ISBN: 978-3-642-38538-4.

[67] B. Hall. *Lie Groups, Lie Algebras, and Representations*. Springer International Publishing, 2003. ISBN: 978-3-319-13466-6.

[68] A. Knapp. *Lie Groups Beyond an Introduction*. Birkhäuser Basel, 2002. ISBN: 978-0-8176-4259-4.

[69] J. Hilgert and K.-H. Neeb. *Lie-Gruppen und Lie-Algebren*. Vieweg+Teubner Verlag, 1991. ISBN: 978-3-528-06432-7.

[70] V. Varadarajan. *Lie Groups, Lie Algebras, and Their Representations*. Springer-Verlag New York, 1984. ISBN: 978-0-387-90969-1.

[71] F. Peter and H. Weyl. "Die Vollständigkeit der primitiven Darstellungen einer geschlossenen kontinuierlichen Gruppe". In: *Mathematische Annalen* 97 (1 1927), pp. 737–755.

[72] M. Gell-Mann. "Symmetries of Baryons and Mesons". In: *Phys. Rev.* 125 (3 1962), pp. 1067–1084.

[73] H. Casimir. "Rotation of a Rigid Body in Quantum Mechanics". PhD thesis. Rijksuniversiteit Leiden, 1931.

[74] I. Schur. "Neue Begründung der Theorie der Gruppencharaktere". In: *Sitzungsberichte der Königlich Preußischen Akademie der Wissenschaften* (1905), pp. 406–432.

[75] F. Kunzelmann. "NLO Corrections to the Production of Heavy Quarks in the Collision of Transversely Polarized Hadrons". Master's thesis. Universität Tübingen, 2020.

[76] P. A. M. Dirac and R. H. Fowler. "The quantum theory of the electron". In: *Proceedings of the Royal Society of London. Series A, Containing Papers of a Mathematical and Physical Character* 117.778 (1928), pp. 610–624.

[77] G. Leibbrandt. "Introduction to noncovariant gauges". In: *Rev. Mod. Phys.* 59 (4 1987), pp. 1067–1119.

[78] L. D. Faddeev and V. N. Popov. "Feynman diagrams for the Yang-Mills field". In: *Physics Letters B* 25.1 (1967), pp. 29–30. ISSN: 0370-2693.

[79] K. Wilson. "Confinement of quarks". In: *Phys. Rev. D* 10 (8 1974), pp. 2445–2459.

[80] T. DeGrand. "LATTICE QCD AT THE END OF 2003". In: *International Journal of Modern Physics A* 19.09 (2004), pp. 1337–1394. ISSN: 1793-656X.

[81] T. DeGrand and C. E. Detar. *Lattice methods for quantum chromodynamics*. World Scientific, 2006.

[82] C. Gattringer and C. Lang. *Quantum Chromodynamics on the Lattice. An Introductory Presentation*. Springer-Verlag Berlin Heidelberg, 2010.

[83] J. Gasser and H. Leutwyler. "Chiral perturbation theory to one loop". In: *Annals of Physics* 158.1 (1984), pp. 142–210. ISSN: 0003-4916.

[84] G. Ecker. "Chiral perturbation theory". In: *Progress in Particle and Nuclear Physics* 35 (1995), pp. 1–80. ISSN: 0146-6410.

[85] V. Bernard and U. Meißner. "Chiral Perturbation Theory". In: *Annual Review of Nuclear and Particle Science* 57.1 (2007), pp. 33–60.

[86] V. S. Vanyashin and M. V. Terentev. "The Vacuum Polarization of a Charged Vector Field". In: *Zh. Eksp. Teor. Fiz.* 48.2 (1965), pp. 565–573.

[87] W. E. Caswell. "Asymptotic Behavior of Non-Abelian Gauge Theories to Two-Loop Order". In: *Phys. Rev. Lett.* 33 (4 July 1974), pp. 244–246.

[88] É. Sh. Egoryan and O. V. Tarasov. "Renormalization of quantum chromodynamics in the two-loop approximation in an arbitrary gauge". en. In: *Theor. Math. Phys.* 41.1 (Oct. 1979), pp. 863–867.

[89] O.V. Tarasov, A.A. Vladimirov, and A.Yu. Zharkov. "The gell-mann-low function of QCD in the three-loop approximation". In: *Physics Letters B* 93.4 (1980), pp. 429–432. ISSN: 0370-2693.

[90] S.A. Larin and J.A.M. Vermaseren. "The three-loop QCD β-function and anomalous dimensions". In: *Physics Letters B* 303.3–4 (Apr. 1993), pp. 334–336. ISSN: 0370-2693.

[91] T. van Ritbergen, J.A.M. Vermaseren, and S.A. Larin. "The four-loop β-function in quantum chromodynamics". In: *Physics Letters B* 400.3–4 (May 1997), pp. 379–384. ISSN: 0370-2693.

[92] M. Czakon. "The four-loop QCD β-function and anomalous dimensions". In: *Nuclear Physics B* 710.1–2 (Mar. 2005), pp. 485–498. ISSN: 0550-3213.

[93] T. Luthe, A. Maier, P. Marquard, and Y. Schröder. "Towards the five-loop Beta function for a general gauge group". en. In: *J. High Energy Phys.* 2016.7 (July 2016).

[94] P. A. Baikov, K. G. Chetyrkin, and J. H. Kühn. "Five-Loop Running of the QCD Coupling Constant". In: *Physical Review Letters* 118.8 (Feb. 2017). ISSN: 1079-7114.

[95] F. Herzog et al. “The five-loop beta function of Yang-Mills theory with fermions”. In: *Journal of High Energy Physics* 2017.2 (Feb. 2017). ISSN: 1029-8479.

[96] P.E. Haagensen and J.I. Latorre. “A Comprehensive Coordinate Space Renormalization of Quantum Electrodynamics to Two-Loop Order”. In: *Annals of Physics* 221.1 (Jan. 1993), pp. 77–105. ISSN: 0003-4916.

[97] H. Burkhardt and B. Pietrzyk. “Update of the hadronic contribution to the QED vacuum polarization”. In: *Physics Letters B* 513.1 (2001), pp. 46–52. ISSN: 0370-2693.

[98] H. Burkhardt and B. Pietrzyk. “Low energy hadronic contribution to the QED vacuum polarization”. In: *Phys. Rev. D* 72 (5 Sept. 2005), p. 057501.

[99] S. Mele. *Measurements of the Running of the Electromagnetic Coupling at LEP*. 2006.

[100] L. D. Landau, A. A. Abrikosov, and I. M. Khalatnikov. “On the elimination of infinities in quantum electrodynamics”. In: *Proceedings of the USSR Academy of Sciences* 95 (3 1954), pp. 497–500.

[101] M. Göckeler et al. “Is There a Landau Pole Problem in QED?” In: *Physical Review Letters* 80.19 (May 1998), pp. 4119–4122. ISSN: 1079-7114.

[102] A. Deur, S. J. Brodsky, and G. F. de Téramond. “The QCD running coupling”. In: *Progress in Particle and Nuclear Physics* 90 (Sept. 2016), pp. 1–74. ISSN: 0146-6410.

[103] J. C. Collins, D. E. Soper, and G. Sterman. “Factorization of Hard Processes in QCD”. In: (2004).

[104] E. Fermi et al. “Azione di sostanze idrogenate sulla radioattività provocata da neutroni”. In: *La Ricerca Scientifica* 2.7-8 (1934), pp. 15–31.

[105] Mark Srednicki. *Quantum Field Theory*. Cambridge University Press, 2007. ISBN: 9780521864497.

[106] J. R. Taylor. *Classical mechanics*. English. Mill Valley, California: University Science Books, 2005. ISBN: 189138922X.

[107] S. Weinberg. *The Quantum Theory of Fields*. Vol. 1. Cambridge University Press, 1995. ISBN: 9781139644167.

[108] J. A. Wheeler. “On the Mathematical Description of Light Nuclei by the Method of Resonating Group Structure”. In: *Phys. Rev.* 52 (11 Dec. 1937), pp. 1107–1122.

[109] W. Heisenberg. “Die „beobachtbaren Größen“ in der Theorie der Elementarteilchen”. In: *Zeitschrift für Physik* 120.7 (July 1943), pp. 513–538. ISSN: 0044-3328.

[110] W. Heisenberg. “Die beobachtbaren Größen in der Theorie der Elementarteilchen. II”. In: *Zeitschrift für Physik* 120.11 (Nov. 1943), pp. 673–702. ISSN: 0044-3328.

[111] W. Heisenberg. “Die beobachtbaren Größen in der Theorie der Elementarteilchen. III”. In: *Zeitschrift für Physik* 123.1 (May 1944), pp. 93–112. ISSN: 0044-3328.

[112] Lowell S. Brown. *Quantum Field Theory*. Cambridge University Press, 1992. ISBN: 9780511622649.

[113] C. Itzykson and J. B. Zuber. *Quantum Field Theory*. International Series In Pure and Applied Physics. New York: McGraw-Hill, 1980. ISBN: 978-0-486-44568-7.

[114] C. Møller. *General properties of the characteristic matrix in the theory of elementary particles*. Vol. 23 No. 1. Matematisk-Fysiske Meddelelser. Det Kongelige Danske Videnskabernes Selskab, 1945.

[115] S. Navas et al. “Review of particle physics”. In: *Phys. Rev. D* 110.3 (2024), p. 030001.

[116] M. Cannoni. “Lorentz invariant relative velocity and relativistic binary collisions”. In: *International Journal of Modern Physics A* 32.02n03 (Jan. 2017), p. 1730002. ISSN: 1793-656X.

[117] R. P. Feynman. “The Theory of Positrons”. In: *Phys. Rev.* 76 (6 1949), pp. 749–759.

[118] E. Leader and E. Predazzi. *An Introduction to Gauge Theories and Modern Particle Physics. CP-Violation, QCD and Hard Processes*. Vol. 2. Cambridge Monographs on Particle Physics, Nuclear Physics and Cosmology. Cambridge University Press, 1996.

[119] G. ’t Hooft and M. Veltman. “Diagrammar”. In: CERN Yellow Reports: Monographs (1973).

[120] M. Veltman. *Diagrammatica: The Path to Feynman Diagrams*. Cambridge Lecture Notes in Physics. Cambridge University Press, 1994.

[121] F. Bloch and A. Nordsieck. “Note on the Radiation Field of the Electron”. In: *Phys. Rev.* 52 (2 1937), pp. 54–59.

[122] T. Kinoshita. “Mass Singularities of Feynman Amplitudes”. In: *Journal of Mathematical Physics* 3.4 (1962), pp. 650–677.

[123] T. D. Lee and M. Nauenberg. “Degenerate Systems and Mass Singularities”. In: *Phys. Rev.* 133 (6B 1964), B1549–B1562.

[124] W. Pauli and F. Villars. “On the Invariant Regularization in Relativistic Quantum Theory”. In: *Rev. Mod. Phys.* 21 (3 July 1949), pp. 434–444.

[125] C.G. Bollini and J.J. Giambiagi. "Dimensional Renormalization: The Number of Dimensions as a Regularizing Parameter". In: *Nuovo Cim. B* 12 (1972), pp. 20–26.

[126] G. 't Hooft and M. Veltman. "Regularization and renormalization of gauge fields". In: *Nuclear Physics B* 44.1 (1972), pp. 189–213. ISSN: 0550-3213.

[127] G. 't Hooft. "Renormalization of massless Yang-Mills fields". In: *Nuclear Physics B* 33.1 (1971), pp. 173–199. ISSN: 0550-3213.

[128] A. A. Slavnov. "Ward identities in gauge theories". en. In: *Theor. Math. Phys.* 10.2 (Feb. 1972), pp. 99–104.

[129] J.C. Taylor. "Ward identities and charge renormalization of the Yang-Mills field". In: *Nuclear Physics B* 33.2 (1971), pp. 436–444. ISSN: 0550-3213.

[130] M. Strickland. *Relativistic Quantum Field Theory, Volume 2*. 2053-2571. Morgan & Claypool Publishers, 2019. ISBN: 978-1-64327-708-0.

[131] G. 't Hooft. "Dimensional regularization and the renormalization group". In: *Nuclear Physics B* 61 (1973), pp. 455–468. ISSN: 0550-3213.

[132] S. Weinberg. "New Approach to the Renormalization Group". In: *Phys. Rev. D* 8 (10 1973), pp. 3497–3509.

[133] W. A. Bardeen, A. J. Buras, D. W. Duke, and T. Muta. "Deep-inelastic scattering beyond the leading order in asymptotically free gauge theories". In: *Phys. Rev. D* 18 (11 Dec. 1978), pp. 3998–4017.

[134] S. B. Libby and G. Sterman. "Jet and lepton-pair production in high-energy lepton-hadron and hadron-hadron scattering". In: *Phys. Rev. D* 18 (9 Nov. 1978), pp. 3252–3268.

[135] A. H. Mueller. "Cut vertices and their renormalization: A generalization of the Wilson expansion". In: *Phys. Rev. D* 18 (10 Nov. 1978), pp. 3705–3727.

[136] R. K. Ellis et al. "Factorization and the parton model in QCD". In: *Physics Letters B* 78.2 (1978), pp. 281–284. ISSN: 0370-2693.

[137] R. K. Ellis et al. "Perturbation theory and the parton model in QCD". In: *Nuclear Physics B* 152.2 (1979), pp. 285–329. ISSN: 0550-3213.

[138] D. Amati, R. Petronzio, and G. Veneziano. "Relating hard QCD processes through universality of mass singularities". In: *Nuclear Physics B* 140.1 (1978), pp. 54–72. ISSN: 0550-3213.

[139] D. Amati, R. Petronzio, and G. Veneziano. "Relating hard QCD processes through universality of mass singularities (II)". In: *Nuclear Physics B* 146.1 (1978), pp. 29–49. ISSN: 0550-3213.

[140] G. Curci, W. Furmanski, and R. Petronzio. "Evolution of parton densities beyond leading order: The non-singlet case". In: *Nuclear Physics B* 175.1 (1980), pp. 27–92. ISSN: 0550-3213.

[141] A. V. Efremov and A. V. Radyushkin. "Field theory approach to processes with large momentum transfer. I. Deep inelastic scattering". en. In: *Theor. Math. Phys.* 44.1 (July 1980), pp. 573–584.

[142] A. V. Efremov and A. V. Radyushkin. "Field theory approach to processes with large momentum transfer II. Production of massive lepton pairs". en. In: *Theor. Math. Phys.* 44.2 (Aug. 1980), pp. 664–673.

[143] A. V. Efremov and A. V. Radyushkin. "Field theory approach to processes with large momentum transfer. III. Gauge theories". en. In: *Theor. Math. Phys.* 44.3 (Sept. 1980), pp. 774–784.

[144] G. T. Bodwin. "Factorization of the Drell-Yan cross section in perturbation theory". In: *Phys. Rev. D* 31 (10 May 1985), pp. 2616–2642.

[145] J. C. Collins, D. E. Soper, and G. Sterman. "All-order factorization for Drell-Yan cross sections". In: *Physics Letters B* 134.3 (1984), pp. 263–268. ISSN: 0370-2693.

[146] J. C. Collins, D. E. Soper, and G. Sterman. "Factorization for short distance hadron-hadron scattering". In: *Nuclear Physics B* 261 (1985), pp. 104–142. ISSN: 0550-3213.

[147] J. C. Collins, D. E. Soper, and G. Sterman. "Soft gluons and factorization". In: *Nuclear Physics B* 308.4 (1988), pp. 833–856. ISSN: 0550-3213.

[148] J. C. Collins and D. E. Soper. "The Theorems of Perturbative QCD". In: *Annual Review of Nuclear and Particle Science* 37.Volume 37, (1987), pp. 383–409. ISSN: 1545-4134.

[149] J. C. Collins. "Hard scattering in QCD with polarized beams". In: *Nuclear Physics B* 394.1 (1993), pp. 169–199. ISSN: 0550-3213.

[150] S. Bailey et al. "Parton distributions from LHC, HERA, Tevatron and fixed target data: MSHT20 PDFs". In: *The European Physical Journal C* 81.4 (Apr. 2021). ISSN: 1434-6052.

[151] J. Collins. "New Definition of TMD Partion Densities". In: *International Journal of Modern Physics: Conference Series* 04 (Jan. 2011), pp. 85–96. ISSN: 2010-1945.

[152] M. G. Echevarría, A. Idilbi, and I. Scimemi. "Soft and collinear factorization and transverse momentum dependent parton distribution functions". In: *Physics Letters B* 726.4–5 (Nov. 2013), pp. 795–801. ISSN: 0370-2693.

[153] John Collins. *Foundations of Perturbative QCD*. Cambridge Monographs on Particle Physics, Nuclear Physics and Cosmology. Cambridge University Press, 2011.

[154] V. N. Gribov and L. N. Lipatov. "Deep inelastic ep scattering in perturbation theory". In: *Sov. J. Nucl. Phys.* 15.4 (1972), pp. 438–450.

[155] L. N. Lipatov. "The parton model and perturbation theory". In: *Sov. J. Nucl. Phys.* 20.1 (1975), pp. 94–102.

[156] G. Altarelli and G. Parisi. "Asymptotic freedom in parton language". In: *Nuclear Physics B* 126.2 (1977), pp. 298–318. ISSN: 0550-3213.

[157] Y. L. Dokshitzer. "Calculation of the structure functions for deep inelastic scattering and e+ e-annihilation by perturbation theory in quantum chromodynamics". In: *Zh. Eksp. Teor. Fiz* 73 (1977), p. 1216.

[158] W. Furmanski and R. Petronzio. "Singlet parton densities beyond leading order". In: *Physics Letters B* 97.3 (1980), pp. 437–442. ISSN: 0370-2693.

[159] A. Gonzalez-Arroyo and C. Lopez. "Second-order contributions to the structure functions in deep inelastic scattering (III). The singlet case". In: *Nuclear Physics B* 166.3 (1980), pp. 429–459. ISSN: 0550-3213.

[160] E.G. Floratos, R. Lacaze, and C. Kounnas. "Space and time like cut vertices in QCD beyond the leading order - non-singlet sector". In: *Physics Letters B* 98.1 (1981), pp. 89–95. ISSN: 0370-2693.

[161] E.G. Floratos, D.A. Ross, and C.T. Sachrajda. "Higher-order effects in asymptotically free gauge theories: (II). Flavour singlet Wilson operators and coefficient functions". In: *Nuclear Physics B* 152.3 (1979), pp. 493–520. ISSN: 0550-3213.

[162] "Higher-order effects in asymptotically free gauge theories: the anomalous dimensions of Wilson operators: E.G. Floratos, D.A. Ross and C.T. Sachrajda, Nucl. Phys. B129 (1977) 66". In: *Nuclear Physics B* 139.4 (1978), pp. 545–546. ISSN: 0550-3213.

[163] E.G. Floratos, C. Kounnas, and R. Lacaze. "Higher order QCD effects in inclusive annihilation and deep inelastic scattering". In: *Nuclear Physics B* 192.2 (1981), pp. 417–462. ISSN: 0550-3213.

[164] A. González-Arroyo, C. López, and F.J. Ynduráin. "Second-order contributions to the structure functions in deep inelastic scattering (I). Theoretical calculations". In: *Nuclear Physics B* 153 (1979), pp. 161–186. ISSN: 0550-3213.

[165] E.G. Floratos, R. Lacaze, and C. Kounnas. "Space- and time-like cut vertices in QCD beyond the leading order—The singlet sector". In: *Physics Letters B* 98.4 (1981), pp. 285–290. ISSN: 0370-2693.

[166] E.G. Floratos, D.A. Ross, and C.T. Sachrajda. "Higher-order effects in asymptotically free gauge theories: The anomalous dimensions of Wilson operators". In: *Nuclear Physics B* 129.1 (1977), pp. 66–88. ISSN: 0550-3213.

[167] G. Curci, W. Furmanski, and R. Petronzio. "Evolution of parton densities beyond leading order: The non-singlet case". In: *Nuclear Physics B* 175.1 (1980), pp. 27–92. ISSN: 0550-3213.

[168] R. Mertig and W. L. van Neerven. "The calculation of the two-loop spin splitting functions P (1) ij (x)". In: *Zeitschrift für Physik C Particles and Fields* 70.4 (May 1996), pp. 637–653. ISSN: 1431-5858.

[169] W. Vogelsang. "Rederivation of the spin-dependent next-to-leading order splitting functions". In: *Phys. Rev. D* 54 (3 Aug. 1996), pp. 2023–2029.

[170] W. Vogelsang. "The spin-dependent two-loop splitting functions". In: *Nuclear Physics B* 475.1 (1996), pp. 47–72. ISSN: 0550-3213.

[171] R. K. Ellis and W. Vogelsang. "The Evolution of parton distributions beyond leading order: The Singlet case". In: (Feb. 1996).

[172] C. F. Berger. "Higher orders in $A(\alpha_s)/[1-x]_+$ of nonsinglet partonic splitting functions". In: *Phys. Rev. D* 66 (11 Dec. 2002), p. 116002.

[173] S. Moch, J.A.M. Vermaseren, and A. Vogt. "Non-singlet structure functions at three loops: Fermionic contributions". In: *Nuclear Physics B* 646.1 (2002), pp. 181–200. ISSN: 0550-3213.

[174] S. Moch, J.A.M. Vermaseren, and A. Vogt. "The three-loop splitting functions in QCD: the non-singlet case". In: *Nuclear Physics B* 688.1 (2004), pp. 101–134. ISSN: 0550-3213.

[175] A. Vogt, S. Moch, and J.A.M. Vermaseren. "The three-loop splitting functions in QCD: the singlet case". In: *Nuclear Physics B* 691.1 (2004), pp. 129–181. ISSN: 0550-3213.

[176] A. Vogt, S. Moch, and J.A.M. Vermaseren. "The three-loop splitting functions in QCD". In: *Nuclear Physics B - Proceedings Supplements* 152.1 (2006), pp. 110–115. ISSN: 0920-5632.

[177] S. Moch et al. "Four-loop non-singlet splitting functions in the planar limit and beyond". In: *Journal of High Energy Physics* 2017.10 (Oct. 2017). ISSN: 1029-8479.

[178] G. Falcioni, F. Herzog, S. Moch, and A. Vogt. "Four-loop splitting functions in QCD – The gluon-to-quark case". In: *Physics Letters B* 846 (2023), p. 138215. ISSN: 0370-2693.

[179] G. Falcioni, F. Herzog, S. Moch, and A. Vogt. "Four-loop splitting functions in QCD – The quark-quark case". In: *Physics Letters B* 842 (2023), p. 137944. ISSN: 0370-2693.

[180] S. Moch et al. "Additional moments and x-space approximations of four-loop splitting functions in QCD". In: *Physics Letters B* 849 (2024), p. 138468. ISSN: 0370-2693.

[181] G. Falcioni et al. "The double fermionic contribution to the four-loop quark-to-gluon splitting function". In: *Physics Letters B* 848 (2024), p. 138351. ISSN: 0370-2693.

[182] T. Gehrmann, A. von Manteuffel, V. Sotnikov, and T.-Z. Yang. "Complete N_f^2 contributions to four-loop pure-singlet splitting functions". In: *Journal of High Energy Physics* 2024.1 (Jan. 2024). ISSN: 1029-8479.

[183] T. Gehrmann, A. von Manteuffel, V. Sotnikov, and T.-Z. Yang. "The NfCF3 contribution to the non-singlet splitting function at four-loop order". In: *Physics Letters B* 849 (2024), p. 138427. ISSN: 0370-2693.

[184] V. Gribov and L. Lipatov. "e+ e-pair annihilation and deep inelastic ep scattering in perturbation theory". In: *Soviet Journal of Nuclear Physics* 15 (1972), pp. 675–675.

[185] H. Georgi and H. D. Politzer. "Quark decay functions and heavy hadron production in QCD". In: *Nuclear Physics B* 136.3 (1978), pp. 445–460. ISSN: 0550-3213.

[186] J.F. Owens. "On the Q^2 dependence of parton fragmentation functions". In: *Physics Letters B* 76.1 (1978), pp. 85–88. ISSN: 0370-2693.

[187] T. Uematsu. "Q^2 dependence of quark and gluon fragmentation functions in a parton picture based on QCD". In: *Physics Letters B* 79.1 (1978), pp. 97–102. ISSN: 0370-2693.

[188] J. Kalinowski, K. Konishi, and T.R. Taylor. "Jet calculus beyond leading logarithms". In: *Nuclear Physics B* 181.2 (1981), pp. 221–252. ISSN: 0550-3213.

[189] M. Stratmann and W. Vogelsang. "Next-to-leading order evolution of polarized and unpolarized fragmentation functions". In: *Nuclear Physics B* 496.1 (1997), pp. 41–65. ISSN: 0550-3213.

[190] A. Mitov, S. Moch, and A. Vogt. "Next-to-next-to-leading order evolution of non-singlet fragmentation functions". In: *Physics Letters B* 638.1 (2006), pp. 61–67. ISSN: 0370-2693.

[191] S. Moch and A. Vogt. "On third-order timelike splitting functions and top-mediated Higgs decay into hadrons". In: *Physics Letters B* 659.1 (2008), pp. 290–296. ISSN: 0370-2693.

[192] A.A. Almasy, S. Moch, and A. Vogt. "On the next-to-next-to-leading order evolution of flavour-singlet fragmentation functions". In: *Nuclear Physics B* 854.1 (2012), pp. 133–152. ISSN: 0550-3213.

[193] M. Cacciari, P. Nason, and C. Oleari. "A study of heavy flavoured meson fragmentation functions ine+e - annihilation". In: *Journal of High Energy Physics* 2006.04 (Apr. 2006), pp. 006–006. ISSN: 1029-8479.

[194] A. De Roeck and R.S. Thorne. "Structure functions". In: *Progress in Particle and Nuclear Physics* 66.4 (2011), pp. 727–781. ISSN: 0146-6410.

[195] E. Perez and E. Rizvi. "The quark and gluon structure of the proton". In: *Reports on Progress in Physics* 76.4 (Mar. 2013), p. 046201.

[196] S. Forte and G. Watt. "Progress in the Determination of the Partonic Structure of the Proton*". In: *Annual Review of Nuclear and Particle Science* 63.Volume 63, 2013 (2013), pp. 291–328. ISSN: 1545-4134.

[197] J. Blümlein. "The theory of deeply inelastic scattering". In: *Progress in Particle and Nuclear Physics* 69 (2013), pp. 28–84. ISSN: 0146-6410.

[198] R. D. Ball et al. "Parton distribution benchmarking with LHC data". In: *Journal of High Energy Physics* 2013.4 (Apr. 2013). ISSN: 1029-8479.

[199] J. Gao, L. Harland-Lang, and J. Rojo. "The structure of the proton in the LHC precision era". In: *Physics Reports* 742 (2018), pp. 1–121. ISSN: 0370-1573.

[200] M. Diehl. "Generalized parton distributions". In: *Physics Reports* 388.2 (2003), pp. 41–277. ISSN: 0370-1573.

[201] C. Mezrag. "An Introductory Lecture on Generalised Parton Distributions". In: *Few-Body Systems* 63.3 (Aug. 2022). ISSN: 1432-5411.

[202] G. Altarelli, R.K. Ellis, G. Martinelli, and So-Young Pi. "Processes involving fragmentation functions beyond the leading order in QCD". In: *Nuclear Physics B* 160.2 (1979), pp. 301–329. ISSN: 0550-3213.

[203] W. Furmanski and R. Petronzio. "Lepton-hadron processes beyond leading order in quantum chromodynamics". In: *Zeitschrift für Physik C Particles and Fields* 11.4 (Dec. 1982), pp. 293–314. ISSN: 1434-6052.

[204] D. de Florian, M. Stratmann, and W. Vogelsang. "QCD analysis of unpolarized and polarized Λ-baryon production in leading and next-to-leading order". In: *Phys. Rev. D* 57 (9 May 1998), pp. 5811–5824.

[205] A. Daleo, C.A. García Canal, and R. Sassot. "Order-α_s^2 corrections to one-particle inclusive processes in DIS". In: *Nuclear Physics B* 662.1–2 (July 2003), pp. 334–358. ISSN: 0550-3213.

[206] D. Anderle, D. de Florian, and Y. Rotstein Habarnau. "Towards semi-inclusive deep inelastic scattering at next-to-next-to-leading order". In: *Physical Review D* 95.3 (Feb. 2017). ISSN: 2470-0029.

[207] J. Haug. "Towards SIDIS at NNLO: Cross-Section and Structure Functions". Master's thesis. Universität Tübingen, 2021.

[208] M. Abele, D. de Florian, and W. Vogelsang. "Approximate NNLO QCD corrections to semi-inclusive DIS". In: *Physical Review D* 104.9 (Nov. 2021). ISSN: 2470-0029.

[209] M. Abele, D. de Florian, and W. Vogelsang. "Threshold resummation at N^3LL accuracy and approximate N^3LO corrections to semi-inclusive DIS". In: *Physical Review D* 106.1 (July 2022). ISSN: 2470-0029.

[210] L. Bonino, T. Gehrmann, and G. Stagnitto. "Semi-Inclusive Deep-Inelastic Scattering at Next-to-Next-to-Leading Order in QCD". In: *Phys. Rev. Lett.* 132 (25 June 2024), p. 251901.

[211] L. Bonino et al. *NNLO corrections to SIDIS coefficient functions*. 2024.

[212] S. Goyal et al. "Next-to-Next-to-Leading Order QCD Corrections to Polarized Semi-Inclusive Deep-Inelastic Scattering". In: *Phys. Rev. Lett.* 133 (21 Nov. 2024), p. 211905.

[213] S. Goyal et al. "NNLO QCD corrections to unpolarized and polarized SIDIS". In: *Phys. Rev. D* 111 (9 May 2025), p. 094007.

[214] J. Haug and F. Wunder. *Single-valued representation of unpolarized and polarized semi-inclusive deep inelastic scattering at next-to-next-to-leading order*. 2025.

[215] J. D. Bjorken. "Asymptotic Sum Rules at Infinite Momentum". In: *Phys. Rev.* 179 (5 Mar. 1969), pp. 1547–1553.

[216] A. Bacchetta, U. D'Alesio, M. Diehl, and C. Miller. "Single-spin asymmetries: The Trento conventions". In: *Physical Review D* 70.11 (Dec. 2004). ISSN: 1550-2368.

[217] R. Meng, F. I. Olness, and D. E. Soper. "Semi-inclusive deeply inelastic scattering at electron-proton colliders". In: *Nuclear Physics B* 371.1 (1992), pp. 79–110. ISSN: 0550-3213.

[218] P. Nadolsky. "Multiple parton radiation in hadroproduction at lepton-hadron colliders". PhD thesis. 2001.

[219] R. Meng, F. I. Olness, and D. E. Soper. "Semi-inclusive deeply inelastic scattering at small q_T". In: *Physical Review D* 54.3 (Aug. 1996), pp. 1919–1935. ISSN: 1089-4918.

[220] T. P. Cheng and A. Zee. "Coincidence Electroproduction and Scaling in the Regge Region". In: *Phys. Rev. D* 6 (3 Aug. 1972), pp. 885–893.

[221] F. Ravndal. "On the azimuthal dependence of semi-inclusive, deep inelastic electroproduction cross sections". In: *Physics Letters B* 43.4 (1973), pp. 301–303. ISSN: 0370-2693.

[222] R. L. Kingsley. "Azimuthal dependence of semi-inclusive deep-inelastic reactions in the parton model". In: *Phys. Rev. D* 10 (5 Sept. 1974), pp. 1580–1586.

[223] G. Köpp, R. Maciejko, and P.M. Zerwas. "Angular asymmetries in hadron distributions of neutrino-nucleon reactions in quantum chromodynamics". In: *Nuclear Physics B* 144.1 (1978), pp. 123–140. ISSN: 0550-3213.

[224] A. Méndez. "QCD predictions for semi-inclusive and inclusive leptoproduction". In: *Nuclear Physics B* 145.1 (1978), pp. 199–220. ISSN: 0550-3213.

[225] A. Méndez, A. Raychaudhuri, and V.J. Stenger. "QCD effects in semi-inclusive neutrino processes". In: *Nuclear Physics B* 148.3 (1979), pp. 499–512. ISSN: 0550-3213.

[226] A. Méndez and T. Weiler. "QCD predictions for jet transverse momentum in leptoproduction". In: *Physics Letters B* 83.2 (1979), pp. 221–226. ISSN: 0370-2693.

[227] H. Georgi. *Lie Algebras In Particle Physics: from Isospin To Unified Theories*. Frontiers in Physics. Taylor and Francis Group, 2000. ISBN: 9780429499210.

[228] H. Fritzsch, M. Gell-Mann, and H. Leutwyler. "Advantages of the color octet gluon picture". In: *Physics Letters B* 47.4 (1973), pp. 365–368. ISSN: 0370-2693.

[229] V. I. Borodulin, R. N. Rogalyov, and S. R. Slabospitskii. *CORE 3.1 (COmpendium of RElations, Version 3.1)*. 2017.

[230] V. Shtabovenko, R. Mertig, and F. Orellana. *FeynCalc 9.3: New features and improvements*. 2020.

[231] V. Shtabovenko, R. Mertig, and F. Orellana. “New developments in FeynCalc 9.0”. In: *Computer Physics Communications* 207 (2016), pp. 432–444. ISSN: 0010-4655.

[232] R. Mertig, M. Böhm, and A. Denner. “Feyn Calc - Computer-algebraic calculation of Feynman amplitudes”. In: *Computer Physics Communications* 64.3 (1991), pp. 345–359. ISSN: 0010-4655.

[233] V. Shtabovenko, R. Mertig, and F. Orellana. “FeynCalc 10: Do multiloop integrals dream of computer codes?” In: *Computer Physics Communications* 306 (Jan. 2025), p. 109357. ISSN: 0010-4655.

[234] V. Barone, A. Drago, and P. Ratcliffe. “Transverse polarisation of quarks in hadrons”. In: *Physics Reports* 359.1-2 (2002), pp. 1–168. ISSN: 0370-1573.

[235] R. P. Feynman. “A Relativistic Cut-Off for Classical Electrodynamics”. In: *Phys. Rev.* 74 (8 1948), pp. 939–946.

[236] R. P. Feynman. “Space-Time Approach to Quantum Electrodynamics”. In: *Phys. Rev.* 76 (6 1949), pp. 769–789.

[237] J. Schwinger. “Quantum Electrodynamics. III. The Electromagnetic Properties of the Electron—Radiative Corrections to Scattering”. In: *Phys. Rev.* 76 (6 1949), pp. 790–817.

[238] G. C. Wick. “Properties of Bethe-Salpeter Wave Functions”. In: *Phys. Rev.* 96 (4 1954), pp. 1124–1134.

[239] G. Passarino and M. Veltman. “One-loop corrections for e^+e^- annihilation into $\mu^+\mu^-$ in the Weinberg model”. In: *Nuclear Physics B* 160.1 (1979), pp. 151–207. ISSN: 0550-3213.

[240] Z. Bern, L. Dixon, and D. Kosower. “Dimensionally regulated one-loop integrals”. In: *Physics Letters B* 302.2-3 (1993), pp. 299–308. ISSN: 0370-2693.

[241] V. E. Lyubovitskij, F. Wunder, and A. S. Zhevlakov. “New ideas for handling of loop and angular integrals in D-dimensions in QCD”. In: *Journal of High Energy Physics* 2021.6 (June 2021). ISSN: 1029-8479.

[242] G. Sterman. *An Introduction to Quantum Field Theory*. Cambridge University Press, 1993. ISBN: 9780511622618.

[243] W. L. Van Neerven. “Dimensional regularization of mass and infrared singularities in two-loop on-shell vertex functions”. In: *Nuclear Physics B* 268.2 (1986), pp. 453–488. ISSN: 0550-3213.

[244] W. Beenakker, H. Kuijf, W. L. van Neerven, and J. Smith. “QCD corrections to heavy-quark production in $p\overline{p}$ collisions”. In: *Phys. Rev. D* 40 (1 1989), pp. 54–82.

[245] P. Aurenche et al. “Scheme invariant higher order QCD predictions for large pT photoproduction reactions”. In: *Nuclear Physics B* 286 (1987), pp. 553–591. ISSN: 0550-3213.

[246] D. de Florian, G. F. R. Sborlini, and G Rodrigo. “Two-loop QED corrections to the Altarelli-Parisi splitting functions”. In: *Journal of High Energy Physics* 2016.56 (10 2016). ISSN: 1029-8479.

[247] G. Altarelli, R.K. Ellis, and G. Martinelli. “Large perturbative corrections to the Drell-Yan process in QCD”. In: *Nuclear Physics B* 157.3 (1979), pp. 461–497. ISSN: 0550-3213.

[248] L. E. Gordon and W. Vogelsang. “Polarized and unpolarized prompt photon production beyond the leading order”. In: *Phys. Rev. D* 48 (7 Oct. 1993), pp. 3136–3159.

[249] T. Hahn. “Generating Feynman diagrams and amplitudes with FeynArts 3”. In: *Computer Physics Communications* 140.3 (2001), pp. 418–431. ISSN: 0010-4655.

[250] V. Shtabovenko. “FeynHelpers: Connecting FeynCalc to FIRE and Package-X”. In: *Computer Physics Communications* 218 (2017), pp. 48–65. ISSN: 0010-4655.

[251] H. Patel. “Package-X: A Mathematica package for the analytic calculation of one-loop integrals”. In: *Computer Physics Communications* 197 (2015), pp. 276–290. ISSN: 0010-4655.

Acknowledgments

First and foremost, I would like to thank my advisor, Prof. Dr. Werner Vogelsang, for granting me the opportunity to pursue this thesis and for introducing me to the field of high-energy physics. I am grateful for the guidance he provided and for the profound insights into theoretical physics he shared. I am especially appreciate his leadership style, which fostered an engaging, collegial and relaxed working atmosphere in his group throughout my PhD.

I thank apl. Prof. Dr. Marc Schlegel for kindly providing a second appraisal for this thesis and for always sharing his knowledge.

I am grateful to the Forschungsgruppe FOR2926 and its spokesperson, Prof. Dr. Vladimir Braun, for the stimulating scientific exchange and engaging seminars that greatly enriched my PhD experience.

I thank apl. Prof. a.D. Dr. Thomas Gutsche for deepening my interest in teaching, for offering many valuable insights, and for all the enjoyable conversations we shared during lunch and coffee brakes.

I thank all current and former scientific staff, PhD students, and Master's students of the seventh floor for creating an enjoyable working atmosphere, for many refreshing conversations, and for inspiring seminars. In particular, I am grateful to Santiago Lopez-Portillo-Chavez, Johannes Scheller, and Robin Feser for making me feel at home at the university at the beginning of my PhD, and to all other members of the seventh floor for keeping that feeling alive.

Special thanks go to Daniel Rein, Ignacio Borca, Juliane Haug, Fabian Wunder, Alexander Fürlinger and Oliver Schürle for their time and effort in proofreading this thesis.

I thank Sabine Werner for all the administrative work she carried out behind the scenes and for her incredibly quick and reliable help whenever I needed support.

I thank the skiing club of the University of Tübingen (ASCT), who welcomed me warmly during the early days of the Corona pandemic and provided much-needed social interaction at that time. I am grateful for the many enjoyable activities, both in winter and especially during the summer.

I thank the many friends I found through kayaking, in particular Lara Wicke, Sarah Rogulj, and Yannick Wolfhard, who where always there when I needed them.

I thank my family for always believing in me and supporting me throughout this journey, for enabling me to pursue physics as my field of study, and for offering counsel and guidance whenever it was needed. I especially thank Greta Bösinger for supporting me in every possible way, for making my life more fulfilling, and for ensuring that it never gets boring.

Thank you all!